Numerical and Experimental Investigation on Single Side, Double Side and Heat Sink Assisted Submerged Arc Welded Butt Joint of Stainless Steels

A Thesis Submitted in

Partial Fulfillment of the Requirements

For the Degree of

DOCTOR OF PHILOSOPHY

by

SRIDHAR P V S S
(Roll No. 10610309)

DEPARTMENT OF MECHANICAL ENGINEERING
INDIAN INSTITUTE OF TECHNOLOGY GUWAHATI
GUWAHATI – 781 039

August 2020

Department of Mechanical Engineering
Indian Institute of Technology Guwahati
Guwahati-781039
INDIA

Certificate

It is certified that the work contained in the thesis entitled **"Numerical and Experimental Investigation on Single Side, Double Side and Heat Sink Assisted Submerged Arc Welded Butt Joint of Stainless Steels**" submitted by **Mr. SRIDHAR P.V.S.S** to the Indian Institute of technology Guwahati for the award of the Degree of Doctor of Philosophy has been carried out under our supervision in the Department of Mechanical Engineering, Indian Institute of Technology Guwahati. This work has not been submitted elsewhere for the award of any other degree or diploma.

Prof. Pankaj Biswas
Professor
Department of Mechanical Engineering
Indian Institute of Technology Guwahati
Guwahati-781039, India.

Prof. Pinakeswar Mahanta
Professor
Department of Mechanical Engineering
Indian Institute of Technology Guwahati
Guwahati-781039, India.

Date: 04/09/2020

Dedicated to

My beloved Parents…

ACKNOWLEDGEMENTS

I would like to express my heartfelt gratitude towards all those who have immensely helped me during this long arduous journey and eventually assisted me to emerge as an experienced researcher and a mature individual.

First and foremost I must express my deepest sense of appreciation and respect for my Thesis Supervisors, Prof.Pankaj Biswas and Prof. Pinakeswar Mahanta for providing me the opportunity to work under their supervision. Their persistent patience and friendliness in the moments of difficulties have always been remembered and also their constant encouragement have played a crucial role in writing the thesis and bringing it to its present form.

I would like to thank my doctoral committee chairman and members Prof. K.S.R.K Murthy, Prof. Sachin D Kore, Prof. Manas Das, and Prof. Chandan Das for carefully reading the reports at various stages of evaluation and providing many useful comments, which have helped in the development of this thesis.

My sincere gratefulness to past and present departmental heads Prof.D.Chakraborty, Prof. P. Mahanta, Prof.A.K.Dass and Prof.S.K.Dwivedy for their kind permission for enrollment, registration and several important supports at IIT Guwahati. I am also grateful to all the faculty members of Mechanical Engineering Department for giving me a comfortable and friendly environment for pursuing my research. I would also like to acknowledge the contribution of office staff, for helping me with various academic as well as non-academic issues.

I would like to express my sense of gratitude to Mr.N.K Das, Assistant Workshop Superintendent and all the staffs of the central workshop especially Mr. Dilip Chetri, Mr.Mrunal sarma, Mr.Minesh Medhi, Mr.Nidul Saikia, Mr.Chandan Banikya, Mr.Gwamchar Baro, Mr.Gakul Das, and Mr.Amzad Khan for extending their help in fabrication of the different experimental set-ups for this research work.

I sincerely acknowledge the assistance received from Dr.Rithuraj Saikia, Mr.Sanjib Sarma, Mr. Nip Borah, Mr.Saifuddin Ahmed, Mr.Jiten Basumatary, and Mr.Monouranjan Dowarah in various experimental proceedings.

I would also like to express my gratitude to the Central Instrument Facility, IIT Guwahati for providing technical support for materials characterization works.

The financial support of this research, which was provided by the Department of Mechanical Engineering, Indian Institute of Technology Guwahati, is gratefully acknowledged.

The most important support for this work came from my parents, (Late) Sri. P.Prabhakar Rao and Smt. P.Usha Rani, for encouraging me to go still further at every point of life. I would like to thank my extended family for all of their love and support through the years, especially at peak of the economy encouraged me to pursue Ph.D on a modest stipend.

Finally the friends form an important part of this long and enduring journey, and without their constant support and encouragement, the completion of this thesis perhaps would have been an impossible task. I would like to thank my friends Manish Kushwaha, Prof.Saurav Suman, Vishnu Nair, Dr.Srikant Prasad, Dr.Arpan Mandal, Dr.Biswajit Parida, Prof.V.Sateeshkumar, Dr.A.Muthuraja, Dr.Prakash Sahoo, Dr.Sumit Aggarwal, Dr.Biplab Das, Dr.Vikas Kumar, Saibal Barik, Paradeep Pankaj, Mateshwar Singh, Abhiraj, Shailesh, Rituraj, Kaushik Pal, Bhaskar Chakarborthi, Subhasis Mazumdar who have made my work memorable. I would therefore be forever grateful to all my friends and well-wishers.

I consider myself privileged and fortunate to work in the Indian Institute of Technology Guwahati. Above all, I am thankful to the Almighty.

14th August, 2020

SRIDHAR P V S S

ABSTRACT

Stainless steels have been extensively used in various industries such as power, petrochemical, nuclear, automotive and other sectors owing to their good corrosive and anti-rust properties. However, certain critical issues like increased distortion, residual stresses and reduced corrosion resistance, still remain an open concern, when these materials are joined with high heat input process like submerged arc welding (SAW). The submerged arc welding process is widely used in fabrication of thick materials due to its ability to achieve greater consistency, higher productivity, deeper penetration, and high deposition rates. The primary process variables in a submerged arc welding (SAW) process that affect the weld quality are welding current (polarity and magnitude), voltage, speed, electrode diameter, length of stickout, composition of flux and width and depth of flux layer. Among these current, voltage and speed are very important process variables. It is important to understand the effect of these process variables in order to achieve good weld quality. Consequently in this thesis experimental and numerical studies were conducted to understand the effect of process variables on weld qualities and to understand the thermo-mechanical behavior of the submerged arc welded joints. The main objective of the present investigation is to study the thermo-mechanical behavior and characterization of submerged arc welded joints and also to develop a suitable technique to minimize distortion.

In this research work, numerical models were developed based on actual experimental bead geometry to study the thermo-mechanical behavior of the weldments. The transient thermal analysis was conducted by incorporation of a moving volumetric heat source with temperature dependent material properties. The heat loss due to convection was considered all over the surface of the plate except at the weld zone. Also the effect of heat loss through fixture was neglected in this study. Subsequently, nonlinear elasto-plastic thermo-mechanical analysis was conducted to determine the residual stresses and distortion. The 3D nonlinear transient elasto-plastic thermo-mechanical model can be effectively used to predict the weld induced distortion in thick stainless steel plates fabricated using submerged arc welding. The results of thermal history and distortion obtained from numerical analysis were compared with the experimental outputs. The deviation of peak temperature between numerical analysis and experiments was

found to be 4.75%, while the deviation between maximum predicted distortion and measured distortion was 9.82%.

The prediction of weld induced distortions of large structures using equivalent loading technique was performed by considering average plastic strains. Here the actual transient phenomena of the weld was simulated by considering the application of separate average loads at start, middle and end regions along the weld line. The results obtained from numerical model were validated with experimental results. This numerical model was further extended to a large welded structure for prediction of weld induced distortion using the proposed equivalent load based technique. For large welding structure, the proposed method was computationally more efficient than thermo-mechanical elastic plastic method. The numerical analysis in this work was performed using the finite element method based software package ANSYS^{TM}.

In the present experimental investigation square butt joints were fabricated with top and bottom reinforcements and without any edge preparation in order to reduce the time and cost involved with edge preparation. Single response and multi response optimization was carried out in order determine the most influential parameters. The mechanical properties of the weldment were studied according to ASTM E8 standard. From the single response optimization technique, it was found that welding current exhibits more to the tensile strength of the weld joint, while for multi response optimization it was welding voltage that contributes highest, followed by welding speed, welding current and length of stickout. It was understood from optimization techniques that the length of stickout shows least influence on weld qualities for a square butt joint. In order to minimize the angular distortion in butt welds a heat sink method was employed. To carry the experiment using heat sink method a complete heat sink setup was designed and developed. The conventional welds were compared with that of heat sink to study the effects of heat sink on angular distortion and mechanical properties. It was found that a maximum reduction in angular distortion of about 10.66% was obtained for welds fabricated with heat sink to that of conventional welds. Enhancement in ultimate tensile strength of 25.82% and yield strength of about 15% were observed for heat sink assisted welds in comparison with conventional welding. Heat sink was effective in removing heat from the welded region and thereby enhanced weld qualities and reduced the angular distortion for square butt joints.

Also in this investigation double side weld joints were fabricated and overall bead profile as well as mechanical properties was investigated. The maximum tensile strength of double sided welded joints reached up to 93.70% of the base material, while a marked enhancement in percentage of elongation of 50.2% to that of base material was observed. These prominent effects on mechanical properties may be due to second weld pass. Finally, the effect of surface active flux on weld bead geometry was studied. The surface active flux TiO_2 enhanced the bead width, while Cr_2O_3 increased the penetration. Also mixture of all fluxes gives better penetration as compared with individual flux. The surface active fluxes were beneficial in improving the bead geometry, without the increase of heat input.

Key words:

Transient thermal analysis, Non-linear, Elasto-plastic, Thermo-mechanical analysis, Equivalent loading technique, Distortion, Optimization, Weldment characterization, Heat sink, Double-sided-weld, Bead profile, Surface active element.

CONTENTS

SL No.		TITLE	Page No.
		Abstract	i
		Contents	iv
		List of Figures	viii
		List of Tables	xiii
1		**Introduction**	1
	1.0	Preamble	1
	1.1	Overview of Submerged Arc Welding	1
	1.2	Residual stress	2
	1.3	Weld induced distortion	4
	1.4	Motivation	4
	1.5	Research objectives	5
	1.6	Contribution of the thesis	6
	1.7	Limitation of the thesis	6
	1.7	Target application	7
	1.8	Organization of the thesis	7
2		**Literature Review**	9
	2.0	General Introduction	9
	2.1	Thermo mechanical analysis on submerged arc welding	9
	2.2	Mechanical characterization studies	13
	2.3	Optimization of welding process parameters	18
	2.4	Closure	22
	2.5	Scope of the thesis	22
3		**Theoretical background and Modeling methodology**	24
	3.0	**Introduction**	24
	3.1	Thermal modelling	24
		3.1.1 Assumptions in the FE model	25
	3.2	3D-FE formulation for heat transfer analysis	25
		3.2.1 Boundary conditions	27
		3.2.2 Derivation of heat flow matrices	28
	3.3	Heat source model	30
	3.4	Thermo-mechanical analysis	30
		3.4.1 Formulation of 3D Finite element stress strain relationship	30
		3.4.2 Structural analysis with material nonlinearities	33
	3.5	Procedure for 3D FE-Analysis	35
	3.6	Equivalent method based on average plastic strain	38
		3.6.1 Average plastic strain	39
		3.6.2 Calculation of equivalent load	39
		3.6.3 Application of equivalent load	40

	3.7	Taguchi's method	42
	3.8	Analysis of variance (ANOVA)	43
	3.9	Theory of Grey relational analysis	44
	3.10	Summary	46
4		**Experimental methodology**	47
	4.0	Introduction	47
	4.1	Fixed welding parameters	47
	4.2	Arc start	48
	4.3	Pilot experiments	48
		4.3.1 Observations from Pilot experiments	48
	4.4	Fixture design	49
		4.4.1 Conventional fixture	49
		4.4.2 Heat sink fixture	50
	4.5	SAW flux	52
	4.6	SAW electrode	52
	4.7	Submerged arc welding machine	53
	4.8	Sample preparation	53
	4.9	Experimentation	54
		4.9.1 Experimental SET-I Determination of influencing process parameters of commercial grade stainless steel in SAW	55
		4.9.2 Experimental SET-II Comparative studies on effect of process parameters on mechanical properties for normal welding and welding with heat sink in single side SAW	57
		4.9.3 Experimental SET-III Effect of process variables on bead geometry and mechanical properties in a double sided welding	59
		4.9.4 Experimental SET –IV Effect of surface active flux on bead geometry	60
	4.10	Testing and characterization	61
		4.10.1 Temperature measurement	61
		4.10.2 Distortion and edge deflection measurement	62
		4.10.3 Tensile test	63
		4.10.4 Vickers micro hardness test	65
		4.10.4.1 Sample preparation for hardness measurement	66
		4.10.5 Microstructure and macrostructure	66
		4.10.6 Fractographic analysis	67
5		**Numerical Results and discussion**	70
	5.0	Introduction	70
	5.1	Thermo-mechanical analysis of single sided single pass Submerged arc welding (SAW)	70

5.1.1 3-D FE modelling analysis 70
5.1.2 Meshing details 72
5.1.3 Modelling of heat source 73
5.1.4 Transient thermal analysis 74
5.1.4.1 Effect of varying welding power on temperature distribution 75
5.1.4.2 Effect of varying welding speed on temperature distribution 76
5.1.4.3 Effect of varying plate thickness on temperature distribution 78
5.1.4.4 Validation of thermal history for single sided SAW FE model 79
5.1.5 Structural analysis of single sided SAW butt joint 80
5.1.5.1 Validation of structural analysis 85
5.1.6 Summary 87
5.2 Prediction of welding induced distortions in large welded Structure using equivalent loading technique 87
5.2.1 Experimental details 87
5.2.2 Methodology 88
5.2.3 Thermal Mechanical Elastic-Plastic (TMEP) method 89
5.2.4 Equivalent load method based (ELM) based on average plastic strain 93
5.2.5 Effectiveness of the proposed method 95
5.2.6 Prediction of weld induced distortion for large structure 105
5.2.7 Summary 107

6 Experimental Results and Discussion 108
6.0 Introduction 108
6.1 Optimization of welding process variables using single response and multi response optimization 108
6.1.1 Optimization of welding process variables using Taguchi method 108
6.1.1.1 Signal to Noise (S/N) Ratio 109
6.1.1.2 Confirmation test 111
6.1.2 Optimization of process variables by Taguchi Grey relational analysis 111
6.1.2.1 Confirmation experiment 116
6.1.2.2 Summary 116
6.2 Comparative study between heat sink welding and conventional welding 116
6.2.1 Thermal history 117
6.2.2 Comparison of weld cross sectional area 117
6.2.3 Comparison of tensile properties for conventional and heat sink welding 120
6.2.4 Comparison of angular distortion 122

		6.2.5 Summary	125
	6.3	Effect of process variables on bead profile and mechanical properties in a double sided (SAW) process	125
		6.3.1 Weld macrostructure	125
		6.3.2 Weld microstructure	126
		6.3.3 Microhardness	129
		6.3.4 Effect of process variables on fusion zone profile	130
		6.3.4.1 Effect of welding current	130
		6.3.4.2 Effect of welding voltage	132
		6.3.4.3 Effect of traverse speed	134
		6.3.5 Effect of process variables on tensile properties	136
		6.3.6 Comparison of angular distortion with single side SAW	140
		6.3.7 Fractrographic examination	141
		6.3.8 Influence of welding current on bead geometry for 12 mm thick plates	141
		6.3.9 Summary	144
	6.4	Effect of surface active flux on bead geometry	144
		6.4.1 Influence of surface active flux on bead width	145
		6.4.2 Influence of surface active flux on reinforcement	146
		6.4.3 Influence of surface active flux on penetration	147
		6.4.4 Summary	149
	6.5	Recommendations on selection of welding parameters	149
7		**Conclusions and Future Scope of the Work**	151
	7.0	Conclusions of the present work	151
	7.1	Future scope of work	155
8		**References**	156
9		**List of Publications**	166

LIST OF FIGURES

SL.No	Title	Page No.
Fig.1.1	(a) Thermal stresses during welding (b) Longitudinal residual stresses after welding	2
Fig.1.2	Representation of development of residual stresses in butt welding	3
Fig.1.3	Types of welding distortion	4
Fig.2.1	Measured and predicted results of angular distortion	11
Fig.2.2	TEM micrograph of weld zone (a) acicular ferrite plates and inclusions (b) irregular MA constituent distribution	16
Fig.3.1	Representation of axis system and regions of a welding plate	26
Fig.3.2	Element 3D-SOLID70	37
Fig.3.3	Element 3D-SOLID45	38
Fig.3.4	Application of equivalent loads	39
Fig.3.5	Illustration of force and moment	41
Fig.3.6	Application of load concerning the weld region and average width of inherent strain zone	41
Fig.3.7	Flow chart of grey relational analysis (GRA)	44
Fig.4.1	Fixture and dimensions of the backing bar	49
Fig.4.2	Working principle of the backing bar	50
Fig. 4.3	CAD model of the heat sink fixture	51
Fig.4.4	(a) Fabricated heat sink fixture (b) Sample mounted on heat sink fixture	51
Fig. 4.5	Submerged arc welding machine	53
Fig. 4.6	Pictorial representation of sample in tack welded condition with root gap	54
Fig. 4.7	Double side Square butt joint configuration with root gap	59
Fig.4.8	Complete setup of temperature measurement	62
Fig.4.9	Measurement of angular distortion with Coordinate measuring machine	63
Fig.4.10	Schematic of sample with measuring points	63
Fig.4.11	Tensile specimen with (a) 25 mm and (b) 50 mm gage length as per ASTM E-8 standard	64
Fig.4.12	(a) Tensile testing machine with sample (b) Extensometer attached to the sample	64
Fig.4.13	Tensile specimens with 50 mm gage length (ASTM)	65
Fig. 4.14	Vickers micro hardness testing machine	65
Fig. 4.15	Illustration of Vickers hardness indentation	65

Fig.4.16	Single disc polishing machine	67
Fig.4.17	Upright optical microscope	67
Fig.4.18	Stereo microscope (Macroscope)	67
Fig.4.19	Field emission scanning microscope	68
Fig.5.1	Illustration of SAW butt joint	71
Fig.5.2	(a) Experimental cross section (b) Developed geometry	72
Fig.5.3	3-D FE model of square butt joint	72
Fig.5.4	FE meshed model of square butt joint	73
Fig.5.5	Temperature distribution during welding process due to moving heat source	74
Fig.5.6	Temperature distribution during cooling phases at a time of 500 sec	75
Fig.5.7	Peak temperature distribution in transverse direction (a) top surface (b) bottom surface of the welded plate (power variation)	76
Fig.5.8	Peak temperature distribution in transverse direction on (a) top (b) bottom surface of the welded plate (speed variation)	77
Fig.5.9	Peak temperature distribution for varying thickness away from weld centre at (a) top surface (b) bottom surface	78
Fig.5.10	Comparison of numerical and experimental thermal profiles at 24 mm away from weld centre line	79
Fig. 5.11	Overall numerical and experimental temperature contour	80
Fig.5.12	Longitudinal residual stress distribution contour for line energy 1859 J/mm	81
Fig. 5.13	von-Mises residual stress distribution contour for line energy 1859 J/mm	82
Fig.5.14	Effect of line energy on longitudinal residual stress perpendicular to the center of weld line	83
Fig 5.15	Effect of line energy on transverse and von-Misses residual stress perpendicular to the center of weld line	83
Fig 5.16	Effect of welding line energy on longitudinal, transverse and von-Mises residual stress along weld center line	84
Fig.5.17	Illustration of measurement locations for distortion	85
Fig.5.18	Comparison between experimentally observed grid point displacement (distortion) and nodal displacement for case-I	86
Fig.5.19	Comparison between experimentally observed grid point displacement (distortion) and nodal displacement for case-III	86
Fig.5.20	Flow chart of the proposed wok	88
Fig.5.21	Application of equivalent loads concerning the weld region and average width of inherent strain zone	89
Fig.5.22	(a) Top surface of the welded butt joint, (b) Cross sectional view of the weld bead	90

Fig.5.23	Edge deflection results for experiment and TMEPA	90
Fig. 5.24	Plastic strain distribution on the top surface of the plate along the transverse direction	91
Fig.5.25	Plastic strain distribution pattern in a longitudinal and transverse direction (Top to bottom)	91
Fig. 5.26	Best fitted curve for the plastic strain distribution on the top surface along transverse direction for the points in the (a) Start, (b) End and (c) Mid regions of the welding direction respectively	93
Fig.5.27	Distribution of Equivalent transverse load along the weld line	94
Fig.5.28	Application of Equivalent load in different regions separately	94
Fig.5.29	(a) Comparative edge deflection results (b) Contour plot for vertical deformation obtained from the proposed method	95
Fig.5.30	Temperature dependent properties of C-Mn steel	96
Fig.5.31	Longitudinal plastic strain (butt joint)	97
Fig.5.32	Transverse plastic strain (butt joint)	97
Fig.5.33	Longitudinal Plastic strain (Fillet joint)	97
Fig.5.34	Transverse Plastic strain (Fillet joint)	97
Fig.5.35	Plot for plastic strain distribution (a) Butt joint model and (b) Fillet joint model	98
Fig.5.36	Transverse plastic strain with its best-fitted curve for (a) Butt joint model and (b) Fillet joint model	99
Fig.5.37	Equivalent transverse load distribution with its best-fitted curve along the weld line direction (a) Butt joint model and (b) Fillet weld joint model	100
Fig.5.38	Distortion contour diagram for butt joint model (a) TMEPA and (b) Proposed method	101
Fig.5.39	(a) Angular deformation and (b) Edge deflection plot for butt joint model	102
Fig.5.40	Distortion contour plot for the fillet joint model (a). TMEPA method, (b). Equivalent load considering start/end loads on the different width of inherent strain zone for different weld region, (c). Equivalent amount on the average width of inherent strain zone without considering the start/end loads separately	103
Fig.5.41	(a) Angular deformation and (b) Edge deflection plot for fillet joint model	104
Fig.5.42	Distortion contour plot for a larger fillet joint model (a). TMEPA method, (b). Equivalent load considering start/end loads on the different width of inherent strain zone for different weld region, (c). Equivalent load on the average width of inherent strain zone without considering the start/end loads separately	105

Fig.5.43	Schematic of Large weld structure	106
Fig.5.44	Vertical or Y- displacement contour plot	106
Fig.5.45	Overall distortion contour plot	106
Fig.6.1	Main effect plot for SN ratios	111
Fig.6.2	Main effect plot for SN ratios of Grey relational grade	115
Fig.6.3	Thermal history profile of conventional and heat sink welding (without and with water cooling)	117
Fig.6.4	Comparison of cross sectional area with and without heat sink welding	118
Fig.6.5	Fusion zone cross sectional area with (a) variation in welding current (b) variation in traverse speed for conventional and heat sink welding	120
Fig.6.6	Tensile plot for conventional and heat sink welding for welding current variation	120
Fig.6.7	Comparison of Tensile property for conventional and heat sink welding with (a) current variation (b) speed variation	121
Fig.6.8	Comparison of angular distortion between conventional and heat sink welding for variation in process variables	123
Fig.6.9	As polished macrostructure (a) Exp. No. 2, 5 and 8 (common parameter) Etched macrostructures of (b) Current variation Exp.No.3 (c) Voltage variation Exp.No.6 (d) Speed variation Exp.No.7	126
Fig.6.10	Microstructure of base metal AISI 304	127
Fig.6.11	Fusion zone and HAZ interface	127
Fig.6.12	Typical microstructure in upper mid region in a weld pool Exp.No.3	128
Fig.6.13	Microstructure of weld zone intersection of top and bottom pass in the for Exp.No.3	128
Fig.6.14	Sample of hardness indentation in the weld zone	129
Fig.6.15	Graph of micro hardness for the Exp.No.4	129
Fig.6.16	Nomenclature of the weld bead with root gap for double sided SAW process	130
Fig.6.17	Effect of welding current on (a) Bead width and reinforcement height (b) Reinforcement area and penetration area (c) Penetration depth and Bead overlap area	132
Fig.6.18	Effect of welding voltage on (a) Bead width and reinforcement height (b) Reinforcement area and penetration area (c) Penetration depth and Bead overlap area	133
Fig.6.19	Effect of traverse speed on (a) Bead width and reinforcement height (b) Reinforcement area and penetration area (c) Penetration depth and Bead overlap area	135

Fig.6.20	Tensile curve of Base metal and Exp.3	137
Fig.6.21	Results of uniaxial tensile testing for variation of (a) welding current (b) welding voltage (c) traverse speed	138
Fig.6.22	Percentage enhancement in elongation with that of base metal	139
Fig.6.23	Comparison of average angular distortion between single sided SAW and double sided SAW	140
Fig.6.24	Fracture surface of tensile specimen for Exp.4	141
Fig.6.25	Representative cross section of 12 mm thick double sided weld	142
Fig.6.26	Effect of welding current on (a) Bead width and reinforcement height (b) Reinforcement area and penetration area (c) Penetration depth and Bead overlap area for 12 mm thick plates	143
Fig.6.27	Cross-sectional view of the weld bead (a) with mixture of all fluxes (b) without flux	145
Fig.6.28	Effect of surface active flux on bead width	146
Fig.6.29	Effect of surface active flux on reinforcement height (mm)	147
Fig.6.30	Effect of surface active flux on penetration	148

LIST OF TABLES

SL.No	Title	Page No.
Table 3.1	Temperature dependent mechanical properties of SS 304	35
Table 3.2	Temperature dependent thermal properties of SS 304	35
Table 4.1	Fixed SAW parameters	47
Table 4.2	Physical quantities and their values for heat sink fixture	50
Table 4.3	Chemical compositions of OK 10.92 L flux	52
Table 4.4	Chemical composition of SA welding electrode	52
Table 4.5	Mechanical properties of the filler wire	52
Table 4.6	Specifications of SAW machine	53
Table 4.7	Chemical composition of stainless steel	56
Table 4.8	Mechanical properties of the parent metal	56
Table 4.9	Welding process parameters and their levels	56
Table 4.10	Experimental parameters in Taguchi L_{18} orthogonal array	56
Table 4.11	Chemical composition austenitic stainless steel	57
Table 4.12	Mechanical properties of the austenitic stainless steel (AISI 304)	57
Table 4.13	Welding process parameters for conventional and heat sink welding	58
Table 4.14	Experiment set for conventional and heat sink welding	58
Table 4.15	Experiment process parameters for 8 mm thick plates	60
Table 4.16	Experiment Process parameters for 12 mm thick plates	60
Table 4.17	Experimental process parameters for welding with and without surface active flux	61
Table 4.18	Detailed specification of equipment used to analyse the welded samples	68
Table 5.1	Process parameters for single sided SAW	74
Table 5.2	Parameters considered for structural analysis for 8 mm thick plate	81
Table.5.3	Numerically predicted and measured peak distortions	85
Table 5.4	Welding process parameters used in this study	88
Table 5.5	Welding parameters	96
Table 5.6	Dimensions of welded structural components	96
Table 5.7	Comparison of TMEP and ELM based on average plastic strain	107
Table 6.1	Input and output parameters for single response optimization	109
Table 6.2	Response table SN Ratios (Larger is better)	110
Table 6.3	ANOVA for SN ratios	110
Table 6.4	Input parameters and responses for Grey relational analysis	112
Table 6.5	Data processing for output performance characteristic (normalization)	113
Table 6.6	Δ_{oi} for all the responses	113
Table 6.7	Grey relational coefficients	114
Table 6.8	Grey relational grade (GRG)	114

Table 6.9	Analysis of variance (ANOVA) for SN ratios of GRG	115
Table 6.10	Results of confirmation experiments	116
Table 6.11	Process variables for conventional and heat sink welding	118
Table 6.12	Cross-sectional area of conventional and heat sink welding	119
Table 6.13	Comparison of mechanical properties between conventional and heat sink welding	122
Table 6.14	Comparison of average angular distortion between conventional and heat sink welding	124
Table 6.15	Results of effect of process variables on fusion zone profile	136
Table 6.16	Average tensile properties of double sided welds	137
Table 6.17	Average results of influence of welding current on bead profile for 12 mm thick plate	143
Table 6.18	Average bead width with and without surface active flux	145
Table 6.19	Average reinforcement height with and without surface active flux	146
Table 6.20	Average depth of penetration with and without surface active flux	148

Chapter 1

Introduction

1.0 Preamble

As civilization advances, various new materials, tools, and engineering systems have also evolved from the ages. Joining materials is inevitable to construct new structures and machine tools. The advances in materials joining technology over the period had led to an improved quality of human life. Fusion welding is a generic terminology, wherein the base material to be joined are melted through the application of heat and subsequent solidification of adjoining parts, often with or without of application of filler material to the molten pool to enhance the strength of the formed joint, Debroy and David (1995). The most common types of fusion welding processes are arc welding, resistance welding, oxy-fuel welding, laser beam welding, plasma arc welding, and electron beam welding. Among these processes, arc welding is widely used in day-to-day industrial applications due to the equipment portability and cost-effectiveness. In this work, both numerical thermo-mechanical analysis and experimental investigation was carried out on joints using submerged arc welding (SAW).

1.1 Overview of Submerged Arc Welding

The Submerged arc welding (SAW) is a category of arc welding that is an extremely versatile process of producing high-quality welds in a thicker section of materials. This process can be carried out in semi-automatic mode or fully automatic mode. In this method, an arc is struck between a bare electrode and the work piece. The welding operation is performed under a blanket of flux; hence, ultraviolet radiation and fumes that are a part of welding operation can be eliminated, unlike in other arc welding processes. The significant advantages of the SAW process are high deposition, deep penetration, smooth bead surface, and high thermal efficiency. Due to these advantages, SAW process is extensively explored in pipe welding, shipbuilding, bridge construction, and pressure vessel fabrication and motor industries. The SAW process is very capable of joining carbon-manganese, low and high alloy steels, ferritic, austenitic stainless steels as well as non-ferrous alloys like nickel, titanium, monel and other non-ferrous materials, Houldcroft (1989). However, very few limitations exist as welding must be performed in horizontal / vertical or near flat positions. The submerged arc welding is not suitable for overhead welding. Also welding may contain slag inclusions and smaller

thickness < 4.8 mm thick, burn through is likely to occur. The materials that are not possible to weld include Cast iron, Al-alloy, Mg-alloy, Pb and Zn cannot be welded, Houldcroft (1989). The process parameters used in SAW are electrode polarity, welding current, wire diameter, arc voltage, welding speed, electrode extension, electrode angle, and flux depth, Mandal (2004). Among these, the vital parameters are welding current, voltage, welding speed, and length of stickout.

1.2 Residual stress

The residual stress caused by welding poses a serious problem in fabrication of structures. The residual stress originates due to a complex mechanism, which comprises of non-uniform distribution of temperature produced by a high intensity heat source in the arc welding. As a result of which incompatible strains generate and to balance this self-equilibrating stresses retain in the welded structure even after the weldment is cooled to room temperature, thus developed stress is termed as residual stress, Mandal (2004). Due to the application of heat, material near the vicinity of molten metal expands and yields compressively and upon cooling it contracts which creates tensile residual stress particularly in longitudinal direction of the weld, Colegrove et al.(2009). This mechanism of the stress field around a weld is illustrated with Fig.1.1.

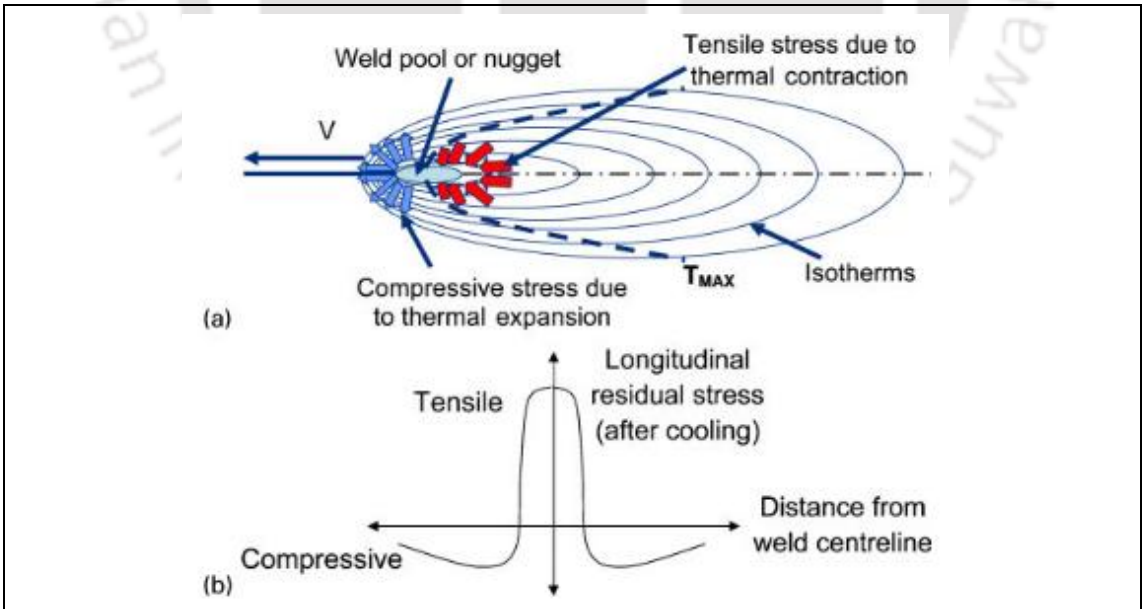

Fig.1.1 (a) Thermal stresses during welding (b) Longitudinal residual stresses after welding, Colegrove et al.(2009).

After welding is completed tensile residual stresses remain in the weld and to balance compressive stress remain far away from the weld. The tensile residual stresses developed around the weld seam are detrimental to the service life of the structure as they can decrease the toughness and fatigue strength drastically in presence of a notch. The development of residual stress in a butt welding can be explained by using the Fig.1.2.

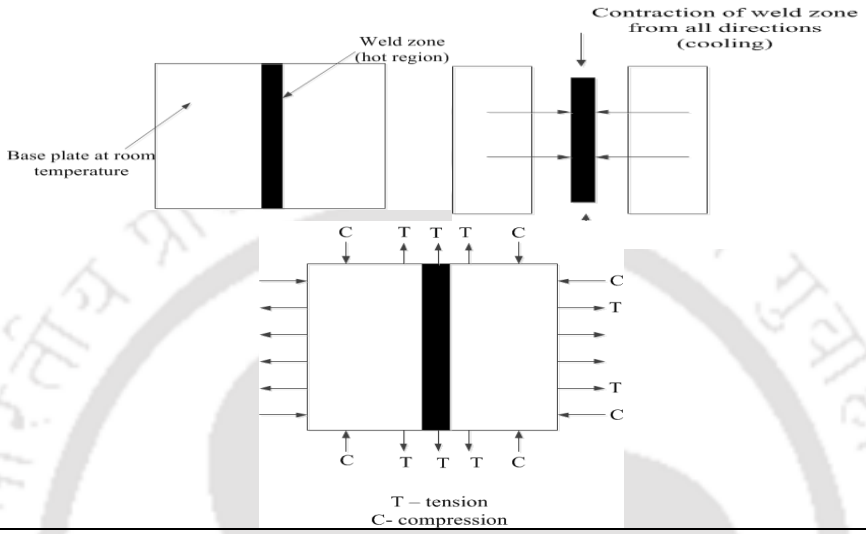

Fig.1.2 Representation of development of residual stresses in butt welding, Mandal (2017)

First consider that weld zone is free from the remaining portion of the plate as shown in Fig.1.2. Then it will contract from all directions when it is cooled to ambient temperature. But actually it is an integral part of the structure which is unaffected by heat source. As a result of which tensile forces are developed along the weld seam in longitudinal as well as transverse direction, while other portions remain in compression. This causes plastic strains to develop. As there is no external force acting on the structure, these internal forces cancels each other. Thus longitudinal tensile force will be countered by compressive force along both sides of weld line and transverse tensile force get countered by compressive force perpendicular to the weld line, Mandal (2017). Even though the concept of residual stress is simple it is difficult to predict quantitatively. The issue with residual stress is that thermal and mechanical components of stress are interlinked, and the number of inputs involved is large, Lindgren (2007). Several factors that influence the residual stress which include geometry of welded structure, its temperature dependent material properties, phase transformations, metallurgical properties and its mechanical boundary conditions, Coules (2013). The effects of residual stress are fracture and fatigue, stress corrosion cracking and distortion, Coules (2013).

1.3 Weld induced distortion

Residual stresses and distortion are primary issues associated with welding. The extensive research on residual stresses and distortion is credited, Masubuchi (1980); Ueda et al.(2012). In fusion welding, heat input is applied across faying surfaces to achieve a weld joint. The material proximate to the weld zone can be subjected to melting, heating, and cooling of adjacent portions of the weld joint. Due to this plastic thermal strain may be developed near the weld region. The result of plastic strains is weld-induced distortion. Further the weld distortions can be categorized as in-plane distortion and out-of-plane distortion, Feng (2005). The residual stresses generated during the welding are mostly concentrated near the vicinity of welded regions, whereas distortion spreads through the fabricated structure. During assembly of the components into the structure, fit-up, and misalignment problems may arise due to distortion. The various types of distortion happen during welding are shown in Fig.1.3.

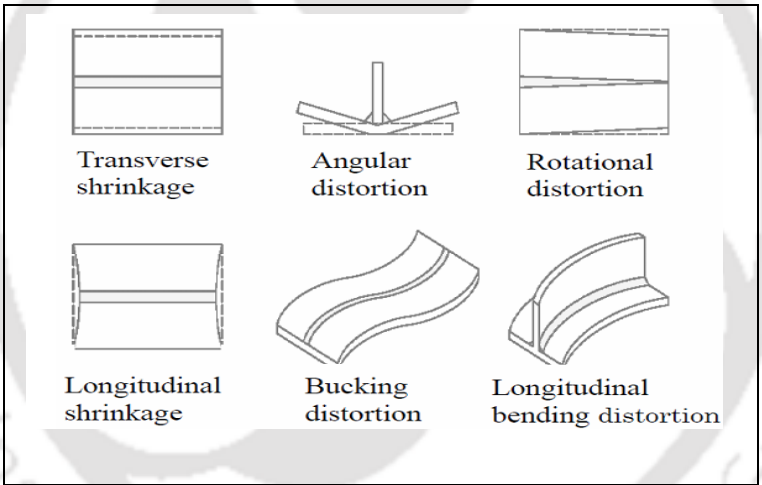

Fig.1.3 Types of welding distortion, Michaleris (2011)

The angle change that occurs due to a non- uniform thermal contraction during cooling in the thickness direction of the plate is called angular distortion. The butt and fillet joints are subjected to angular distortion. Stainless steels are sensitive to heat input, and they are more susceptible to distortion as compared with mild steels. Hence, suitable heat input and joint geometry are important while welding of stainless steel to mitigate the distortion.

1.4 Motivation

Submerged arc welding is a high productivity process to join different kinds of steels that find their application in onshore and offshore structures. The austenitic stainless steel type 304 grade is widely used in chemical, petrochemical, paper and pulp, metallurgical industries,

and power plants due to their excellent corrosion resistance, which results in low maintenance cost, Michler (2015). The fabrication of stainless steels is commonly carried out with gas tungsten arc welding, gas metal arc welding and manual metal arc welding. The Submerged arc welding (SAW) is relatively rarely used in fabrication, even though this method yields high performance and excellent quality joints. In SAW, high heat inputs are applied, which causes the distortion and formation of wanted brittle phases such as carbides along the grain boundaries in the heat-affected zone of the welded joint, Niagaj (2014). The inclusion of brittle phases can lead to reduced corrosion resistance, increased distortion, residual stress, and high incidence of in-service failures. As compared with mild steels, the austenitic stainless steels possess low room temperature thermal conductivity (14.6 W/mK) and a high mean coefficient of thermal expansion (17 μm/m^{o}C), Davis (1994) due to which these steels are more susceptible to weld distortion. In addition, the role of joint geometry, weld process variables also play a significant role in attaining the desired features for the resultant weldment. The majority of works on SS 304 have been reported on other welding processes. Very few works were reported on SS 304 with submerged arc welding. By making suitable joint geometry and selection of appropriate process variables, it is possible to reduce weld distortion and achieve excellent mechanical properties.

1.5 Research objectives

The objectives of the present work are established based on the technical gaps found in the published literature are abridged as follows:

- Numerical studies on effects of SAW process parameters on temperature distributions and residual stresses for single sided SAW using a volumetric moving heat source model.
- Development of a numerical methodology to predict the welding induced distortions in large weld structure through Improved Equivalent Load Method Based on Average Plastic Strains.
- Optimization of SAW process parameters using single response and multi response methods.
- Comparative studies of effect of process parameters on mechanical properties and angular distortion between a single sided single pass conventional welding and heat sink welding.
- Effect of process variables on bead geometry and mechanical properties in double sided welding.
- Effect of surface active flux on bead geometry.

1.6 Contribution of the thesis

The significant contributions of the present work are given as follows:

- Volumetric moving heat source model was used to simulate the temperature distributions.
- Effect of process parameters on temperature distributions and residual stresses in a single-side SAW with actual bead geometry.
- Prediction of welding induced distortions in large welded structure through Improved Equivalent Load Method based on average plastic strains.
- A detailed experimental study was carried out to evaluate the influence of process variables on weldment properties of stainless steel. Influencing parameters for individual as well as multiple quality characteristics were also proposed using Taguchi analysis and Grey-Taguchi technique.
- A new fixture was designed to carry out welding under heat sink conditions. Also the weld qualities were compared between with and without heat sink with respect to different process variables for AISI 304 steel.
- Double sided submerged arc welding (DSSAW) was conducted on AISI 304 steel by varying the process parameters. The comparative study on distortion between DSSAW with single sided SAW was carried out.
- Study on effect of surface active flux on bead geometry for AISI 304 stainless steel was explored.

1.7 Limitation of the thesis

The present research work is based on the identified technical gaps from the exhaustive literature review on submerged arc welding. From the literature review it was observed that numerical studies and fabrication of stainless steels especially austenitic stainless steels using SAW was sparsely found. In this thesis numerical and experimental studies on SAW of stainless steels was explored. The experimental work in this thesis covers square butt welding of single side, double side and heat sink assisted welding of stainless steels. Additionally, effect of surface active elements on weld bead geometry was investigated. However, Numerical simulation considering heat sink was not conducted in this study. Also, impact and corrosion studies on SAW joints were not performed in this investigation.

1.8 Target application

Austenitic stainless steels can be used in varying environments such as ambient temperature or below, and elevated temperatures due to their excellent corrosion resistance. Some areas where austenitic stainless steels find applications in industries are:

- Marine transportation, Chi et al., (2007).
- Components used in power, petrochemical industries and nuclear plants like boiler tubing, headers and steam pipes fabrication, Smith and Farrar (1993); Toma et al., (2011).

Fabrication of medium-thick plates using other welding techniques like gas metal arc welding (GMAW) and gas tungsten arc welding (GTAW) necessitates the use of more multipass to achieve the complete weld. Whereas with submerged arc welding (SAW), minimum passes are sufficient to achieve a full weld joint with high quality, and this enhances the cost-effectiveness of the whole process. Hence, with these advantages of submerged arc welding (SAW), austenitic stainless steel can be considered for fabrication in critical applications in the industry using SAW process.

1.9 Organization of the thesis

The present thesis focuses on covers the optimization of process variables for obtaining the top and bottom reinforcement in single pass of thick steel plate. One of the main goals of the research work is to reduce the angular distortion which is a major issue in stainless steel butt joints. In the present work a study was also conducted between conventional and heat sink welding of austenitic stainless steel. The thesis also focuses on effect of surface active elements on weld bead geometry. The contents of the thesis are divided into six chapters. The details are as follows:

Chapter 1 opens with brief introduction about submerged arc welding and weld distortion.

Chapter 2 explores briefly the published literature on optimization of process parameters, mechanical characterization, distortion studies and numerical simulation. The research work on double sided SAW and heat sink welding were also discussed.

Chapter 3 details the theoretical back ground and analysis on finite element formulation, Taguchi analysis and Grey-Taguchi analysis.

Chapter 4 elaborates the experimental procedure and methods followed to carry out welding. It also provides the techniques to analyze weld quality.

Chapter 5 deals elaborately the results and discussion on numerical thermo-mechanical analysis.

Chapter 6 deals with the analysis of results and discussion on the experimental work.

Chapter 7 shows the conclusions of the research work and relevant scope for future research work.

Finally the thesis is completed and ended with references.

Chapter 2

Literature Review

2.0 General Introduction

The austenitic stainless steels are widely used in fabrication industries due to their excellent corrosion resistance. Typically these are used in joining of nuclear reactor cooling pipes, pressure vessels, valve bodies and in process industries such as dairy industry, chemical and petro-chemical industries etc. Among various grades of austenitic stainless steels AISI 304 is extensively used due to superior corrosion resistance and low temperature impact strength. However, the physical properties of these steels make them prone to greater weld induced distortion when they are joined using high heat input welding process such as submerged arc welding (SAW).

In this chapter a comprehensive literature review on numerical and experimental studies on submerged arc welding are carried out. To understand the SAW process parameters and their influence on the bead geometry, metallurgical and mechanical aspects, and thermo-mechanical studies are elucidated.

The literature review in this thesis is broadly classified into following categories:

- Thermo-mechanical analysis on submerged arc welding
- Mechanical characterization studies
- Optimization of welding process parameters

The details about the literature review on above topics are presented in the subsequent sections.

2.1 Thermo-mechanical analysis on submerged arc welding

Weld thermal cycles influence various parameters such as distortion, residual stresses, and microstructure of weld and HAZ hardness. Since, local heating and cooling occurring during the welding process affects the weld thermal cycles which are critical for the process. Residual stresses and strains introduced during arc welding processes have been identified as prime contributing factors that determine the ultimate service life of the fabricated weldment namely fatigue, fracture, and stress corrosion cracking. Many experimental methods are developed to characterize the residual stresses and strains which include X-ray, neutron

diffraction, hole drilling method, Barkhausen noise method, ultrasonic, contour methods and demountable mechanical gauge measurement, Withers and Bhadeshia (2001). However, use of these methods in shop floor is restricted due high equipment cost or accuracy. Therefore application of numerical analysis based on finite element analysis is a viable option in prediction of residual stresses and weld induced distortions in welded structures.

Andersson (1978) investigated the residual stress distributions on top and bottom surfaces of the butt welded plate by SAW process using 2-D models. The phase transformation during cooling was considered due to their influence on residual stresses in weldment. Comparative studies on FE results and experimental results showed that there was close agreement between them. Wen et al. (2001) modeled the multi-wire SAW used in fabrication of thick wall pipe line to study the heat transfer characteristics of fusion and heat affected zone using 2-D and 3-D models. The geometric distortion and residual stresses can be minimized by optimization of process parameters.

Fanous et al., (2003) developed element movement technique to study residual stress in welding and compared this with element birth technique. They observed that residual stresses obtained were lesser, when welding a free plate than compared with a plate which was a part of structure. The element movement technique was better since thermal interaction between weld pool and base plate can be obtained, thereby reducing the analysis time.

Mahapatra et al., (2006, 2007) conducted numerical studies to predict temperature distributions and distortions in single side fillet and butt joints. Also, experiments are conducted to validate the numerical results. To study the effect of constraints on distortions in one side fillet joints, tack welds are made at several locations. The distortion patterns and thermal history obtained from FE model matched well with experimental results. Also, it can be inferred from their study that applying constraints at proper locations can mitigate the angular distortion in one side fillets welds fabricated using SAW.

Mahapatra et al., (2008) utilized 3D FEM to predict the angular distortion of the double pass butt weld for mild steel. Simulation process incorporates filler material deposition, and temperature-dependent material properties. Experiments are also conducted to validate the numerical results. Fig.2.1 shows the measured and predicted results of the angular distortion.

The measurements for angular distortion are recorded from the plate edge parallel to the weld line. The simulation results obtained were in close agreement with experimental values. Bhide et al., (2006) analyzed weld induced residual stresses in HSLA-65 grade steel. Experimental measurements were conducted using blind hole drilling technique to determine longitudinal residual stresses and distortion. The peak values of tensile residual stresses were identified in the weld zone and these becomes compressive far away from weld line.

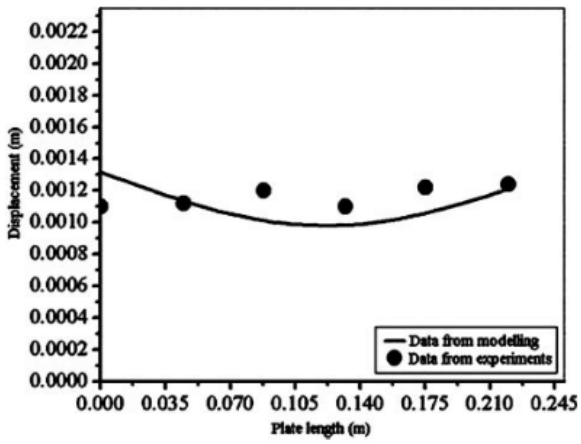

Fig.2.1 Measured and predicted results of angular distortion, Mahapatra et al., (2008)

As a result of added variation in thorough thickness stress the welding joints were subjected to longitudinal bowing distortion. The results obtained in numerical analysis matched fairly well with experimental results.

Biswas and Mandal (2010) established the welding methodology for minimizing angular distortions in single pass single sided butt welds and used FEM software ANSYS. In their study 8 to 12 mm thick M.S plates were used. They developed macros to simulate moving distributed heat source, metal deposition for accounting top and bottom reinforcements a time step and meshing scheme. Temperature distributions and distortions obtained by simulations were closely matched with experimental data and only 3 to 8% deviations were noticed. Biswas et al., (2010) developed a heat source model for estimating the thermal history and distortions in a double sided fillet joint and was found the angular distortions and peak temperatures predicted were well matched with experimentally achieved results.

A pseudolinear equivalent rigidity model was developed to predict temperature history and distortions in a bead-on-plate joint, Adak and Mandal (2010). The developed model was found to be computationally superior to the available FE code for prediction of temperature

history and edge deflections. Forouzan et al., (2012) conducted numerical simulation of arc welded spiral pipes and introduced unfural mapping (UM) technique to overcome the difficulties in adopting Goldak's double ellipsoidal model to the model. UM technique virtually unfolds the pipe into a flat surface and converts the spiral surface of the weld into a straight line. The obtained numerical data was validated with hole drilling experimental results.

Nart and Celik (2013) analysed residual stresses and distortion for a bead-on-plate weld. They adopted double ellipsoidal heat source model to predict temperature distributions. The developed can be adopted was capable of predicting residual stresses even for uneven bead cross-sections. Culha (2014) developed a simulation technique to determine the temperature-stress distribution, gradient and nodal displacement of plates joined by SAW. The 2-D model was assumed in the study. It was observed that material was plastically deformed in the weld zone and thermal stresses approach the yield strength of the material. The shrinkage of plate at the bottom was a result of steep gradient in the thermal stresses from weld zone to the bottom of the plate.

Cho et al., (2014) formulated 3-D numerical simulations of heat transfer and fluid flow on two wire tandem submerged arc welding. These simulations were examined to the study the temperature profiles, velocity fields, weld pool shape and size. It was observed that high current in the leading electrode results in the deeper penetration. A good agreement between CFD simulations and experimental results were obtained in their study. Podder et al.(2014) developed a generalized solution for a heat source model with submerged arc welding of low carbon and M.S plates. The physical phenomena like forces of buoyancy, Lorentz and Marangoni were taken into account while establishing the model.

Nezamdost et al., (2016) adopted Goldak's model for fusion zone and reinforcement zone to predict the temperature distribution in pipe steel fabricated by SAW process. They compared peak temperature distributions obtained between axi-symmetric 2-D and 3-D models and found that 3-D model yielded more accurate result.

Zargar et al., (2016) studied the effect of welding sequence on residual distortion in fillet welds using 3-D finite element simulation. The vertical deflection obtained from numerical analysis matched very closely with experimentally measured data. Pandey et al., (2016) and Mondal et al., (2017) studied angular deformation of fillet welds produced by submerged arc

welding and found that welds made by single sided welding and welding direction has pronounced effect angular distortion.

Xu et al., (2017) compared the residual stress induced by TIG and laser beam welding process. A combined heat source model which consists of conical and cylindrical models was used to predict thermal process of laser welding, whereas double ellipsoidal heat source was applied to simulate TIG welding. The predicted residual stresses, temperature histories and fusion profiles were well matched with experimental results in both the cases. It was established that laser beam welding is more advantageous than TIG on welding of type 304 austenitic stainless steel.

Ansaripour et al., (2019) conducted FE simulation to determine residual stress and distortion and results were utilized for modeling in genetic algorithm and harmony search. The results found using artificial neural network and multi-objective optimization algorithms were suitable for optimizing the weld induced residual stresses and distortion.

2.2 Mechanical characterization studies

Multipass submerged arc welding of 316 L stainless steel was carried out to investigate the effect of multipass on mechanical properties. It was observed that with increase in number passes mechanical properties namely hardness and tensile strength tends to be improved Gowrisankar et al. (1987). Piatti and Vedani (1990, 1989) fabricated 316 stainless steel of 50 mm thickness with double 'U' groove geometry with 28 weld passes and observed variation in ferrite content and its morphology across the weld geometry, which are due to the multiple thermal cycles experienced by the material. Also the tensile strength of the deposited weld metal is lower to that of solution annealed weld metal.

Khallaf et al., (1997) studied the crack susceptibility in medium carbon steel (C45) fabricated by SAW. It was concluded that tendency of crack formation is more for thin plates than thick plates. Chandel et al., (1998) focused their study on effect of metal powder addition on the mechanical properties of the ASTM A283 steel plates. Addition of metal powder resulted in improved toughness of welded joints with that of without metal powder addition. Zhang and Dorn (1999) investigated the mechanical properties of nuclear grade pressure vessel steel A508CL3 using narrow gap submerged arc welding. Researchers explored the possibility of

micro shear test to estimate the degradation of mechanical properties of welded joint and A508CL3 material.

Brito et al., (2001) conducted post weld heat treatment on ASTM A537 pressure vessel steel fabricated by SAW. It was established that post weld heat treatment resulted in reduced mechanical properties in the base metal as well as in HAZ. McPherson et al., (2003) made comparative studies between submerged arc welding (SAW) and laser welding of 316LN austenitic stainless steels and duplex 2205 steels. Mechanical testing was carried out using all weld metal tensile samples in longitudinal direction. Transmission electron microscopy (TEM) studies were performed in the weld region and it was found that some intermetallic phases were present. It was also observed that the intermetallic phases were not found to affect weld metal properties. The distortion levels observed in laser welding was found to be on lower side as compared with SAW. Their study confirmed that SAW process was a viable option in fabrication of 316LN and duplex 2205 steels.

Srinivasan et al., (2004) fabricated super martensitic stainless steels with a variety of electrode materials. Plates joined with matching electrode materials exhibited over match of joint properties and in contrary, they were more susceptible to hydrogen induced cracking. Nowacki and Rybicki (2005) investigated the effect of heat input on duplex steels (UNS S31803) and found that increase in heat input improves the weld shape coefficient and decreases the risk of cracks. In addition, it can have positive influence on mechanical properties. The influence of active and non-active fluxes on the mechanical properties of the ASTM A36 plate welds were studied by, Mercado et al., (2007). Upon using non-active flux higher toughness and ductility was observed which were due to formation of pearlite and ferrite in the weld zone. The chromium and molybdenum in active flux promoted the formation of acicular ferrite and fine carbides in the weld zone showing highest hardness and toughness.

Taban et al., (2008) carried out submerged arc welding of modified X2CrNi12 stainless steel. Comparative studies were carried out by varying the electrode consumables and were tested for joint strength. For determining the mechanical properties, joints for various cases were characterized for bend test and toughness.

Prasad and Dwivedi (2008) investigated the effect of welding current and speed on metallurgical and mechanical properties of high strength low alloy steel (HSLA) joints.

Results were discussed in view of heat input to the weld joint. As heat input was varied different proportions of microstructural phases, (ferrite and pearlite) were observed in weld zone and HAZ. Kolhe and Datta (2008) correlated the relation between mechanical properties and microstructure for a multipass single 'V' groove butt joint. Studies were carried out on microstructure, phase analysis and mechanical properties. For evaluation of mechanical properties hardness measurement (bulk and micro) and charpy tests were performed. It was concluded that weld heat input plays a significant role in controlling the percentage of phases in the weld structures. At higher heat input lesser graphitic phase was observed while there was a steep rise in ferrite phase. In addition, it was observed that increase in the ferrite content increases the toughness of the welds. The width of heat-affected zone on top side of the weld was more than the bottom side of the weld.

Bang et al., (2009) observed that impact touchiness of welds increase with increase in flux basicity which is due presence of low oxygen content. Singh and Pandey (2009) proposed the usage of slag as flux by enriching with deoxidizers and alloying elements. Authors found that a mechanical property obtained with recycled slag conforms to ASME SFA 5.17-89. Nagalakshmi et al., (2010) studied the evolution of microstructure, CTOD and fracture characteristics of the P91 weldment. Authors fabricated P91 with root pass welding with GTAW and subsequently welded with SMAW and SAW welding. It was found that base metal exhibits higher toughness when compared to weld metal, which was due to tempered martensite and globular carbides. Their study reveals that weld metal have lower CTOD (Crack tip opening displacement) values compared with base metal at room temperature and zero deg. which were due to coarse martensite and precipitates of carbide were also surrounded by delta ferrite sub grains.

Yan et al., (2010) studied the microstructural features and mechanical characteristics of AISI 304 stainless steels fabricated using TIG, Laser and hybrid TIG-Laser welding process. It was observed that welds fabricated using laser welding exhibited highest tensile strength while TIG welded joints showed lowest strength. The joints fabricated with TIG welding failed with ductile fracture and laser and hybrid TIG-laser welds failure was by shear fracture. It was concluded that laser and hybrid TIG-laser welding is suitable for industrial applications due to possibility of welding in high speeds.

Fletcher et al., (2011) studied the effect of Ti/N ratios on mechanical and metallurgical properties of line pipe steel. Microstructural study reveals fine grain ferrite and islands of

pearlite were noticed in the weld zone. Hardness of the second weld pass was improved which is due to the effect of precipitation hardening. Jang et al., (2011) fabricated 316L austenitic stainless steel by modified flux core arc welding process to study ductile dip cracking (DDC) susceptibility. It was observed that DDC occurred in the weld reheated region. The fracture surfaces were observed to be wavy and highly deformed.

Moeinifar et al., (2011) fabricated X80 micro-alloyed steel using four wire tandem SAW. The simulated microstructure was compared with that of experimental microstructure and observed to have suitable similarity. It was observed that prior-austenite grain size was a responsible factor which determines the charpy impact energy in the real and thermally simulated CGHAZ. Toma et al., (2011) conducted experiments on series 304 austenitic steel using direct current (+ve) and alternating square wave current for 25 mm thick plates with neutral flux and chromium compensating flux and found that CVN impact specimens at cryogenic temperatures broke in ductile fashion and best results on test were obtained with AC square wave and neutral flux.

A detailed microstructural characterization of the fusion zone was conducted by means of scanning electron microscope, transmission electron microscopy, electron back scattered diffraction and optical microscopy on a low carbon bainitic steel, Lan et al. (2012). Different microstructures were observed inside the weld zone such as acicular ferrite, coarse granular ferrite and fine polygonal ferrite. Transmission electron microscopy (TEM) was used to comprehend the complex mechanism of the weld microstructure. Fig.2.1 shows the TEM micrographs of weld microstructure.

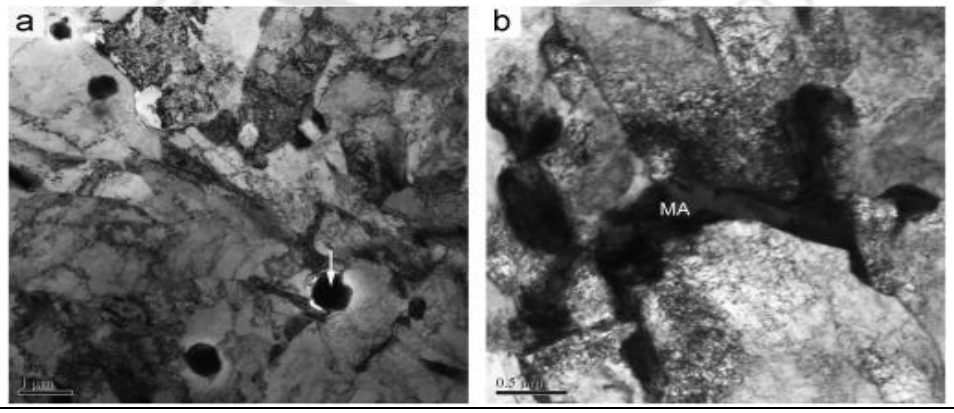

Fig.2.2 TEM micrograph of weld zone (a) acicular ferrite plates and inclusions (b) irregular MA constituent distribution, Lan et al., (2012).

It can be observed from Fig.2.2 that small inclusions were located within ferrite laths. The large inclusion marked with arrow was responsible for positive impact on nucleation of acicular ferrite. The inclusions with complex oxides of Ti, Al, Mn, Si, O, and Mg were observed. Smaller martensite-austenite (MA) constituents with high dislocation density were noticed along ferrite plate boundary. It was observed that fine grain heat affected zone (FGHAZ) contains more retained austenite than weld metal (WM) and coarse grain heat affected zone (CGHAZ). Also their study reveals that polygonal ferrite (PF) was located in FGHAZ and don't assumes specific orientation with austenite in the weld metal. Rajani et al., (2012) fabricated 316L stainless steel by gas tungsten arc welding (GTAW). Metallographic studies were conducted to study the effect of preheat on weld and HAZ. It was concluded that preheat can drastically reduce the amount of delta ferrite formed in the weld zone.

Shen et al., (2012) studied the effect of heat input on bead geometry in single wire and double wire SAW for ASTM A709 Grade 50 steel for a 20 mm thick plate. With increase in heat input there observed an increase in electrode melting efficiency in single wire SAW while plate melting efficiency does not change with single wire and double wire SAW. Amanie et al., (2012) fabricated SA516 grade 70 steel of 17 mm using double side welding. In their study it was found that welding current directly affects the electrode melting rate, cooling rates and weld metal chemistry.

Kiran et al., (2012) studied weld bead profile for tandem SAW of HSLA steels. The effect of leading current and trailing current on reinforcement height, penetration and weld width were analyzed using response surface methodology. It can be derived from their study that leading current influences penetration, while reinforcement height and penetration were affected by trailing current. Luo et al., (2013) fabricated duplex stainless steel by double side SAW. Mechanical and microstructural characterization was performed to study the effectiveness of the weld joints. Study reveals that control of heat input is necessary to achieve good weld joints. Ramakrishnan et al., (2013) and Ramakrishnan and Muthupandi (2013) explored the possibility of addition of cold wire to tandem and narrow gap SAW for fabrication of SA299 plates. The authors observed an improvement in toughness at subzero temperatures and significant reduction in HAZ with the use of this method.

Zhang et al., (2013) studied mechanical properties and residual stress of ANSI 304 joints fabricated by fiber laser welding. As compared between CO_2 and Nd:YAG welds the tensile

residual stresses generated by fiber welds were lowest, while mechanical properties obtained were superior than CO_2 welds. It was observed that solidified microstructure in the weld zone was different from that of base material. Kumar and Shahi (2014) studied mechanical properties of 304 austenitic stainless steels by gas tungsten arc welding. Fractrographic studies on the joints shows that all joints failed by ductile mode. It was observed that heat input has significant influence on the weld joints.

Unnikrishnan et al., (2014) made bead on plate welding of 304 stainless steel using shielded metal arc welding (SMAW). EBSD studies were conducted on welded samples and it was found that texture in the heat affected zone was not consistent, while base metal and fusion zone exhibited strong texture. Nakhaei et al., (2016) fabricated 304L austenitic stainless steel using advanced A-TIG welding. The shielding gas used in their experiments was Ar and CO_2 in the outer layer and pure Ar at the inner layer in order to prevent the consumption of tungsten electrode. It was observed that due to the double shielding gas effect a fine grain microstructure was achieved in the weld metal.

Alali et al., (2017) fabricated 20 mm thick 316L stainless steel by electron beam welding (EBW). It was observed that weld microstructure consists of columnar and equiaxed dendritic ferrite structure in a matrix of austenite. The hardness of HAZ and base metal was superior as compared with weld zone. The EBSD studies have confirmed that grains in the weld zone were weakly oriented and exhibited high Schmid factor intensity with an interception between strong and weak grain at weld centerline. Yilmaz and Mustafa (2017) worked on AH 36 ship building steel plates to study the effect of weld groove and with and without ceramic backing on tensile strength and low temperature toughness.

2.3 Optimization of welding process parameters

Welding process variables namely welding current, voltage, traverse speed, length of stick out, electrode diameter, electrode angle, electrode polarity and type of flux plays a vital role in achieving the desired weld quality. Researchers made several attempts to optimize the process variables using different optimization techniques to achieve the satisfactory weld quality and those are discussed briefly in this session.

Robinson (1961) investigated the effect of welding current and electrode polarity on melting rate of flux and electrode in a single wire SAW. It was observed that as welding current

increases, consumption of flux and melting rate of electrode are found to be enhanced. Further author also concluded that highest electrode melting rate for direct current electrode negative (DCEN), alternating current (AC) and direct current electrode positive (DCEP) for a particular welding current. Also, flux consumption is highest for electrode polarities (AC) followed by (DCEN) and (DCEP) for a specified set value of current. The author also noticed the DCEN results in higher electrode melting rate than DCEP, which is due to higher temperature of the electrode in case of DCEN as compared with DCEP. While a decrease in voltage has resulted in reduction in flux consumption rate and increase in electrode melting rate.

Renwick and Patchett (1976) investigated the effect of welding current on deposition rates. Their study reveals that SAW process when operated above a transition current yield best results. Chandel (1987) conducted experiments to determine the influence of process parameters on electrode melting rate for 19 mm thick ASTM A36 grade plates. It was observed that for a given current electrode melting rate was higher for smaller electrode diameter for longer electrode extension and DCEN polarity. Further for same welding variables DCEP polarity yields lowest electrode melting rate and AC polarity is the intermediate of the both polarities. It is concluded that welding voltage and power source don't have any prominent effect on electrode melting rate.

Yang et al., (1992) conducted BOP experiments on ASTM A36 grade steel of 19 mm thickness plates that larger bead width is influenced by voltage and smaller electrode extension and also developed regression mathematical equations for predicting bead width. Chandel et al. (1997) theoretically related the welding variables with resultant bead geometry in SAW of mild steel plates and concluded electrode diameter doesn't influence the weld quality. Submerged arc welding is a high deposition process used for welding of thick plates also besides this it can also be used for surfacing application.

Tsai et al., (1996) adopted soft computing techniques to model the process variables for submerged arc welding process variables in hard facing of steel mill rolls. A simulated annealing algorithm was implemented to search optimum process variables in the process. It was concluded that the new approach to optimization had enhanced the performance of the process. A 20 mm thick structural steel was cladded using 316L austenitic stainless steel and mathematical models were developed to optimize the input parameters, Murugan and Parmar (1997). It was observed that cladded surface possess good ductility and resistance towards

inter-granular corrosion. The martensitic stainless steel was used as hard facing layer on mild steel plate, Tarng and Yang (1998). It was concluded that welding parameters significantly affect the rate of deposition and dilution in a hard facing process and hence, optimization of the parameters yields improvement in overall process output.

Chandel (1998) studied the effect of process variables on flux consumption. It was concluded that welding current and electrode extension significantly affect the flux to electrode melting ratio in the process. In addition to that flux consumption rate was higher for direct current electrode negative (DCEN) as compared with direct current electrode positive (DCEP) for same process variables.

The bead-on-plate and bead-on-joint experiments were carried out on 6 mm thick carbon steel plates and developed mathematical models to predict the true cause and effect relationship between input and output process parameters, Gunaraj and Murugan (2000, 1999a, 1999b). Lee et al. (2000) worked on 38 mm thick low carbon steel plates and discovered that heat input and polarity combined put together affects the weld bead size ratio. Tarng et al. (2002) performed hard facing on mild steel plates with stainless steel flux cored electrode and used multi response optimization technique to predict multiple weld qualities.

Murugan and Gunaraj (2005) developed mathematical models using factorial technique for prediction of critical dimensions in pipe fabrication. Kanjilal et al., (2006) fabricated low carbon steel of 18 mm thick with a combination of different fluxes and welding parameters. Studies were conducted on weld chemistry and mechanical properties. It was observed that polarity plays a key role in weld metal chemical composition while mechanical properties were influenced by welding parameters. Also process variables namely welding speed and current influences, weld metal carbon and manganese content respectively. Kanjilal et al., (2007) in their study found that CaO as flux ingredient enhances the mechanical and impact properties of the steel due to its interaction with CaF_2 and Al_2O_3.

Karaoğlu and Seçgin (2008) developed mathematical models using curvilinear regressions from the experimental data and sensitivity analysis was conducted to determine the most sensitive process variables. Several researchers, Datta et al., (2008a, 2008b, 2008c); Dhas and Kumanan (2011); Om et al., (2012) have proposed various statistical techniques to predict the weld qualities and strength of welded joint.

Kumar et al., (2011) adopted factorial designs to evaluate the effect of independent process parameters. In their study two different submerged arc welding (SAW) fluxes having different basicity indexes namely 0.8 and 1.6 were used. It was observed that high amounts of CaO and MgO present in flux with basicity index of 1.6 causes pickup of carbon from base metal which leads to lowering of hardness. Many non-conventional techniques such as artificial neural network (ANN), digital signal processing (DSP) and graphical technique (GT) were adopted by Ghosh et al., (2011a, 2011b, 2011c) to study the influence of process parameters on weld outputs.

Om and Pandey (2013) adopted two factorial design to study the effect of polarity, heat input and submerged arc welding (SAW) process parameters on dilution and HAZ size. Electrode negative (EN) reduces the dilution approximately by 20%, hence (EN) polarity can be used for cladding, hard facing etc. Also electrode negative (EN) polarity produces less HAZ size. It was found that there exist a linear relationship between heat input and HAZ size for both the polarities. Rao and Kalyankar (2013) fabricated Cr-Mo-V pressure vessel steel and used teaching learning (TLBO) based technique to obtain optimized parameter setting for each response.

Sarkar et al., (2014) presented Analytical hierarchy process (AHP) based on Taguchi method to optimize the weld parameters for bead-on-plate welding. It was identified that effect of wire feed rate was dominant over other process variables in achieving overall bead geometry. Singh et al. (2016) developed mathematical models to study the effects of weld polarity on weld geometry. It was found that except reinforcement all other output responses were influenced by electrode positive polarity.

Hayajneh et al., (2018) studied the factors affecting the bending distortion of ‘I’ beam using design of experiments (DOE) and identified that increase in voltage increases distortion, while increase in travel speed reduces the distortion.

2.4 Closure

Many researchers have attempted to understand the welding process. This chapter has dealt with the comprehensive discussion on the contributions made by the earlier researchers. The application of finite element technique made it possible to predict thermal history, residual stresses and distortion. Several characterization techniques are used to determine the strength of the weld joint. At last a discussion on optimization of the welding process parameters using statistical and non-conventional techniques are detailed.

2.5 Scope of the thesis

Welding is most widely used fabrication process due to its reliability and ease of fabrication in a spectrum of industries like aerospace, shipbuilding, automobiles, nuclear and in general engineering fabrication. The merits of welded joints include high joint efficiency, low fabrication cost, air and water tightness. Even though welding has numerous advantages, there are some limitations inherent with the process. The major concerns with regard to welding are distortion and residual stresses. Distortion and residual stresses can be controlled but cannot be completely eliminated. Hence, with the application of numerical simulation it is possible to predict them. These occur due to temperature gradients prevailing between heat source and the base material. To achieve desired joint strength the welding process variables need to be properly selected for a particular material and also according to the type of weld joint. So, by optimization of process variables it is possible to achieve desired properties.

As the heat source moves along the joint interface, the temperature distribution across the weld plate varies. In order to predict the thermal history across the joint interface a transient thermal analysis was performed using a volumetric heat source to predict the temperature distribution in a square butt joint. Also variation of transient thermal history with respect to power changes and speed variation were also considered. In addition to this the effect of plate thickness on temperature history was also predicted. Further thermo-mechanical analysis was also carried out to predict the residual stresses and distortion for variation in line energy. Finally, an improved method to predict the weld induced distortion for large structures was proposed in this work.

Experiments were carried out on commercial grade stainless steel to predict the optimum process variables for a square butt joint. In this research work an attempt was made to design

and fabricate a heat sink setup to weld austenitic stainless steel. The heat sink welding experiments were conducted in order to minimize the angular distortion in a square butt joint. Also similar parameters were used to fabricate a square butt joint for comparison with heat sink welding. Double sided welding of austenitic stainless steel plates without edge preparation was carried out to study the effect of process variables on overall bead profile and mechanical properties. Also, a comparison of angular distortion with single side welding was carried out. Finally effect of surface active flux on bead geometry was studied in this thesis.

Chapter 3

Theoretical Background and Modeling Methodology

3.0 Introduction

In the present work, transient elasto-plastic nonlinear thermo-mechanical analysis was carried out to predict the weld induced thermal history, residual stresses and distortion using Finite element method (FEM). Apart from FE analysis, the optimization of welding process parameters was carried out using design of experiments (DOE). The details of theoretical background of FE analysis and DOE are presented in this chapter.

The applications of finite element analysis (FEA) in design and development of engineering structure is well proven. It is imperative that it is possible to achieve good productivity and product quality by better understanding the effect of various process parameters. Typically stages in the manufacturing cycle of an industrial component include welding, forming, metal casting and other allied processes; finite element model will enable the designer to understand the physical behavior of the part in service. With FE model, it is possible to predict the occurrence of stresses and deformations and susceptibility of components to sudden failures in service. Hence, FE simulation tools can be used to optimize different stages in a manufacturing process.

The welding arc generates high temperatures, which causes change in grain size in the vicinity of the arc and generate thermal stresses and strains in the welded component due to uneven cooling and heating. These strains and stresses results in the permanent deformation and induce residual stresses in the work piece. The stresses can reduce the strength of the structure and hence it is susceptible to fatigue, fracture and lowers corrosion resistance. The initial step in prediction of residual stresses is determination of temperature distributions.

3.1 Thermal modeling

The heat is transferred from weld pool to surroundings by means of conduction, convection and available research mostly focuses on simpler cases. Moreover several material properties of the molten metal are not accurately well established. In arc welding, only a small portion of metal is in molten condition and remaining portion of structure is solid. Hence, a 3D

Finite element analysis was implemented to evaluate the heat flow and ensuing temperature distribution over an entire plate.

3.1.1 Assumptions in the FE model:

The following assumptions were made while formulating the thermal model for submerged arc welding process.

- All thermal properties were considered as a function of temperature.
- Linear Newtonian convective cooling was assumed on all surface of the model.
- Heat loss from the fixture was not considered in this study.
- Forced convection was not considered in this numerical analysis.
- The total heat transferred from arc and metal droplets are combined together and stated as overall arc heat transfer efficiency.
- Thermal efficiency (η) of the SAW the process encompasses heat loss due to radiation, heat conduction from an electrode, heat expended for burning of flux, and electrode melting.
- In this investigation element birth and death was used to simulate weld metal deposition. Element death involves multiplying their stiffness matrix by a reduction factor. The strain of the killed element was set to zero. Element birth was achieved by reactivation of the previously killed element. After reactivation of the element all, the values such as stiffness, mass, element loads were resumed to their respective values.
- In structural analysis, rate independent linear kinematic work hardening together with von Mises yield criterion was considered.

3.2 3D-FE formulation for heat transfer analysis

The following model describes the axis system, weld line (S1) and base zone (S2) are detailed in the Fig.3.1.

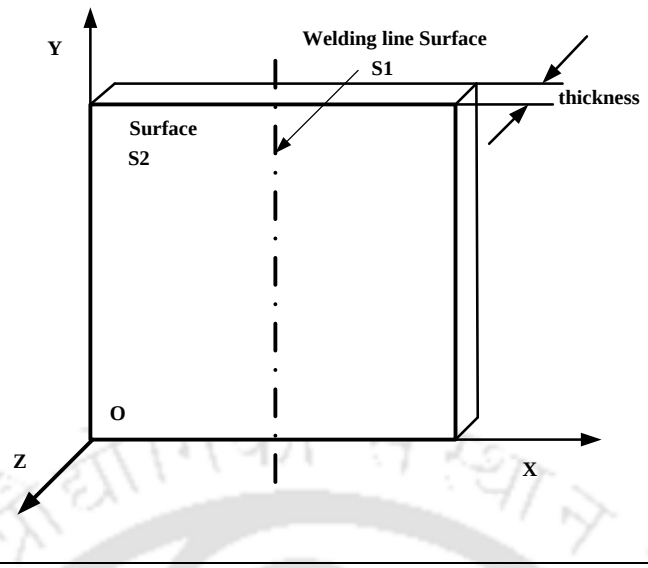

Fig.3.1 Representation of axis system and regions of a welding plate

The governing differential equation for heat conduction for a homogenous, isotropic solid without heat generation in the rectangular coordinate system (x,y,z) can be expressed as:

$$\frac{\partial}{\partial x}\left[K\frac{\partial T}{\partial x}\right]+\frac{\partial}{\partial y}\left[K\frac{\partial T}{\partial y}\right]+\frac{\partial}{\partial z}\left[K\frac{\partial T}{\partial z}\right]=\rho c\frac{\partial T}{\partial t} \tag{3.1}$$

where K = thermal conductivity, T = temperature, ρ = density of the material, c = specific heat and t = time. The above equation can be written as:

$$\rho c\frac{\partial T}{\partial t}=-\{L\}^{T}\{q\} \tag{3.2}$$

where $\{L\}=\begin{Bmatrix}\frac{\partial}{\partial x}\\ \frac{\partial}{\partial T}\\ \frac{\partial}{\partial z}\end{Bmatrix}$ = vector operator and $\{q\}$ = heat flux vector.

$\{L\}^{T}\{q\}=\nabla.\{q\}$ and $\{L\}T=\nabla T$ where, ∇ represents grad operator.

The Fourier's law is used to relate the heat flux vector to the thermal gradient. Therefore,

$\{q\}=-[D]\{L\}T$

where $[D] = \begin{pmatrix} K & 0 & 0 \\ 0 & K & 0 \\ 0 & 0 & K \end{pmatrix}$ = conductivity matrix, the negative sign indicating the heat flow is occurring in the direction of decreasing temperature. After substituting the value of $\{q\}$, the above equation can be written as follows:

$$\rho c \frac{\partial T}{\partial t} = -\{L\}^T \left([D]\{L\}T\right) \tag{3.3}$$

For solving the equation (3.3), boundary conditions need to be defined.

3.2.1 Boundary conditions

The following boundary conditions were used in the present work.

(i) Initial condition

A specified initial temperature for the welding that covers all the elements of the specimen:

$T = T_\infty$ for t =0

where T_∞ is the ambient temperature.

To develop first and second boundary conditions we consider energy balance at the work surface as:

Heat supply = Heat loss.

(ii) First boundary condition

A specific heat flow acting over surface S1

q_n = -q_{sup}

The quantity q_n represents the component of the conduction heat flux vector normal to the work surface. The quantity q_{sup} represents the heat flux supplied to the work surface in, from an external welding arc.

$$q_n = \{q\}^T \{n\} \text{ on the surface S1 for } t > 0 \tag{3.4}$$

where $\{n\}$ = unit outward normal vector.

(iii) Second boundary condition

Considering heat loss (q_{conv}) due to convection over surface S2 (Newton's law of cooling):

$q_n = q_{conv}$ or

$$\{q\}^T \{n\} = h_f \left(T - T_\infty\right) \text{ on surface S2 for } t > 0 \tag{3.5}$$

Pre-multiplying equation (3.3) by a virtual change in temperature, integrating over the volume of the element, combining with equation (3.4) and (3.5), and with some arithmetic operation we get:

$$\int_{vol} \left(\rho c \delta T \left(\frac{\partial T}{\partial t} \right) + \{L\}^T (\delta T) \left([D] \{L\} T \right) \right) d\,(vol) = \int_{S1} \delta T q_{sup} d(S1) + \int_{S2} \delta T h_f \left(T_\infty - T\right) d(S2) \tag{3.6}$$

where

vol = volume of the element,

δT = an allowable virtual temperature $\left(= \delta T(x, y, z, t)\right)$.

3.2.2 Derivation of heat flow matrices

As stated before, the variable T was allowed to vary both in space and time. This dependency is expressed as:

$$T = \{N\}^T \{T_e\} \tag{3.7}$$

where

$T = T(x,y,z,t)$ = temperature,

$\{N\} = \{N(x, y, z, t)\}$ = element shape function and

$\{T_e\} = \{T_e(t)\}$ = nodal temperature vector of element.

The time derivatives of equation (3.7) may be written as:

$$\dot{T} = \frac{\partial T}{\partial t} = \{N\}^T \left\{ \dot{T}_e(t) \right\} \tag{3.8}$$

δT has the same form as T:

$$\delta T = \{\delta T_e\}^T \{N\} \tag{3.9}$$

The combination of $\{L\}T$ is written as:

$$\{L\}T = [B]\{T_e\}$$

where

$$[B] = \{L\}\{N\}^T \tag{3.10}$$

The variational statement of equation (3.6) can be combined with equation (3.7 to 3.10) to yield:

$$\int_{vol}\left(\rho c\{\delta T_e\}^T\{N\}\{N\}^T\left\{\dot{T}_e\right\}d(vol)\right)+\int_{vol}\left(\{\delta T_e\}^T[B]^T[D][B]\{T_e\}d(vol)\right)=$$

$$\int_{S1}\{N\}q_{\sup}d(S1)+\int_{S2}T_\infty\{N\}h_f d(S2)-\int_{S2}h_f\{N\}\{N\}^T\{T_e\}d(S2) \tag{3.11}$$

The density ρ is assumed to remain constant and specific heat c may vary over the element. Finally $\{T_e\}$, $\left\{\dot{T}_e\right\}$ and $\{\delta T_e\}$ are nodal quantities and do not vary over the element, so that they also may be taken out from the integrals. Now, since all quantities are pre-multiplied by $\{\delta T_e\}$, this term may also be dropped from the final equation. The solution is obtained using FE package Ansys™.

The above equation (3.11) can be condensed to:

$$\rho\int_{vol}c\{N\}\{N\}^T d(\text{vol})\left\{\dot{T}_e\right\}+\int_{vol}[B]^T[D][B]d(vol)\{T_e\}=\int_{S1}\{N\}q_{\sup}d(S_1)$$

$$+\int_{S2}T_\infty\{N\}h_f d(S2)-\int_{S2}h_f\{N\}\{N\}^T\{T_e\}d(S2) \tag{3.12}$$

The equation (3.12) can be re-written as:

$$\left[C_e^{\,t}\right]\left\{\dot{T}_e\right\}+\left(\left[K_e^{\,tb}\right]+\left[K_e^{te}\right]\right)\{T_e\}=\left\{Q_e^f\right\}+\left\{Q_e^c\right\} \tag{3.13}$$

where

$\left[C_e^{\,t}\right]=\rho\int_{vol}c\{N\}\{N\}^T d(\text{vol})$ = element specific heat input matrix,

$\left[K_e^{\,tb}\right]=\int_{vol}[B]^T[D][B]d(vol)$ = element diffusion conductivity matrix,

$\left[K_e^{tc}\right]=\int_{S2}h_f[N][N]^T\,\mathrm{d}(S2)$ = element convection surface conductivity matrix,

$\left\{Q_e^f\right\}=\int_{S1}\{N\}q_{\sup}d(S_1)$ = element heat flow vector for surface *S1* and

$\left\{Q_e^c\right\}=\int_{S2}T_\infty h_f\{N\}d(S2)$ =element convection surface *S2* heat flow vector.

The element specific heat matrix $\left[C_e^{\,t}\right]$ is evaluated from the specific heat of the material. In the transient thermal modeling enthalpy is incorporated as a function of temperature. Enthalpy *H* is the integral of heat capacity with respect to temperature.

$$\rho c = \frac{dH}{dT} \text{ or } H = \int \rho c dT \tag{3.14}$$

3.3 Heat source model

The heat source model defines the distribution of heat input into the weld joint by the welding arc. The welding heat source not only impinges on the surface but also in through thickness direction. Hence distribution of heat in welding can be assumed as volumetric. Heat source model gives important information regarding heat spread in to the base material from the fusion zone. In the present investigation uniform volumetric heat distribution was applied all along the weld bead. The heat input per unit volume was calculated by using the following equation:

$$Q = \frac{\eta W}{v} \tag{3.15}$$

where η = 0.85, Easterling (1992) is the arc efficiency of the welded material and *W* is the arc power in SAW and *v* is the volume of the active element of the weld bead. To incorporate the heat loss due to convection the constant convection was used in this present analysis as 20 W/m^{2}K, Mandal (2009).

3.4 Thermo-mechanical analysis

For predicting the welding residual stresses and distortion, at first thermal analysis was carried out to determine nodal temperatures as function of time. In the second step a non-linear elasto-plastic analysis was carried out from the obtained results of thermal analysis for prediction of residual stresses and distortions.

3.4.1 Formulation of 3D Finite element stress strain relationship

The structural analysis of welding is involved with thermal stress and material non-linearity. The formulation of stress-strain used is described below:

The stress strain relationship is represented by the following equation:

$$\{\sigma\} = [D]\{\varepsilon^e\} \tag{3.16}$$

where

$[D]$ = stress-strain correlation stiffness matrix

$\{\varepsilon^e\} = \{\varepsilon\} - \{\varepsilon^t\}$ = elastic strain vector

$\{\varepsilon^t\}$ = thermal strain vector

$\{\sigma\}$ = stress vector = $[\sigma_x \sigma_y \sigma_z \sigma_{xy} \sigma_{yz} \sigma_{zx}]^T$ and

$\{\varepsilon\}$ = total strain vector = $[\varepsilon_x \varepsilon_y \varepsilon_z \varepsilon_{xy} \varepsilon_{yz} \varepsilon_{zx}]^T$

The equation (3.16) may also be inverted to:

$$\{\varepsilon\} = \{\varepsilon^t\} + [D^{-1}]\{\sigma\} \tag{3.17}$$

For three dimensional cases the thermal strain vector can be represented as:

$$\{\varepsilon^t\} = \Delta T [\alpha_x \alpha_y \alpha_z 000]^T \tag{3.18}$$

where α_x, α_y and α_z = thermal expansion coefficient in x, y and z direction.

The temperature difference is

$\Delta T = T - T_\infty$ Where, T is the instantaneous temperature at any given point.

$[D]^{-1}$ = is the compliance matrix.

The compliance matrix for 3 dimensional case can be written as

$$[D]^{-1} = \begin{bmatrix} \frac{1}{E_x} & \frac{-\nu_{xy}}{E_x} & \frac{-\nu_{xz}}{E_x} & 0 & 0 & 0 \\ \frac{-\nu_{yx}}{E_y} & \frac{1}{E_y} & \frac{-\nu_{yz}}{E_y} & 0 & 0 & 0 \\ \frac{-\nu_{zx}}{E_z} & \frac{-\nu_{zy}}{E_z} & \frac{1}{E_z} & 0 & 0 & 0 \\ 0 & 0 & 0 & \frac{1}{G_{xy}} & 0 & 0 \\ 0 & 0 & 0 & 0 & \frac{1}{G_{yz}} & 0 \\ 0 & 0 & 0 & 0 & 0 & \frac{1}{G_{xz}} \end{bmatrix} \tag{3.19}$$

where

ν_{xy} = major Poisions ratio

ν_{yx} = minor Poisions ratio

E_x , E_y and E_z = Young's modulus in *x*, *y*, *z* direction

G_{xy} , G_{yz} and G_{xz} = shear modulus in *xy*, *yz* and *xz* planes respectively

Since the $[D]^{-1}$ matrix is presumed to be symmetric

$$\frac{\nu_{yx}}{E_y} = \frac{\nu_{xy}}{E_y} \tag{3.20}$$

$$\frac{\nu_{zx}}{E_z} = \frac{\nu_{xz}}{E_z} \tag{3.21}$$

and

$$\frac{\nu_{zy}}{E_z} = \frac{\nu_{yz}}{E_y} \tag{3.22}$$

For isotropic material $E_x = E_y = E_z$ and $\nu_{xy} = \nu_{yz} = \nu_{xz}$. From the above equations it can be written that:

$$\varepsilon_x = \alpha_x \Delta T + \frac{\sigma_x}{E_x} - \frac{\nu_{xy}\sigma_y}{E_x} - \frac{\nu_{xz}\sigma_y}{E_x} \tag{3.23}$$

$$\varepsilon_y = \alpha_y \Delta T - \frac{\nu_{xy}\sigma_y}{E_x} + \frac{\sigma_y}{E_y} - \frac{\nu_{yz}\sigma_z}{E_y} \tag{3.24}$$

$$\varepsilon_z = \alpha_z \Delta T - \frac{\nu_{xz}\sigma_x}{E_x} + \frac{\sigma_z}{E_z} - \frac{\nu_{yz}\sigma_y}{E_y} \tag{3.25}$$

$$\varepsilon_{xy} = \frac{\sigma_{xy}}{G_{xy}} \tag{3.26}$$

$$\varepsilon_{yz} = \frac{\sigma_{yz}}{G_{yz}} \tag{3.27}$$

$$\varepsilon_{xz} = \frac{\sigma_{xz}}{G_{xz}} \tag{3.28}$$

where typical terms are:

ε_x = direct strain in the x direction

σ_x = direct stress in x direction

ε_{xy} = shear strain in the x-y plane

σ_{xy} = shear stress on the x-y plane

$$\sigma_x = \frac{E_x}{h}\left(1-(v_{yz})^2\frac{E_z}{E_y}\right)(\varepsilon_x-\alpha_x\Delta T)+\frac{E_y}{h}\left((v_{xy})+v_{xz}v_{yz}\frac{E_z}{E_y}\right)$$

$$(\varepsilon_y-\alpha_y\Delta T)+\frac{E_z}{h}(v_{xy}+v_{yz}+v_{xy})(\varepsilon_z-\alpha_z\Delta T) \quad (3.29)$$

$$\sigma_y = \frac{E_y}{h}\left(1-(v_{xz})^2\frac{E_z}{E_x}\right)(\varepsilon_y-\alpha_y\Delta T)+\frac{E_y}{h}\left(v_{xy}+v_{xz}+v_{yz}\frac{E_z}{E_y}\right)$$

$$(\varepsilon_x-\alpha_x\Delta T)+\frac{E_z}{h}(v_{yz}+v_{xz}+v_{xy}\frac{E_y}{E_x})(\varepsilon_z-\alpha_z\Delta T) \quad (3.30)$$

$$\sigma_z = \frac{E_z}{h}(v_{xz}+v_{yz}+v_{xy})(\varepsilon_x-\alpha_x\Delta T)+\frac{E_z}{h}\left(v_{yz}+v_{xz}+v_{xy}\frac{E_y}{E_x}\right)$$

$$(\varepsilon_y-\alpha_y\Delta T)+\frac{E_z}{h}\left(1-(v_{xy})^2\frac{E_y}{E_x}\right)(\varepsilon_z-\alpha_z\Delta T) \quad (3.31)$$

$$\sigma_{xy} = G_{xy}\varepsilon_{xy} \quad (3.32)$$

$$\sigma_{yz} = G_{yz}\varepsilon_{yz} \quad (3.33)$$

$$\sigma_{xz} = G_{xz}\varepsilon_{xz} \quad (3.34)$$

where

$$h = 1-(v_{xy})^2\frac{E_y}{E_x}-(v_{yz})^2\frac{E_z}{E_y}-(v_{xz})^2\frac{E_z}{E_x}-2v_{xz}v_{yz}v_{xy}\frac{E_z}{E_x}$$

When the shear moduli G_{xy}, G_{yz}, G_{xz} are not different for isotropic materials, they reduce to form as:

$$G_{xy} = G_{yz} = G_{xz} = \frac{E_x}{2(1+v_{xy})}$$

3.4.2 Structural analysis with material nonlinearities

The structural material non-linearities generally include non-linear plasticity and nonlinear elasticity, Awang (2002); Fanous et al., (2003). The equation (3.16) can be written by considering material properties in plastic state as:

$$\{\varepsilon^e\} = \{\varepsilon\} - \{\varepsilon^t\} - \{\varepsilon^p\} \quad (3.35)$$

$$\{\sigma\} = [D]\{\varepsilon\} - \{\varepsilon^t\} - \{\varepsilon^p\} \quad (3.36)$$

where $\{\varepsilon^p\}$ = plastic strain vector, $[K_e]$ is the element stiffness matrix, $[K_e^f]$ is the element foundation stiffness matrix, $\{F_e^t\}$ is the element thermal load vector, $[M_e]$ is the element mass matrix, $\{a\}$ is acceleration vector, $\{F_e^n\}$ is the vector of nodal forces applied to the elements and $\{F_e^p\}$ is the element pressure vector.

By considering the principle of virtual work and equation (3.16) the stress-strain equation can be written as:

$$\left([K_e][K_e^f]\right)\{u\} - \{F_e^t\} = [M_e]\{a\} + \{F_e^p\} + \{F_e^n\} \tag{3.37}$$

The equations were derived based on ANSYS™ Theory reference compiled by, Kohnke, (2009) and text books on finite element analysis, Rao (2011); Tai-Ran (1986).

The elastic strain $\{\varepsilon^e\}$ was modeled using isotropic Hook's law with temperature dependent mechanical properties such as Young's modulus and Poisson's ratio mentioned in Table 3.1. The thermal strain $\{\varepsilon^t\}$ was incorporated in the numerical analysis using temperature dependent coefficient of thermal expansion shown in Table 3.2. The plastic strain $\{\varepsilon^p\}$ was considered using rate independent plastic model with the following features: the von-Mises yield surface, temperature dependent mechanical properties, and linear kinematic hardening model. Kinematic hardening is an important feature and it accounts for material points typically experience both loading as well as unloading during welding process, Radraj (2003).

While welding stainless steels solid state transformation don't occur in stainless steel base metal and in weld metal hence, the total strain vector can be decomposed into three parts Deng and Murakawa (2006) and is given by equation (3.35).

Table.3.1 Temperature dependent mechanical properties of SS 304, Deng and Murakawa (2006)

Temperature (^oC)	Density (g/mm^3)	Yield stress (MPa)	Youngs modulus (GPa)	Poisson's ratio
0	0.790	265	198.5	0.294
100	0.788	218	193	0.295
200	0.783	186	185	0.301
300	0.779	170	176	0.310
400	0.775	155	167	0.318
600	0.766	149	159	0.326
800	0.756	91	151	0.333
1200	0.737	25	60	0.339
1300	0.732	21	20	0.342
1500	0.732	10	10	0.388

Table.3.2 Temperature dependent thermal properties of SS 304, Deng and Murakawa (2006)

Temperature(^oC)	Specific heat (J/g^oC)	Thermal Conductivity (J/mm^oC s)	Coefficient of Thermal expansion $\times 10^-5$ ($^oC^{-1}$)
0	0.462	0.0146	1.70
100	0.496	0.0151	1.74
200	0.512	0.0161	1.80
300	0.525	0.0179	1.86
400	0.54	0.018	1.91
600	0.577	0.0208	1.96
800	0.604	0.0239	2.02
1200	0.676	0.0322	2.07
1300	0.692	0.0337	2.11
1500	0.7	0.12	2.16

3.5 Procedure for 3D FE-analysis

The 3D–FE analysis in this investigation is carried out using commercially available ANSYS^{TM} software. The procedure consists of 3D transient thermal analysis followed by structural analysis. The methodology in the ANSYS^{TM} consists of three stages namely pre-processing phase, solution and general post processor. Major steps in FE-analysis are given below:

1. A Solid model was created as per the actual specimen dimensions.
2. The created model was discretized into finite elements i.e., fragment the problem into elements and nodes.

3. The non-uniform element size distribution was considered in this work. The elements closer to the weld zone were given finer mesh size and far from weld zone were specified as coarser mesh size. This was done in order to save computational time.
4. The elements selected for transient thermal and structural analysis were SOLID70 and SOLID45 respectively.
5. Temperature dependent material properties were imposed on the FE model.
6. The pre-processing phase in the analysis constitutes steps (1) – (5).
7. The solution phase consists of defining analysis type, applying loads, setting initial, and boundary conditions.
8. The time history post processor gives the temperature values at different nodes with reference to elapsed time. The results obtained from thermal analysis were imposed as load in the structural analysis.
9. The element SOLID45 was used in structural analysis. Structural properties were introduced into the FE model in this phase and constraints were imposed.
10. In the post processing phase, important information like thermal history, residual stresses and deformations were acquired.

The thermal and structural analyses were carried out using an element SOLID 70 and SOLID45 respectively. The 3D elements used in the present numerical analysis were briefly discussed in the following paragraphs.

The SOLID70 is a 3D thermal solid element contains 8 nodes with single degree of freedom i.e., temperature at each node. This element is capable of performing 3D steady state and transient thermal analysis ANSYS^{TM} Theory reference compiled by, Kohnke (2009). Fig.3.2 shows element 3D SOLID70 with eight nodes.

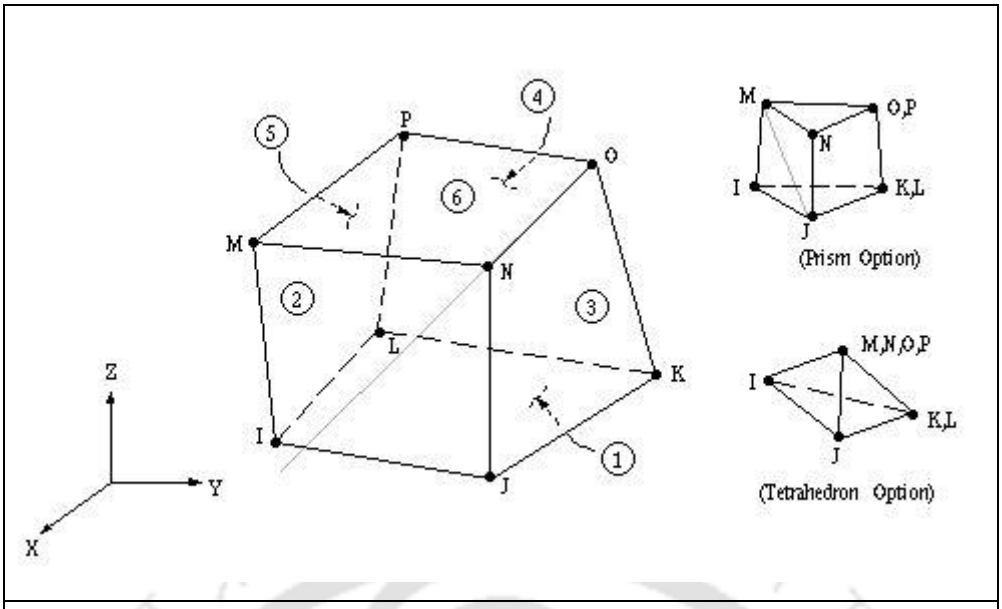

Fig.3.2 Element 3D-SOLID70, Kohnke (2009)

In addition, SOLID70 can compensate for mass transport heat flow from a constant velocity field. The heat fluxes / convection are applied as surface loads on element faces as shown in Fig.3.2. The rate of heat generation was given as input element body at the nodes. The solution output from this element is obtained as nodal temperatures. The element SOLID70 was substituted by an equivalent structural element SOLID45 in structural analysis.

The SOLID45 a brick element has 8 nodes and three degrees of freedom at each node such as translations in the nodal x, y and z directions. The element is used for 3D structural modeling of isotropic solids. This element can analyze plasticity, creep, swelling, stress stiffening, large deflection, and large strain for the model, ANSYS™ Theory reference compiled by Kohnke (2009). Fig.3.3 shows 3D-SOLID45 structural element with 8 nodes.

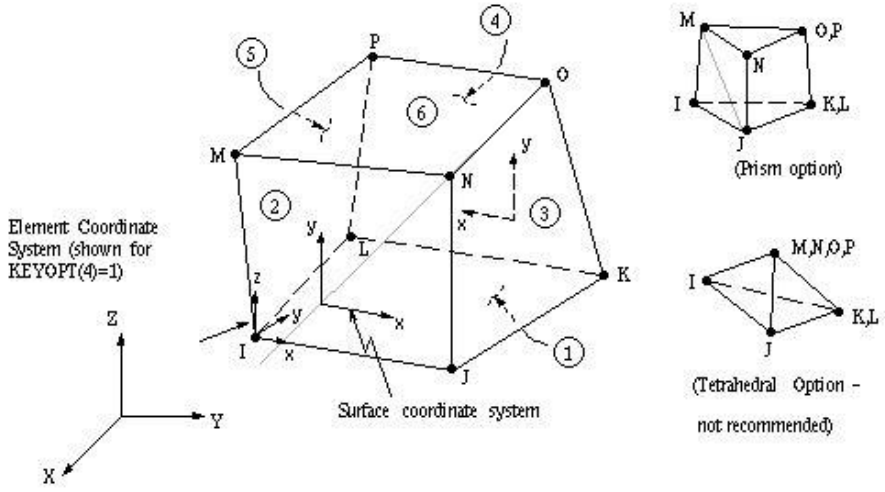

Fig.3.3 Element 3D-SOLID45, Kohnke (2009)

Pressures may be input as surface loads on the element faces as shown by the circled numbers in Fig.3.3.The solution output with the element contains of nodal displacements in the overall nodal solution. The SOLID45 is capable of yielding additional outputs such as normal component of stresses in x, y, and z directions; principle stresses; and shear stresses.

3.6 Equivalent method based on average plastic strain

Prediction of welding deformations using conventional thermal-elasto plastic FE analysis takes huge computational time and large computer memory even for small size weld specimens. Hence, welding deformations for large structures are not directly predicted using this method rather equivalent load technique based on average plastic strains was implemented in this research work. This equivalent load method uses mechanical forces such as forces and moments, hence very fine meshing is not required for analysis. The average value of plastic strain is calculated over the width of the weld zone from the vertical displacement measured from experimentation. The average value of plastic displacement was obtained by integrating the plastic strain distribution over the width of weld zone. The obtained displacement is divided by the width of weld zone to get the average plastic strain. Equivalent plastic loads were calculated based on obtained average plastic strain. Finally loads were applied region wise along the transverse direction. Three significant steps in this

technique are calculation of average plastic strain, equivalent load and application of equivalent load. These three steps are explained as follows:

3.6.1 Average plastic strain

The average value of longitudinal and transverse plastic strain is calculated from the equation (3.38), Biswas et al., (2011).

$$\hat{\varepsilon}^{p}_{x,y} = \frac{1}{w}\int_{-w/2}^{w/2} \varepsilon^{p}_{x,y}(y).d(y) \tag{3.38}$$

where w is width of weld zone, $\varepsilon^{p}_{x,y}$ is plastic strain distribution along transverse direction and $\hat{\varepsilon}^{p}_{x,y}$ is the average plastic strain.

3.6.2 Calculation of equivalent load

The equivalent loads namely force and displacement are determined from respective cross sectional area of weld seam. All loads such as forces in longitudinal and transverse direction, moments in longitudinal direction are represented by the equations (3.39-3.42). Fig.3.4 depicts the application of equivalent load.

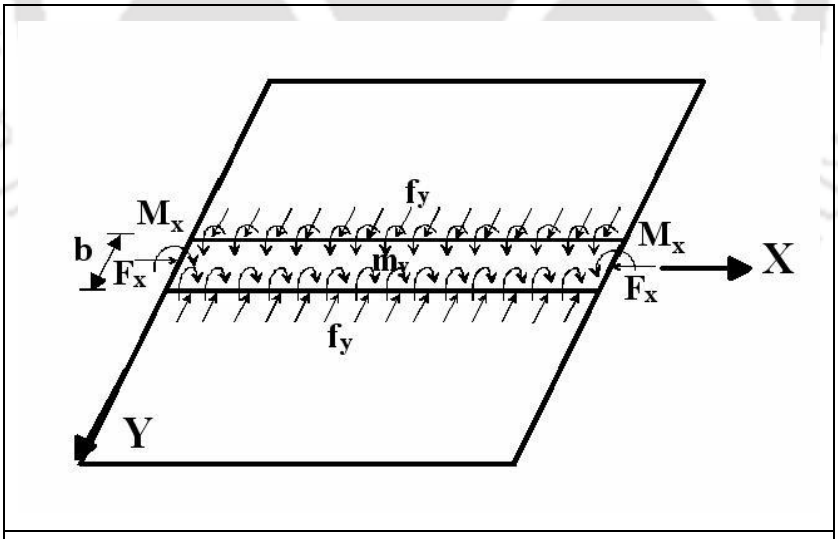

Fig.3.4 Application of equivalent loads

$$F_x = E \times \bar{\varepsilon}_x \times t \times w \tag{3.39}$$

$$F_y = E \times \bar{\varepsilon}_y \times t \times w \tag{3.40}$$

$$M_x = F_y \times \frac{t}{2} \tag{3.41}$$

$$M_y = F_x \times \frac{t}{2} \tag{3.42}$$

where E is Young's modulus, F_x, F_y are equivalent longitudinal and transverse forces respectively, $\bar{\varepsilon}_x, \bar{\varepsilon}_y$ are longitudinal and transverse plastic strains respectively, M_x,M_y are equivalent moments about longitudinal and transverse axes respectively, w represents width of the weld zone, and t is thickness of the plate.

3.6.3 Application of equivalent load

The load was imposed on the individual nodes along the line parallel to the welding direction at the width of average inherent plastic strain zone. The width of the plate was large as compared to the thickness of the plate, hence the plate was assumed as thin plate. It was found that stress distribution was almost linear through the thickness of the plate. In this technique mid surface of plate was preferred for all observations and calculations of average plastic strain and equivalent loads. Hence, equivalent loads were applied along the mid surface of the plate. In this work 3D structural element SOLID45 which was used in FE thermo-mechanical elastic-plastic analysis was also used, Canonsburg (2013). This solid element only permits three translational degrees of freedom, i.e. no rotational degree of freedom. It restricts the application of moment as the nodal loads for structural analysis. On that account, the concept of resolving a point force to another collinear point with a force and a couple was considered. Hence, the load (force and moment) applied on the nodes located on the mid plane of the plate were resolved to a single force on the collinear nodes located on the top surface of the plate as shown in Fig.3.5.

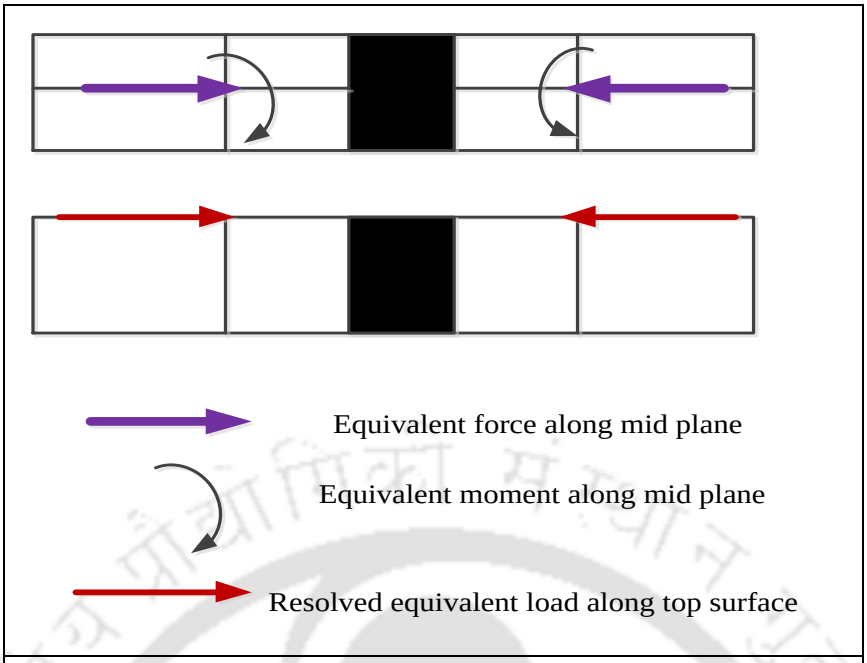

Fig.3.5 Illustration of force and moment

Thus, the nodal loads were applied separately in three regions illustrated in the schematic diagram shown in Fig.3.6.

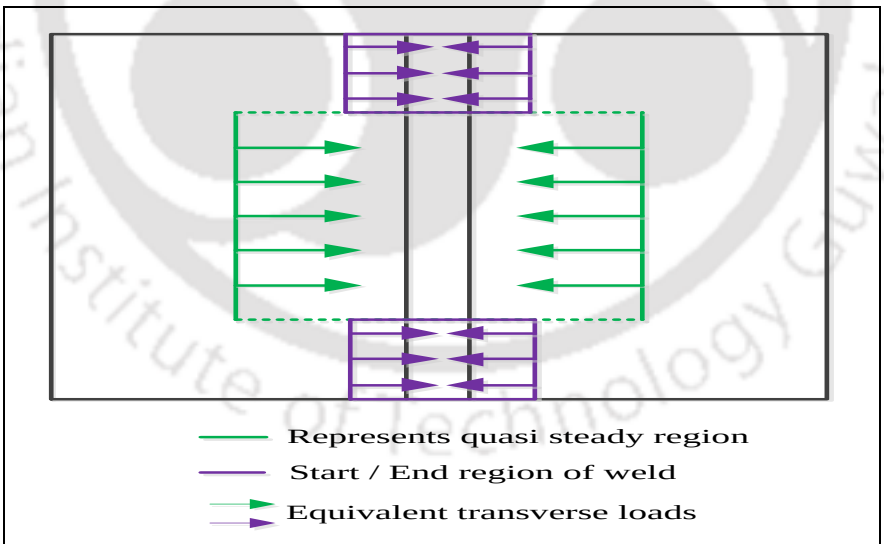

Fig.3.6 Application of load concerning the weld region and average width of inherent strain zone

The weld seam length was categorised into three parts depending on the distribution of plastic strains and variation of inherent strain zone width, Mochizuki et al., (2007). The length of start and end regions of the weld line is assumed as 20 mm. The remaining portion of the

weld seam i.e, middle region where plastic strain distribution is almost uniform is regarded as quasi-state region. The average width of the three regions namely start, end and middle portion is decided based on distribution of inherent plastic strain in their respective regions.

3.7 Taguchi's method

This method was developed by Dr. Genichi Taguchi of Nippon Telephone and Telegraph Company, Japan. It is a robust, simple, and more efficient technique for optimizing process parameters. This technique combines the advantage of the Design of Experiments with optimization of control parameters to attain the best results in a process. In this method, the main parameters that influence the process are arranged in rows, which are called Orthogonal Arrays. These orthogonal arrays are designed in such a way that they give rise to the minimized variance for the experiments with an optimal set of control parameters. These arrays facilitate conducting a well-balanced set of a minimum number of experiments. For evaluating the process parameters, Taguchi's method utilizes a statistical measure of performance called Signal to Noise (S/N) ratio. The signal-to-noise ratio measures the variation in the response relative to the nominal or target value. There are three standard Signal to Noise ratios typically used in Taguchi's study, namely larger-the-better, smaller-the-better, and nominal-the-best; these can be chosen depending on the goal of the experiment, Taguchi et al., (2007). Irrespective of the type of quality characteristic, a higher S/N ratio relates to an improved quality characteristic. Therefore optimal level in the experiment corresponds to the highest S/N ratio. In our experiments larger-the-better criteria was used as the output responses for ultimate tensile strength.

The expression for S/N ratio (smaller-the-better) is defined by the equation as follows, Muthuramalingam and Mohan (2013).

$$\text{S/N ratio (smaller-the-better)} = -10\log_{10}\left(\frac{1}{n}\right)\left[\sum y^2\right] \tag{3.43}$$

The S/N ratio for (larger-the-better) is expressed as follows, Koilraj et al., (2012); Lin (2004).

$$\text{S/N ratio (larger the better)} = -10\log_{10}\left(\frac{1}{n}\right)\sum_{i=1}^{n}\frac{1}{y^2} \tag{3.44}$$

3.8 Analysis of Variance (ANOVA)

Further, ANOVA (Analysis of Variance) is calculated to determine the important process parameters that have statistically significance. ANOVA is an acronym of Analysis of variance, which can give important conclusions based on experimental data. This method gives the level of interaction between the factors for a particular output. It separates total variability of output into contributions rendered by each factor and error. It can be given as

$$SS_T = SS_f + SS_e \tag{3.45}$$

Where, $SS_T = \sum_{j=1}^{p} \left(\gamma_j - \gamma_m\right)^2$ and SS_T is the total sum of squared deviations about the mean, Roy (2010).

p is number of experiments in the orthogonal array

γ_j mean response for jth experiment

γ_m grand mean of the response

SS_f sum of squared deviations due to each factor

SS_e sum of squared deviations due to error

In ANOVA mean square deviation is defined as (MSD) sum of squared deviation to the degrees of freedom. The F value for fisher's ratio is defined as the ratio of mean squared deviation for a term to the mean squared deviation for the error term. The MSD, fisher's ratio, and percentage contribution are expressed by the following relations, Roy (2010).

$$\text{Mean square (MSD)} = \frac{\text{Sum of squares (SS)}}{\text{Degrees of freedom (DF)}} \tag{3.46}$$

F is the variance ratio also called Fishers ratio which is defined as

$$F_{\text{calculated}} = \frac{\text{MSD of any term (main or combined effect)}}{\text{MSD for error term}} \tag{3.47}$$

The percentage contribution of each factor can be estimated using the following formula:

$$\%\ \text{Contribution} = \frac{SS_f}{SS_T} \tag{3.48}$$

The optimum parameter combination can also be predicted with S/N ratio optimization method. In the orthogonal experiment it is possible to separate the effects of each parameter at stated levels. The calculations for ANOVA and response tables were done using

commercially available software. In the present work optimization of welding parameters using Taguchi's Method is proposed. For fixing the process variables several trial runs were conducted in the initial phase of experimentation. The trials were conducted systematically to identify the ranges of welding variables in submerged arc welding process to attain full penetration achieve top and bottom reinforcement in square butt welding of stainless steel.

3.9 Theory of Grey relational analysis

Limitation of the Taguchi's method is it is suitable for single response optimization problems. But in engineering processes input variables need to be optimized for more than one output response. Grey relational analysis (GRA) is a powerful technique which addresses the multi-response optimization problems. The grey relational analysis was first proposed by, Deng (1992). The GRA coupled with Taguchi's method can be effectively used multi-response optimization problems. This method can analyze in situations when unknown or vague information is present about the outcome of process parameters on system responses, Kasman (2013). The procedure of GRA is illustrated in the Fig.3.7.

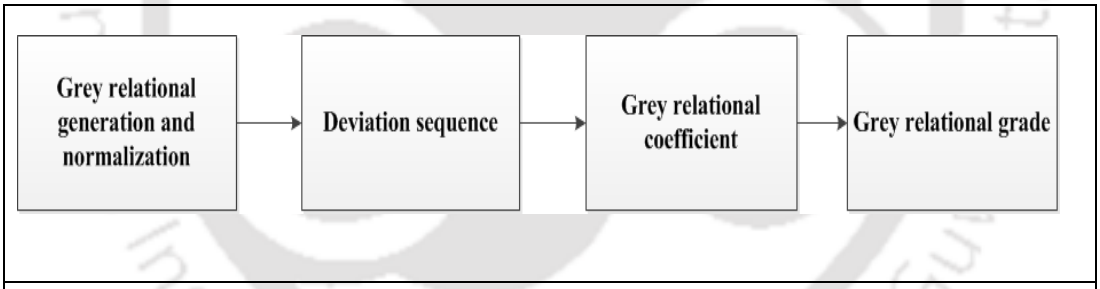

Fig.3.7 Flow chart of grey relational analysis (GRA)

The description of the Fig.3.7 is detailed below:

a) The experimental data (output responses) is normalized between 0 and 1. The process is termed as Generation of Grey relational generation (GR gen). There are three criteria used for normalization of experimental data namely lower the better, higher the better and nominal the better. The lower the better criterion is chosen if the objective is to minimize the output responses. In Grey relational generation bead width, reinforcement, and distortion are normalised for Lower the better criteria and this is expressed as, Datta et al., (2008):

$$x_i(k) = \frac{\max y_i(k) - y_i(k)}{\max y_i(k) - \min y_i(k)} \tag{3.49}$$

The mechanical properties of the weld joint such as ultimate tensile strength (UTS) follows higher the better criteria is stated as, Datta et al., (2008):

$$x_i(k) = \frac{y_i(k) - \min y_i(k)}{\max y_i(k) - \min y_i(k)} \tag{3.50}$$

Where $x_i(k)$ the value of Grey relation generation, $\min y_i(k)$ is the smallest value of $y_i(k)$ for the kth response and $\max y_i(k)$ is the largest value of $y_i(k)$ for kth response.

The deviation sequence is obtained from GR gen data by subtracting from 1.

b) The Grey relational coefficient (GRC) expresses the relation between the reference data (experimental output) and the normalized data. The grey relational coefficient is calculated from the normalized data. The formula for grey relation coefficient is $\xi_i(k)$

$$\xi_i(k) = \frac{\Delta\min + \psi\Delta\max}{\Delta_{oi}(k) + \psi\Delta\max} \tag{3.51}$$

Where, ψ is the distinguishing coefficient and lies between $0 \le \psi \le 1$ and is assumed to be 0.5, since it constitutes both larger the better and smaller the better. $\Delta_{oi} = \|x_o(k) - x_i(k)\|$ the difference of absolute value of $x_o(k)$ and $x_i(k)$ is called deviation sequence. In the equation $x_0(k)$ is ideal sequence where (k = 1, 2, 3, 4….18) for responses.

$\Delta_{\min} = \forall j^{\min} \in i \forall k^{\min} \| x_o(k) - xj(k) \|$ =smallest value of Δ_{0i} ;

$\Delta_{\max} = \forall j^{\max} \in i \forall k^{\max} \| x_o(k) - xj(k) \|$ = largest value of Δ_{0i} .

Averaging of Grey relation coefficient leads to Grey relation grade (GRG). The GRG reveals the information about the strength of the relationship between reference data and the normalized data. The value of GRG lies between 0 and 1. The largest GRG value is desirable. The mean sum of GRC gives GRG and is calculated by the formula $\gamma_i = \frac{1}{n}\sum_{k=1}^{n} \xi_i(k)$ where n is the number of process responses, Lin (2004); Meena and Azad (2012). The higher grey relation grade (GRG) indicates closer to optimal response in the process.

3.10 Summary

In this chapter, all aspects of finite element formulation related to thermal and structural analysis are detailed. This chapter also highlights the theoretical back ground behind prediction of weld induced distortion by equivalent loading method (ELM) based on average of plastic strain for large structures. Finally a brief introduction on optimization techniques namely Taguchi's and Grey relational analysis are deliberated.

Chapter 4

Experimental Methodology

4.0 Introduction

In this chapter, experimental details on submerged arc welding (SAW) of stainless steel and austenitic stainless steel are elaborately discussed. The optimization of process variables for single side single pass (SAW) was performed using Taguchi and Grey-Taguchi technique for stainless steel. The effect of individual process variables on weld qualities were studied for AISI 304 austenitic stainless steel for single sided-single pass SAW and double-sided SAW. Also, in this chapter an attempt was made to design and develop the heat sink for (SAW) welding. In order to ensure the weld quality further joints were subjected to mechanical and microstructural studies. Finally, effect of surface active flux on weld bead geometry was explored.

4.1 Fixed welding parameters

While performing the experiments with square butt joint configuration certain welding conditions were held constant throughout the welding process. These parameters are mentioned in the Table.4.1.

Table 4.1 Fixed SAW parameters

Parameters	Value
Welding process	DC
Polarity	Direct current electrode positive (DCEP)
Electrode size	3.2 mm
Wire feed rate	Automatic
Filler wire angle	Vertical 90^{o}
No. of filler wires	Single
Type of flux	Agglomerated neutral chromium compensating
Additional filler wire or metal powder additives	NIL
Type of weld	Square Butt
Preheat	None
Welding electrode grade	AWS/SFA 5.9 ER 308L

4.2 Arc start

The arc start is difficult in SAW, because space between the electrode and the work piece is filled with flux powder. In the present work, the arc was started by sharp wire start method. The tip of the electrode is cut mechanically by means of a wire cutter, to form a sharp chisel like edge, so that current density at the tip increases. Then the electrode was lowered to make a superficial contact with the work piece. The flux was applied and then welding is commenced. When the welding power supply is switched on then due to short circuiting of the electrode and work piece the sharp point melts away rapidly and starts the arc.

4.3 Pilot experiments

The Pilot experiments were conducted to determine the allowable range of welding parameters for joining the material. Proper control of welding parameters was very much necessary to achieve desired weld quality. The operating variables used in the current study are welding current, voltage, welding speed and length of stickout. The experiments were focused systematically by keeping three variables constant and varying the other. This was performed to determine the effect of individual variable on joint quality.

4.3.1 Observations from pilot experiments

Among the welding parameters, welding current was most significant parameter for SAW as it controls electrode melting, penetration and extent of base metal fusion. When the welding current was increased keeping other variables constant, it was visually observed that excessive penetration and reinforcement were seen. It was found that below certain level of current the welded joint was not complete due to lack of penetration. Upon increase in arc voltage, keeping current and speed constant, it resulted in flat and wide bead. Further increase in voltage had produced very wide bead and with some weld cracks. In addition, when voltage was reduced further, narrow and high bead was observed. The welding speed is another important parameter, which has negative effect on weld size and penetration. Upon increasing the speed, the applied heat input per unit length decreases, lesser filler metal gets deposited hence, less reinforcement height. In addition, it was also observed that bead size was reduced. At high speeds undercut, porosity and irregular bead shape were formed. As speed was reduced further, excessive reinforcement and bottom bead were seen. Length of stick out (LSO) in submerged welding as a general rule should be about 8 times the diameter

of the electrode wire. In the present pilot trials LSO was also observed to effect on weld quality. Finally, proper parametric envelopes were identified for joining in this research work with square butt configuration.

4.4 Fixture design

In the present investigation, two types of fixtures were used to carry out the welding experiments. Experiments on stainless steel (Jindal-JSLU SD) and austenitic stainless steel type 304, namely single-sided and double-sided SAW were conducted with the normal fixture. One set of experiments on single-sided SAW were performed with a heat sink fixture for carrying out comparative studies with normal single-sided SAW.

4.4.1 Conventional fixture

The main function of welding fixture is to position the work piece firmly during the welding operation. Fig.4.1 indicates the actual welding fixture with work holding clamps and dimensions of the backing trough used in the present study.

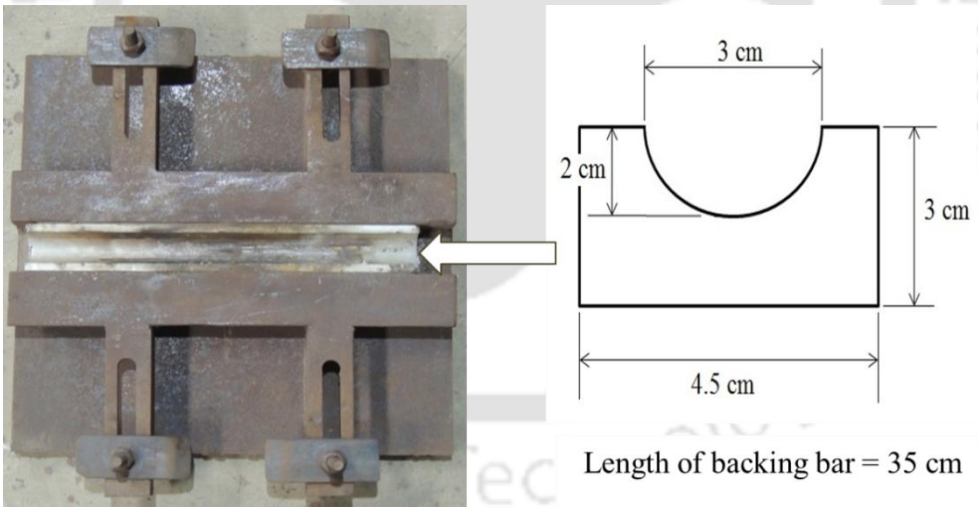

Fig.4.1 Fixture and dimensions of the backing bar

The backing bar was fabricated by machining an aluminium slab to achieve a deep semi-circular geometry and was fitted into the fixture. The flux was filled into the backing bar, and specimens positioned over it and were held employing clamps before the commencement of welding operation. Fig. 4.2 depicts the working principle of the backing bar.

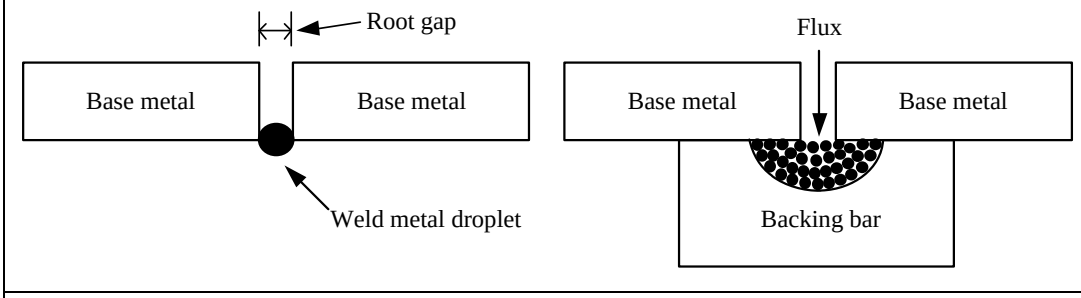

Fig.4.2 Working principle of the backing bar

The purpose of flux filling is to hold the molten metal and to get the required bottom reinforcement. The main advantage of using flux filled backing bar is that it can be reused many times, thereby minimizing the cost of production.

4.4.2 Heat sink fixture

Essentially heat sink fixture is the same as normal fixture, except it consists of water spray channels located beneath the fixture. The objective of designing this fixture is to remove the heat from the weld zone so that heat spread to the remaining part of the plate is reduced; hence, the resultant distortion and HAZ can be kept a minimum. The CAD model of the heat sink fixture is shown in Fig. 4.3. The actual fabricated fixture and sample mounted on fixture were shown in the Fig.4.4 (a) and (b) respectively. The physical quantities and their values are shown in Table. 4.2.

Table 4.2 Physical quantities and their values for heat sink fixture

Physical quantities	Values
Length of the backing bar	350 mm
Radius of backing bar	15 mm
Distance between weld centreline and start region of heat sink	30 mm
Width of the cooling channels	35 mm
Diameter of spray pipe	8±0.25 mm
Flow rate of water	4 (l/min)

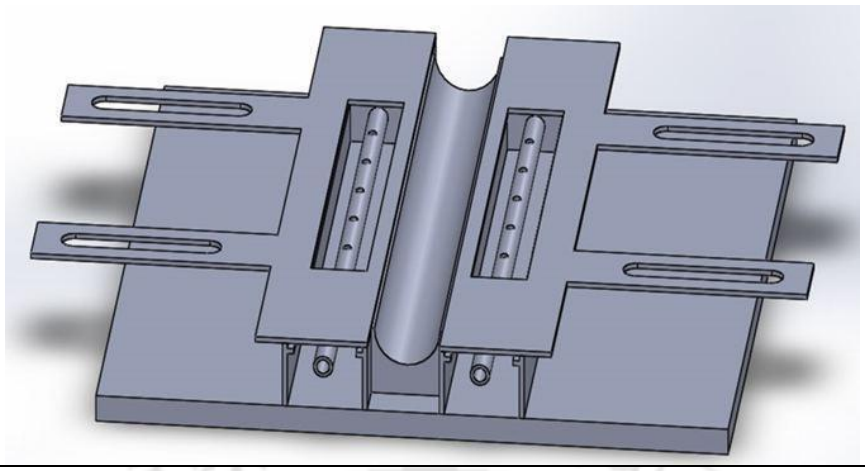

Fig.4.3 CAD model of the heat sink fixture

Fig.4.4 (a) Fabricated heat sink fixture

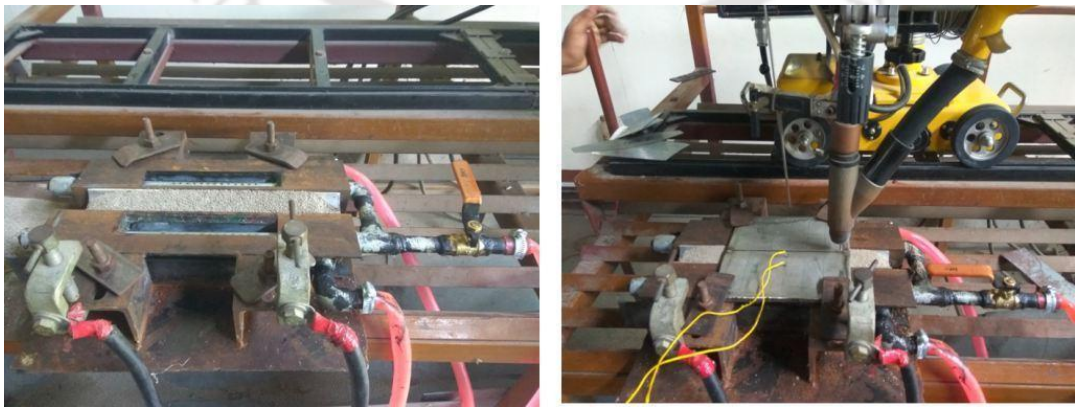

Fig.4.4 (b) Sample mounted on heat sink fixture

4.5 SAW flux

In SAW process the arc and molten metal are covered by a blanket of flux. Hence, the selection of flux is crucial in the SAW process. In the present investigation the flux used was ESAB OK Flux 10.92L, which is an agglomerated chromium alloying neutral flux. The alloying elements in the flux compensate the loss of chromium in the arc during welding. The basicity index of the flux is 1, and its grain size is 0.2 - 1.6 mm and confirms with EN ISO 14174 standards. In this research work, flux was re-dried to 300^{o}C for 2 hrs. before commencing of the welding operation, since flux is hygroscopic and has a tendency to absorb moisture from the atmosphere. The chemical composition of the flux from manufacturer's catalogue is given the Table 4.3.

Table 4.3 Chemical compositions of OK 10.92 L flux

Composition	CaO + MgO	SiO_2 + TiO_2	CaF_2	Al_2O_3+MnO	Fe
wt. %	30	35	10	20	Bal.

4.6 SAW electrode

The filler wire (Make: ADOR) used for welding of SS 304 confirms to AWS/SFA 5.9 ER 308L with 3.2 mm diameter. The chemical composition and mechanical properties of the electrode used in the present study are given in the Tables 4.4 and 4.5 respectively. The welds are made with constant current power source with electrical output as Direct current electrode positive (DCEP) and work piece was connected to negative.

Table 4.4 Chemical composition of SA welding electrode (wt.%)

C	Si	Mn	Cr	Ni	S	Cu	Mo	P	Fe
0.03	0.3-0.65	1.0-2.5	19.5-22.0	9.0-11.0	0.03	0.75	0.75	0.03	Bal.

Table 4.5 Mechanical properties of the filler wire

Specification	UTS (kgf/mm^2)	Yield Strength (kgf/mm^2)	% Elongation
AWS/SFA 5.9 3.2 mm dia.	65	48	45

4.7 Submerged arc welding machine

The fully automatic SAW machine, ADOR FONTECH TORNADO M-1250 and Welding Tractor FD 1X-200TZ were used in the present research work. The main specifications of the machine and tractor are shown in the Table. 4.6. The submerged arc welding machine used in the experimental investigation is shown in Fig. 4.5.

Table 4.6 Specifications of SAW machine

MODEL	TORNADO M-1250
Output current	150A~1250A
Duty cycle	60%
Diameter of welding wire	Φ3 ~ Φ6 mm
Power source characteristic	Constant current (CC) / constant voltage (CV)
Welding Tractor movement	Rail
Range of wire feed rate	0.5m/min~2.5m/min

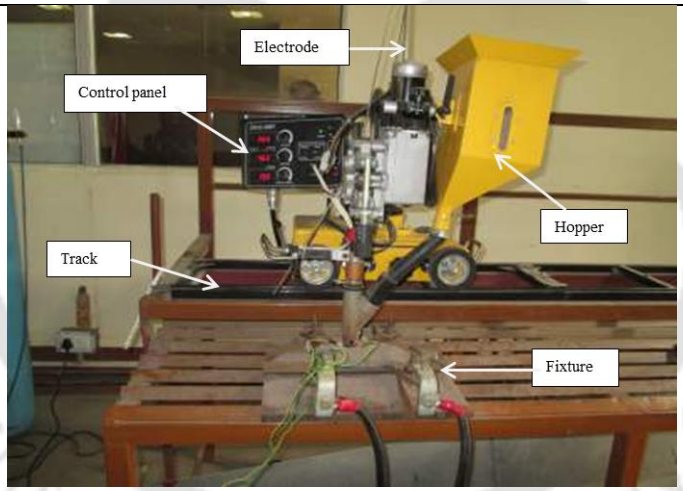

Fig.4.5 Submerged arc welding machine

4.8 Sample preparation

The samples for SA welding were prepared from flat plate material. After initial marking with a center punch on the plate, samples were sectioned using plasma torch. Further, all the edges of the samples were grinded to remove the burrs and HAZ. The prepared plates were further sectioned using wire cut electric discharge machine (WEDEM). The edges of the plates were degreased with acetone to remove any contamination. The samples to be welded were tack welded on top and bottom sides with manual metal arc welding with ER 308 L

electrode with a root gap of 2.5 mm prior to the commencement of welding operation. The same root gap was maintained constant for all plate thickness. Fig. 4.6 pictorial illustration of sample in tack welded condition with root gap.

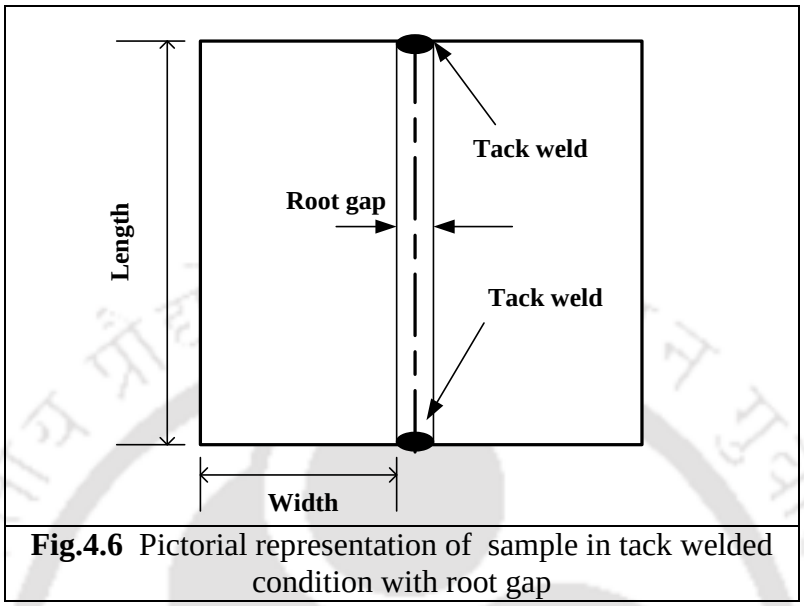

Fig.4.6 Pictorial representation of sample in tack welded condition with root gap

4.9 Experimentation

In the present investigation, two type's stainless steels were used for conducting welding experiments. These materials are commercial grade (Jindal-JSLU SD) stainless steel and austenitic stainless steel (AISI 304). The experimental part of the research was divided into few sub divisions based on materials and procedure implemented in the experiments. The succeeding paragraphs briefly narrate the sub divisions in the present experimental work:

Experimental SET-I is for welding of commercial grade (Jindal-JSLU SD) stainless steel where experiments were conducted to determine the influencing input parameters for SAW process. In this part, a total of 18 experiments were conducted based on mixed Taguchi design of experiments with orthogonal array (L-18) and by varying three parameters in three levels and one parameter in two levels.

Experimental SET-II exhibits welding of austenitic stainless steel (AISI 304) by varying the process parameters to determine their effect on mechanical properties and distortion. A total of nine experiments were conducted by varying the three input welding parameters. In addition, a similar set of another nine samples were welded using a specially designed heat sink fixture. The objective is to make a comparative study between with heat sink and without heat sink on mechanical properties and distortion produced by SAW process.

Experimental SET-III represents the double sided welding of AISI 304 by varying the process parameters. A total of nine experiments were conducted by varying the input parameters to determine their individual effect on weld quality. The another objective in this set is also to make a comparative study between double sided welding and single sided welding on the distortion of SAW process.

Experimental SET-IV represents the bead-on-plate welding of AISI 304 by application of surface active elements with process variable combinations. A total of fifteen experiments were conducted in this phase. The objective in this phase is to study the effect of surface active elements on bead geometry. To ascertain their effect weld beads made with surface active flux were compared with normal weld beads.

For performing different set of experiments a separate set of input parameters for each of experiments were considered. The detailed set of input parameters were discussed in the respective set of experiments. Experimental procedure for each set of experiments is detailed in the following sub sections.

4.9.1 Experimental SET-I: Determination of influencing process parameters of commercial grade stainless steel in SAW

In the present work, two stainless steel plates (Jindal-JSLU SD), with dimensions of 150 mm×75 mm×8 mm of each were used as the work piece material to make single sided single pass square butt joint. All plates were welded in the square butt condition without any edge preparation in a single pass. The chemical composition of stainless steel (in wt. percentage) is given in the Table 4.7. The mechanical properties of the parent metal are shown Table 4.8. Prior to the commencement of the welding operation, the tack-welded samples are positioned in the fixture and held rigidly by means of clamps. The root gap in square butt welds is set in order to facilitate the passage of molten filler metal from top of work piece to root of the weld. In the present investigation root gap for a square butt welding is fixed as 2.5 mm. The specifications of flux and wire are given Tables 4.3 and 4.4. The submerged arc welding machine used for the study is fully automatic (Make: ADOR Fontech -1250) is shown in Fig.4.5. There are several parameters independently control the SAW process. Extensive preliminary experiments were carried out to determine the most important parameters affecting the weld quality. It was found that welding current, voltage, traverse speed and length of stick out are most prominent process variables, and hence these were taken into consideration in the present work. The welding current, voltage and welding speed were

varied in three levels; length of stick out is varied in two levels. The details of experimental parameters and their respective levels are depicted in the Table. 4.9. The Taguchi's L-18 matrix used in the present study is detailed in the Table. 4.10.

Table 4.7 Chemical composition of stainless steel (Jindal-JSLU SD) (wt.%)

C	Mn	Si	Cr	Ni	P	S	Mo	Cu	Fe
0.17	9.52	0.38	14.93	0.42	0.045	0.020	0.002	1.94	Bal.

Table 4.8 Mechanical properties of the parent metal (Jindal-JSLU SD)

Tensile strength (MPa)	Yield strength (MPa)	Elongation (%)
682.31	328.66	32.89

Table 4.9 Welding process parameters and their levels

SL.	Parameters	Notation	Factors Levels		
1.	Current	I (A)	445	455	465
2.	Voltage	V (V)	26.5	27.5	28.5
3.	Welding speed	S (mm/s)	5.0	5.14	5.27
4.	Length of stick out	LSO (mm)	23	25	--

Table 4.10 Experimental parameters in Taguchi L_{18} orthogonal array

Exp.No.	Length of Stick out (mm)	Voltage (V)	Current (A)	Welding Speed (mm/s.)
1	23	26.5	445	5.00
2	23	26.5	455	5.14
3	23	26.5	465	5.27
4	23	27.5	445	5.00
5	23	27.5	455	5.14
6	23	27.5	465	5.27
7	23	28.5	445	5.14
8	23	28.5	455	5.27
9	23	28.5	465	5.00
10	25	26.5	445	5.27
11	25	26.5	455	5.00
12	25	26.5	465	5.14

13	25	27.5	445	5.14
14	25	27.5	455	5.27
15	25	27.5	465	5.00
16	25	28.5	445	5.27
17	25	28.5	455	5.00
18	25	28.5	465	5.14

Upon completion of experimental work, test specimens were prepared from the respective weldment to evaluate the weld quality. The weld qualities studied in the experimentation were ultimate tensile strength (UTS), top bead width (TBW), top reinforcement height (TRH) and angular distortion (AD). The mentioned weld qualities were taken into account while optimizing the input process variables.

4.9.2 Experimental SET-II: Comparative studies on effect of process parameters on mechanical properties for normal welding and welding with heat sink in single side SAW

In this phase of experimental work austenitic stainless steel of type AISI 304 of 200 × 100 × 8 mm thick were joined in square butt configuration. The sample preparation for welding was same as stated in experimental set –I. The chemical composition of the base material (type AISI 304) is shown in the Table 4.11. The mechanical properties of the austenitic stainless steel (type AISI 304) are shown in Table 4.12.

Table 4.11 Chemical composition austenitic stainless steel (wt.%)

C	Mn	Si	Cr	Ni	P	S	Al	Co
0.024	1.89	0.59	18.91	8.43	0.017	0.011	0.011	0.093
Cu	Nb	Ti	V	Pb	Sn	Fe		
0.478	0.052	0.041	0.045	0.014	0.02	Bal.		

Table 4.12 Mechanical properties of the austenitic stainless steel (AISI 304)

Tensile strength (MPa)	Yield strength (MPa)	Elongation (%)
709.3	301.5	54.0

In present experimentation the heat sinking was achieved by spraying water (cooling source) at a pre-determined distance from the welding torch, while the welding is carried out. While performing heat sink welding proper care is taken, such that cooling medium i.e., water is kept sufficiently away from the weld zone, in order to avoid any electrical hazard and contamination of SAW flux. The inlet connection of the water sink pipe system was connected to the regular water line and a control valve is set to the fixture. The flow rate of the water cooling medium is estimated prior to commencement of the experiments with help of stop watch for different valve positions. Finally a suitable flow rate was chosen for all experiments. In this phase of experimentation a total of eighteen experiments were carried out i.e, nine with heat sink setup and nine with conventional fixture. The process parameters considered were welding current, voltage and welding speed which were varied at three levels. Throughout the experiments length of stick out was kept constant i.e, 25 mm. The CAD solid model of the heat sink fixture is shown in Fig. 4.3. The welding parameters adopted in this study are tabulated in Table. 4.13. The welding experiments carried out in this study are given in the Table 4.14.

Table 4.13 Welding process parameters for conventional and heat sink welding

SL.No	Parameters	Notation	Values		
1.	Current	I (A)	410	420	430
2.	Voltage	V (V)	23	24	25
3.	Welding speed	S (mm/s)	5.55	6.11	6.66
4.	Length of Stick out	LSO (mm)	25	25	25

Table 4.14 Experiment set for conventional and heat sink assisted welding

Sl No.	Current (A)	Voltage (V)	Welding speed (mm/s)
1	***410***	23	5.55
2	***420***	23	5.55
3	***430***	23	5.55
4	430	***23***	5.55
5	430	***24***	5.55
6	430	***25***	5.55
7	430	25	***5.55***
8	430	25	***6.11***
9	430	25	***6.66***

Table 4.14 indicates the experimental set of input parameters for conventional and heat sink assisted welding. These experiments were carried out by systematically varying one parameter and keeping others constant. This was done in order to study the effect of individual variable on weld quality. In this phase of study the effect of heat sink on fusion zone area, mechanical properties, and distortion were compared with that of conventional SAW welding.

4.9.3 Experimental SET-III: Effect of process variables on bead geometry and mechanical properties in a double sided welding

In this experimental set austenitic stainless steel (type AISI 304) of 8 and 12 mm thick were double sided welded in square butt configuration. For 8 mm thick plates nine experiments were conducted by varying each of the input parameter namely welding current, voltage and speed. In case of 12 mm thick plates three each experiment with only welding current variation were studied. The experimental procedure is same as that mentioned in Experimental SET-I. The same heat input is assumed on both sides of the plate for double side welding in this investigation. Fig.4.7 DSSAW square butt joint configuration with root gap. For all the samples weld qualities were estimated on one side of the plate i.e., the second weld run.

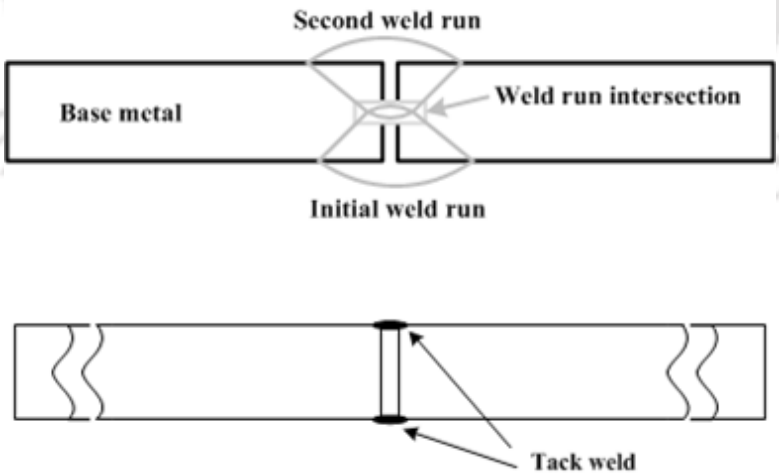

Fig.4.7 Double side Square butt joint configuration with root gap.

In double sided SA welding ideally up to 60 to 70 % penetration of the base material thickness in each pass is desirable for obtaining good joint strength, Parmar (2001). For measurement of bead profiles, the digital images were imported into imaging software followed by calibration and measurement. The bead width is the uncovered surface of a weld

on the side from which the welding was performed. The bead width was measured on top width of the fusion zone. The weld penetration is the depth of a groove weld which stretches out into the base of a joint and was estimated on the centreline of root cross sectional area. The reinforcement is characterised as excess weld metal from upper surface of the work piece. The one terminology specific to double side welding is the weld run intersection also called transition zone is the portion of area re-melted by the second pass in a double side SAW. The experimental process variables for 8 and 12 mm thick plates are detailed in the Tables. 4.15 and 4.16.

Table 4.15 Experiment process parameters for 8 mm thick plates

Exp.	Welding current (A)	Welding speed (mm/s)	Voltage (V)	Length of stick out (mm)
1	340/365/390	7.08	24	25
2	365	7.08	22/24/26	25
3	365	6.80/7.08/7.36	24	25

Table 4.16 Experiment Process parameters for 12 mm thick plates

Exp.	Welding current (A)	Welding speed (mm/s)	Voltage (V)	Length of stickout (mm)
1	400	5.83	27	25
2	430	5.83	27	25
3	460	5.83	27	25

In this experimental set out responses namely weld bead geometry, mechanical properties, angular distortion was studied. Also a comparative study between angular distortion of single side and double side was performed in this experimental phase.

4.9.4 Experimental SET –IV: Effect of surface active flux on bead geometry

In this experimental phase welding was performed on 8 mm thick austenitic stainless steel plates by applying surface active elements. The surface active elements used in this investigation are SiO_2, Cr_2O_3, TiO_2 and mixture of all elements. For comparison purpose weld beads are made without surface active (SA) elements. The process of welding with SA elements is explained as follows:

- Required quantities of SA elements were taken in clean container and acetone was added to form slurry.
- With help of a brush this slurry was applied on the surface after which welding is commenced. Table.4.17 shows welding parameters are used in this phase of study.

Table 4.17 Experimental process parameters for welding with and without surface active flux

Exp.	Welding current (A)	Welding speed (mm/s)	Voltage (V)	Length of stickout (mm)
1	260	7.36	28	25
2	280	7.36	29	25
3	300	7.36	30	25

In this study effect of SA elements on weld pool geometry namely weld width, reinforcement height, and penetration were studied. Also a comparative study was made on welds without SA elements.

4.10 Testing and characterization

This section describes various the methods to evaluate the weld quality and thermal history measurement. The weld qualities were examined by destructive as well as non-destructive tests such as distortion measurement, tensile test, micro-hardness, macro-structural and microstructural studies, and fractographic examination.

4.10.1 Temperature measurement

The calibrated thermocouples were attached to the specimen at an appropriate distance from weld center line with the help of a thermocouple attaching machine (Make: Dyna weld). The other end of the thermocouple was connected to the multiplexer which in turn is connected to the Data acquisition system (Make: Agilent) for recording the thermal history of the welded sample. The time interval for capturing the temperature data is set as 200 ms. The setup depicting the measurement of temperature during the welding and welding in process is given in the Fig.4.8.

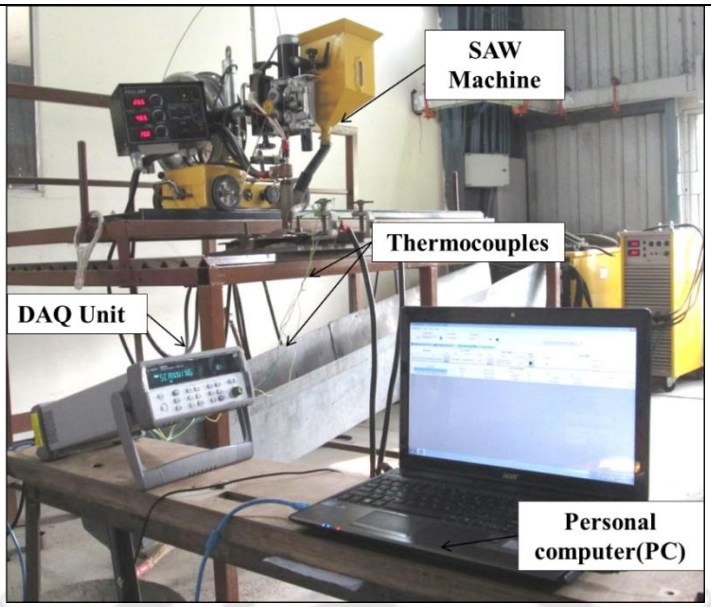

Fig.4.8 Complete setup of temperature measurement

4.10.2 Distortion and edge deflection measurement

The welding distortion and edge deflection in a butt joint were measured with coordinate measuring machine (Make: Carl Zeiss, USA). Figs.4.9 and 4.10 shows angular distortion measurement setup using CMM and schematic of sample with measuring points respectively. In Fig.4.10 the 'X' represents the perpendicular distance from one end of the weld bead to the edge of the plate across transverse direction to the weld. The 'Y' in Fig. 4.10 represents the perpendicular distance from center of the plate till plate edge along the longitudinal direction to the weld. The work piece under observation was placed on a V Block and positioned on the horizontal bed of the machine. With the help of trisquare straight lines are scribed on the top face of the specimen. The control points for measurement were marked with the help of center punch. The coordinate measurement machine was interfaced with U-Soft software. The included angle between the two collinear lines was measured. Three readings were taken transversely, one at the top edge and bottom edge and other at center of the welded sample. The distorted angle is measured using the formula:

$$\theta = \frac{(180 - \beta)}{2} \tag{4.1}$$

where β = Included angle of the welded sample in degrees

θ = Angle of distortion in degrees

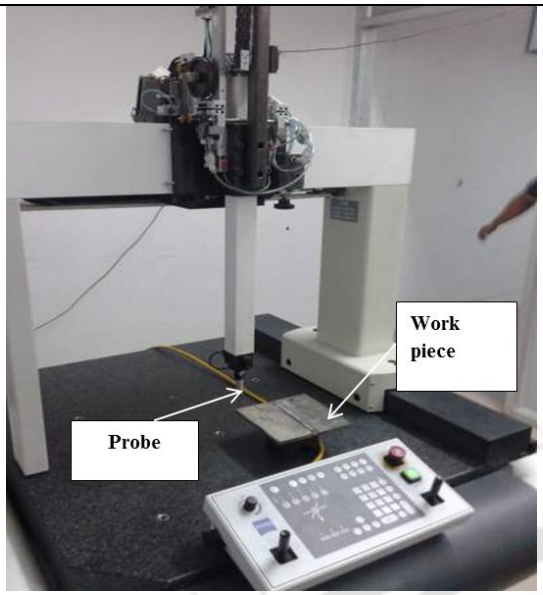

Fig.4.9 Measurement of angular distortion with Coordinate measuring machine

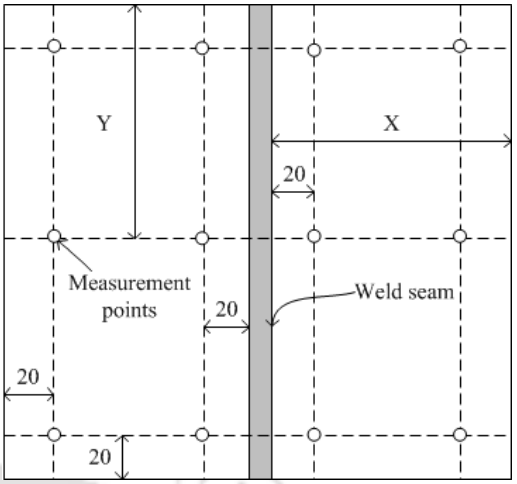

Fig.4.10 Schematic of sample with measuring points for distortion measurement

The edge deflection of the welded sample was determined as the difference in the initial and final readings for vertical positions of the marked points along the edge on the top surface of the weld plate. Firstly, the vertical position of the marked points was recorded on Coordinate Measuring Machine (CMM) for unwelded samples. Once the welding has been performed, new vertical positions of the same marked points are again recorded. Finally, the welding induced vertical distortion on edge is determined by the change in the vertical positions of the marked locations.

4.10.3 Tensile test

The tensile test falls under the category of destructive testing and is normally used to ensure the quality of samples. Tensile test is very helpful during the development of new materials, since material properties obtained in this test can be readily compared with the existing ones. Tensile test was conducted in a universal testing machine (MAKE: BISS: MEDIAN 250). All tensile tests were carried out at the rate of 1 mm/ min cross head speed. The detailed specification of the tensile testing machine is given in Table 4.18 which is placed at the end of this chapter. All the samples are prepared as per ASTM E-8 standards. The tensile samples tested for experiment SET-I have a gage length of 25 mm and the rest of experiment sets have a gage length of 50 mm. The tensile samples are cut transverse to the direction and weld bead is retained during testing. Two tensile samples are extracted from the welded plate and

the average of two was used to analyse the tensile behaviour of the weldment. Figs. 4.11 (a) and (b) show the dimensions of the tensile specimen for 25 mm and 50 mm gage length. Fig. 4.12 (a) and (b) show the tensile testing machine with sample and in other fitted with extensometer respectively. Fig. 4.13 shows the prepared tensile specimens for 50 mm gage length.

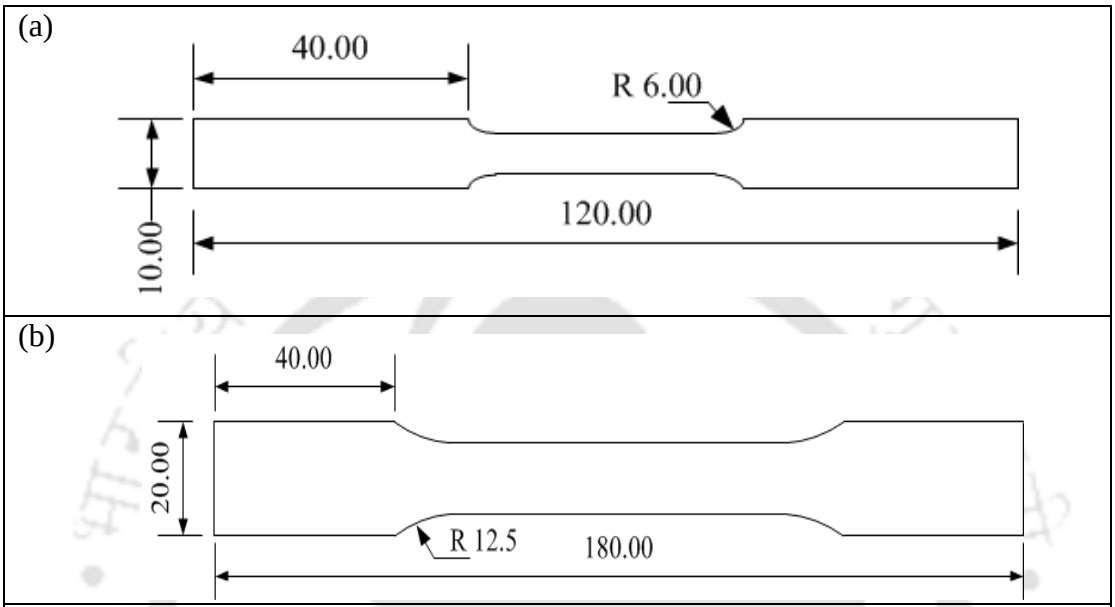

Fig.4.11 (a) and (b) Tensile specimen with 25 mm and 50 mm gage length as per ASTM E-8 standard (All dimensions are in mm)

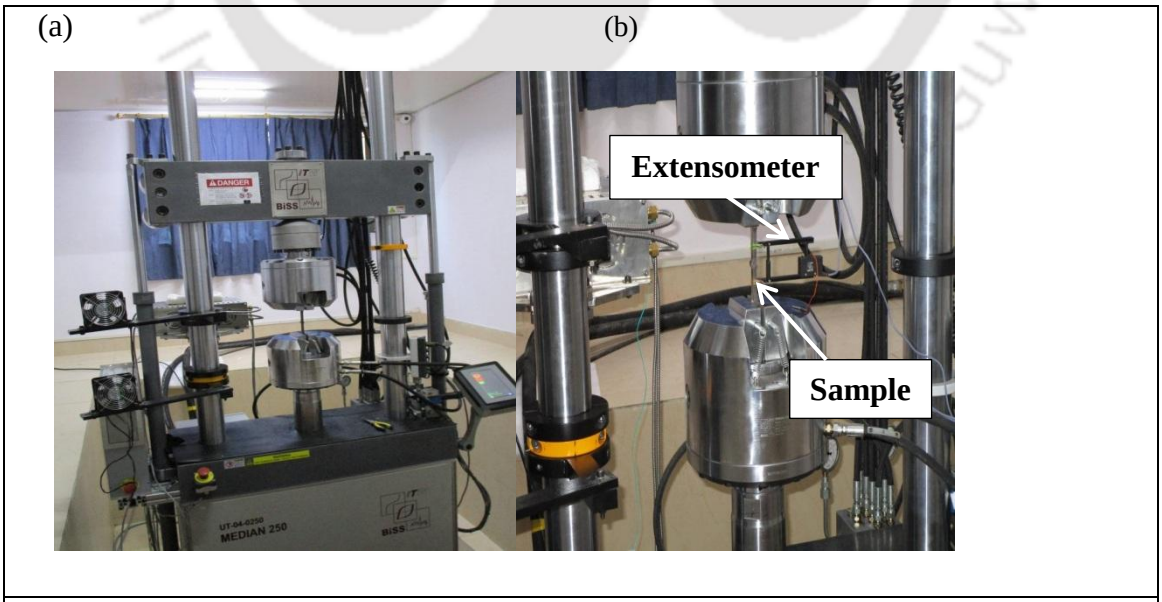

Fig.4.12 (a) Tensile testing machine with sample and (b) extensometer attached to the sample.

Fig.4.13 Tensile specimens with 50 mm gage length (ASTM E 8)

4.10.4 Vickers micro hardness test

The Vickers hardness testing method is widely used for hardness measurement of welded samples. In this method a diamond pyramid indenter with square base is used and the angle between opposite faces of the pyramid is 136^{o}. Hence a geometrically similar indentation can be obtained for all loads. With the help of the microscope the diagonals of the indentation are measured to determine the hardness of the test specimen.

Fig.4.14 Vickers micro hardness testing machine

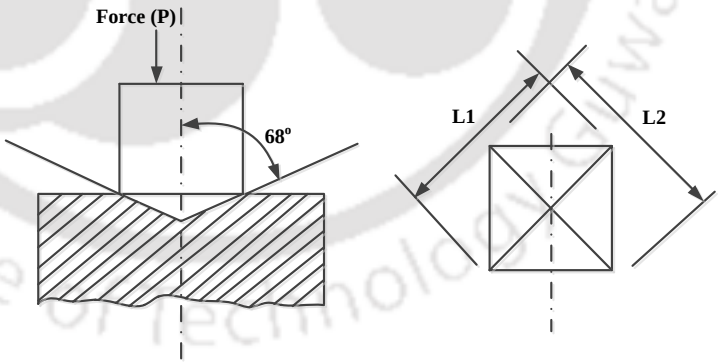

Fig.4.15 Illustration of Vickers hardness indentation

The Vickers hardness number (VHN) is stated as follows:

$$\text{VHN} = \frac{2P\sin 68^{o}}{L^{2}} = \frac{1.854P}{L^{2}} \qquad (4.2)$$

where P is applied force in kgf and L is the arithmetic mean of the both diagonals.

4.10.4.1 Sample preparation for hardness measurement

The samples for hardness were sectioned perpendicular to the weld in such a way that it consists of weld metal and some portion of base metal. Fig. 4.14 shows the Vickers hardness indenter used in this investigation. Fig. 4.15 shows the illustration of Vickers indentation. The detailed specification of the equipment is given in the Table.4.18 which is placed at the end of this chapter. These samples are ground using silicon carbide papers of grades 320 to 1500 grit size in order to obtain a burr free and smooth surface. The Vickers micro hardness of the welded sample is recorded with 0.5 kg load and a dwell time of 15 sec. with Buehler automatic testing machine to record the hardness in the various regions of the weld specimen. For getting the desired accuracy three readings are noted in the same region of the sample.

4.10.5 Microstructure and macrostructure

After welding is complete the transverse section of the samples are extracted from the welded plate. For studying the microstructure these samples were ground using silicon carbide papers of grades 320, 600, 800, 1000, 1200, 1500 and 2000 grit size. Fig.4.16 shows the single disc polishing machine used in the present investigation. These samples were then polished using 0.3 micron Al_2O_3 (Buehler, USA) on a velvet cloth. The mirror finished samples were then etched with Glyceregia (3% Glycerol, 2 – 5 % HCl and 1% HNO_3) to reveal the microstructure of the base metal, HAZ, Fusion zone and Interface zone. The etched samples were washed thoroughly and dried with a dryer. The microstructure at distinct locations in the sample of study were viewed and captured with an upright optical microscope (Make: Carl Zeiss) coupled with AXIOVISON image analysis software. Fig. 4.17 shows the upright microscope used in this experimentation. The detail specification of polishing machine and upright microscope is shown in the Table.4.18 which is given at the end of this chapter.

After completing the microscopic examination, all the samples were subjected to macroscopic study. Fig.4.18 shows the Nikon SMZ-25 stereomicroscope (Macroscope) used in the present investigation. Table.4.18 shows the detail specification of the microscope which is given at the end of this chapter. The macroscopic examination is helpful in identifying some of the defects like blow holes, cracks and flux inclusions. The main features

that were investigated in macroscopic study are weld bead width, reinforcement height, depth of penetration, area of penetration, area of reinforcement and weld run intersection.

Fig.4.16 Single disc polishing machine

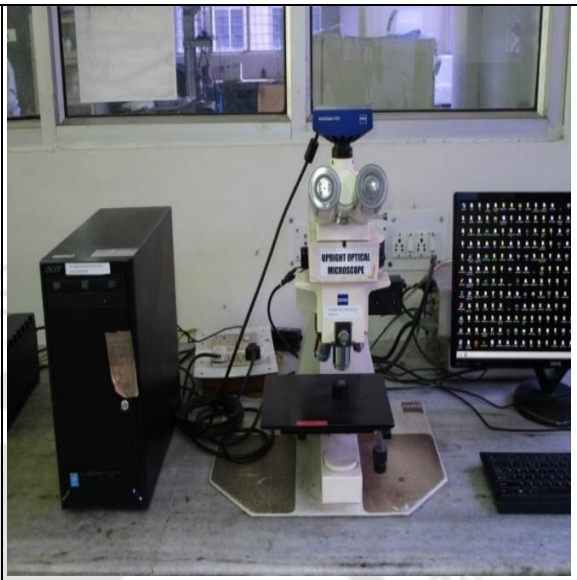

Fig.4.17 Upright optical microscope

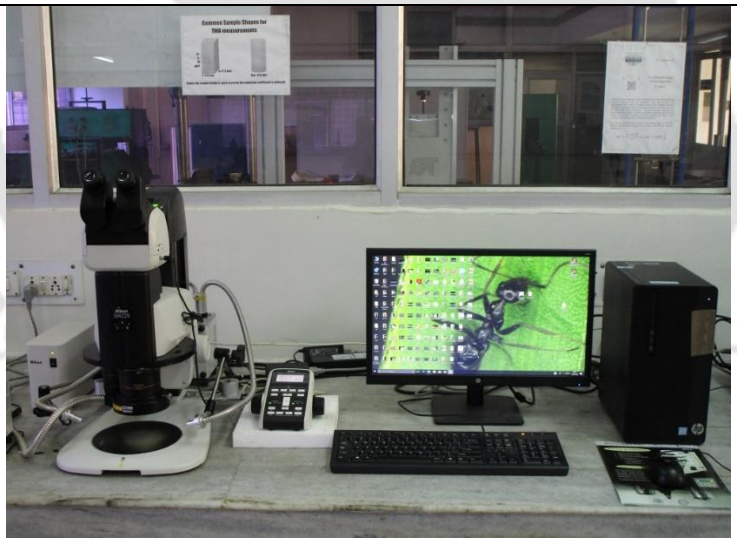

Fig.4.18 Stereo microscope (macroscope)

4.10.6 Fractographic analysis

The fractographic examination is a part of failure analysis. It is used extensively in the industry to identify the root cause of the failure of a machine or a component. In the present investigation fractographic analysis was accomplished by means of field emission electron

microscopy (FESEM). Fig. 4.19 shows FESEM (Carl Zeiss; Model: Sigma) which was used in the present study. Details of its specification are tabulated in Table.4.18 which is given at the end of this chapter. The fracture surface of tensile specimen was sectioned by means of wire EDM machine. The sample is washed with distilled water and then ultra-sonicated in the acetone until the greases and contaminations were eliminated. The fractographs are helpful in identifying the nature of the fracture in a tensile specimen.

Fig.4.19 Field emission scanning microscope

Table 4.18 Detailed specification of equipment used to analyse the welded samples

Equipment Designation	Manufacturer & Model	Specifications
Servo Hydraulic UTM	BISS, INDIA UT-06-0250 MEDIAN 250	• Capacity: (±) 250 kN • Stroke: 150 mm (aprox.) • Drive: Servo-Hydraulic • Specimen types : Flat, round, threaded • Test conditions : Strain/Stress/Displacement Controlled • Test: Tension, compression and ¾ point bend test, Low cycle fatigue tests, High cycle fatigue tests, Fatigue crack propagation tests, K1c and J1c fracture toughness tests, Creep tests, Stress relaxation tests, shear tests, Constant true strain rate tests
Variable speed Polisher/ Grinder	Chennai Metco. Model: PMV 008 BANIPOL VT	• 8'' single disc polisher • 0.5 HP A.C motor

Hardness tester	Buehler, Micromet-2101	• Indentation force: 1, 10, 50, 100, 300, 500, 2000 g force • Dwell time: 5 to 60 sec at interval of 5 sec.
Optical Microscope	Carl Zeiss Axiotech-100HD, 3D	• Magnification: 100 X • Table movement: 3 axis measuring system, reflected light measuring stage 75 mm × 55 mm × 50 mm • Camera: Axio-Cam and Axiovision software (4.8.2)
Stereo Microscope (Macroscope)	Nikon SMZ-25	• Optical system: Parallel-optics type (zooming type), Apochromat optical system • Zoom ratio: 25:1 • Total Magnification: 3.15-315X • Observation methods: Bright Field, Epi Fluorescence, Simple Polarizing (with P2-POL Simple Polarizing Attachment), Dark Field (with P-DF LED Dark Field Unit), Oblique lighting
Field Emission Scanning Electron Microscope (FESEM)	Carl Zeiss Sigma	• Specimen chamber: 330 mm inner ϕ, 270 mm height • Magnification: 10X to 300,000X • Detectors: in-lens SE (in-lens secondary), SE (secondary electron) and BS (backscatter electron)

Chapter 5

Numerical Results and Discussion

5.0 Introduction

In this chapter results of non-linear elasto-plastic thermo-mechanical analysis are presented. The results of non-linear thermo-mechanical analysis carried out in this present investigation consist of following subsections:

- 3-D Transient thermal analysis using a volumetric heat source.
- Thermo-mechanical analyses of single sided singe pass SAW process.
- Prediction of welding induced distortions in large weld structure.

5.1 Thermo-mechanical analysis of single sided single pass Submerged arc welding (SAW)

In this section, nonlinear elasto-plastic thermo-mechanical FE modeling approach for single sided SAW is presented. The transient thermal history, residual stresses and distortion pattern of the square but joint are predicted by 3-D Finite Element (FE) analysis. The thermo-mechanical analysis is performed using commercially available software (ANSYS^{TM}). The methodology adopted and results obtained from numerical analysis are presented and discussed in this session.

5.1.1 3D-FE modelling details

The thermal history and the resulting residual stresses and deformation were studied by means of finite element analysis. In order to accurately predict thermal history and residual stresses in a butt joint, 3-D finite element method was adopted. In this investigation thermo-mechanical analysis was carried by means of uncoupled formulation. First, thermal history from the model was computed by heat conduction analysis. The heat transfer was considered to be governed by Fourier's law of heat conduction. Secondly, temperature history is attained by each node was employed as thermal load in the subsequent structural analysis with appropriate material model for predicting residual stresses, and resulting residual deformation. The detailed theoretical back ground pertaining to thermo-mechanical analysis is presented in chapter 3. The present formulation considers temperature dependent thermo-physical and mechanical properties and is presented in chapter 3.

The 3-D FE model was meshed using 8 node brick elements. The SOLID70 thermal element was used in transient thermal analysis due to its 3-D thermal conduction capability. The transient thermal history captured from the 3-D thermal analysis was used as an input to perform the non-linear elasto-plastic thermo-mechanical analysis. For structural analysis, SOLID70 thermal element was replaced with compactible structural element i.e. SOLID45 to perform the structural analysis. The schematic diagram of the butt-weld joint is shown in Fig. 5.1.

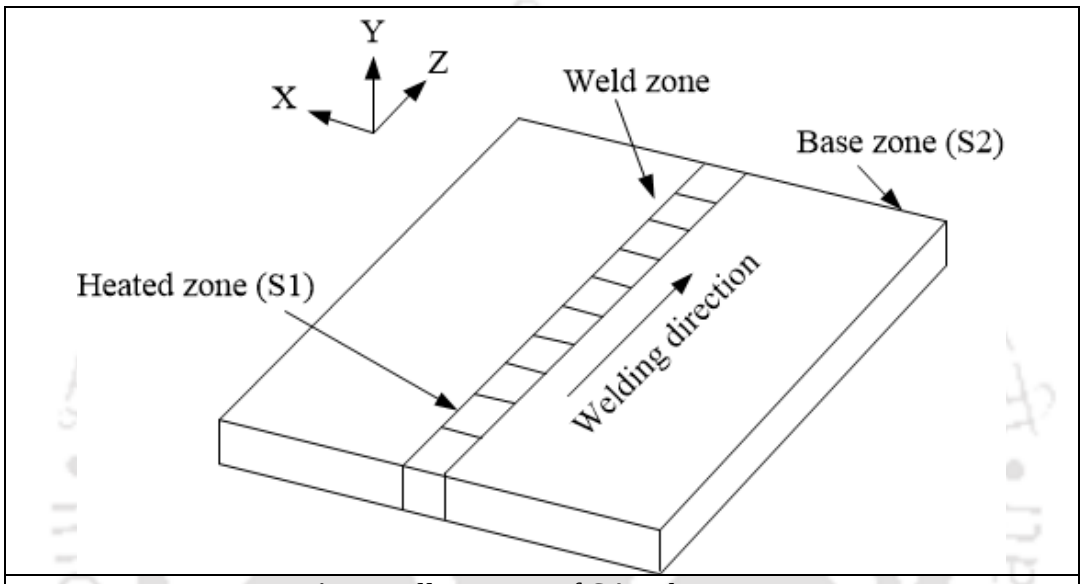

Fig.5.1 Illustration of SAW butt joint

The transverse section of weld bead obtained from experimental work was captured by Nikon SMZ25 microscope with a magnification of 0.5X. The experimentally obtained weld bead geometry was used in the development of 3D FE model. The experimental procedure for submerged arc welding of square butt joint is mentioned in chapter 4. Fig.5.2 (a) and (b) shows the experimental weld cross section and developed geometry of butt joint. Fig.5.3 shows finite element model of single sided square butt joint.

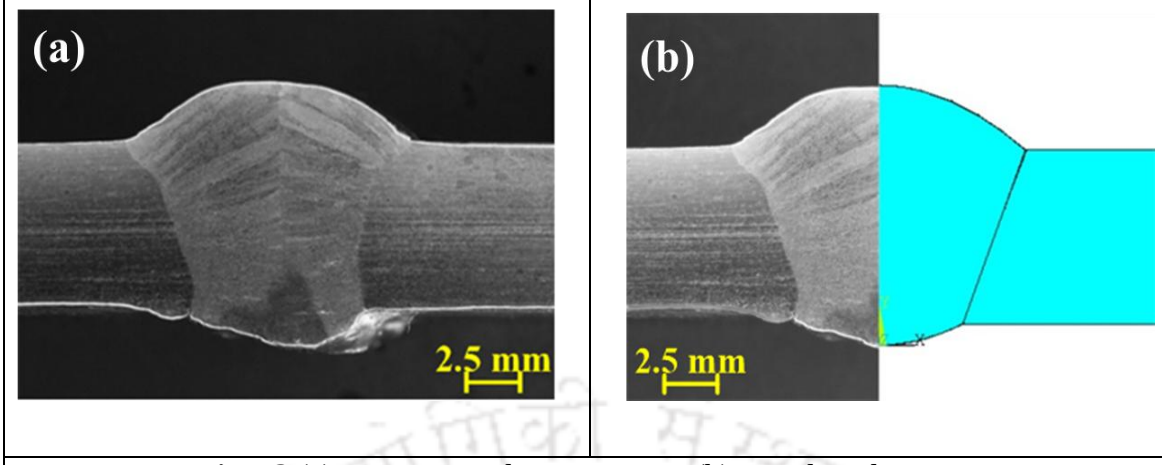

Fig.5.2 (a) Experimental cross section (b) Developed geometry

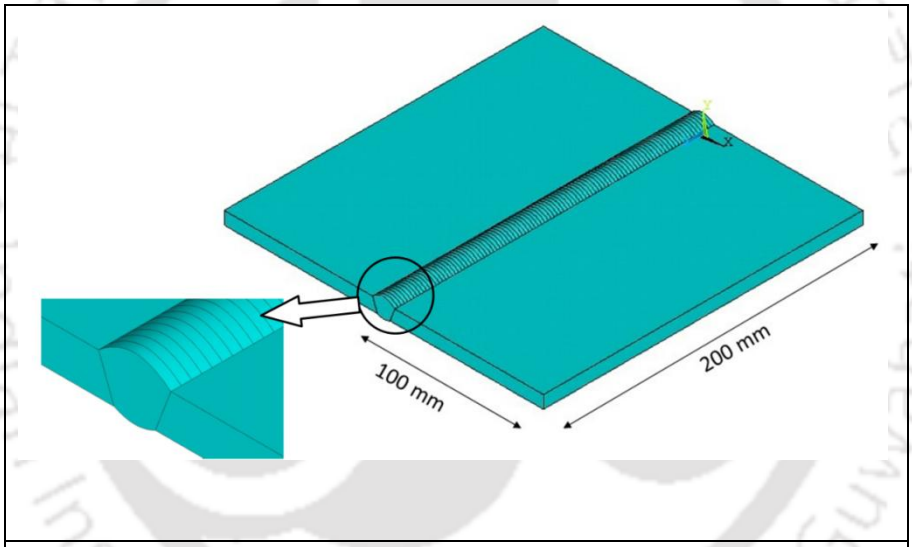

Fig.5.3 3-D FE model of square butt joint

5.1.2 Meshing details

A rigorous mesh sensitivity analysis was carried out to determine the optimum meshing parameters like element size, number of elements and spacing ratio. The uniform fine mesh was used along welding region to obtain accurate temperature field in high temperature gradient regions of fusion zone and heat affected zone (HAZ). The farther region was discretized with coarse mesh to minimize the computational time. In the fusion zone, elements of size 0.5 mm × 0.5 mm were considered and spacing ratio of 0.05 was used in the farther region. The 3-D meshed model of square butt joint is shown in Fig. 5.4.

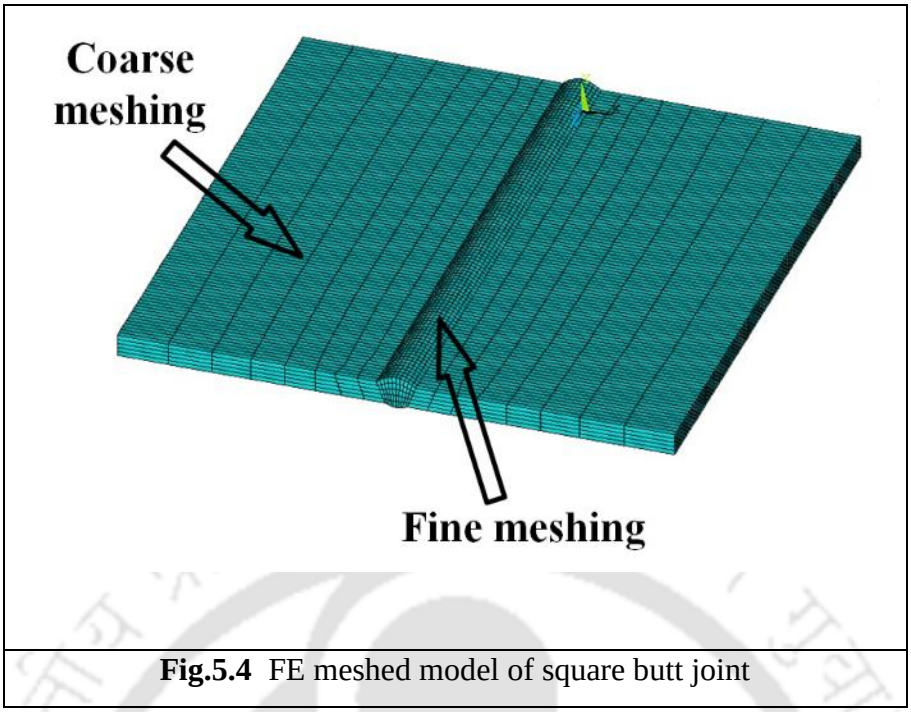

Fig.5.4 FE meshed model of square butt joint

5.1.3 Modelling of heat source

The heat source plays a vital role in welding operation to obtain overall thermal history of the welded specimen. The geometry of weld bead was taken from the experimental result. The numerical simulation of the welding process was performed by applying a uniform heat generation on the weld bead. The moving co-ordinate volumetric heat source model was developed by considering element “birth and death” technique. The element "birth and death" technique was implemented only in transient thermal analysis study and was applied in two steps.

Initially, all the elements located at the weld zone were killed, and an empty weld zone is obtained. Subsequently, the volumetric heat source simulates the weld bead formation by activating the elements located at the weld zone bead by bead with time.

The heat input per unit volume (Q) is calculated by using the following equation.

$$Q = \frac{\eta W}{v} \tag{5.1}$$

where η is the thermal efficiency of the heat source and W is the welding power and v is the volume of the active weld bead element as shown in Fig. 5.3.

5.1.4. Transient thermal analysis

In present investigation transient thermal analysis was carried out by varying arc power, welding speed and thickness. Table 5.1 denotes the processing variables and the different thickness used in the analysis.

Table 5.1 Process parameters for single sided SAW

SET. No.	Welding arc power (W)	Welding speed (mm/s)	Plate thickness (mm)
SET-I	23 V × 430 A = 9890 W 24 V × 430 A = 10320 W 25 V × 430 A = 10750 W	5.55	8.0
SET-II	10320 W	5.55 6.11 6.66	8.0
SET-III	10750 W	5.55	8.0 10.0 12.0

Figs.5.5 and 5.6 show the moving heat source's transient temperature contour over the top surface of the 8 mm thick plate for the process variable voltage of 24 V, current of 430 A and speed of 5.55 mm/s during welding and cooling phase respectively.

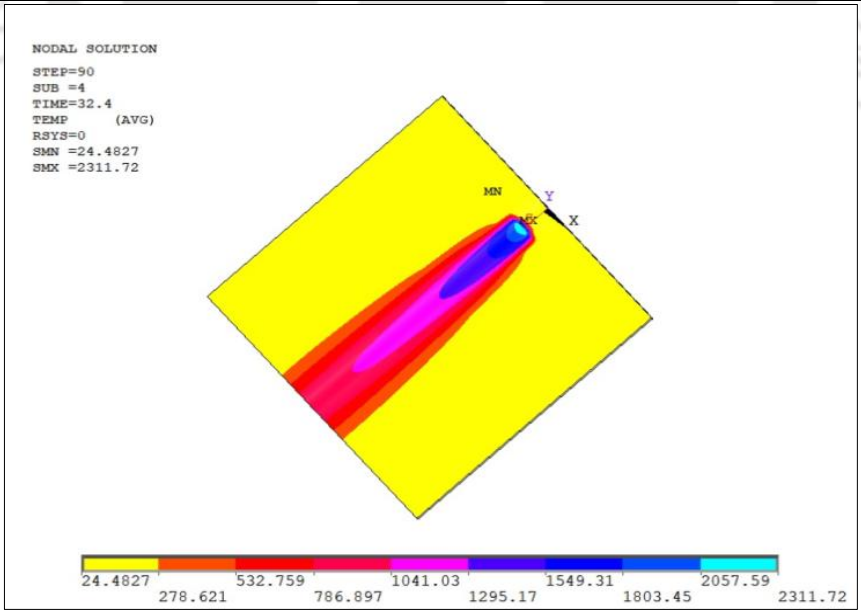

Fig.5.5 Temperature distribution during welding process due to moving heat source

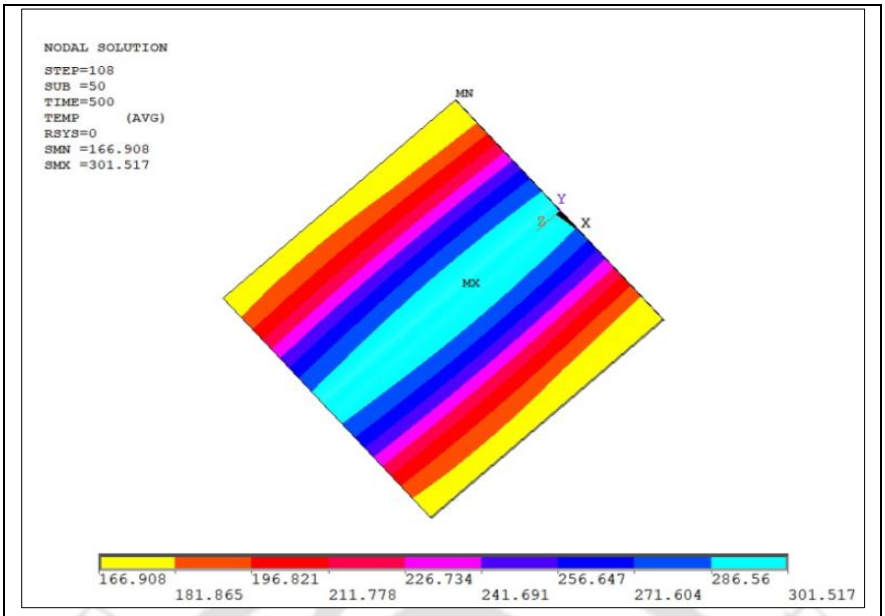

Fig.5.6 Temperature distribution during cooling phases at a time of 500 sec

5.1.4.1 Effect of varying welding power on temperature distribution

In the SET-I three different welding arc powers namely 9890 W, 10320 and 10750 W were chosen for the constant welding speed of 5.55 mm/s to study the peak temperature distribution with variation in welding arc power. Fig.5.7 (a) and Fig. 5.7 (b) represent the peak temperature distribution from the weld center line in transverse direction on top and bottom surface of the weld plate respectively under the varying welding power and constant welding speed of 5.55 mm/s. It is observed that peak temperature increases with increase in welding power on both top and bottom side of the plate. The peak temperature of 2239.16 °C, 2307.71°C and 2382.35°C were obtained for welding arc power of 9890 W, 10320 W and 10750 W on top surface of the plate respectively as shown in Fig. 5.7 (a). The peak temperature was increased to 6.4 % by increasing the welding arc power from 9890 W to 10750 W on top surface of the plate. The peak temperature at the bottom side is lower than top surface due to heat loss along thickness direction.

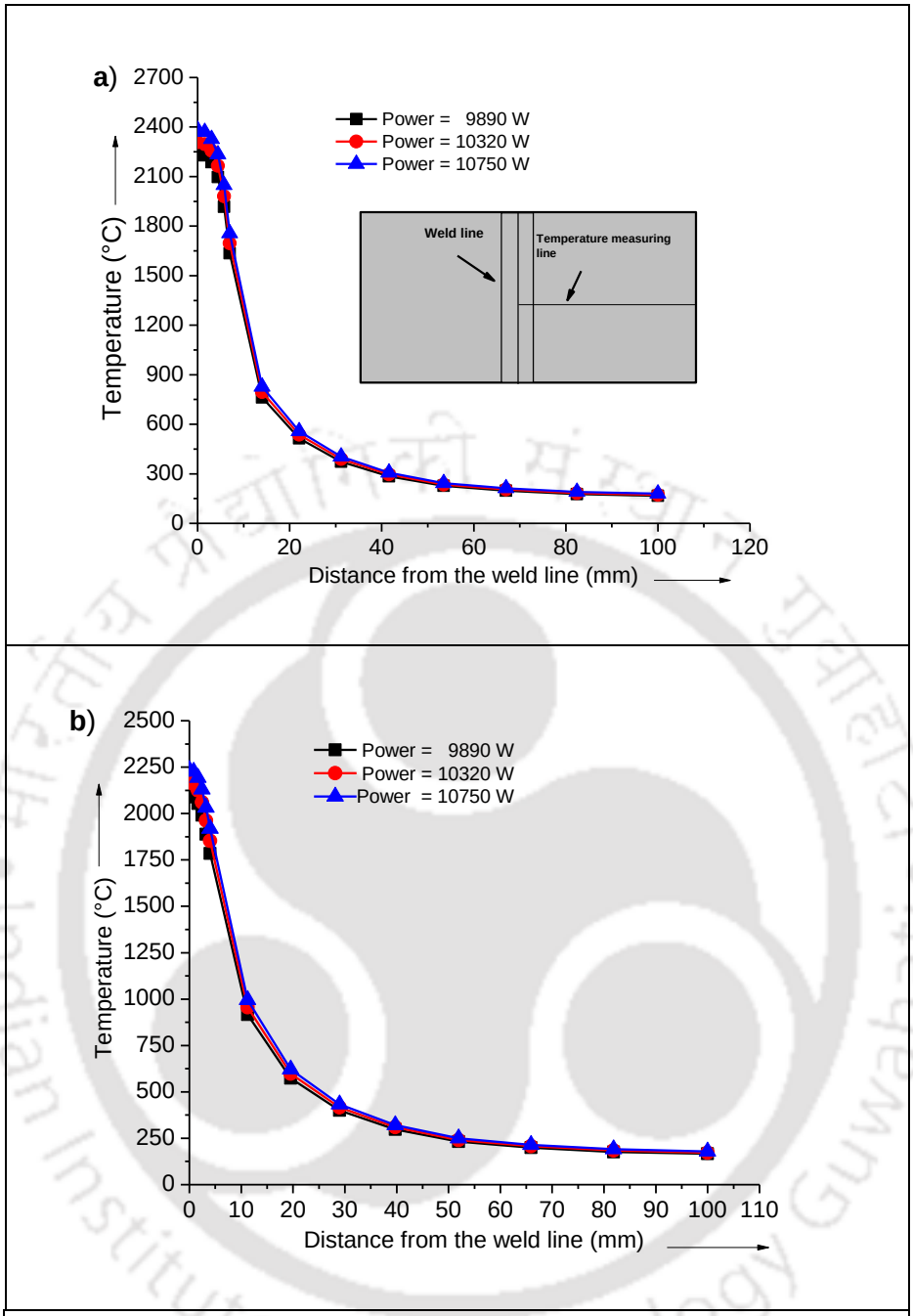

Fig.5.7 Peak temperature distribution in transverse direction (a) top surface (b) bottom surface of the welded plate with power variation

5.1.4.2 Effect of varying welding speed on temperature distribution

In the SET-II three different welding speeds namely 5.55 mm/s, 6.11 mm/s and 6.66 mm/s were chosen for the constant arc power of 10320 W to study the peak temperature distribution with variation in welding speed. Figs. 5.8 (a) and (b) represent the peak temperature distribution on top surface and bottom surface from the weld line in transverse direction under varying welding speed at constant power of 10320 W.

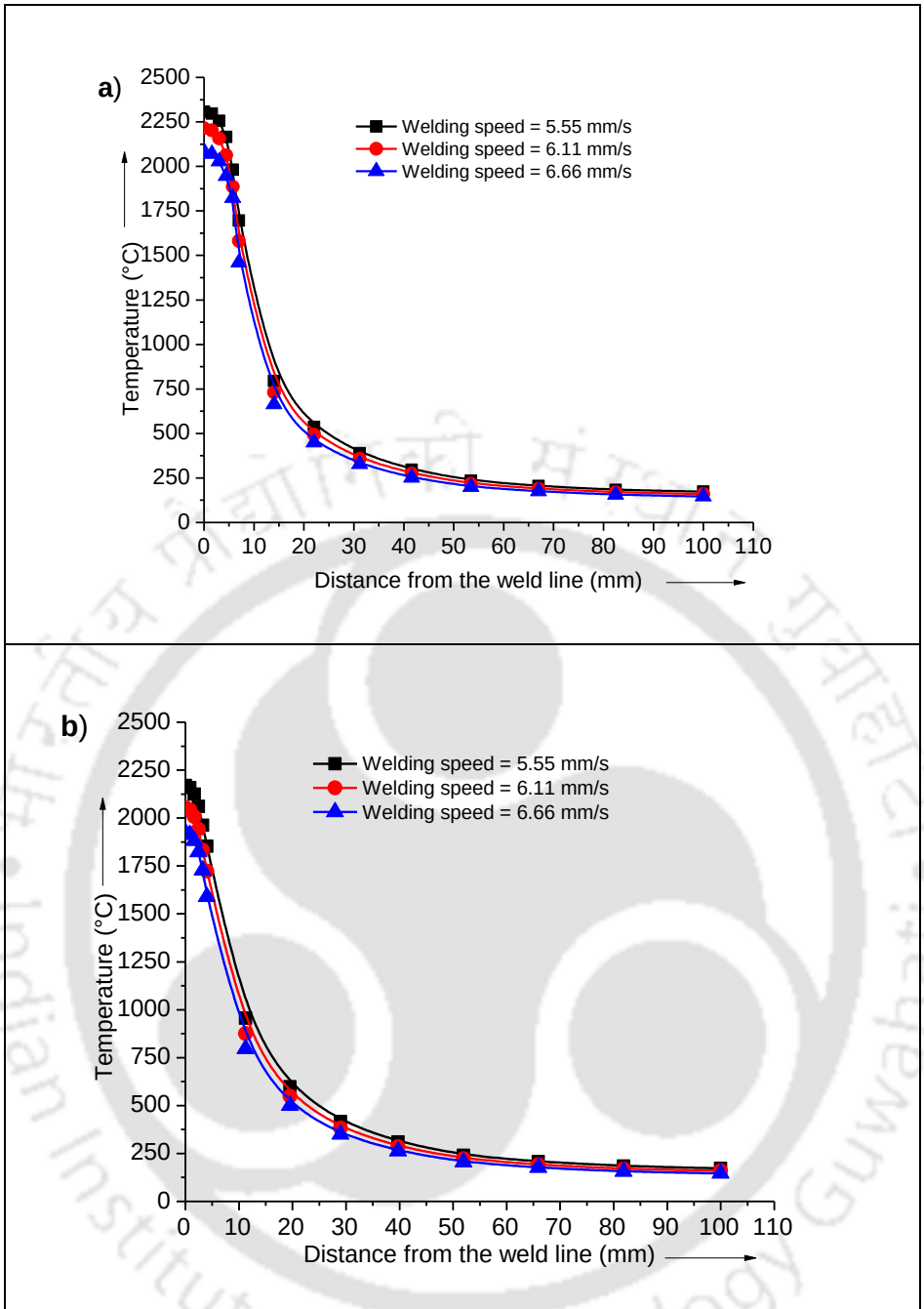

Fig.5.8 Peak temperature distribution in transverse direction on (a) top (b) bottom surface of the welded plate with speed variation

It is observed that peak temperature reduces with increase in welding speed on both top and bottom side of the plate. The peak temperatures of 2307.71 °C, 2215.28 °C and 2083.57 °C were obtained at welding speed of 5.55 mm/s, 6.11 mm/s and 6.66 mm/s respectively as shown in Fig.5.8(a). Hence the peak temperature was increased to 3.98 % by reducing the welding speed from 6.66 mm/s to 6.11 mm/s. The peak temperatures recorded on bottom side were lower with that of top side of the plate.

5.1.4.3 Effect of varying plate thickness on peak temperature distribution

In the SET-III three different plate thicknesses namely 8, 10, 12 mm were chosen for the constant welding power of 10750 W and welding speed 5.55 mm/s study the peak temperature distribution with variation in plate thickness. Figs. 5.9 (a) and (b) represent the peak temperature distribution from the weld centre line towards the transverse direction on top surface and bottom surface under varying thickness at constant welding speed of 5.55 mm/s and welding power of 10750 W respectively.

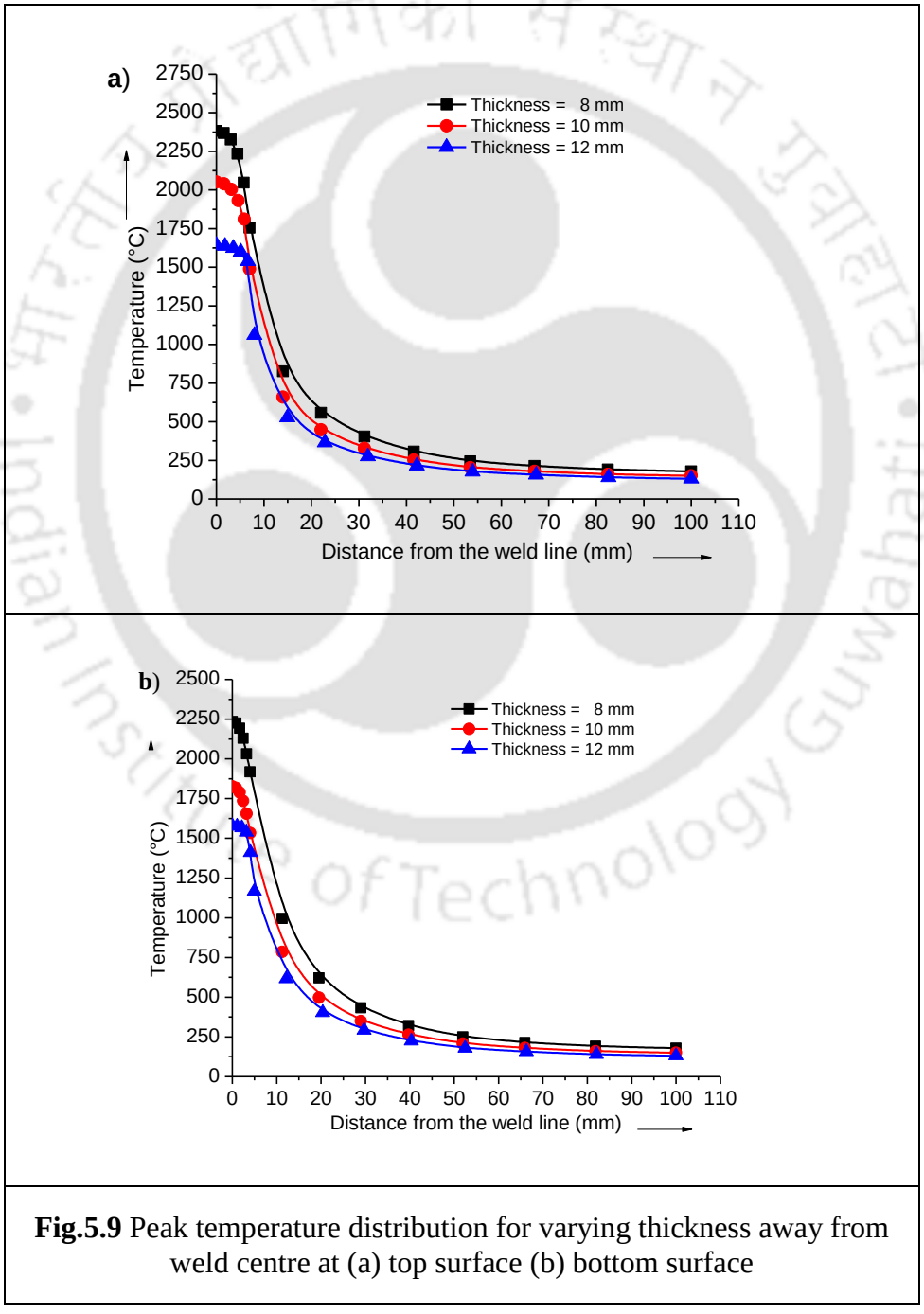

Fig.5.9 Peak temperature distribution for varying thickness away from weld centre at (a) top surface (b) bottom surface

It is observed that peak temperature decreases with increase in plate thickness on both top and bottom side of the plate. The peak temperatures of 2382.35 °C, 2051°C and 1642.4 °C were obtained for plate thickness of 8 mm, 10 mm and 12 mm respectively on top surface of the plate as shown in Fig. 5.9 (a). Hence the peak temperature was reduced to 14.0 to 19.9 % by increasing the welding plate thickness from (8 to10) mm and (10 to12) mm respectively.

5.1.4.4 Validation of thermal history for single sided SAW FE model

To capture the temperature distribution during welding 'K' type thermocouple was spot welded on the work piece and is connected to a data logger (Agilent 3497A) via multiplexer and these were interfaced to a personal computer (PC). The details of the temperature measurement are given in chapter 4. The thermal profile obtained at 24 mm away from weld center line for process parameter (24 V, 430 A and 6.11 mm/s) is compared with numerical results is shown in Fig. 5.10.

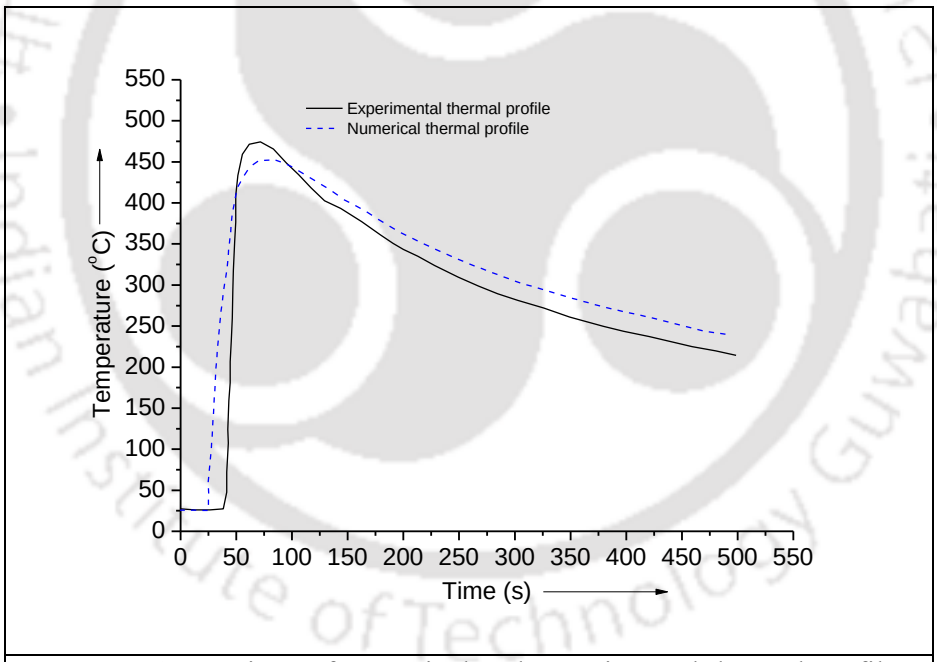

Fig.5.10 Comparison of numerical and experimental thermal profiles at 24 mm away from weld centre line

The comparison between the numerically and experimentally obtained cross sectional view of welded sample at a (24 V, 430 A and 6.11 mm/s) is shown in Fig. 5.11.

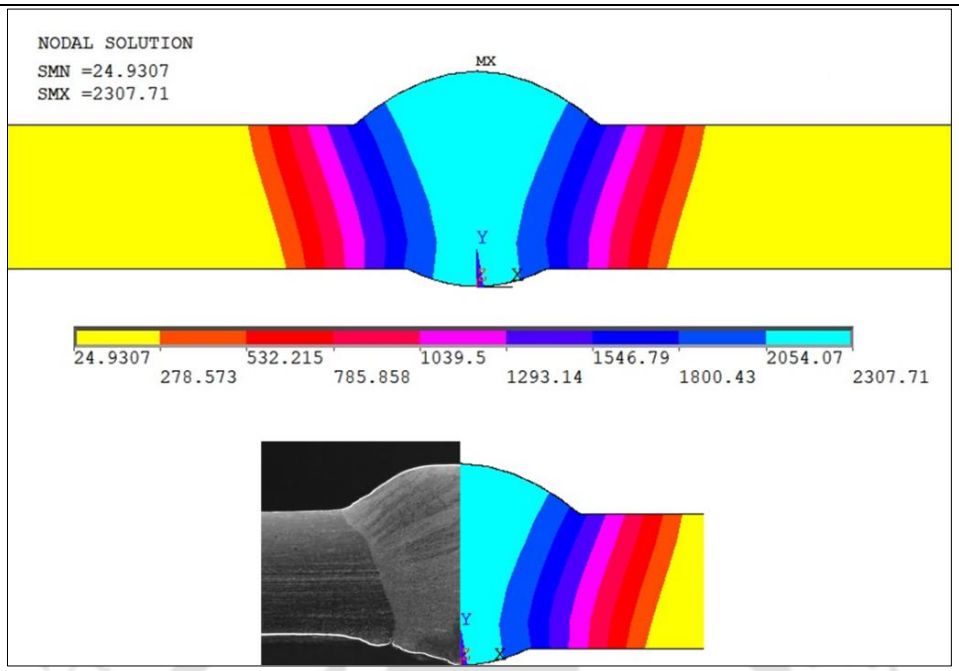

Fig.5.11 Overall numerical and experimental temperature contour

It is observed that the maximum temperature reaches at weld zone (i.e., 2307.71 ^{o}C) when the welding process has been completed. The temperature value decreases when further moving away from the centre line of the weldment. Similarly, maximum temperature values decrease as the distance from centre line increases. The transient thermal profile obtained from FE analysis was compared fairly well with experimental thermal profile with a maximum percentage error of 4.57 % for peak temperature as shown in Fig. 5.10. There is a good agreement-between the FE obtained cross sectional isotherm and experimentally obtained macrograph as shown in Fig. 5.11. Therefore, the good comparison showed that the established 3D thermal model can be used to predict the transient thermal history in the SAW for thick stainless steel plates.

5.1.5 Structural analysis of single sided SAW butt joint

After thermal analysis, the transient thermal history was considered as a thermal load in the structural model to perform the nonlinear elasto-plastic thermos-mechanical analysis. Based on welding current, voltage and speed the line heat energy was calculated which is shown in Eq. 5.2.

$$q = \frac{V \times I}{ws} \tag{5.2}$$

where q is the line energy, V is the welding voltage, I is the welding current and '*ws'* is welding speed. The effects of line energy on residual stresses distribution are shown Figs.5.12 to 5.16. The various parameters used to study the effect of line heat energy on residual stresses distribution and distortion is shown in Table 5.2.

Table 5.2 Parameters considered for structural analysis for 8 mm thick plate

Case No.	Welding Arc Power	Welding Speed	Line energy (J/mm)
CASE-I	24 V × 430 A = 10320 W	5.55 mm/s	1859
CASE-II	24 V × 430 A = 10320 W	6.11 mm/s	1689
CASE-III	24 V × 430 A = 10320 W	6.66 mm/s	1548

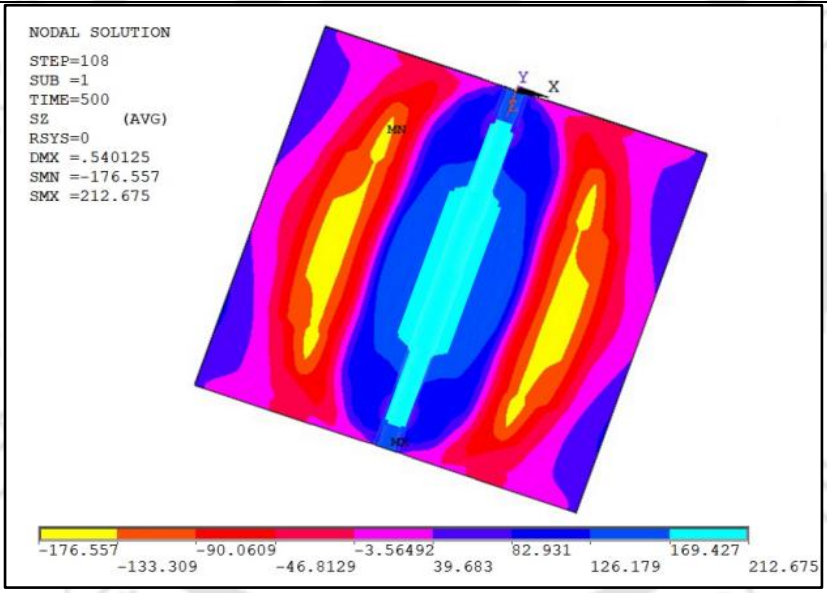

Fig.5.12 Longitudinal residual stress distribution contour for line energy 1859 J/mm

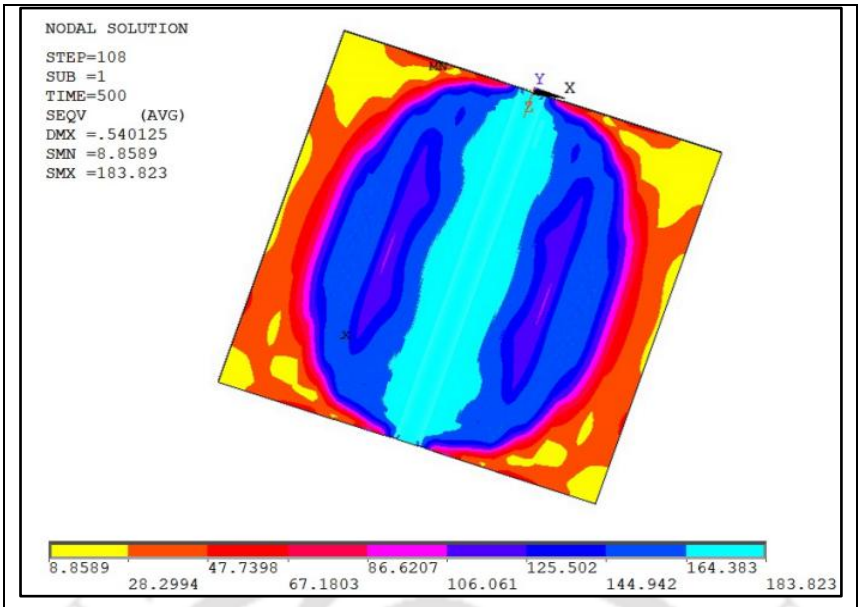

Fig.5.13 von-Mises residual stress distribution contour for line energy 1859 J/mm

Fig.5.12 shows the longitudinal residual stress distribution contour for line energy 1859 J/mm. It can be observed from the Fig.5.12 longitudinal residual stress is tensile in the weld zone and HAZ, while away from weld zone it gradually becomes compressive stress with increasing distance from weld center line. The maximum magnitude of longitudinal tensile residual stress is observed in the weld zone. This tensile residual stress causes the plastic deformation to retain in welded specimen, and these residual stresses remain even after the weldment is cooled to ambient temperature. Fig.5.13 shows von-Mises residual stress distribution contour for line energy 1859 J/mm. It is observed that von-Mises tensile stress is tensile in nature in the weld zone.

Fig.5.14 shows that effect of line energy on longitudinal residual stress perpendicular to the weld line on top surface of plate. From the Fig.5.14 it can be observed that as line energy increases from 1548 J/mm to 1859 J/mm the longitudinal residual stress is found to increase. The increase in line energy corresponds to lower welding speed of 5.55 mm/s, which results in higher heat input into the material. The nominal longitudinal residual stress at weld line for line energies of 1549 J/mm, 1689 J/mm and 1859 J/mm are 190.6 MPa, 194.2 MPa and 197.6 MPa respectively. Away from the weld line the longitudinal residual stress becomes compressive in nature.

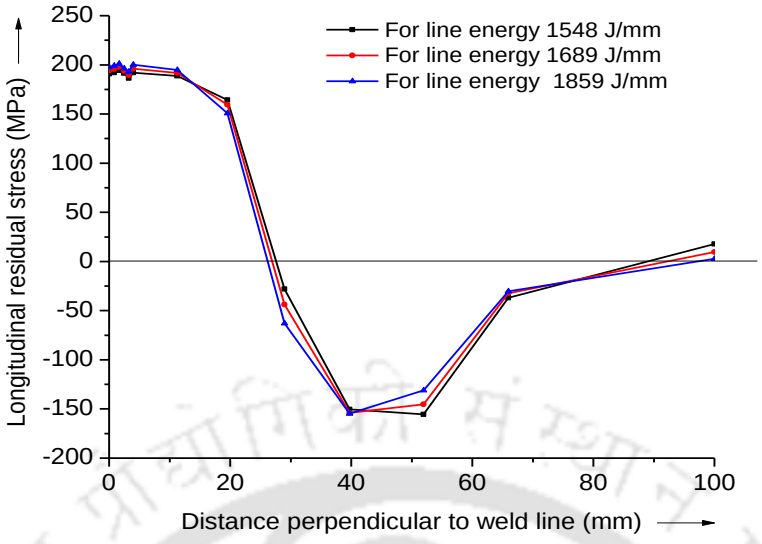

Fig.5.14 Effect of line energy on longitudinal residual stress perpendicular to the center of weld line

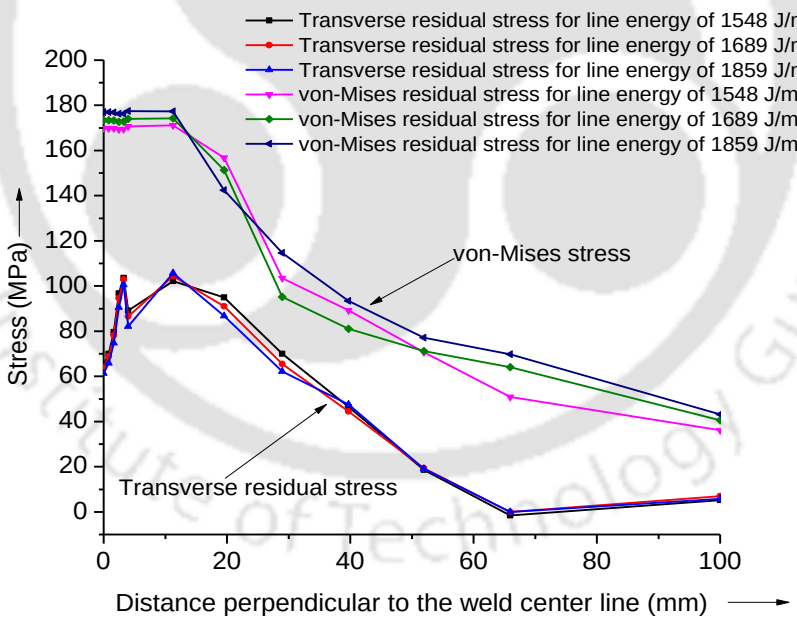

Fig.5.15 Effect of line energy on transverse and von-Misses residual stress perpendicular to the center of weld line

Fig.5.15 shows the effect of line energy on transverse and von-Mises residual stress perpendicular to weld line on the top surface of the plate. It can observed that as line energy increases transverse residual stresses and von-Mises stress are found to increase. It is observed from the Figs.5.14 and 5.15 that maximum magnitude of transverse residual stress

is lower than the longitudinal residual stress. It is clearly seen that transverse residual stress is tensile near the weld line and it gradually decreases away from weld line. The residual stress highly depends on temperature gradient hence the magnitude of residual stress at the farther regions of the plate is of smaller magnitude compare to that of weld line. The von-Mises residual stress is tensile and almost uniform in the weld zone and HAZ and decreases gradually towards the end of the welded plate.

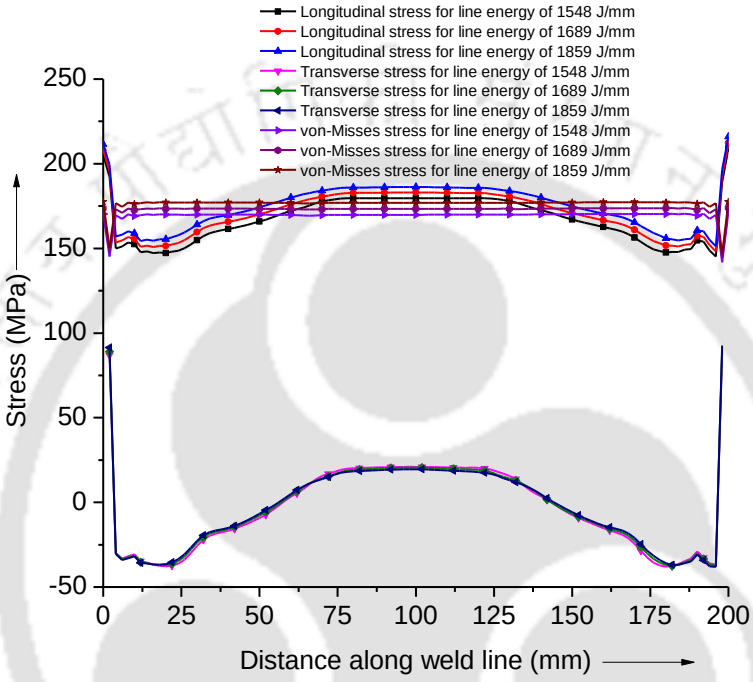

Fig.5.16 Effect of welding line energy on longitudinal, transverse and von-Mises residual stress along weld center line

Fig.5.16 represents the effect of welding line energy on longitudinal, transverse and von-Mises residual stress along the weld line on top surface of the welded plate. It can be clearly seen from Fig.5.16 that the pattern of longitudinal stresses are uniform around the mid region of weld line and gradually decline toward the end and sharply raises at the start and end portion of the plate. Irrespective of the magnitude longitudinal residual stress remains tensile in nature throughout the weld line. Transverse residual stresses are tensile at start and end portions of the weld line. These stresses becomes compressive at begin and end regions and gradually increases to tensile and remain constant at the mid region of the plate. It can be clearly observed from these plots that magnitudes of longitudinal residual stress is higher that of transvers stress. The von-Mises residual stresses are tensile and remain constant throughout the length of the weld line. It can be concluded that as line energy increases from

1548 J/mm to 1859 J/mm longitudinal, transverse and von-Mises stress are found to increase, because heat input increase as the welding speed reduces. The heat input has dominant effect on longitudinal and transverse residual stresses. Higher heat input causes steep rise in peak temperatures in the weld zone which causes more plastic deformation.

5.1.5.1 Validation of structural analysis

For validation of numerical data, the displacement along the edge parallel to weld line of specimens was recorded using coordinate measuring machine. Fig.5.17 depicts the location of points in a sample for distortion measurement. The 'X' and 'Y' represents the transverse and longitudinal distance of the specimen respectively.

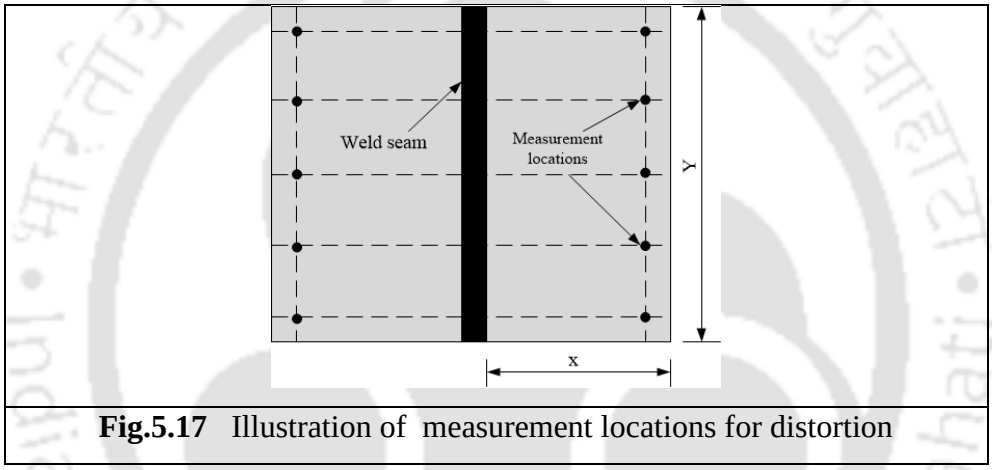

Fig.5.17 Illustration of measurement locations for distortion

The comparisons between numerically and experimentally obtained distortions are validated for case-I and case-III are shown in Figs.5.18 and 5.19 respectively. The maximum distortion obtained was higher in case-I as compared to case-III because of higher line energy. The maximum distortions obtained from experiments and numerical analyses are given in Table.5.3.

Table.5.3 Numerically predicted and measured peak distortions

SL.No.	Predicted maximum distortion (mm)	Measured maximum distortion (mm)	Deviation (%)
Case-I	0.5399	0.5083	5.85
Case-III	0.3810	0.4225	9.82

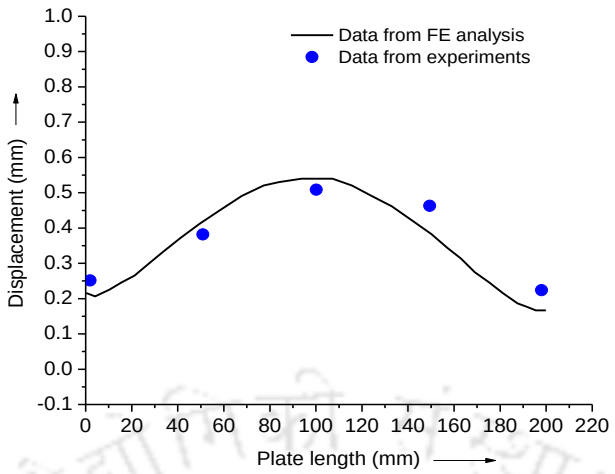

Fig.5.18 Comparison between experimentally observed grid point displacement (distortion) and nodal displacement for case-I

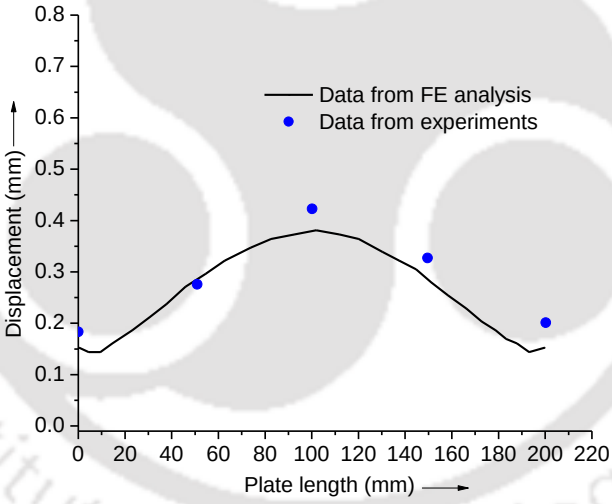

Fig.5.19 Comparison between experimentally observed grid point displacement (distortion) and nodal displacement for case-III

It can be observed from Table.5.3 a maximum of 5.85% and 9.82% deviation is observed for case-I & III respectively. It is evident from Figs.5.18 and 5.19 that there is a good agreement between FE obtained maximum distortion and experimentally observed values. It can be concluded that the established 3D thermo-mechanical model can be used to predict distortions in the SAW of thick stainless steel plates.

5.1.6 Summary

In the present work a 3 dimensional volumetric heat source is used to predict the temperature distribution in a single side single pass square butt joint. Also the effect of process parameters and varying plate thickness on thermal history was also studied. It is observed that the peak temperatures obtained from numerical model were well matched with that of experimental data. The structural analysis was carried out to study the effect of line energy on residual stresses and distortion. The distortion results obtained from numerical model were very close to experimental result.

5.2 Prediction of welding induced distortions in large welded Structure using equivalent loading technique

In general, welding structures are exposed to non-uniform rapid heating and cooling. Due to this residual stresses and distortions originate in the welded structure. As a result of which the final assembled structures undergo defects like misalignment, directional mismatch etc. To correct these issue post-weld operations like mechanical straightening, line heating etc. are required which require extra costs in terms of energy, material losses and labour cost. As a result, prediction and analysis of welding deformations before the actual welding practice plays an important role to control it at the design stage. Welding distortions can easily be determined experimentally. However, it is almost impractical to determine them for large weld structures.

In the present investigation initially the austenitic stainless steel (AISI SS 304) weld joint was analyzed using thermo-mechanical elasto-plastic (TMEP) method in which thermal and structural outcomes were validated with the experimental results. Subsequently, the weld joint is modeled using equivalent load method in this proposed work. It includes applying the equivalent loads based on average plastic strains obtained from (TMEP) method.

5.2.1 Experimental details

For validating the numerical results experiments were carried out to fabricate austenitic stainless steel (AISI SS 304) weld of square butt joint without edge preparation. The dimensions of plate used in this investigation are 150 × 75 × 10 mm^3. The process parameters used to fabricate the butt joint are shown in Table. 5.4

Table 5.4 Welding process parameters used in this study

Welding current (A)	Voltage (V)	Traverse speed (mm/s)	Arc efficiency (%)
445	26.5	5	90

The detailed procedure adopted to carry out temperature and vertical edge deflection measurements are mentioned in chapter 4.

5.2.2 Methodology

The flow chart explains the procedure adopted in the proposed work is shown in Fig. 5.20.

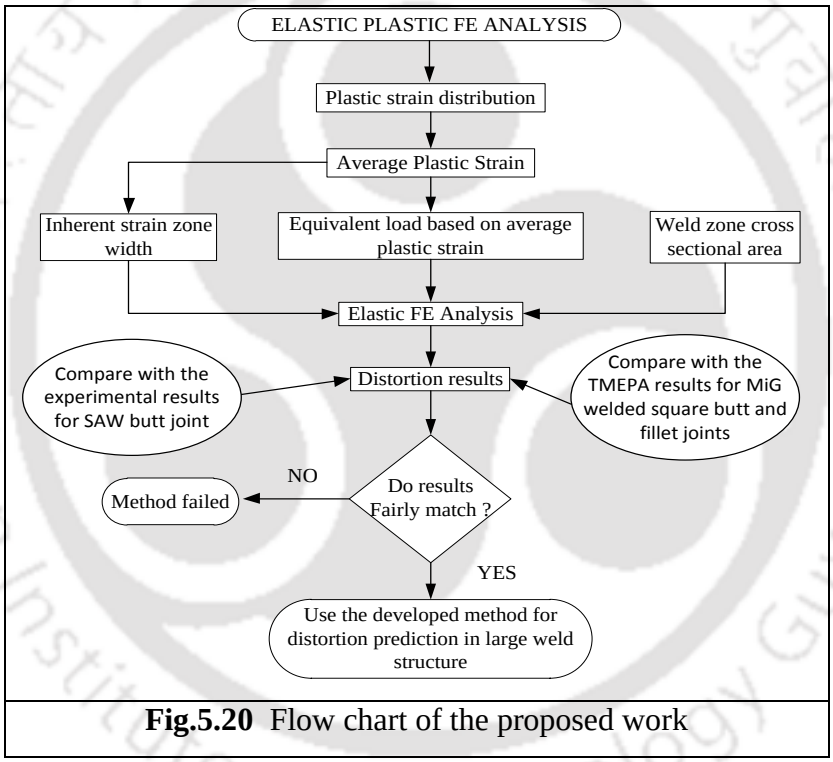

Fig.5.20 Flow chart of the proposed work

The flow chart is shown in Fig.5.20 is briefly explained as follows:

- Experimental investigation was carried out to fabricate SAW square butt joint and deflections along the edge of the plate were measured.
- Initially, weld joint is modelled using thermal-mechanical elastic-plastic (TMEP) method and the results of thermal and structural analysis are validated with experimental results.
- Next, the same weld joint is also modelled using proposed equivalent load method. It comprises of applying the equivalent loads based on the average plastic strains distribution obtained from TMEP analysis on the same weld joint model.

- Individual equivalent loads were separately applied at start / end and rest of the quasi-state regions to determine the real distribution of inherent plastic strains in longitudinal and transverse directions. Fig.5.21 represents the application of equivalent loads along the weld line.

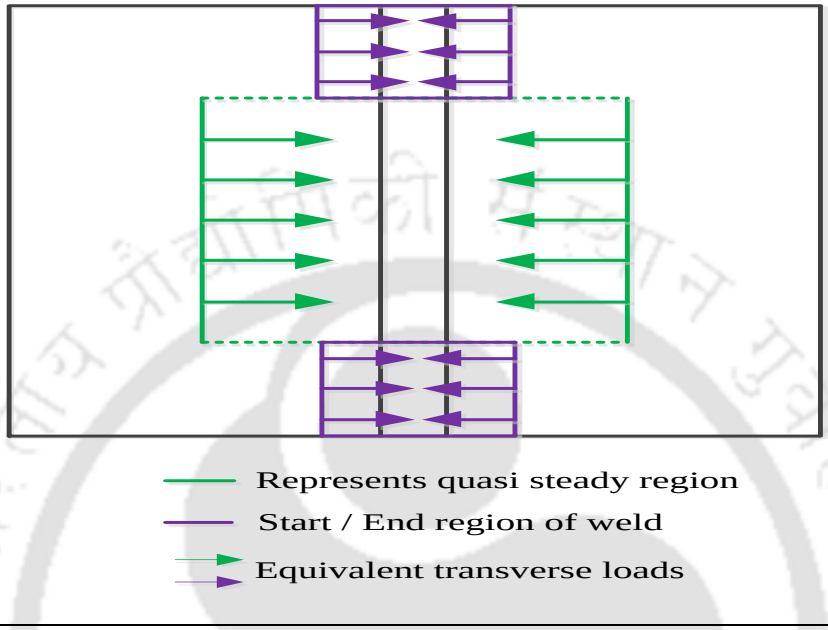

Fig.5.21 Application of equivalent loads concerning the weld region and average width of inherent strain zone

- To confirm the effectiveness of the proposed method the published results of butt and fillet joint fabricated with gas metal arc welding (GMAW) were modelled using proposed method.
- Finally the large structure has been also modelled based on the outcomes obtained from butt and fillet joint and proposed method is used to determine overall weld-induced distortions.

5.2.3 Thermal Mechanical Elastic-Plastic (TMEP) method

The transient thermal history obtained from TMEP analysis was validated with experimental result. Fig.5.22 represents one of the square-butt welded joints along with its cross-sectional view of the weld bead, which assures the quality of the weld.

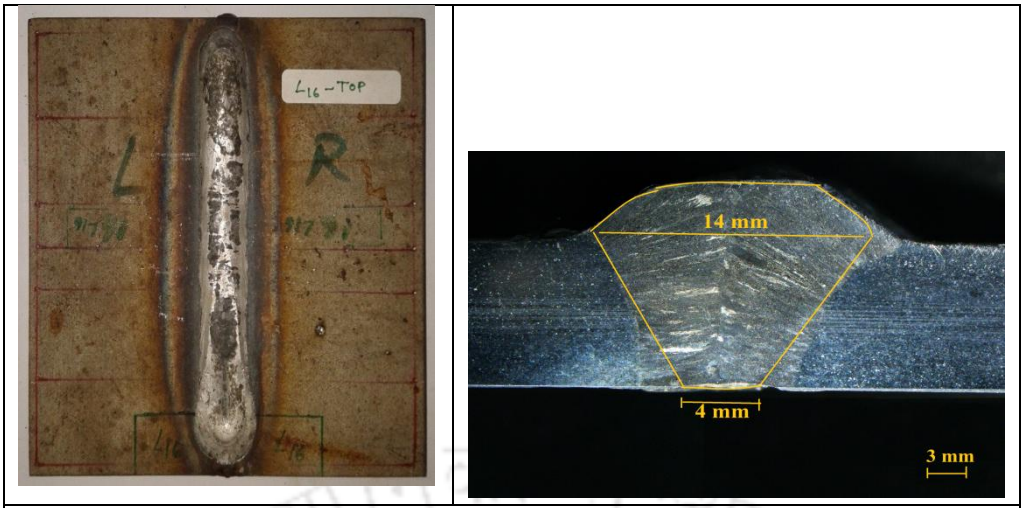

Fig.5.22 (a) Top surface of the welded butt joint, (b) Cross sectional view of the weld bead

Fig.5.23 represents the edge deflection of the welded plate. It is observed that the TMEP result matches well with experimental result. It can be concluded that the TMEP results can be set as a level of accuracy to verify the effectiveness of any equivalent methods of distortion prediction. Hence, conducting experiments can be avoided. Fig.5.24 represents the plastic strain distribution on mid plane of the plate. It can be observed that both the plastic strains (longitudinal and transverse) are compressive in and near the weld zone. The contour plots are also shown in Fig.5.25. It is observed that magnitude of longitudinal plastic strain is lower as compared with transverse plastic strain. It can be implied that contribution of longitudinal plastic strain was negligible as compared with transverse plastic strain on the overall distortion of the model.

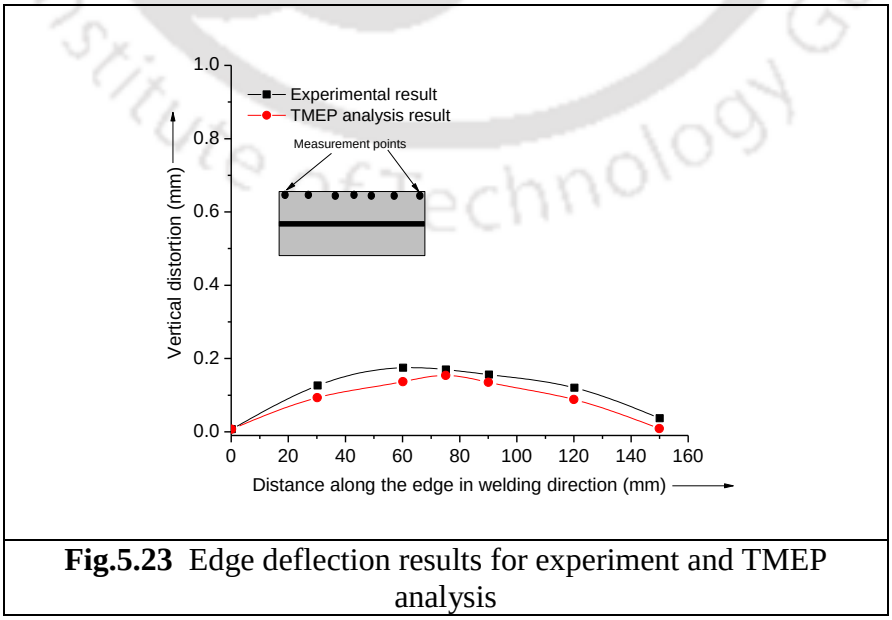

Fig.5.23 Edge deflection results for experiment and TMEP analysis

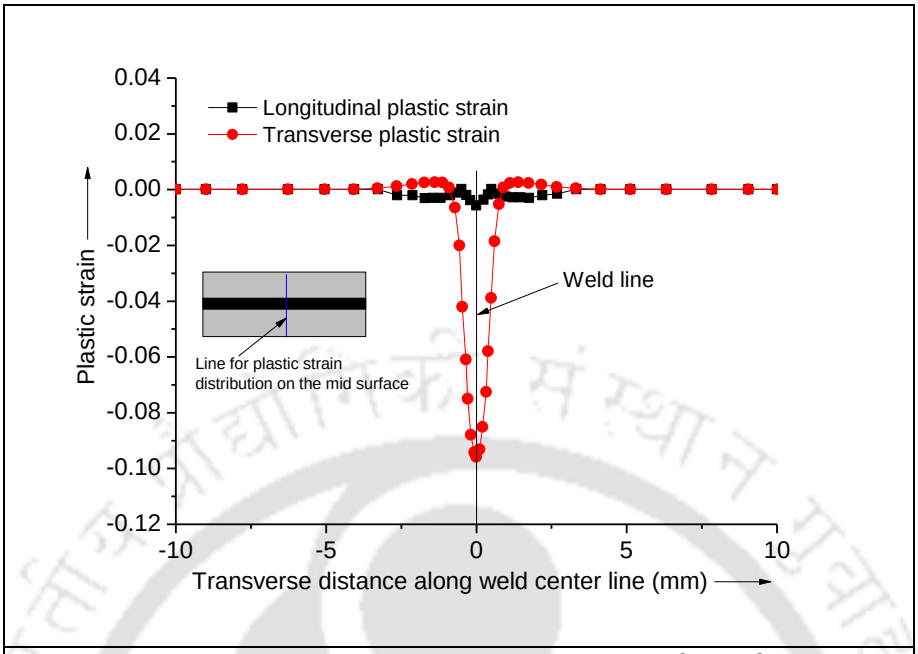

Fig.5.24 Plastic strain distribution on the top surface of the plate along the transverse direction

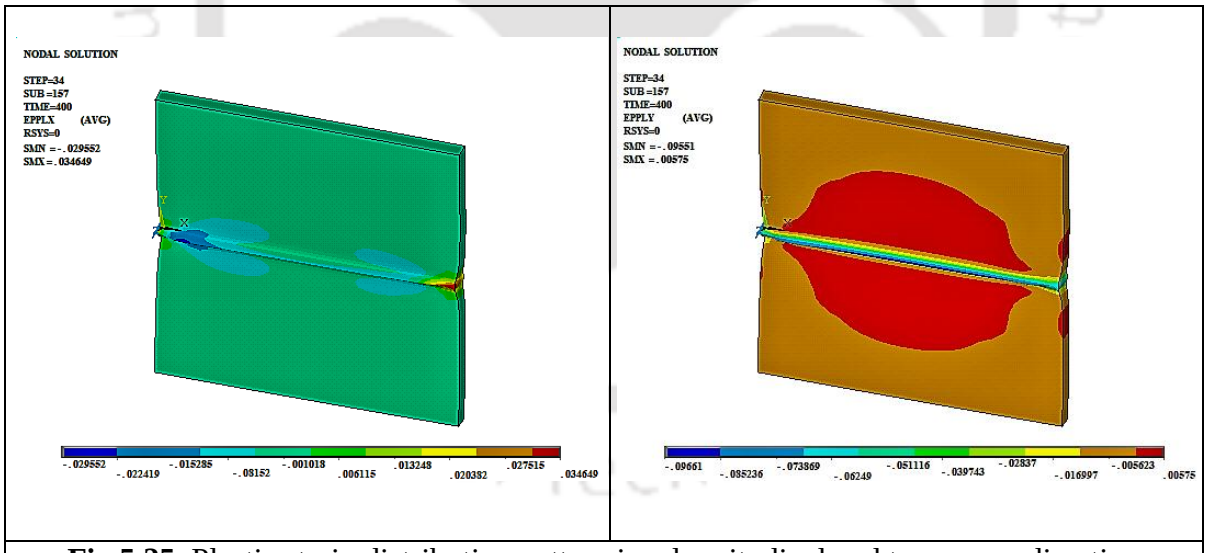

Fig.5.25 Plastic strain distribution pattern in a longitudinal and transverse direction (Top to bottom)

The transverse plastic strain value with their best-fitted curve (Adjusted R^2 value ≥ 0.8) is determined for different locations throughout the weld length. The plastic strain distribution, along with its best-fitted curves for the midsection of three distinct regions is shown in Fig. 5.26.

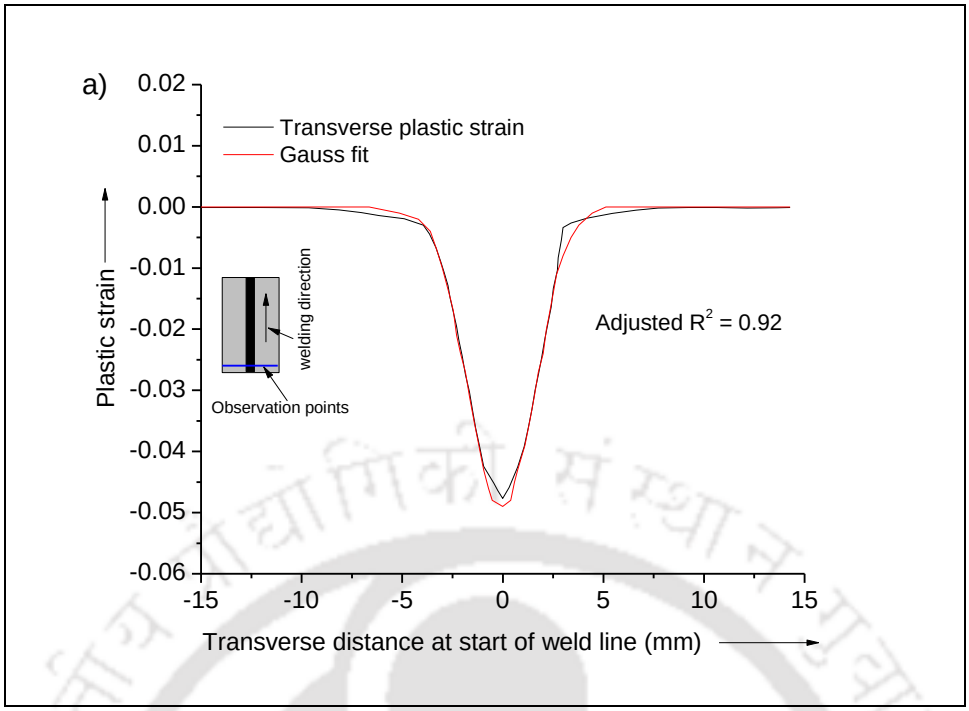

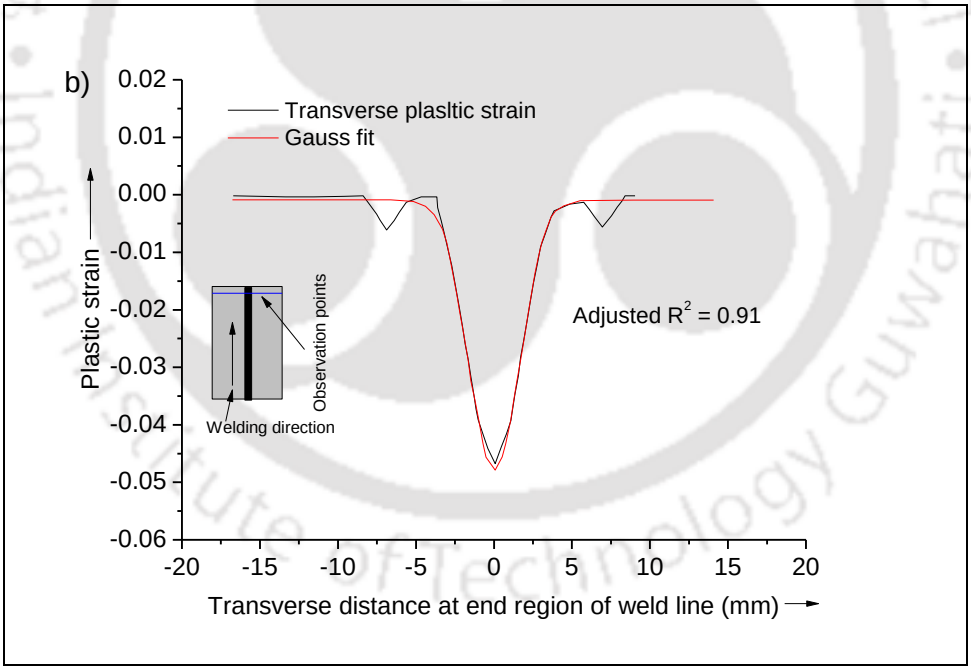

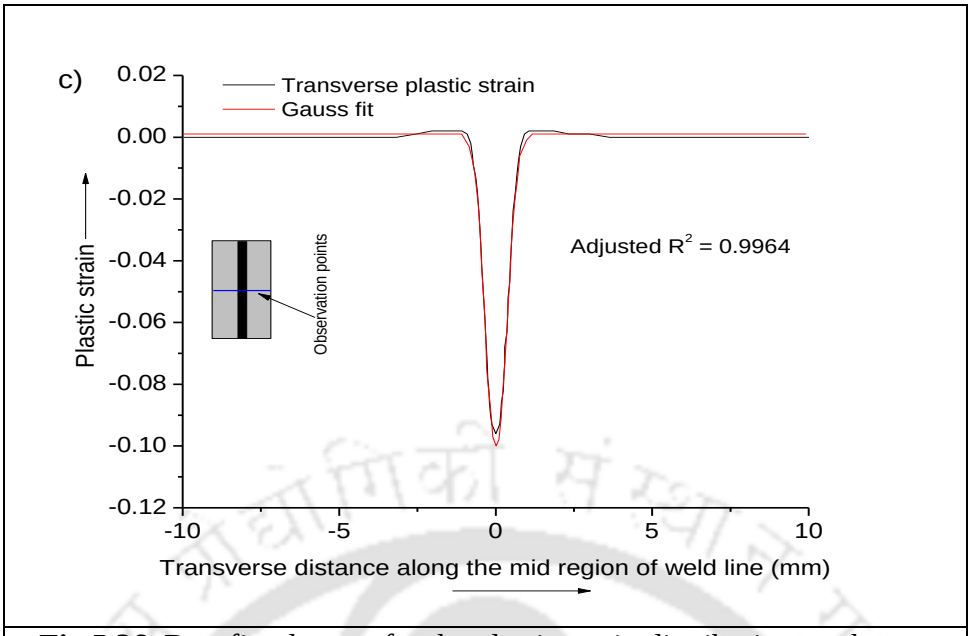

Fig.5.26 Best fitted curve for the plastic strain distribution on the top surface along transverse direction for the points in the (a) Start, (b) End and (c) Mid regions of the welding direction respectively

5.2.4 Equivalent load method based (ELM) based on average plastic strain

The average values for transverse plastic strain obtained at different locations from TMEP method were utilized to calculate the equivalent load. The equivalent load values for different areas are plotted as shown in Fig.5.27. The region-wise average equivalent loads were applied as the nodal load on the nodes located at the average width of inherent plastic strain distribution on the top surface of the weld joint model as shown in Fig.5.28. The average width of the inherent plastic strain zone was estimated as 8 mm, 9 mm and 20 mm for the start, end and quasi-static regions respectively.

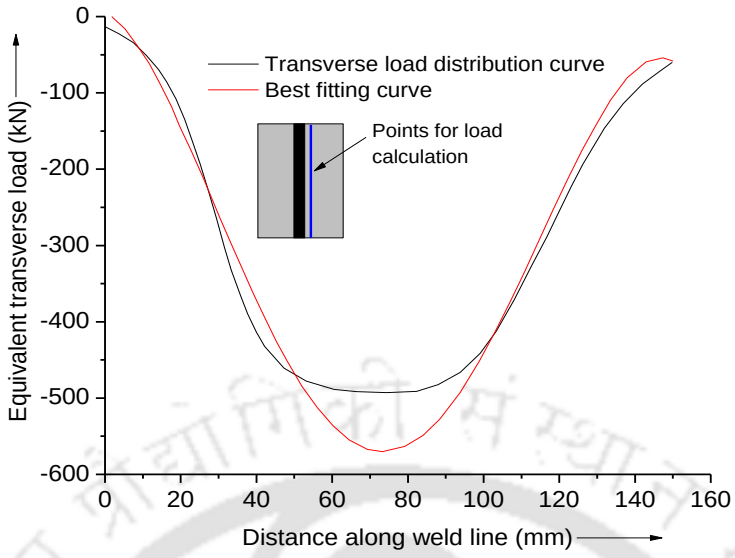

Fig.5.27 Distribution of Equivalent transverse load along the weld line

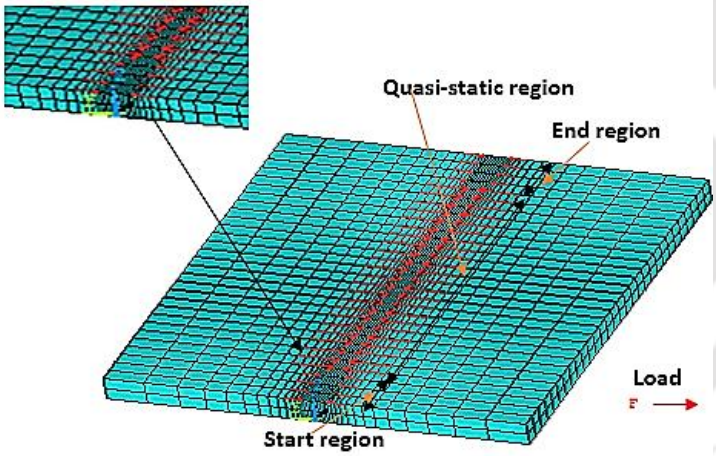

Fig.5.28 Application of Equivalent load in different regions separately

Fig.5.29 presents the edge deflection results from the proposed method, along with experimental results. The results are reasonably equivalent in terms of distortion pattern with a slight difference in the peak values. Furthermore, these results are quite close to TMEP analysis results.

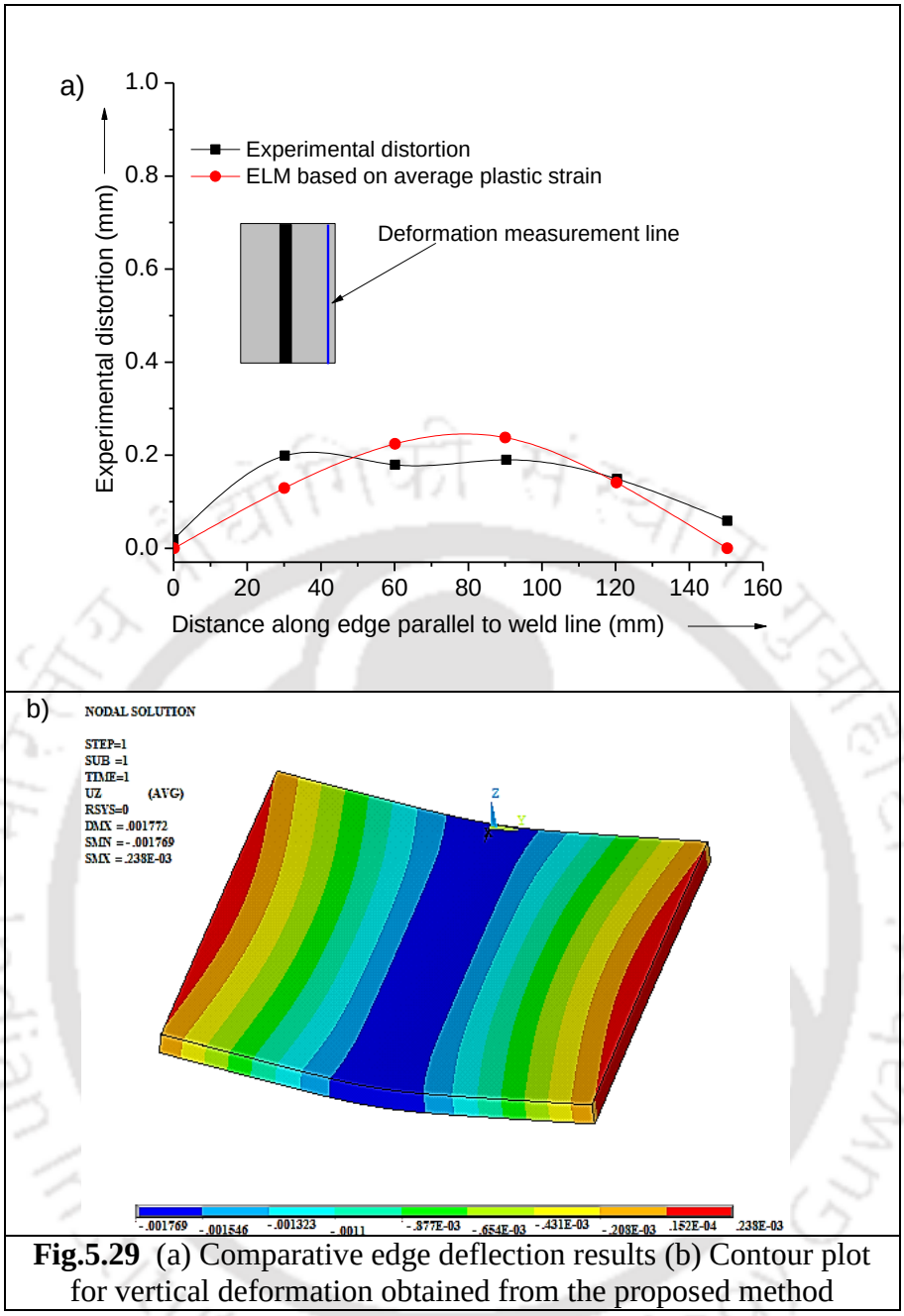

Fig.5.29 (a) Comparative edge deflection results (b) Contour plot for vertical deformation obtained from the proposed method

5.2.5 Effectiveness of the proposed method

The effectiveness of the proposed method was evaluated by considering the welding parameters and weld models (Butt and Fillet joints) from the published literature, Biswas et al., (2011) to perform TMEPA on both butt and fillet joints. The distortion results obtained from TMEPA were taken as the benchmark to verify the effectiveness of the proposed method in prediction of the welding distortion. The welding process variables and the plate dimensions of the welded joint models are tabulated in Table. 5.5 and Table. 5.6 respectively.

Table 5.5 Welding parameters, Biswas et al., (2011)

Welding Current (A)	Welding Voltage (V)	Welding Speed (mm/s)	Arc Efficiency (%)
230	27	3	80

Table 5.6 Dimensions of welded structural components, Biswas et al., (2011)

Weld joint model	Dimensions
Butt joint	240 mm × 100 mm × 10 mm
Fillet joint	The base plate (240 mm × 100 mm × 10 mm) Web plate (240 mm × 50 mm × 06 mm) Throat leg length (4 mm)

The temperature-dependent material properties of C-Mn steel are shown in Fig.5.30. The thermo-mechanical analysis was performed for both the weld joint models. For fillet joint double-sided simultaneous weld pass was considered. Figs.5.31 to Fig.5.34 shows the plastic strain contour diagram for butt and fillet joint models in longitudinal and transverse directions respectively. Fig.5.35 presents the plastic strain distribution on the mid surface of the butt joint and fillet joint models.

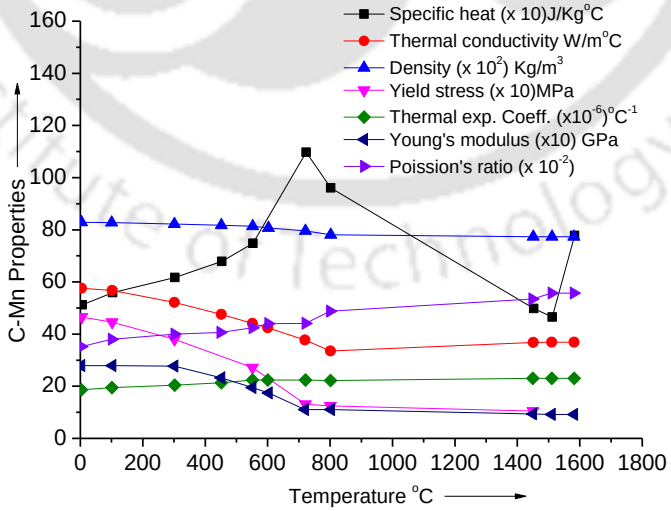

Fig.5.30 Temperature dependent properties of C-Mn steel, Biswas et al., (2011)

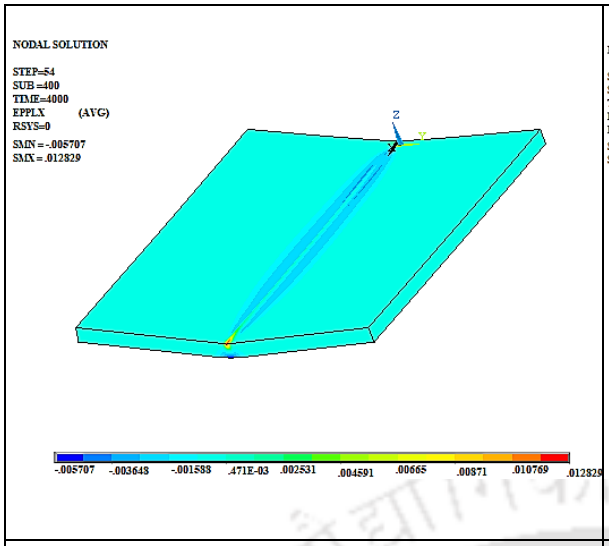

Fig.5.31 Longitudinal plastic strain (butt joint)

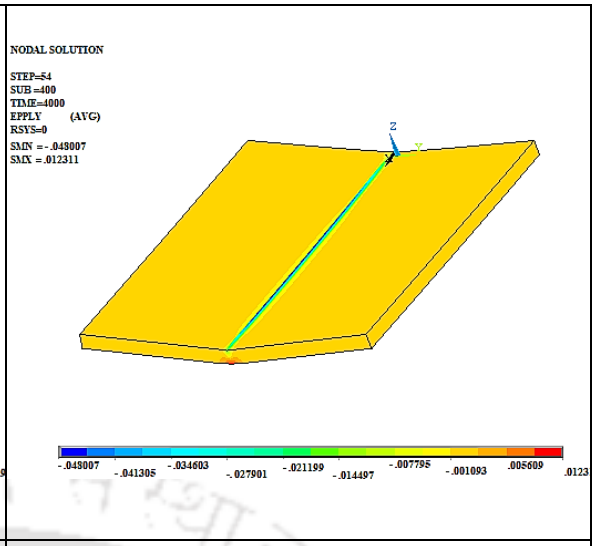

Fig.5.32 Transverse plastic strain (butt joint)

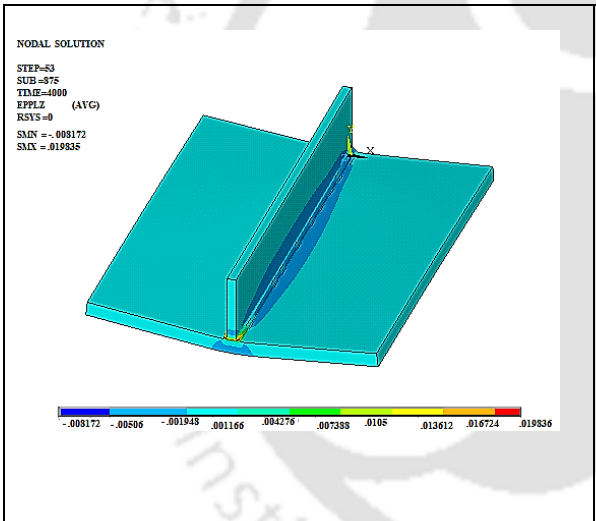

Fig.5.33 Longitudinal Plastic strain (Fillet joint)

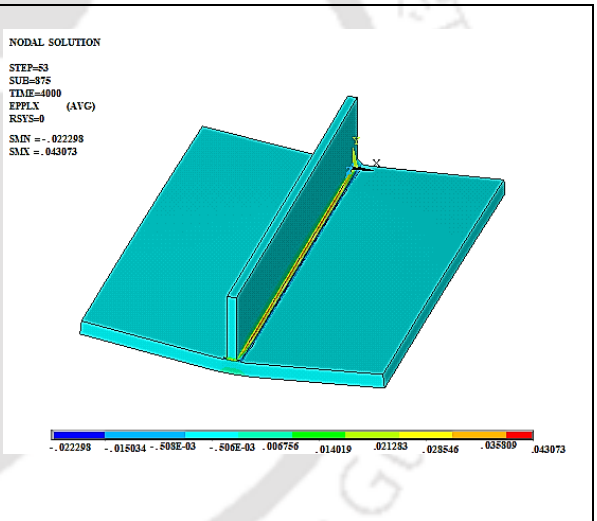

Fig.5.34 Transverse Plastic strain (Fillet joint)

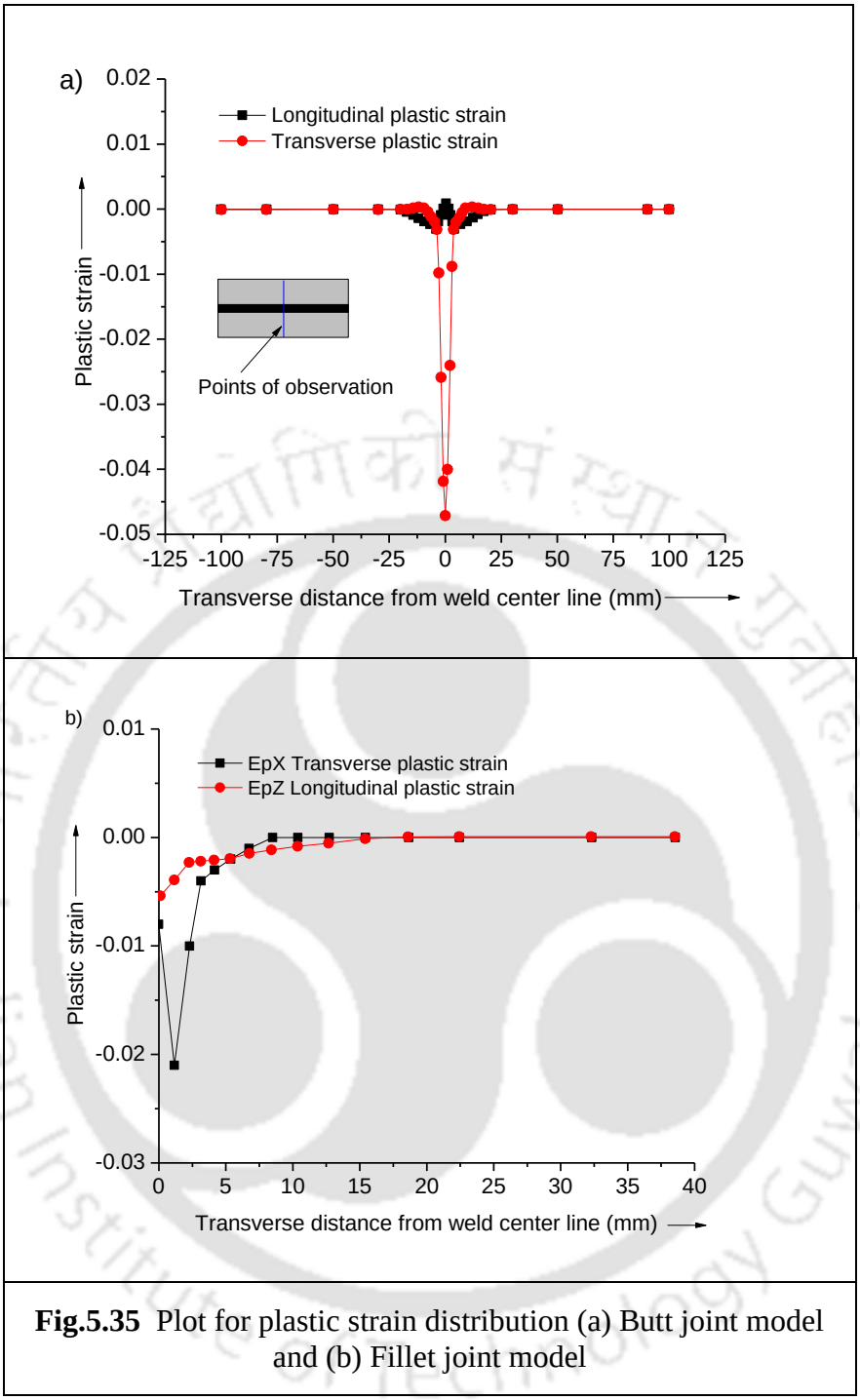

Fig.5.35 Plot for plastic strain distribution (a) Butt joint model and (b) Fillet joint model

It is assumed that longitudinal plastic strain distribution has been neglected in this study. Fig.5.36 shows the transverse plastic strain distribution plot along with its best-fitted curve for both butt and fillet joint models.

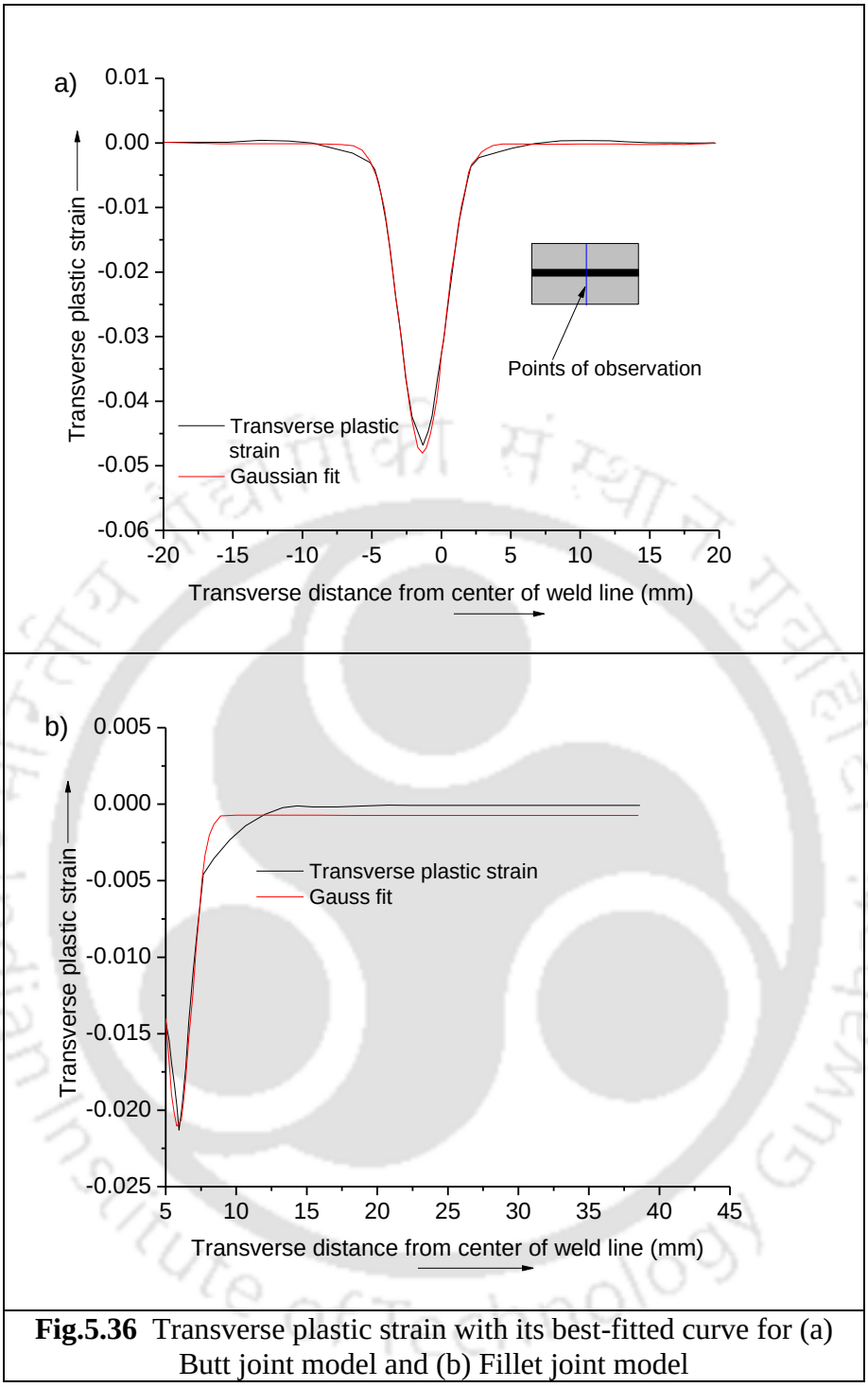

Fig.5.36 Transverse plastic strain with its best-fitted curve for (a) Butt joint model and (b) Fillet joint model

Initially average plastic strains are calculated after which equivalent loads were determined. The equivalent transverse load distribution along the weld line is shown in Fig.5.37 along with their best-fitted curve for both the butt and fillet joints, respectively.

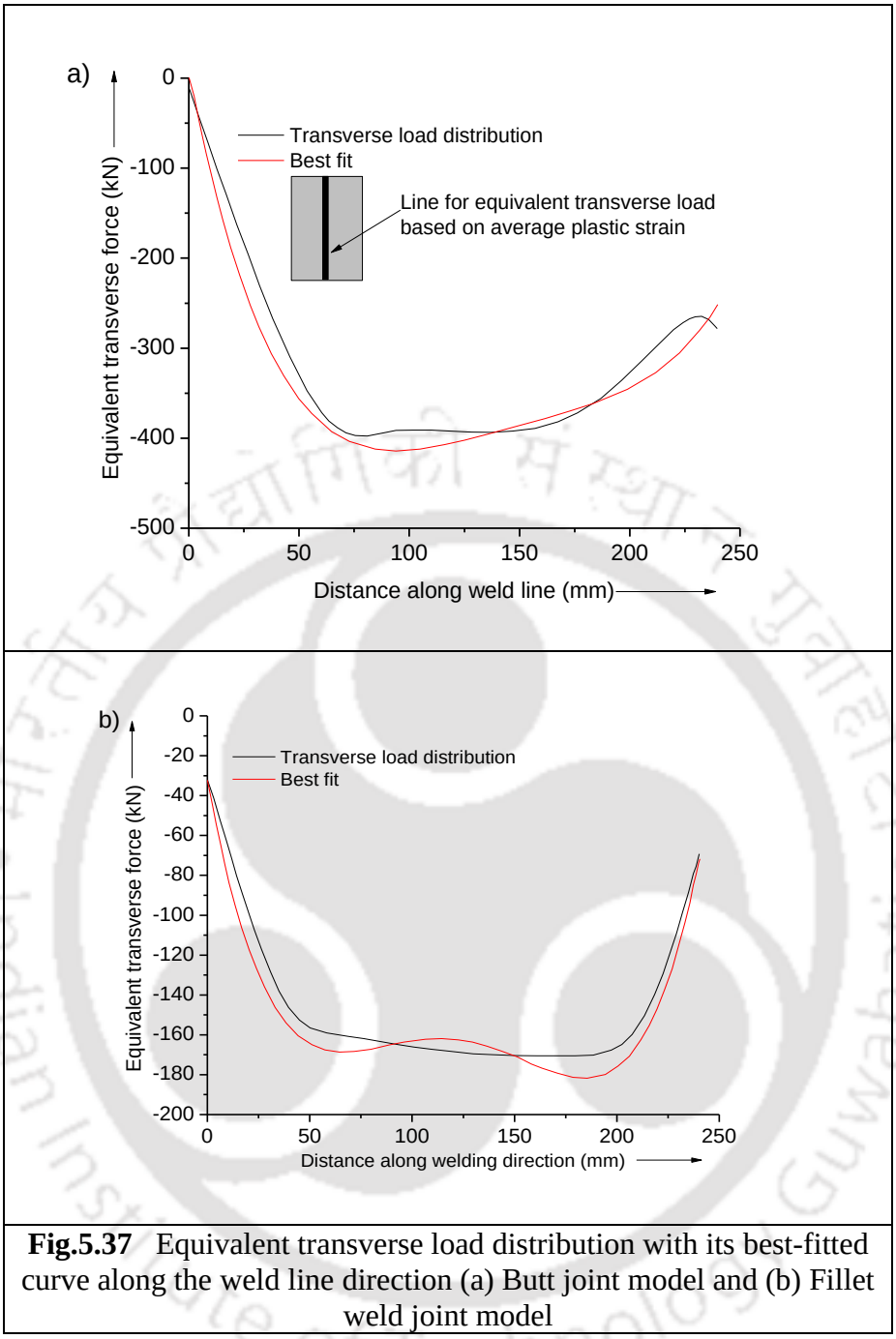

Fig.5.37 Equivalent transverse load distribution with its best-fitted curve along the weld line direction (a) Butt joint model and (b) Fillet weld joint model

Again, by using the best-fitted curve for equivalent load distribution, the average value of load was calculated for three respective weld regions. These loads were applied as nodal load in the same way at the width of average inherent strain zone. Finally, the vertical distortion contour plot for a butt joint model obtained from both the elastic-plastic analysis and elastic analysis is shown in Fig.5.38. The deformations in terms of angular deformation and edge deflection are shown in Fig.5.39. From Fig.5.39 it is observed that the results fairly matched, i.e. the proposed method results are quite close to the elastic-plastic results.

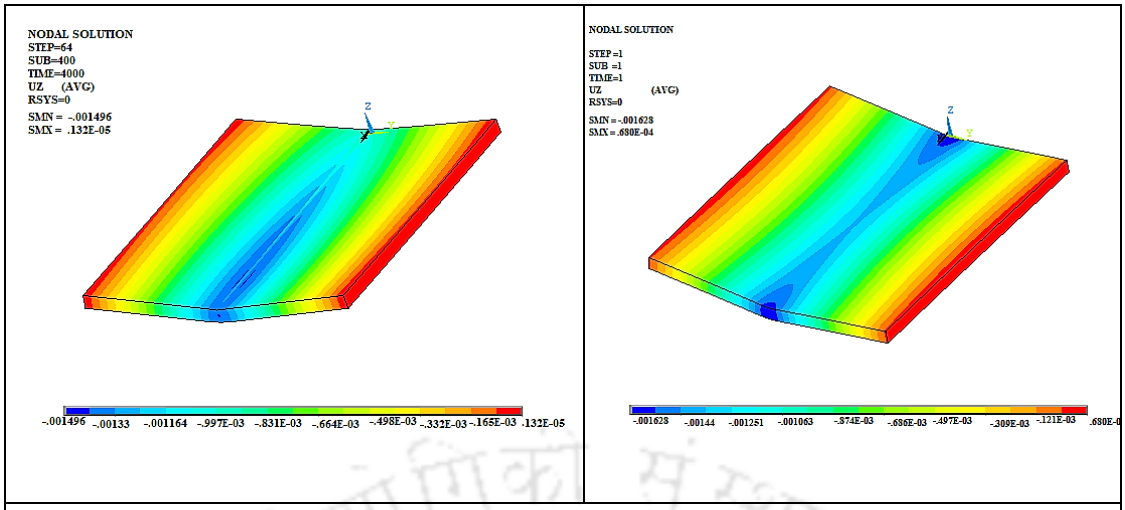

Fig.5.38 Distortion contour diagram for butt joint model (a) TMEP analysis and (b) Proposed method

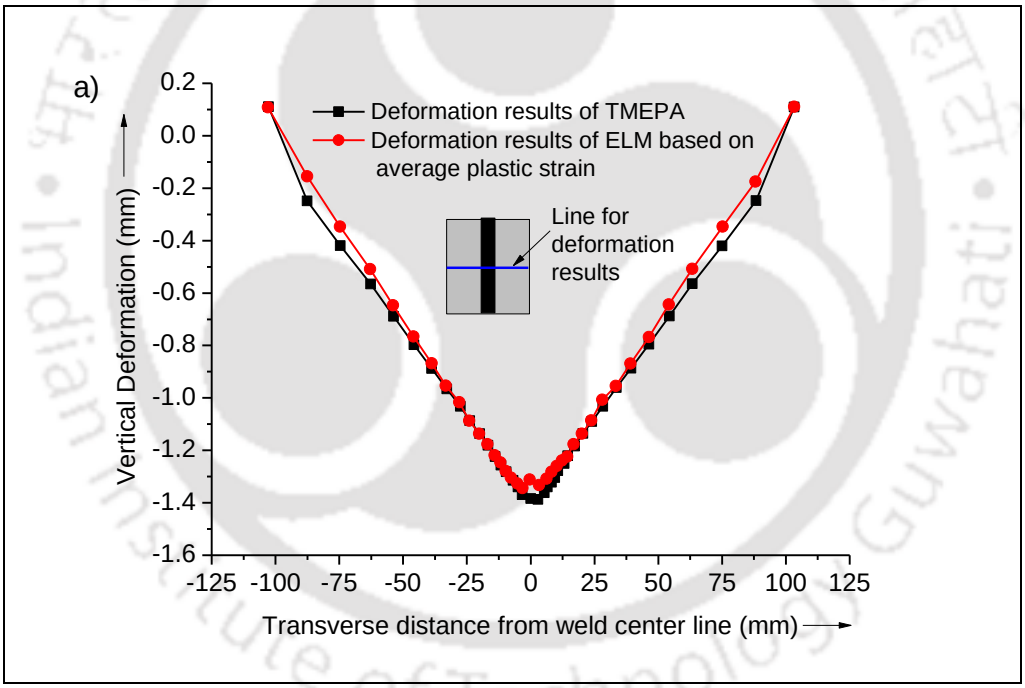

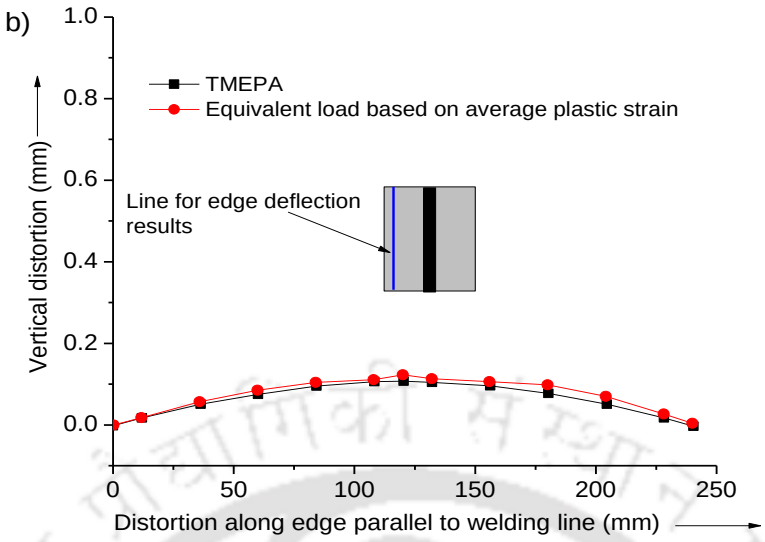

Fig.5.39 (a) Angular deformation and (b) Edge deflection plot for butt joint model

In the case of fillet joint, an elastic analysis was also performed for a constant equivalent load method to explicitly compare the advantage of the improved equivalent load method over constant equivalent load. Fig.5.40 shows the contour diagram of vertical deformation in a fillet joint for all the three methods along with the curves showing angular deformation and edge deflection in Fig.5.41. From Fig.5.41, it is observed that the proposed method is an efficacious method to predict the distortion results.

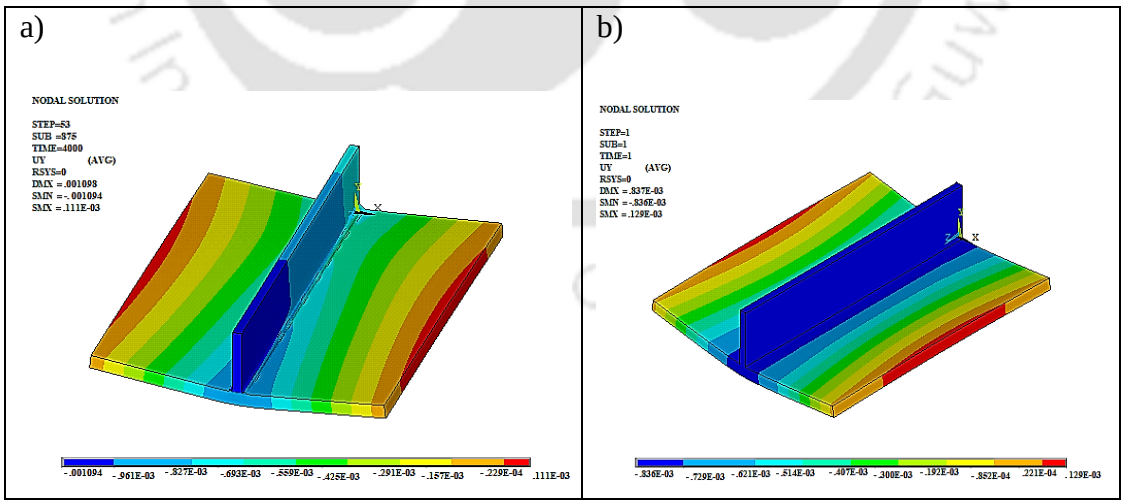

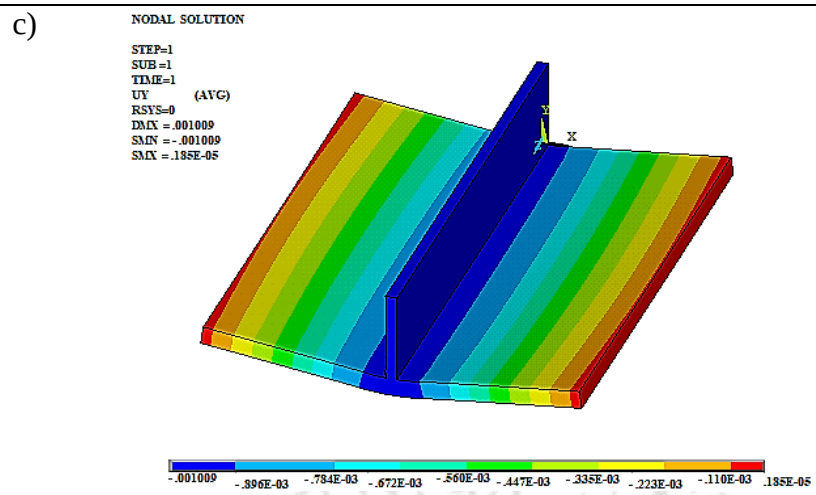

Fig.5.40 Distortion contour plot for the fillet joint model (a). TMEPA method, (b). Equivalent load considering start/end loads on the different width of inherent strain zone for different weld region, (c). Equivalent amount on the average width of inherent strain zone without considering the start/end loads separately

From Fig.5.41 (b), it can be observed that the edge deflection results drastically improved with the region-wise equivalent load method whereas, the angular deformation is negligibly affected as compared to edge deflection results.

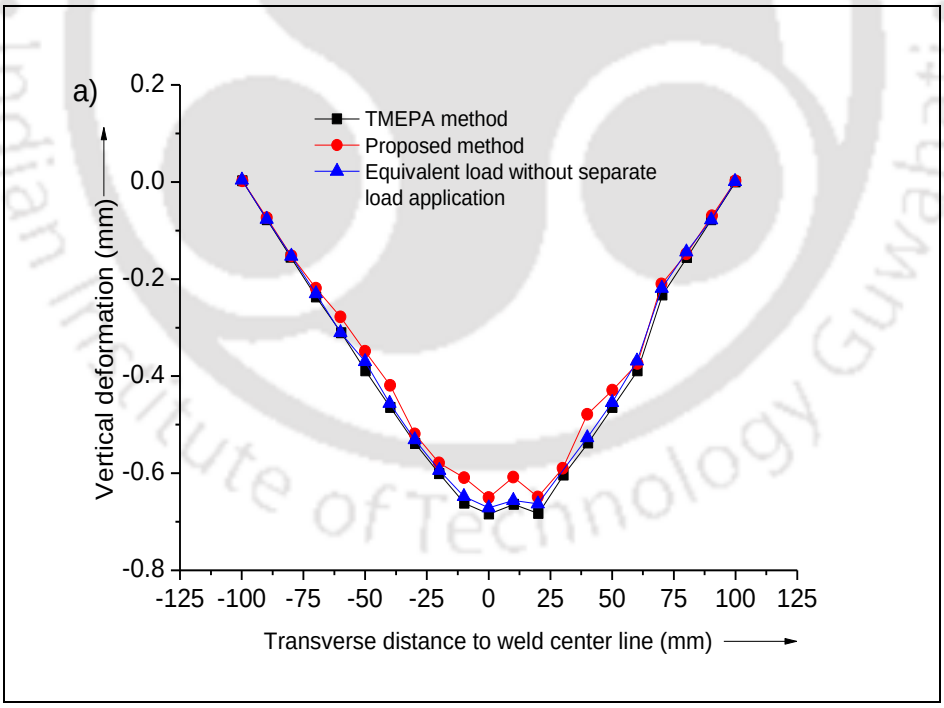

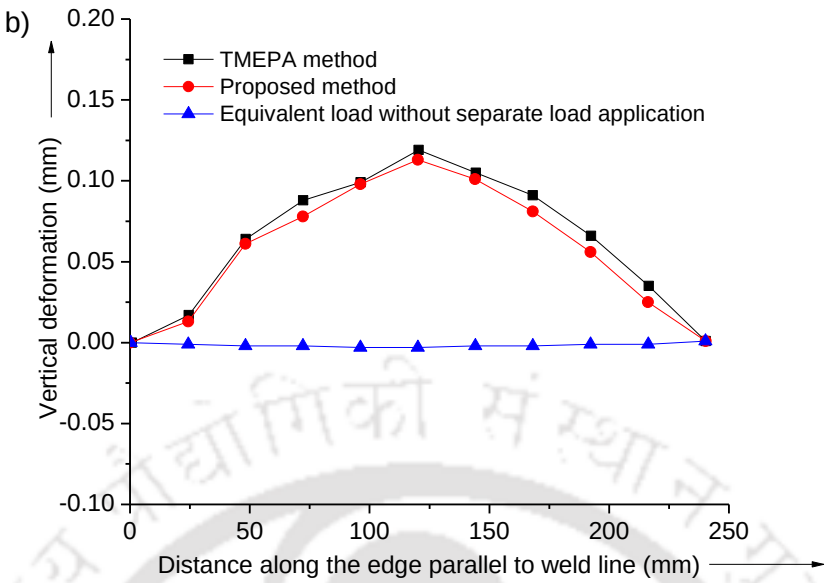

Fig.5.41 (a) Angular deformation and (b) Edge deflection plot for fillet joint model

This method is proposed to predict the weld-induced distortion in a large weld structure. Therefore, the same fillet joint model was modelled for the extended weld length of 600 mm, which is almost three times larger. The corresponding equivalent load results obtained for the smaller weld model was applied. The same inherent strain zone width values calculated for the small weld were employed in the respective start, end and mid regions. The length of the different areas was taken in the same proportion of the weld length as for the small weld joint model. A larger fillet joint model was also analysed using TMEPA to validate the effectiveness of the proposed method. Fig.5.42 shows the contour diagram of vertical distortion in the larger fillet joint model for all three cases.

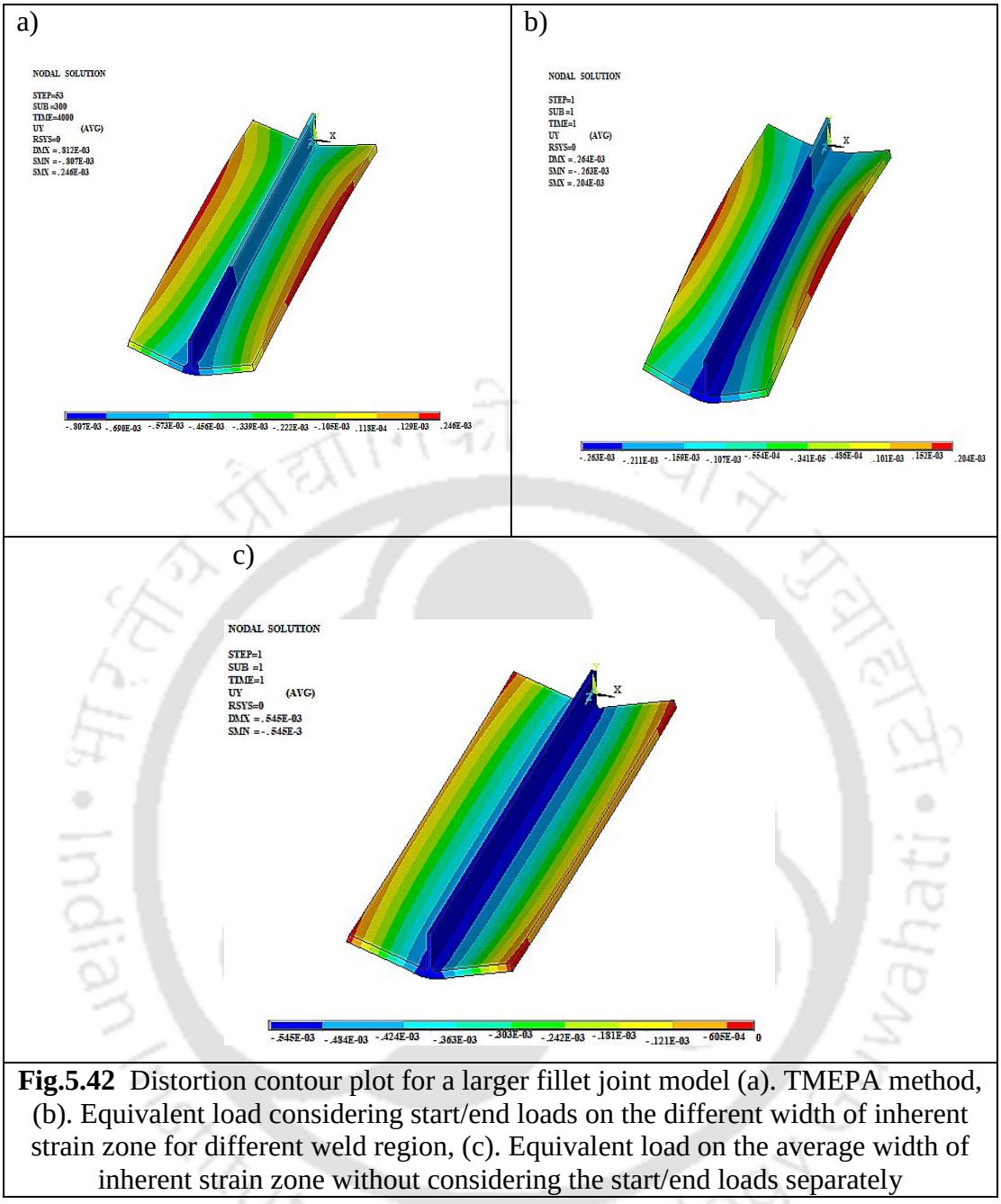

Fig.5.42 Distortion contour plot for a larger fillet joint model (a). TMEPA method, (b). Equivalent load considering start/end loads on the different width of inherent strain zone for different weld region, (c). Equivalent load on the average width of inherent strain zone without considering the start/end loads separately

5.2.6 Prediction of weld induced distortion for large structure

A large weld structure with two stiffeners was modelled with the proposed method for predicting the welding induced distortion. The stiffeners were assumed to be welded with the same welding parameters for the fillet joint considered in the earlier section. The large weld structure consists of the base plate (2400×2000×10 mm^3) and two stiffeners (2400×50×6 mm^3). The welded construction was modelled and analysed based on the plastic strain results obtained from the smaller weld joint models. To accommodate the sequence welding effect for welding of two stiffeners one after another, PSTRES ON was implemented (in

ANSYS^{TM}, APDL) to use the pre-stress condition, Canonsburg (2013). The same rigid body structural boundary conditions were also applied to constrain the six degrees of freedom of the whole weld structure. The schematic of the weld structure is shown in Fig.5.43 along with rigid body boundary condition.

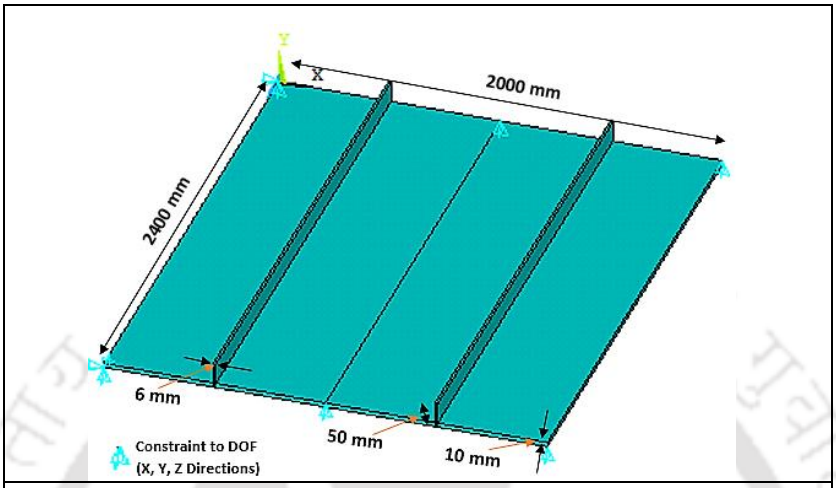

Fig.5.43 Schematic of Large weld structure

Fig.5.44 presents the contour plot of vertical or say Y displacement for the large weld structure. The maximum deflection is observed at the mid-region of both side edges and the region in between the two stiffeners. The overall distortion contour plot is also shown, in Fig.5.45.

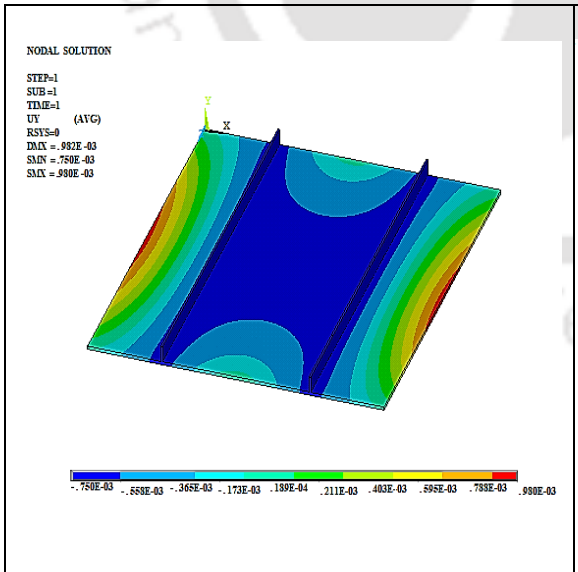

Fig.5.44 Vertical or Y- displacement contour plot

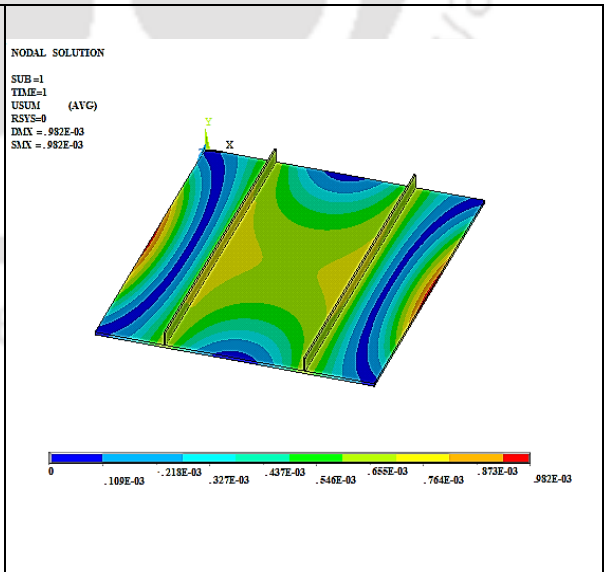

Fig.5.45 Overall distortion contour plot

Finally, a large weld structure (about 10 times larger) is analyzed using the proposed method successfully. It is observed that computational time for the analysis of large structure has been significantly reduced as compared with TMEP method and is detailed in Table 5.7.

Table.5.7 Comparison of TMEP and ELM based on average plastic strain

Configuration of computer	**TMEPA**	**ELM based on average plastic strain**
Windows XP, 2.6 GHz processor, 3 GB RAM	2-3 days computational time	~1 minute

5.2.7 Summary

In this investigation an improved equivalent load method based on average plastic strains is used to predict the distortion in large structures. The weld joint is modelled by thermal-mechanical elastic-plastic (TMEP) method and the results of structural results are validated with that of experimental results. The results of numerical model are in good agreement with experimental data. The equivalent load technique is implemented to predict the inherent strains in longitudinal and transverse directions. Effectiveness of the numerical model is ascertained by validation with the published data for butt and fillet joint. Finally large structure is modelled based on the outcomes obtained from butt and fillet joint for estimation of weld induced distortion in large structure. As compared with traditional TMEP analysis the proposed equivalent method based on average strains consumed significantly less computational time.

Chapter 6

Experimental Results and Discussion

6.0 Introduction

In this chapter results of the experimental investigation are presented. The results covered in this chapter are as follows:

- Optimization of welding process variables using single response and multi response optimization.
- Effect of heat sink on weld qualities
- Comparison between heat sink welding and normal welding.
- Effect of process variables on bead profile and mechanical properties in a double sided SAW process.
- Effect of surface active flux on bead geometry.

6.1 Optimization of welding process variables using single response and multi response optimization

6.1.1 Optimization of welding process variables using Taguchi method

Submerged arc welding consists of multiple input process variables such as welding current, voltage, welding speed, electrode diameter and length of stickout etc. These process parameters determine the quality characteristic of the process. These variables are to be properly controlled in order to achieve desired weld quality. In this work welding current (I), voltage (V), welding speed (S) and length of stickout (LSO) were considered as variables and other fixed parameters in this work are mentioned in Table 4.1. Before fixing the process parameters trial experiments were conducted by gradually varying one variable to determine their effect on individual variable keeping remaining variables constant. Finally the entire parameter envelope is divided into respective levels for use in this optimization process. In this work, mix level, four factor Taguchi's design of experiments was used to conduct the experiments. The matrix is L18 orthogonal array with one parameter set at 2 levels and remaining three parameters at 3 levels. Thus there are 18 experimental runs and interaction effects of process parameters on ultimate tensile strength (UTS) were accounted in this study.

Detailed experimental methodology and SAW process variables and their levels are mentioned in Table.4.9 in chapter 4.

6.1.1.1 Signal to Noise (S/N) Ratio

Taguchi's method uses S/N ratio in order to determine the optimal parameter settings. In Taguchi's technique, the setting of parameters will always maximize the S/N ratio irrespective of the type of response, Davis (1978). The S/N ratio depends on the type of the quality characteristic. In the present study, Larger-the-better (LB) criterion is chosen, since it is always desirable to have higher UTS to the welded joint. The S/N ratio for larger the better can be calculated using the following relation:

$$\text{S/N ratio (larger the better)} = -10\log_{10}\left(\frac{1}{n}\right)\sum_{i=1}^{n}\frac{1}{y^2} \tag{6.1}$$

where y is the performance characteristic in the experiment at i^{th} observation and n is the number of repetitions. Table 6.1 shows the input and output for single response optimization.

Table 6.1 Input and output parameters for single response optimization

LSO (mm)	V	I (A)	S (mm/s)	UTS (MPa)	SN ratio
23	26.5	445	5.00	471.16	53.46
23	26.5	455	5.14	574.44	55.18
23	26.5	465	5.27	476.31	53.55
23	27.5	445	5.00	566.39	55.06
23	27.5	455	5.14	607.71	55.67
23	27.5	465	5.27	550.19	54.81
23	28.5	445	5.14	435.49	52.77
23	28.5	455	5.27	528.00	54.45
23	28.5	465	5.00	513.06	54.20
25	26.5	445	5.27	540.49	54.65
25	26.5	455	5.00	565.56	55.04
25	26.5	465	5.14	461.22	53.27
25	27.5	445	5.14	455.36	53.16
25	27.5	455	5.27	539.68	54.64
25	27.5	465	5.00	532.76	54.53
25	28.5	445	5.27	522.04	54.35
25	28.5	455	5.00	509.31	54.13
25	28.5	465	5.14	483.63	53.69

Table 6.2 Response table SN Ratios (Larger is better)

Level	LSO	V	I	S
1	54.35	54.20	53.91	54.41
2	54.17	54.65	54.86	53.96
3		53.94	54.01	54.41
Delta	0.19	0.71	0.94	0.45
Rank	4	2	1	3

The response Table 6.2 provides the ranking of the input parameter for a specified output viz., UTS. The welding current occupies the primary position followed by voltage, speed, and length of stickout.

Table 6.3 ANOVA for SN ratios

Source	DF	Seq.SS	Adj.SS	Adj.M.S	F	% Contribution
LSO	1	0.156	0.581	0.581	4.53	1.46
V	2	1.552	1.966	0.983	7.66	14.55
I	2	3.229	3.229	1.614	12.57	30.27
S	2	0.802	0.802	0.401	3.12	7.52
I × S	4	4.154	4.152	1.038	8.09	38.95
Residual error	6	0.770	0.770	0.128		7.22
Total	17	10.667				100

Table 6.3 shows the results of Analysis of variance (ANOVA). Analysis of variance is used to determine the influence of the factors on the selected response. ANOVA separates total variability of output into contributions rendered by each factor and error.

From ANOVA, it can be clearly seen that welding current contributes highest with 30.27 % followed by welding voltage with 14.55 % and welding speed with 7.52 %. The length of stick out contributes the least to the output response i.e., ultimate tensile strength (UTS). In this work interaction of process variables namely welding current and speed are considered to study their effect on the output response. The interaction of welding current × speed contribution is 38.95 %. It can be concluded that interaction of process variables plays a significant role in the welding process.

Fig.6.1 indicates the Main effects plot that gives corresponding input parameters in X axis and SN ratio in Y axis.

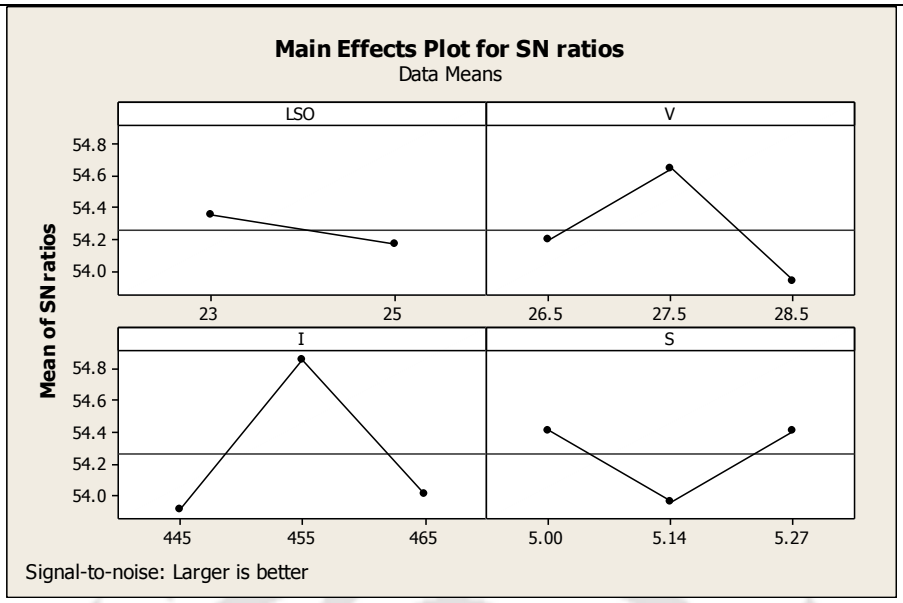

Fig.6.1 Main effect plot for SN ratios

Fig.6.1 shows the optimal parameter combination for getting ultimate tensile strength (UTS) which is LSO1-V2-I2-S3 i.e., length of stickout at 23 mm, voltage at 27.5 V, current at 455 A and welding speed at 5.27 mm/s.

6.1.1.2 Confirmation test

It is observed that the optimised variables given by main effect plot doesn't fall under L18 orthogonal array, therefore a confirmation test was conducted with three repetitions and UTS was found to be 612.42 MPa which confirmed the optimal parameter setting. Taguchi's method was successfully implemented for single response optimization. To perform optimization for all output responses a multi response optimization method is essential. The multi-response optimization method for all responses together was performed using Grey-Taguchi analysis in the succeeding section.

6.1.2 Optimization of process variables by Taguchi Grey relational analysis

To determine the optimal parameter setting, SN ratio was used in Taguchi's method and this method is suitable for single response optimization. But this method is not possible to use in case of multi response optimization. Therefore, to implement multi-response optimization problem, the Grey relation analysis (GRA) converts multi-response problem to single response optimization. In the present work, four output responses were considered namely

top bead width (TBW), top reinforcement height (TRH), ultimate tensile strength (UTS) and angular distortion (AD).

The process of Grey relational analysis is presented in chapter 3. The steps involved and the results are presented in this section. Table 6.4 presents the input parameters and output responses.

Table 6.4 Input parameters and responses for Grey relational analysis

LSO	Voltage	Current	Speed	TBW (mm)	TRH (mm)	UTS (MPa)	AD (deg.)
23	26.5	445	5.00	17.74	1.87	471.16	0.382
23	26.5	455	5.14	18.45	2.31	574.44	0.342
23	26.5	465	5.27	17.59	2.32	476.31	0.334
23	27.5	445	5.00	19.83	3.02	566.39	0.425
23	27.5	455	5.14	17.74	2.21	607.71	0.659
23	27.5	465	5.27	18.15	3.52	550.19	0.483
23	28.5	445	5.14	20.18	2.88	435.49	0.540
23	28.5	455	5.27	20.02	3.55	528.00	0.415
23	28.5	465	5.00	19.55	1.75	513.06	0.508
25	26.5	445	5.27	17.20	2.09	540.49	0.548
25	26.5	455	5.00	17.22	2.41	565.56	0.528
25	26.5	465	5.14	15.94	2.38	461.22	0.433
25	27.5	445	5.14	17.67	2.32	455.36	0.422
25	27.5	455	5.27	18.03	3.36	539.68	0.375
25	27.5	465	5.00	18.38	2.77	532.76	0.385
25	28.5	445	5.27	20.89	2.33	522.04	0.491
25	28.5	455	5.00	19.85	2.49	509.31	0.334
25	28.5	465	5.14	18.37	2.48	483.63	0.248

The initial step involves the normalization of measured quality characteristics data which were normalised between 0 and 1. This step is called grey relational generation. In the work TBW, TRH and AD were normalized by using Lower the better criteria using the equation 3.49, while ultimate tensile strength was considered for Higher the better criteria using the equation 3.50. Data processing for each performance characteristic is shown in Table 6.5. Next step is to calculate Grey relational coefficient based on normalized data. It is calculated to represent the correlation between the desired and actual experimental data. The Grey relational coefficient is calculated by the equation 3.51. Before calculation of Grey relational coefficient (GRC), Δ_{oi} is the difference of the absolute value was found and is shown in Table 6.6. The calculated Grey relational coefficient is mentioned in Table 6.7.

Table 6.5 Data processing for output performance characteristic (normalization)

TBW_LB	TR_LB	UTS_HB	AD_LB
0.6356	0.9331	0.2071	0.6750
0.4921	0.6885	0.8068	0.7706
0.6659	0.6818	0.2370	0.7915
0.2146	0.2941	0.7600	0.5699
0.6366	0.7426	1	0
0.5532	0.0133	0.6660	0.4285
0.1443	0.3805	0	0.2901
0.1756	0	0.5371	0.5940
0.2702	1	0.4504	0.3678
0.7451	0.8121	0.6096	0.2702
0.7407	0.6406	0.7552	0.3196
1	0.6518	0.1494	0.5495
0.6500	0.6846	0.1153	0.5764
0.5772	0.1036	0.6049	0.6916
0.5073	0.4334	0.5648	0.6678
0	0.6771	0.5025	0.4084
0.2100	0.5883	0.4286	0.7910
0.5087	0.5961	0.2795	1

Table 6.6 Δ_{oi} for all the responses

TBW	TR	UTS	AD
0.3644	0.0668	0.7928	0.3249
0.5079	0.3114	0.1931	0.2293
0.3341	0.3181	0.7629	0.2084
0.7854	0.7058	0.2399	0.4300
0.3634	0.2573	0	1
0.4468	0.9866	0.3339	0.5714
0.8557	0.6194	1	0.7098
0.8244	1	0.4628	0.4059
0.7298	0	0.5495	0.6321
0.2549	0.1878	0.3903	0.7297
0.2593	0.3593	0.2447	0.6803
0	0.3481	0.8505	0.4504
0.3500	0.3153	0.8846	0.4235
0.4228	0.8963	0.3950	0.3083
0.4927	0.5665	0.4351	0.3321
1	0.3228	0.4974	0.5915
0.7900	0.4116	0.5713	0.2081
0.4913	0.4039	0.7204	0

Table 6.7 Grey relational coefficients

TBW	TR	UTS	AD
0.5784	0.8820	0.3867	0.6061
0.4960	0.6162	0.7213	0.6855
0.5994	0.6111	0.3958	0.7057
0.3889	0.4146	0.6757	0.5376
0.5791	0.6601	1	0.3333
0.5280	0.3363	0.5995	0.4666
0.3688	0.4466	0.3333	0.4132
0.3775	0.3333	0.5192	0.5519
0.4065	1	0.4763	0.4416
0.6623	0.7268	0.5615	0.4065
0.6585	0.5818	0.6713	0.4236
1	0.5894	0.3702	0.5260
0.5882	0.6132	0.3611	0.5413
0.5418	0.3580	0.5586	0.6185
0.5036	0.4687	0.5346	0.6008
0.3333	0.6076	0.5012	0.4580
0.3875	0.5484	0.4666	0.7052
0.5043	0.5531	0.4096	1

Table 6.8 Grey relational grade (GRG)

Exp.1	Exp.2	Exp.3	Exp.4	Exp.5	Exp.6	Exp.7	Exp.8
0.613	0.629	0.578	0.504	0.643	0.482	0.390	0.445
Exp.9	Exp.10	Exp.11	Exp.12	Exp.13	Exp.14	Exp.15	Exp.16
0.581	0.589	0.583	0.621	0.525	0.519	0.526	0.475
Exp.17	Exp.18						
0.527	0.616	= 0.553 (Average GRG)					

The average grey relational grade for the experiments was 0.553. By averaging the Grey relational coefficients, Grey relational grade (GRG) was determined which is shown in Table 6.8. This GRG converts the multi response problem into a single response optimization problem, which was further analysed using Taguchi's method to determine the optimal solution. Fig. 6.2 shows the main effects plot for SN ratios of Grey relational grade. Table 6.9 shows the analysis of variance (ANOVA) for SN ratios of Grey relational grade.

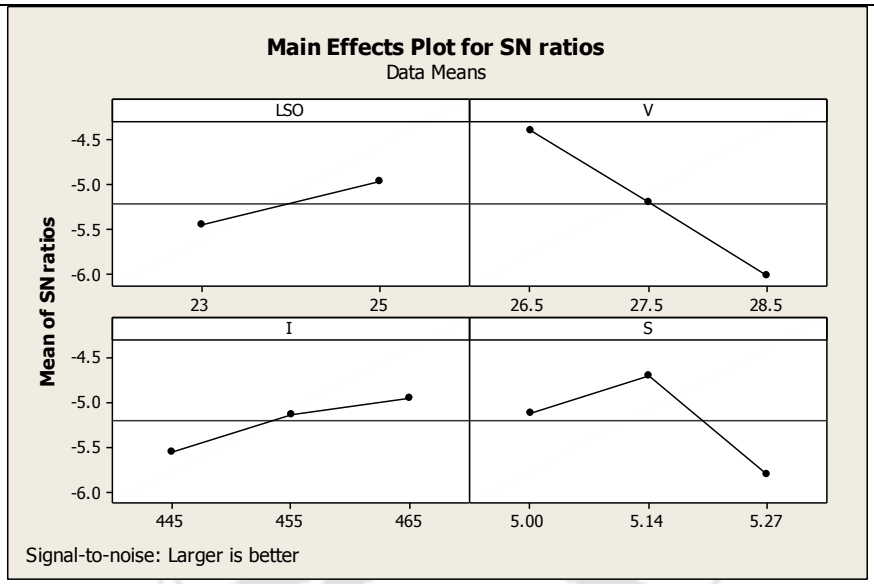

Fig.6.2 Main effect plot for SN ratios of Grey relational grade

Table 6.9 Analysis of variance (ANOVA) for SN ratios of GRG

Source	DF	Seq.SS	Adj.SS	Adj.M.S	F	% Contribution
LSO	1	1.021	1.021	1.021	1.44	4.04
V	2	7.855	7.855	3.927	5.53	31.12
I	2	1.126	1.662	0.830	1.17	4.46
S	2	3.757	1.577	0.778	1.10	14.88
V × I	4	6.753	4.684	1.171	1.65	26.75
V × S	4	3.304	3.304	0.826	1.16	13.09
Residual error	6	1.420	1.420	0.709		5.62
Total	17	25.236				100

Fig. 6.2 shows the main effect plots for SN ratios of grey relational grade (GRG). It can be observed from the plot that optimal parameter setting for this multi response problem is LSO2-V1-I3-S2. Table 6.9 shows the analysis of variance for SN ratios of GRG. It can be observed that welding voltage has highest contribution which is 31.12% amongst the individual factors. This was followed by the contribution of welding speed and current which are 14.88% and 4.46% respectively. The length of stickout has the least contribution amongst all. In this work interactions were considered among the primary contributing factor (voltage) and rest of the factors to determine their effects on output. It was found that voltage × current

contributes to 26.75 % while, voltage × speed contribution is 13.09 %. It can be concluded that interactions has significant contribution to the process output.

6.1.2.1 Confirmation experiment

For confirmation of experimental results three experimental runs were performed for same optimal parameter settings as suggested in Taguchi's method. The observed values of responses are tabulated in Table 6.10.

Table 6.10 Results of confirmation experiments

SL No.	TBW (mm)	TRH (mm)	UTS (MPa)	AD (deg.)
EXP No.1	15.44	2.23	602.53	0.32
EXP No.2	15.68	2.10	610.53	0.34
EXP No.3	15.77	2.18	608.12	0.36

6.1.2.2 Summary

The optimal parameters for getting quality weld are voltage at 26.5 V, current at 465 A, speed at 5.14 mm/s and length of stickout at 25 mm, with a fixed root gap of 2.5 mm and by using the electrode polarity of direct current electrode positive (DCEP). Hence multi response optimization was successfully performed using Grey-Taguchi method.

6.2. Comparative study between heat sink welding and conventional welding

Austenitic stainless steel such as 304 type is a choice of materials in chemical and fertilizers industries due to their good corrosion resistance. Normally tensile residual stresses are introduced into the weld root and its neighbourhood. Once the structure is subjected to functional load, the state of stress develops into complicated in nature. The direct exposure of weld root region to corrosive medium causes tensile residual stresses to be generated in the weldment. These tensile residual stresses have a profound effect on stress corrosion cracking, inter-granular corrosion, creep, etc. Hence controlling residual stress and distortion is essential to ensure good weld qualities.

In this section an attempt is made to study the effect of heat sink on angular distortion and mechanical properties in austenitic stainless steel (AISI 304) welds joined using a SAW process. To study the heat sink process and find its effect on weldment the results obtained were compared with that of conventional welds with same process variables. The heat sink welding was accomplished by design and fabrication of a fixture and the procedure is detailed

in chapter 4 of experimental methodology. The results presented in this chapter include comparison of thermal profile, angular distortion, weld cross sectional area, and tensile properties obtained for heat sink and conventional welds.

6.2.1 Thermal history

The temperature measurement of the weld joint is obtained by installing K-type thermocouple at the distance of 24 mm from the weld line on the top surface of the work piece is shown Fig. 4.8. Fig. 6.3 shows the recorded thermal history of conventional welded specimen and heat sink welded specimen for the welding parameter 410 A, 23 V and 5.55 mm/s. It is observed that peak temperatures obtained with and without water cooling are 391.76^{o}C and 395.62^{o}C respectively. The difference in the peak temperature was only marginal, while the cooling rate was observed to be significantly enhanced for water cooled specimen relative to that of weld without water cooling. Therefore from this thermal history plot it can be established that heat sinking have significantly enhanced the cooling rate.

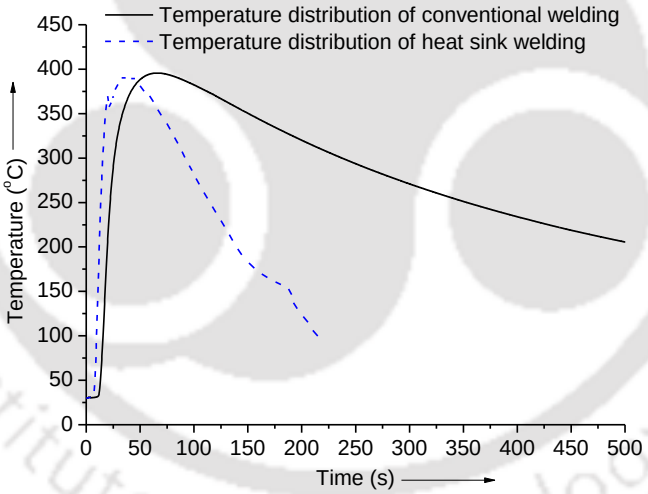

Fig.6.3 Thermal history profile of conventional and heat sink welding (without and with water cooling)

6.2.2 Comparison of weld cross sectional area

Fig. 6.4 depicts the representative cross section of heat sink welds and conventional welds for different process parameters.

Cross section of heat sink welds	Cross section of conventional welds
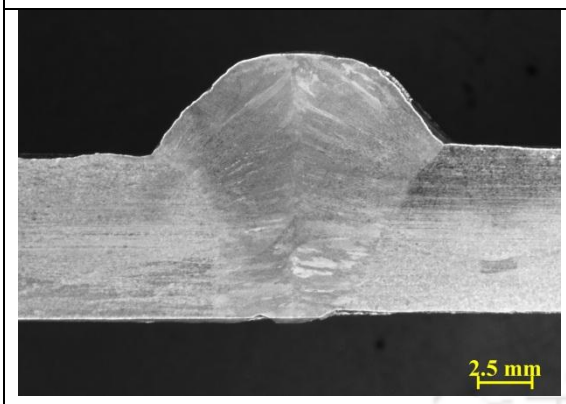	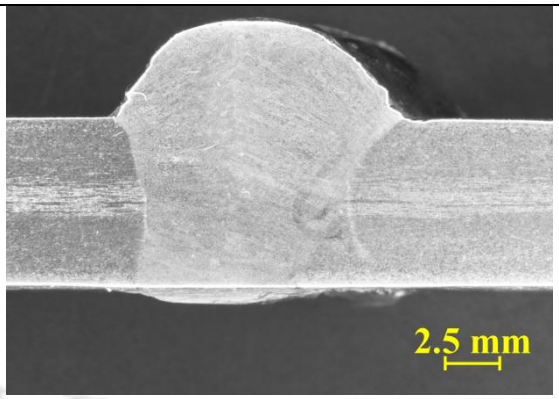
H.S-Exp. 11 CRA : 116.53 mm^2 420 A, 23 V, 5.55 mm/s	Exp. 2 CRA : 122.39 mm^2 420 A, 23 V, 5.55 mm/s
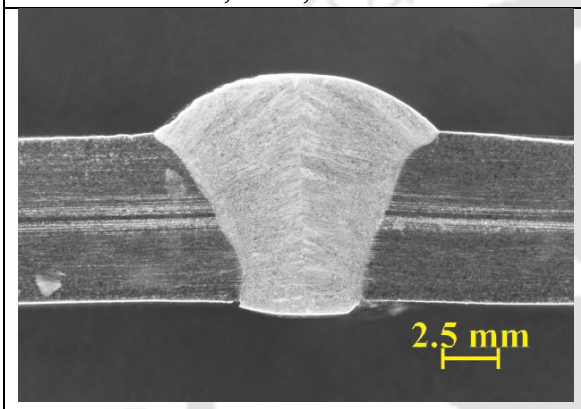	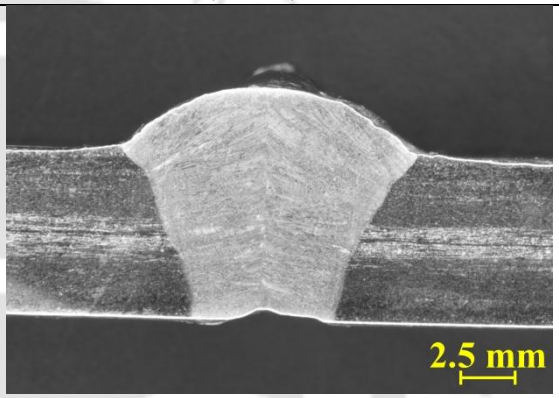
H.S-Exp. 18 CRA : 94.68 mm^2 430 A, 25 V, 6.66 mm/s	Exp.9 CRA : 107.08 mm^2 430 A, 25 V, 6.66 mm/s

Fig.6.4 Comparison of cross sectional area with and without heat sink welding

From the macro structural cross-section of the welds, it can be observed that welds are free from defects such as cracks, flux inclusions and porosities. The welding parameters used in this experimentation are presented in Table 6.11.

Table 6.11 Process variables for conventional and heat sink welding

Sl No.	Current (A)	Voltage (V)	Welding speed (mm/s)
1	***410***	23	5.55
2	***420***	23	5.55
3	***430***	23	5.55
4	430	***23***	5.55
5	430	***24***	5.55
6	430	***25***	5.55
7	430	25	***5.55***
8	430	25	***6.11***
9	430	25	***6.66***

From the Fig.6.4, it can be observed that weld cross sectional area decreases with the water cooling welding whereas for conventional welding it is more when welding is done with same parameters. This is due to rapid removal of heat from the fusion zone as the water channels placed away from the weld center line. The smaller fusion zone obtained from heat sinking might minimize size of heat affected zone, hence the chances of sensitization can be minimum or eliminated. The austenitic stainless steels when exposed in the range of 850^{o}C to 400^{o}C, it becomes sensitized which can lead to intercrystalline corrosion. Therefore, a reduction in dwell time during cooling in the sensitization range can decrease the chances of intercrystalline corrosion. Jiang et al., (2012) carried out numerical simulations on multipass welding of 316L stainless steel. Jiang et al., (2012) observed that when conventional welding was carried out then the dwell time to cool between 850^{o}C to 400^{o}C was 13 s, while with heat sink it was 6.5 s. Hence, the use of heat sink was found to be effective in reducing the dwell time in austenitic stainless steel.

Table 6.12 represents the weld cross sectional area obtained for conventional and heat sink welding with variation in welding current and welding speed.

Table 6.12. Cross-sectional area of conventional and heat sink welding

Welding process variable	Cross sectional area (mm^2) for conventional welding	Cross sectional area (mm^2) for heat sink welding	% Reduction
Welding current (A)	For constant voltage and speed of 23 V, 5.55 mm/s respectively		
410	110.91	103.64	6.55
420	122.39	116.53	5.03
430	131.46	125.23	4.97
Welding speed (mm/s)	For constant current and voltage of 430 A, 25 V respectively		
5.55	138.74	123.39	11.06
6.11	124.28	119.02	4.23
6.66	107.08	94.68	11.58

Fig.6.5 (a) and (b) show the comparisons of cross sectional area of welds for variation in welding current and welding speed. It can be observed from the Table 6.12 that percentage reduction in cross sectional area varies between 4 to 11 % approximately. It can be

concluded that welding speed has much influence on reduction in fusion joint cross-sectional area.

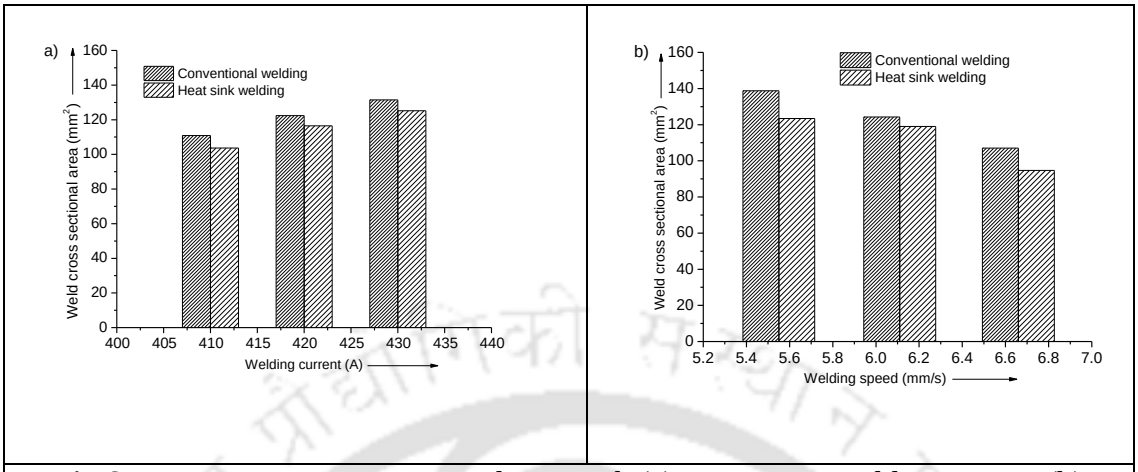

Fig.6.5 Fusion zone cross sectional area with (a) variation in welding current (b) variation in welding speed for conventional and heat sink welding

6.2.3 Comparison of tensile properties for conventional and heat sink welding

Tensile test was conducted as per ASTM E8 standard. Two samples were extracted from each welded plate and the average results are presented in this discussion. Fig.6 shows the tensile plot between conventional and heat sink welding for variation with welding current for the parameter with welding current at 420A, voltage at 23 V and welding speed at 5.55 mm/s is shown for the purpose of representation.

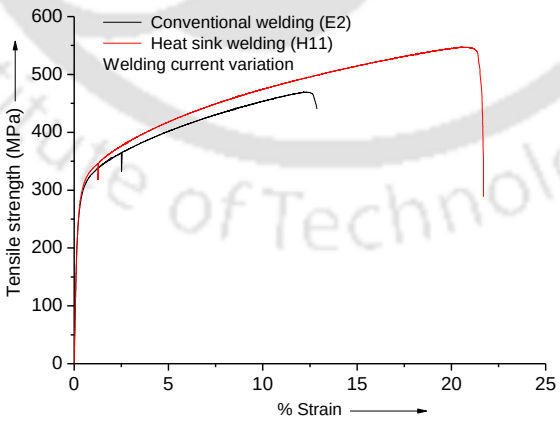

Fig.6.6 Tensile plot for conventional and heat sink welding for welding current variation

It is observed from the Fig.6.6 that tensile strength obtained for heat sink welds were higher than that of conventional welds. The effect of welding current and welding speed on average tensile properties for conventional and heat sink welds are presented in Figs.6.7 (a) and (b).

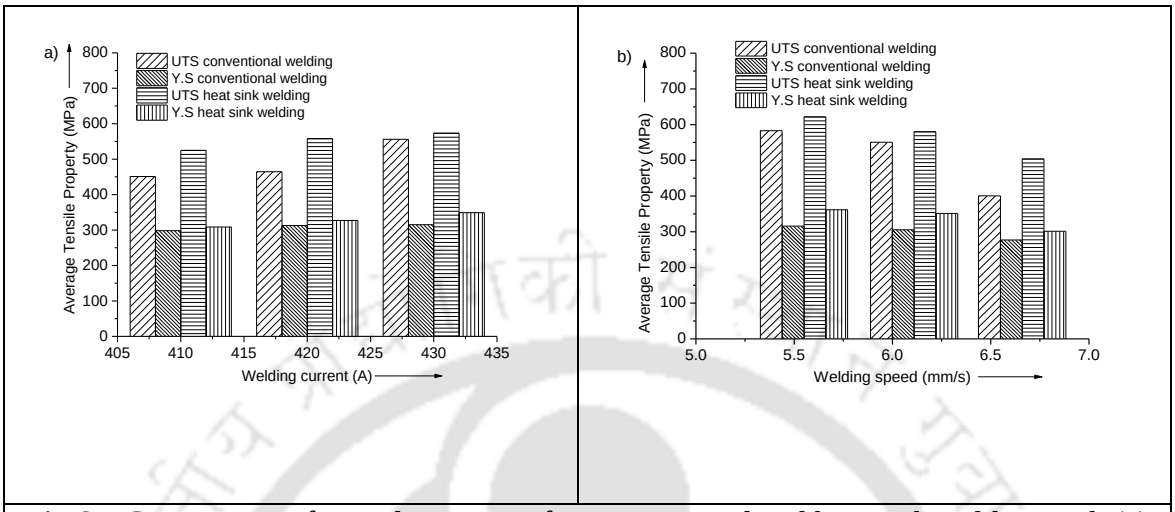

Fig.6.7 Comparison of Tensile property for conventional and heat sink welding with (a) current variation (b) speed variation

Table 6.13 represents the mechanical properties obtained for conventional and heat sink welding with variation in welding current and welding speed.

It can be observed from Table 6.13 that a maximum of about 20 % enhancement in ultimate tensile strength (UTS) is obtained when welding current is varied from 410 A to 430 A and about 10 % enhancement in yield strength (Y.S) was achieved. When welding speed was varied from 5.55 mm/s to 6.66 mm/s, an enhancement of 25 % in ultimate tensile strength and 15 % improvement in yield strength was observed for heat sink welding compared to conventional welding. Also heat sink converts the tensile residual stresses into compressive residual stresses in the fusion zone there by mitigating the stress corrosion cracking, Yangida and Koide (2008). The enhancement in mechanical properties can be attributed due to formation of compressive residual stresses in and around the fusion zone, Lim et al. (2018).

Table 6.13 Comparison of mechanical properties between conventional and heat sink welding

Welding process variable	UTS (MPa)	Y.S (MPa)	UTS (MPa)	Y.S (MPa)	% enhancement in UTS	% enhancement in Y.S
	Conventional welding		Heat sink welding			
Welding current (A)	For constant voltage and speed of 23 V, 5.55 mm/s respectively					
410	450.92	298.16	524.91	308.61	16.41	3.50
420	464.63	312.63	557.80	327.09	20.05	4.63
430	556.08	315.06	573.22	349.05	3.08	10.79
Welding speed (mm/s)	For constant current and voltage of 430 A, 25 V respectively					
5.55	582.95	316.00	621.53	361.82	6.62	14.50
6.11	550.69	305.57	580.20	351.48	5.86	15.02
6.66	400.33	276.96	503.68	301.20	25.82	8.75

6.2.4 Comparison of angular distortion

Fig.6.8 shows the effect of welding current, voltage and speed on angular distortion between conventional welding and heat sink welding.

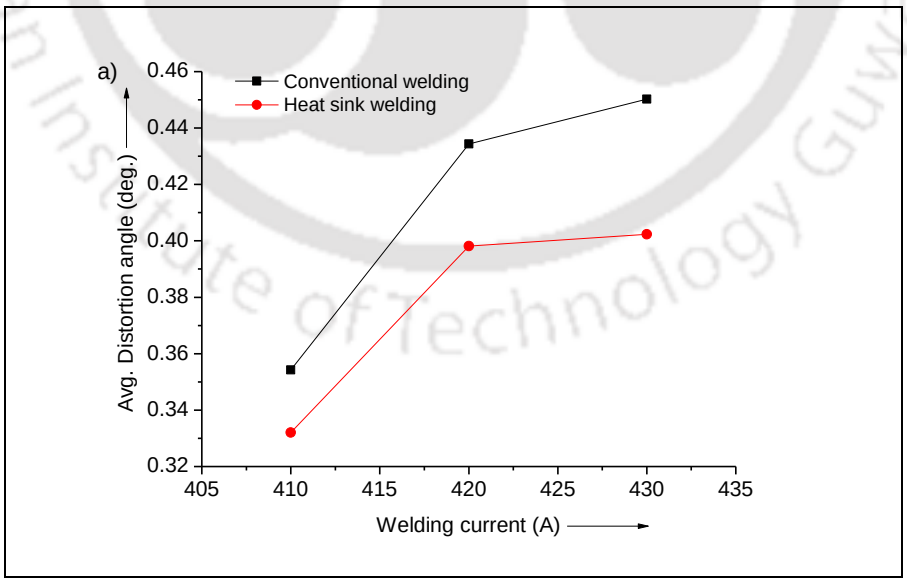

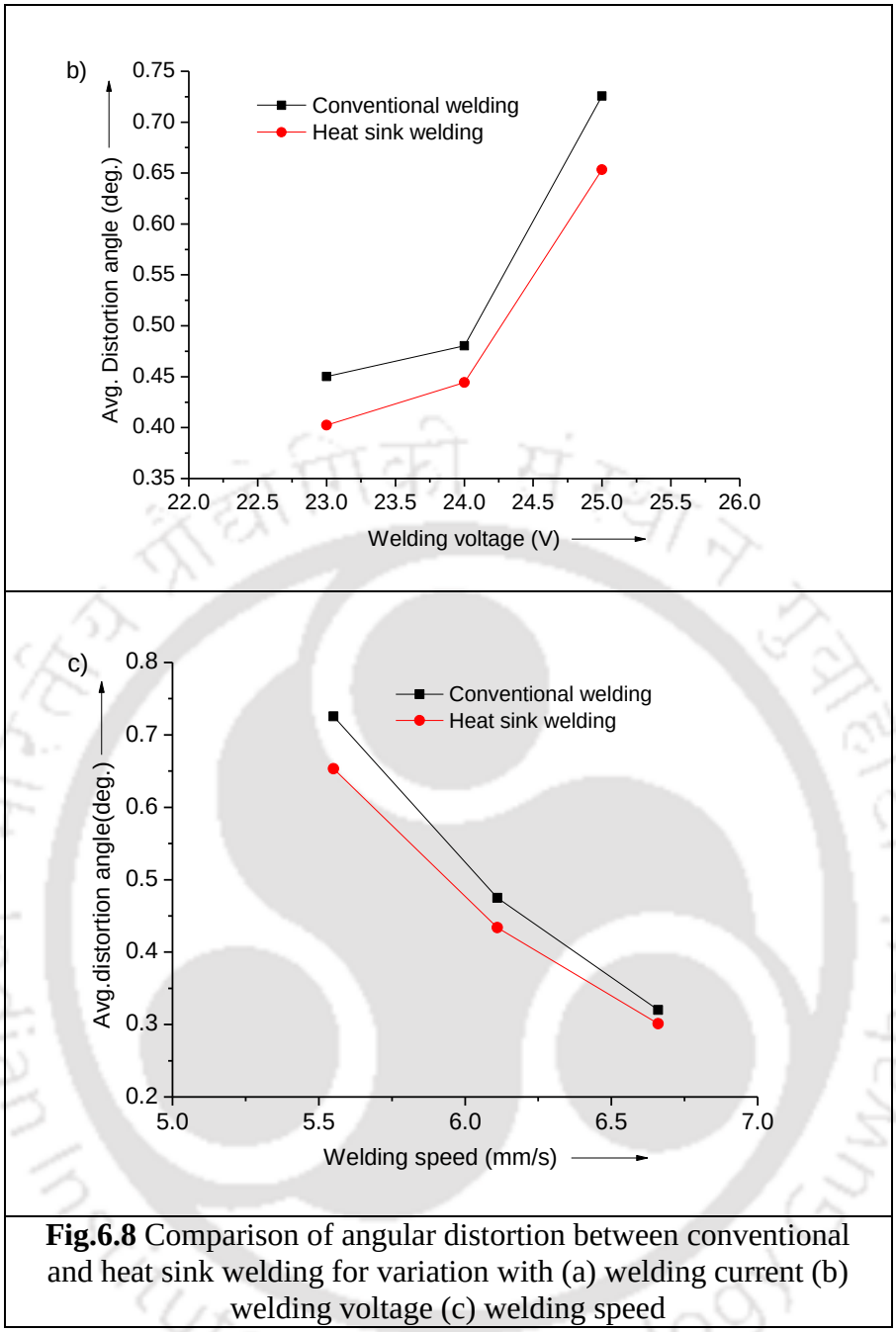

Fig.6.8 Comparison of angular distortion between conventional and heat sink welding for variation with (a) welding current (b) welding voltage (c) welding speed

From Fig.6.8 (a), it can be seen that as the welding current is increased the distortion also gradually increased up to intermediate current and after that it shows a drooping trend for conventional as well as heat sink welding. The maximum beneficial effect to heat sink on angular distortion can be observed at higher welding currents. Fig. 6.8 (b) shows the effect of welding voltage on angular distortion. It can be observed that as welding voltage is increased there is a steep rise in the distortion. This is due to the fact that as voltage increases bead width on the top increases, due to which it increases shrinkage forces acting towards the top surface of the butt joint increase as compared with the bottom shrinkage forces. Hence, at

higher voltages, more angular distortion was observed. Fig.6.8 (c) shows the effect of welding speed on distortion. It can be clearly seen that as welding speed increases the angular distortion reduces which was due to less heat input supplied to the weld joint. It was also observed that at higher welding speeds, the difference of angular distortion between conventional and heat sink welding is marginal. Table 6.14 shows the comparison of angular distortion between conventional and heats sink welding.

Table 6.14 Comparison of average angular distortion between conventional and heat sink welding

Exp No.	Welding process variable	Average angular distortion for conventional welding	Average angular distortion for heat sink welding	% Reduction
Welding current (A)	For constant voltage and speed of 23 V, 5.55 mm/s respectively			
Exp No.1	410	0.354	0.332	6.215
Exp.No.2	420	0.434	0.398	8.295
Exp.No.3	430	0.450	0.402	10.667
Welding voltage (V)	For constant current and speed of 430 A, 5.55 mm/s respectively			
Exp.No.4	23	0.450	0.402	10.667
Exp.No.5	24	0.481	0.444	7.692
Exp.No.6	25	0.725	0.653	9.931
Welding speed (mm/s)	For constant current and voltage of 430 A, 25 V respectively			
Exp.No.7	5.55	0.725	0.653	9.931
Exp.No.8	6.11	0.475	0.433	8.842
Exp.No.9	6.66	0.320	0.301	5.938

From Table 6.14, it can be observed that maximum reduction in angular distortion of about 10.66 % is obtained for Exp.No.3, while lowest reduction is obtained for Exp.No.9. The mechanism of distortion mitigation through heat sink involves the removal of heat rapidly from the fusion zone (i.e. reducing the peak temperature in the fusion zone) thereby keeping the base metal cooler hence the young's modulus and yield strength of the base material are not much lowered which resulted in lowered distortion. Hence, from this study it can be

concluded that heat sink welding is found to be effective in enhancing the weld qualities in austenitic stainless steel.

6.2.5 Summary

In this investigation a comparative study is conducted between conventional and heat sink welding. To perform heat sink welding a fixture was designed and fabricated. Fusion zone cross section, mechanical characterization and angular distortion studies were performed. As compared with conventional welding the heat sink welds exhibited superior mechanical properties and reduced distortion.

6.3 Effect of process variables on bead profile and mechanical properties in a double sided (SAW) process

In this section, the results of effect of process variables on bead geometry and mechanical properties in a double sided submerged arc welding (SAW) of AISI 304 austenitic stainless steel of 8 mm thick are presented. Further, the effect of welding current on bead profile in a 12 mm thick plate is also studied. The procedures adopted in fabrication of double sided submerged arc welding (DSSAW) are detailed in chapter 4 of experimental methodology. The results presented in this section include macrostructure, microstructure, bead geometry and mechanical properties. Also a comparison of distortion with single side (SAW) welding is presented.

Experiments were conducted by keeping two parameters constant while varying the other was done in order to study their individual effect.

6.3.1 Weld macrostructure

Generally, welded joints are prone to cracks, micro porosities, slag inclusions, incomplete penetration etc. Therefore, it is required to ensure that no such weld defects should arise during or due to experiments. All weld samples were visually inspected before proceeding to further characterization. It was observed that for all process variable combinations no such defects were detected. Fig.6.9 shows the representative macrostructures of the Exp.2, 3, 6 and 7 respectively. Also, it is to be noted that Fig.6.9 represents the fusion zone profile for a common parameter used in Exp. 2, 5 and 8.

6.3.2 Weld microstructure

The microstructure of as received AISI 304 stainless steel consists of equiaxed austenite grains and deformation twins that were formed during thermos-mechanical processing. Fig.6.10 shows the microstructure of the as received base metal. The microstructure of weld metal consists of columnar dendritic grains of delta ferrite and in a matrix of austenite with no sign of equiaxed grains. Fig.6.11 shows the interface zone between fusion zone and HAZ and weld zone. From Fig.6.11 it can be observed that the microstructure in the vicinity of the weld pool consists of equiaxed grains of austenite. Also it is clearly seen that dendritic crystals seen are emerging perpendicular from the fusion line.

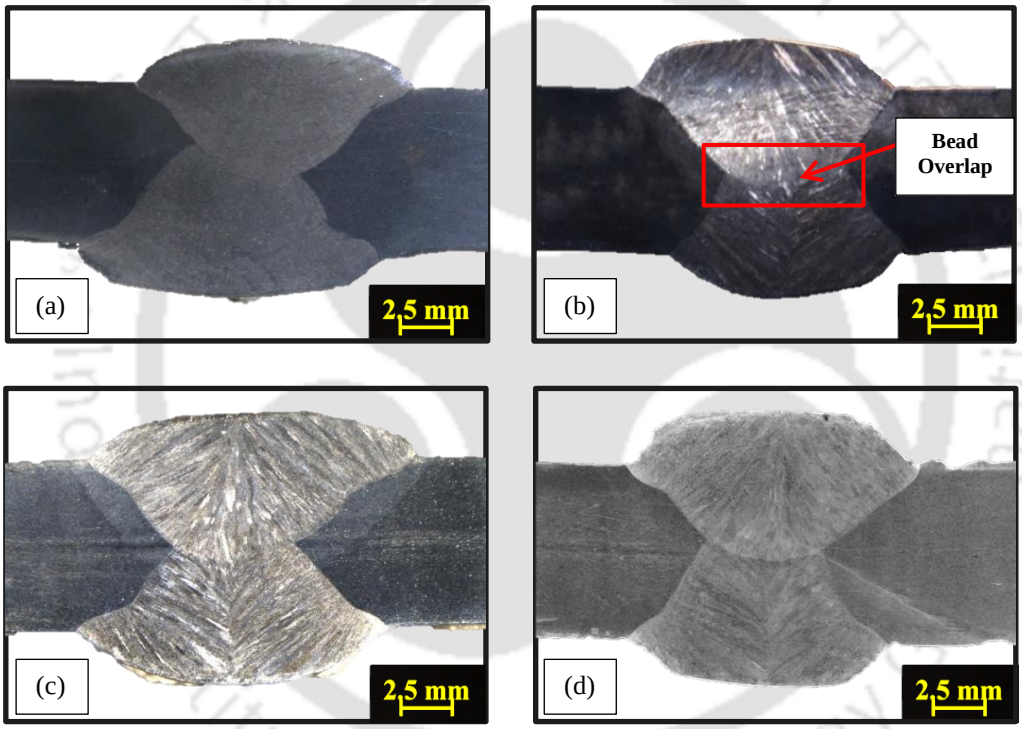

Representative **Figs.6.9** As polished macrostructure (a) Exp. No. 2, 5 and 8 (common parameter) Etched macrostructures of (b) Current variation Exp.No.3 (c) Voltage variation Exp.No.6 (d) Speed variation Exp.No.7

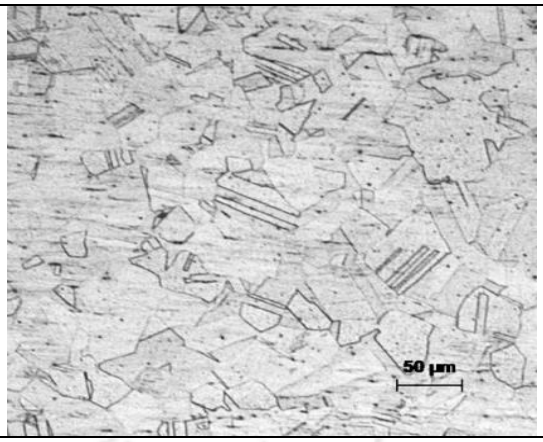

Fig.6.10 Microstructure of base metal AISI 304

Equiaxed grains of austenite are observed in the vicinity of the weld zone. The solidification of weld pool is a dynamic mechanism with epitaxial growth of crystals and is due to variations in the temperature gradient within the weld pool results in different growth rate of crystals.

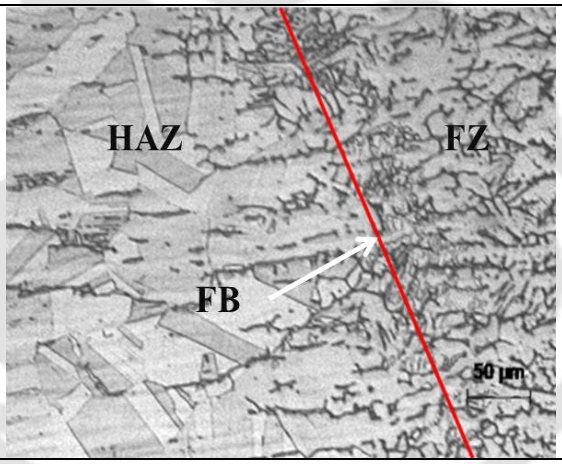

Fig.6.11 Fusion zone and HAZ interface

In weld solidification mechanics, important parameters that affect the microstructure are temperature gradient within the weld pool (G), growth rate (R) and degree of undercooling (ΔT) and alloy composition (C_o), Lampman (1997). All these parameters essentially vary from location to location and also differ with different welding process and welding conditions. Due to this microstructure of weld pool diverge from location to location within the fusion zone. Two types of morphology of delta ferrite were observed within the weld metal as shown in Fig.6.12.

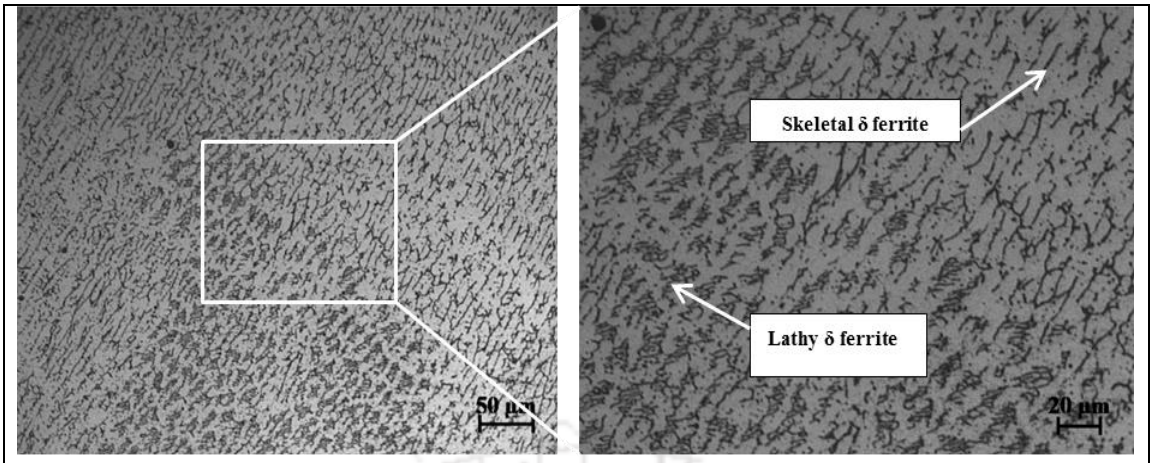

Fig.6.12 Typical microstructure in upper mid region in a weld pool Exp.No.3

The white portions in the microstructure correspond to austenite and the darker portions are delta ferrite. From Fig.6.12 it can be observed that morphology of delta ferrite varies from lathy ferrite to skeletal ferrite in the fusion zone. The intersection region of the weld pass is shown in Fig.6.13 where in on one side i.e. in the 2nd pass side the skeletal delta ferrite is observed.

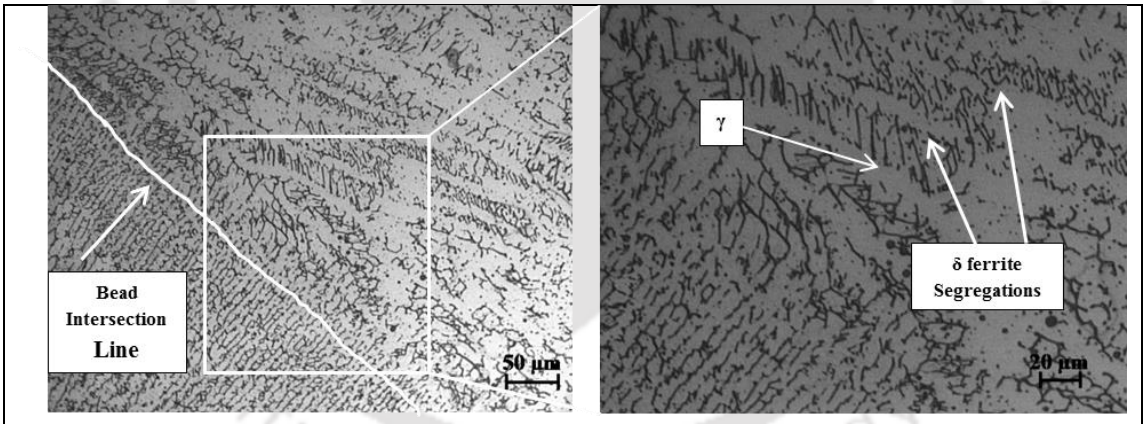

Fig.6.13 Microstructure of weld zone intersection of top and bottom pass in the for Exp.No.3

Similar types of morphologies of delta ferrite are observed in all regions of all the weld samples. These types of occurrences are due to the different thermal cycles and cooling rates within the weld zone, Mirshekari et al., (2014). Also, in austenitic stainless steels, delta ferrite phase is desirable as it prevents weld from hot cracking, Lippold and Kotecki (2005); Kou, (2003).

6.3.3 Microhardness

The micro hardness was recorded 2 mm away from the top and bottom plate surface and along transverse to weld centre line. The micro hardness of the base material is the average of five measurements taken at an interval of 0.5 mm and hardness was found to be ~214 HV. A sample of Vickers hardness indentation in the weld zone is shown in the Fig.6.14.

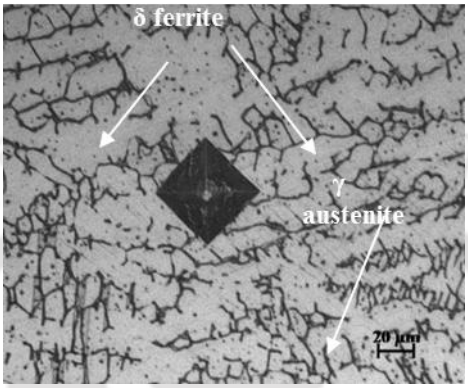

Fig.6.14 Sample of hardness indentation in the weld zone

The micro hardness of all samples was measured. The micro hardness obtained for Exp.4, is explained. The micro hardness distribution in the (a) top (b) middle (c) bottom run for the welded sample is shown Fig. 6.15.

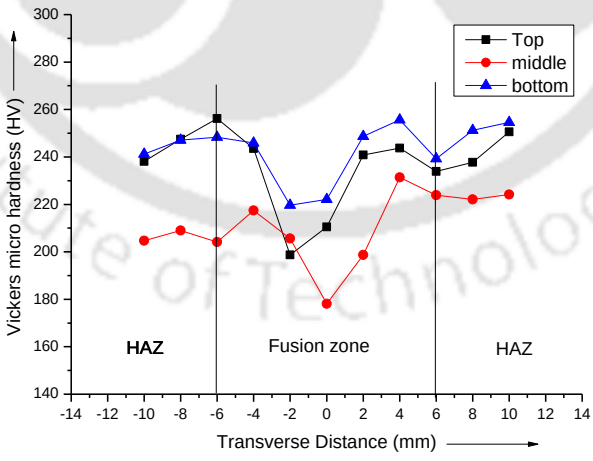

Fig.6.15 Graph of micro hardness for the Exp.No.4

From Fig.6.15 it can be observed that hardness in the center line of the fusion zone is less than HAZ. The minimum hardness of 178.1 HV was observed in the weld intersection portion of the fusion zone. The intersection portion of the weld gets remelted during second

run leading to dissolution and reduction of other phases in the austenite matrix, thus less hardness was obtained. Also it can be clearly noticed that hardness increases gradually towards the HAZ from the center of the fusion zone. The hardness along the weld centreline is lowest compared with top layer and bottom layer of the welded sample.

6.3.4 Effect of process variables on fusion zone profile

In this work, the individual effect of each process variable is studied, while keeping all other parameters constant. The weld bead nomenclature of double sided SAW process is illustrated in the Fig.6.16 The plates were joined with same heat input i.e., same welding parameters on both sides. Hence, weld bead profile parameters such as bead width (b_w), reinforcement height (r_h), penetration area (p_a), reinforcement area (r_a), depth of penetration (p_d) were measured for single side, i.e., 2nd weld pass.

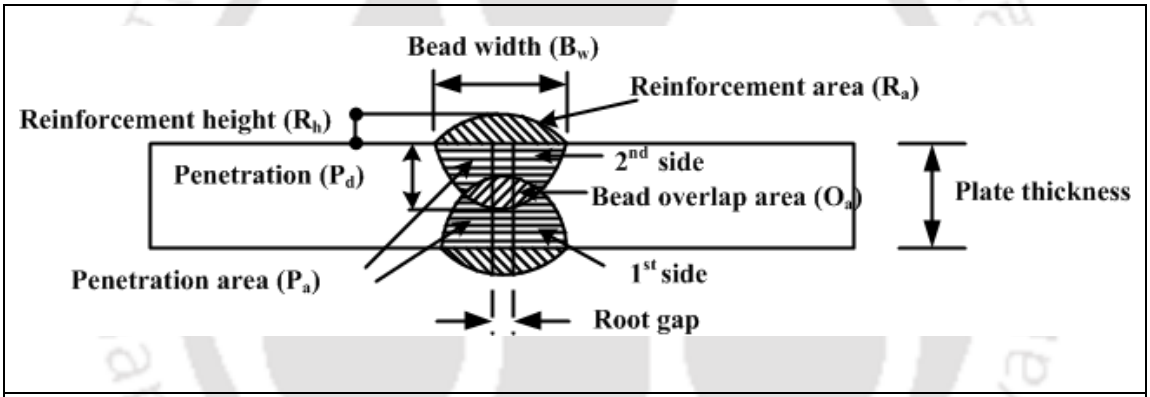

Fig.6.16 Nomenclature of the weld bead with root gap for double sided SAW process

The average results of three samples were considered for analysing the fusion zone profile.

6.3.4.1 Effect of welding current

Figs.6.17(a)-(c) depict the effect of welding current on bead width, reinforcement height, reinforcement area, penetration area, penetration depth, and bead overlap area.

From Figs.6.17 (a)-(c), it is evident that weld bead parameters namely bead width (B_w), reinforcement height (R_h), penetration area (P_a), reinforcement area (R_a), penetration depth (P_d), and bead overlap area (O_a) generally increases with increase in welding current from 340 A to 390 A. From Fig.6.17 (a), it can be clearly observed that weld width increases initially and after which it reduces slightly, with further increase in current, but is higher than the initial weld width. From Fig.6.17 (b), it can be seen that as welding current increases, the

reinforcement area and penetration area gradually increase. The welding current is the most crucial process variable in submerged arc welding (SAW). The amount of heat generated during the welding process is directly proportional to the square of the welding current.

From Fig.6.17 (c), it can be witnessed that penetration depth increased almost linearly with an increase in welding current since the welding current has a pronounced effect on the depth of penetration. According to Murugan and Gunaraj (2005), the effect of welding current can be explained as follows: The welding current increases the momentum of filler metal droplets, and these impinges the weld pool causes deep penetration.

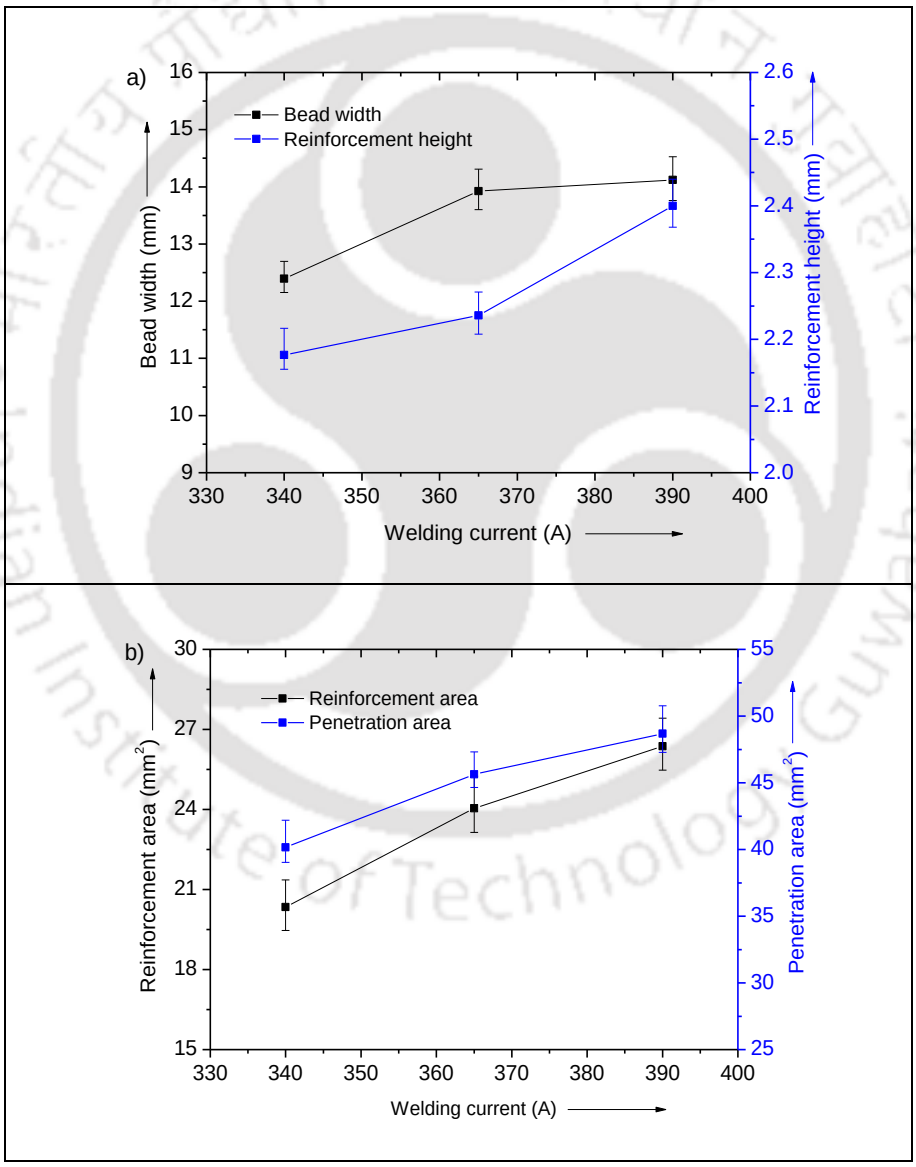

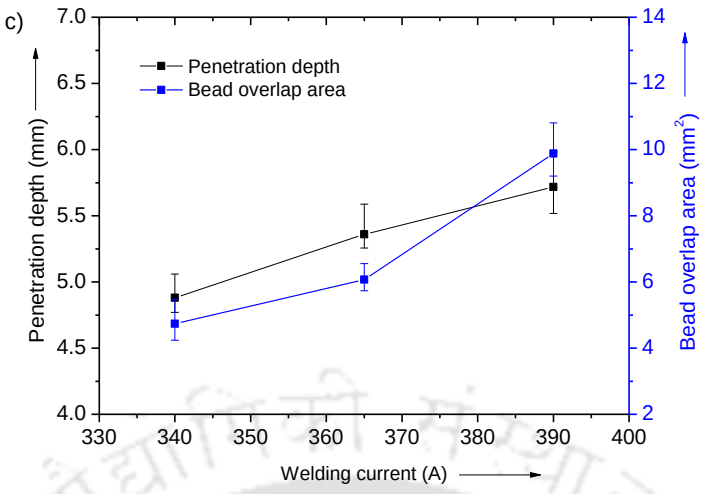

Fig.6.17 Effect of welding current on (a) Bead width and reinforcement height (b) Reinforcement area and penetration area (c) Penetration depth and Bead overlap area

Keeping all parameters constant, with increasing the welding current, the penetration, electrode deposition rate, bead width, and weld cross-sectional area enhance or increase. Also, it is noticed that the bead overlap area increases as welding current was varied from 340 A to 390 A, which is due to higher heat input and larger fusion zone size at increased welding currents.

6.3.4.2 Effect of welding voltage

Figs. 6.18 (a)-(c) depict the effect of welding voltage on bead width, reinforcement height, reinforcement area, penetration area, penetration depth, and bead overlap area. The welding voltage is the electrical potential difference between the tip of the filler wire and the surface of the molten weld puddle. From Fig.6.18 (a), it is evident that an increase in welding voltage from 22 V to 26 V while keeping all other parameters constant, has resulted in a steady increase in weld bead width. The increase in voltage increases the arc length, hence more melting at the surface due to large arc spread, which increases weld width. The welding voltage has a direct effect on the shape of the fusion zone profile and external bead appearance. Increase in voltage results in flatter bead, and hence reinforcement height reduces with increase in welding voltage. From Fig.6.18 (b), it is clear that the reinforcement area decreases and penetration area increases with an increase in voltage.

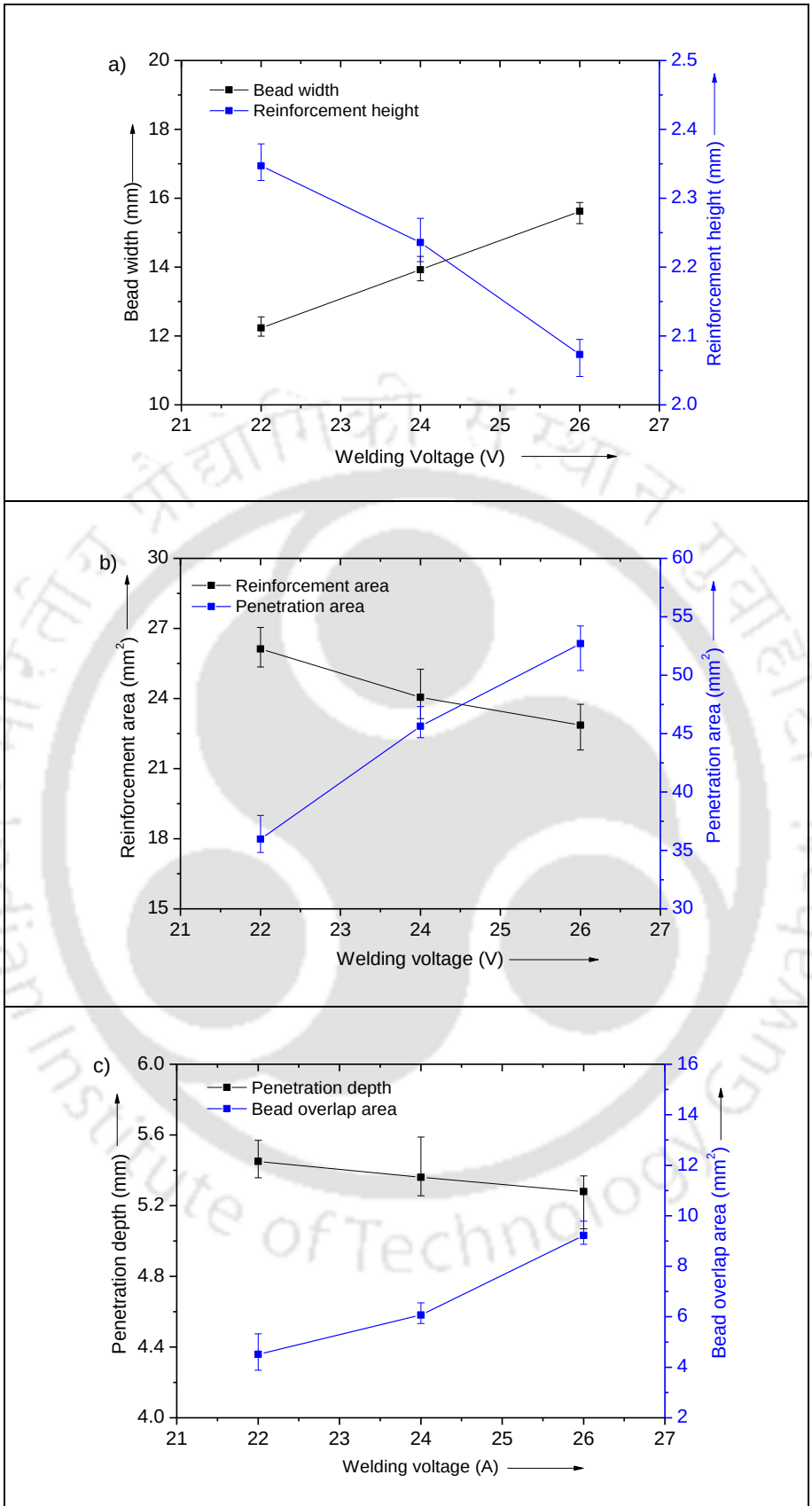

Fig.6.18 Effect of welding voltage on (a) Bead width and reinforcement height (b) Reinforcement area and penetration area (c) Penetration depth and Bead overlap area

The increase in penetration area attributes to the widening of the weld pool at the expense of penetration depth. It is observed from Fig.6.18 (a) and Fig.6.18 (b) that the reinforcement height and area reduce with an increase in voltage, as welding voltage doesn't appreciably affect the electrode melting rate.

From Fig.6.18(c) as the voltage is increased from 22 V to 26 V, there is a slight reduction in the depth of penetration. Increased depth of penetration (P_d) at low voltages is attributed to flow of heat in the thickness direction and smaller arc length, which causes a positive effect on penetration depth and more reinforcement height. It can be concluded that the effect of welding voltage on penetration is only marginal. Also, as the voltage is increased from 22 V to 26 V bead overlap area increases and this is due to the increase in the penetration area at a higher voltage.

6.3.4.3 Effect of welding speed

Figs.6.19 (a)-(c) depict the effect of welding speed on bead width, reinforcement height, reinforcement area, penetration area, penetration depth, and bead overlap area.
Fig (a) shows the effect of welding speed on bead width and reinforcement height. It is observed from Fig.6.19 (a) that bead width and reinforcement height decrease with increase in welding speed. This reduction is due to heat input applied per unit length into the joint decreases with increase in welding speed, and hence lesser filler metal is deposited, which leads to smaller weld bead and less reinforcement height. It can be concluded that welding speed has an inverse effect on bead width and reinforcement height. From Fig.6.19 (b), it is observed that with increase in welding speed both reinforcement area and penetration area reduce, which was due to less time the base metal had exposed to the heat of welding arc. From Fig.6.19 (c) it is evident that as welding speed increases penetration as well as bead overlap area was reduced. It was observed that at lower welding speed, i.e., 6.8 mm/s the higher depth of penetration is noticed, while other operating parameters were held constant. The average results of the weld bead and fusion zone size are shown in Table.6.15.

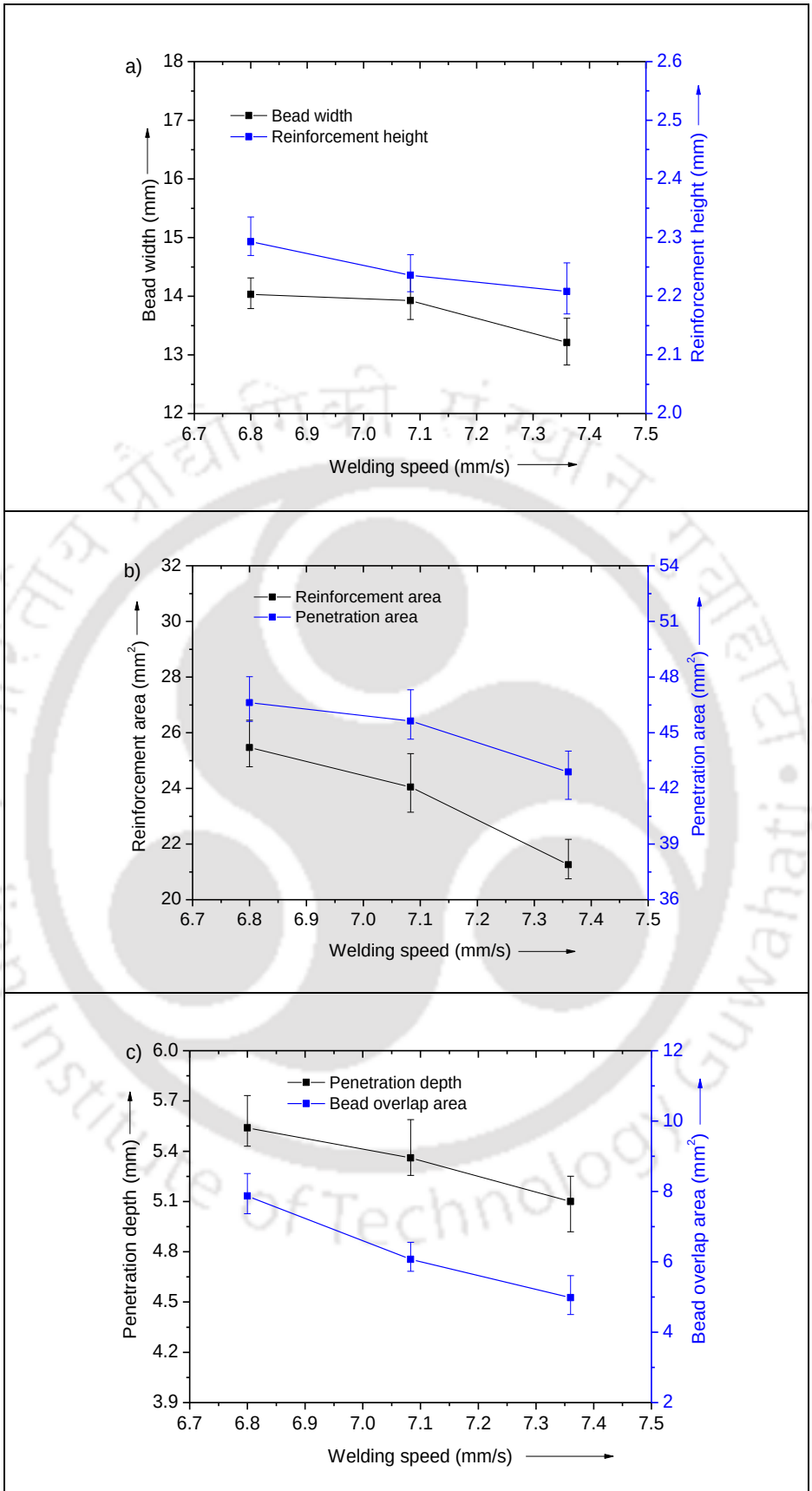

Fig.6.19 Effect of welding speed on (a) Bead width and reinforcement height (b) Reinforcement area and penetration area (c) Penetration depth and Bead overlap area

Table.6.15 Results of effect of process variables on fusion zone profile

Parameter set	B_w (mm)	R_h (mm)	P_d (mm)	R_a (mm^2)	P_a (mm^2)	O_a (mm^2)
Welding current variation						
Exp.1	12.39	2.18	4.88	20.34	40.15	4.74
Exp.2	13.93	2.24	5.36	24.05	45.63	6.07
Exp.3	14.12	2.40	5.72	26.37	48.68	9.88
Welding Voltage variation						
Exp.4	12.23	2.35	5.45	26.12	35.96	4.51
Exp.5	13.93	2.24	5.36	24.05	45.63	6.07
Exp.6	15.62	2.07	5.28	22.86	52.7	9.22
Welding speed variation						
Exp.7	14.03	2.29	5.54	25.46	46.63	7.87
Exp.8	13.93	2.24	5.36	24.05	45.63	6.07
Exp.9	13.21	2.21	5.10	21.25	42.89	4.98

In the parameter set the experiment '2' is included in all the three parameter variations. Hence the results of exp. (2,5,8)* are same.

6.3.5 Effect of process variables on tensile properties

The tensile test was carried out under standard test procedures as described in ASTM E8 standards and was performed at ambient temperature. The average base material (BM) UTS is 714.16 MPa, yield strength (YS) is 302.9 MPa, and elongation is 54.57%. The two samples were taken from a welded sample and average was considered in this study. Fig. 6.20 represents the tensile curve of the base material and Exp.3. The average tensile properties are mentioned in Table 6.16.

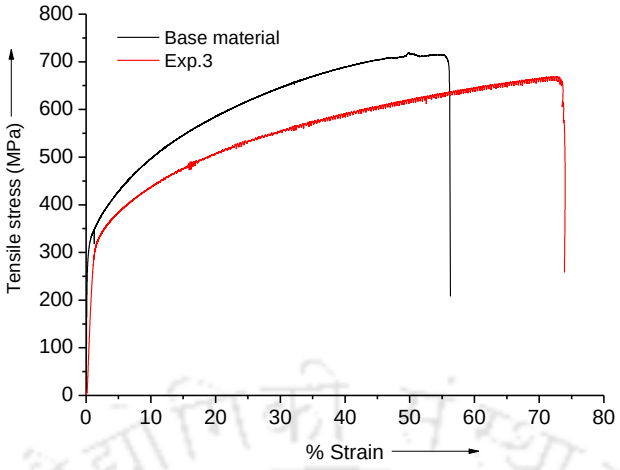

Fig.6.20 Tensile curve of Base metal and Exp.3

Table.6.16 Average tensile properties of double sided welds

Parameter set	Tensile strength (MPa)	% TS of BM	% Elongation
Exp.1	633.90	88.76	70.51
Exp.2	660.32	92.46	76.49
Exp.3	669.13	93.70	74.00
Exp.4	570.44	79.88	65.20
Exp.5	660.32	92.46	76.49
Exp.6	653.42	91.50	81.99
Exp.7	648.25	90.77	81.75
Exp.8	660.32	92.46	76.49
Exp.9	644.22	90.21	78.19

Figs.6.21 (a)-(c) show the influence of individual welding parameters namely current, voltage and welding speed on tensile strength (UTS). The UTS of the welded joint ranges from 570.44 MPa to 669.13 MPa. The percentage tensile strength of samples with that of base material ranges from 79.88 % to 93.70%. The maximum tensile strength of the double sided welded samples is 669.13 MPa which reached up to 93.70% of the base material tensile strength.

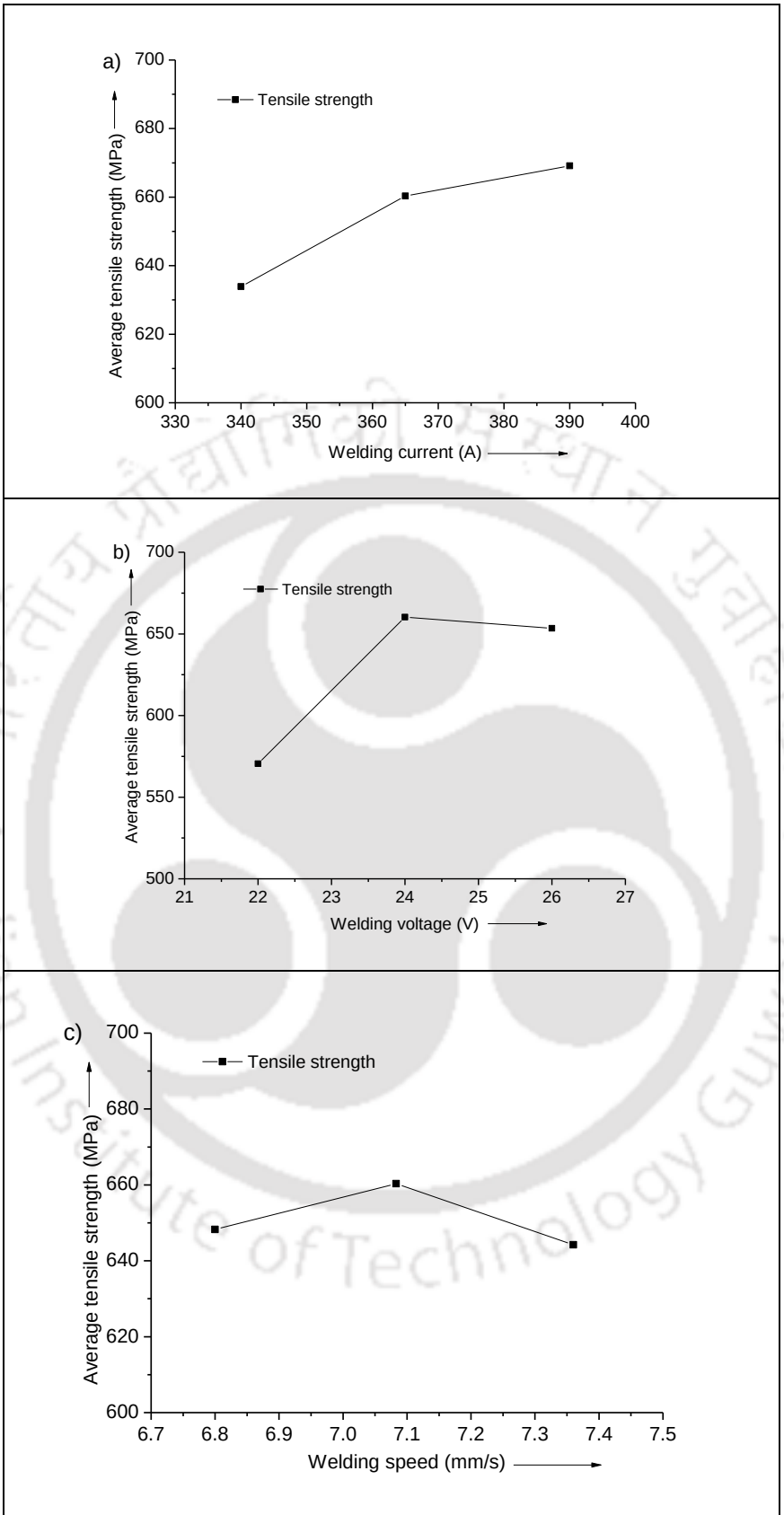

Fig.6.21 Results of uniaxial tensile testing for variation of (a) welding current (b) welding voltage (c) welding speed

It is observed from Fig.6.21 (a) that the tensile strength increases with increase in welding current and attains the peak value. It can be inferred that welding current has profound influence on mechanical properties of a welded joint. Similarly from Fig.6.21 (b), it can be noted that as welding voltage increases, tensile strength initially, after which it is observed that there is a decreasing trend. From Fig.6.21 (c), it can witnessed that as welding speed increases tensile strength is found to be enhanced up to intermediate speed after which it shows a downward trend. Therefore, this downward trend can be articulated that the rate of heat input per unit length is reduced at increased speeds which lead to smaller fusion zone size. The welding speed is important parameter from productivity point of view in a welding process.

Fig.6.22 shows the percentage enhancement in % elongation of double sided welded samples with that of base material.

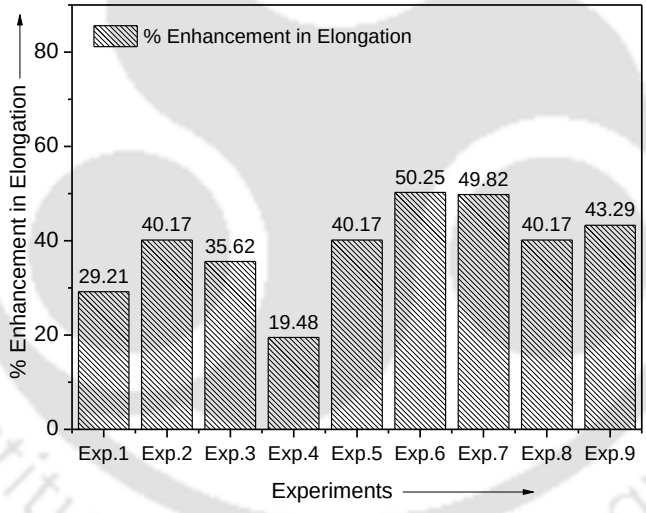

Fig.6.22 Percentage enhancement in elongation with that of base metal

It is observed from Fig.6.22 that a maximum of 50.2% enhancement in elongation with that of base material is obtained for Exp.6 in DSSAW and lowest for Exp.4, i.e., 19.48%. The percentage of elongation of all double-sided welded samples has surpassed the percentage of elongation of the base material. From this result, it can be concluded that double-sided welding has effectively retained its ductility of the weld seam.

6.3.6 Comparison of angular distortion with single sided SAW

The angular distortion in butt welds depends on type of the welding process, heat input, type of material, plate thickness, plate width and joint geometry. In the present investigation angular distortion obtained in the single sided weld was compared with a double sided weld. Fig.6.23 shows the comparison of average angular distortion between single-sided SAW and double-sided SAW.

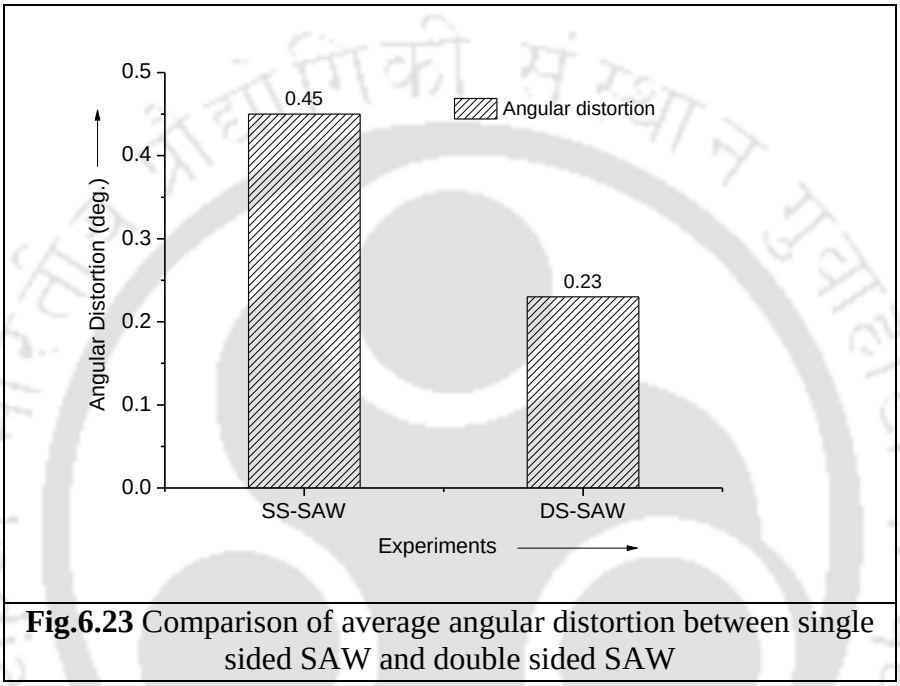

Fig.6.23 Comparison of average angular distortion between single sided SAW and double sided SAW

The average angular distortion of DS-SAW welded sample (Exp.3) is compared with a welding parameter (430 A, 23 V, 5.55 mm/s) of single-sided SAW. It is observed that the angular distortion obtained for DS-SAW (0.23^{o} deg.) which is much lesser than the single-sided SAW (0.450^{o} deg.). As much as 48.88 % reduction in angular distortion with respect of single-sided SAW was obtained. In double-sided submerged arc welding, the initial pass produces the bottom reinforcement. The final angular distortion produced after the 2nd pass will be minimal because the bottom bead reinforcement produced in the 1st pass acts as a constraint for the subsequent pass, Mahapatra et al., (2008). Hence, double-sided SAW can be one of the options to control the angular distortion in medium to thick plates.

6.3.7 Fractrographic examination

For understanding the mode of failure in the tensile specimen, the fracture surface of the tensile specimen is examined under high-resolution FESEM. The failure of the welded joint occurred from the weld region for all the DSSAW samples.

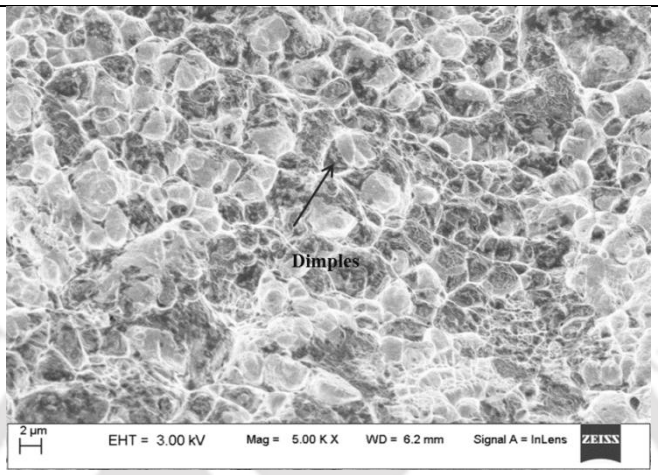

Fig.6.24 Fracture surface of tensile specimen for Exp.4

Fig.6.24 shows the fracture surface of the tensile sample for Exp.4 which have achieved lowest UTS. It is observed that the fracture is ductile in nature, with equiaxed dimples distributed non-homogenously over the fracture surface which indicates that material has sufficiently undergone plastic flow before failure. The fracture surface of the dimple rupture comprises peaks and valleys. The dimple rupture mode fracture is associated with nucleation of voids at the inclusions in the material, Lippold (2015). In general, deeper the dimples better is the ability of the material to undergo plasticity before failure.

6.3.8 Influence of welding current on bead geometry for 12 mm thick plates

In this section the effect of welding current on bead geometry for 12 mm thick austenitic stainless steel plate is presented. The welding current is varied at three levels namely 400 A, 430 A and 460 A, while welding voltage and welding speed were held constant at 27 V and 5.83 mm/s respectively.

Fig.6.25 shows the representative macrostructure of a 12 mm thick double sided weld of the austenitic stainless steel.

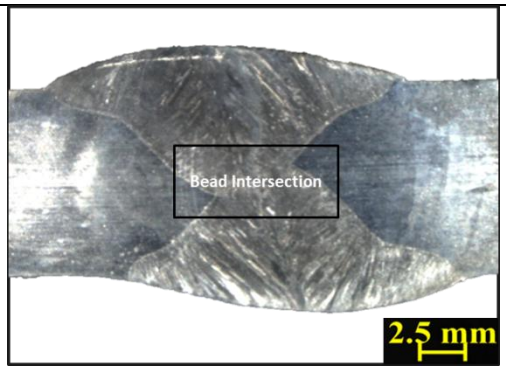

Fig.6.25 Representative cross section of 12 mm thick double sided weld

From Fig.6.25, it is clearly observed that top bead and bottom bead intersect at the middle of the fusion zone to achieve a continuous weld across the cross section. Also it can be seen that grains grow perpendicular from the base metal and these grains extend up to the weld center.

Figs.6.26 (a)-(c) represent the effect of welding current on bead width, reinforcement height, reinforcement area, penetration area, penetration depth, and bead overlap area for a 12 mm thick plate. The influence of welding current on bead profile is shown in Table. 6.17.

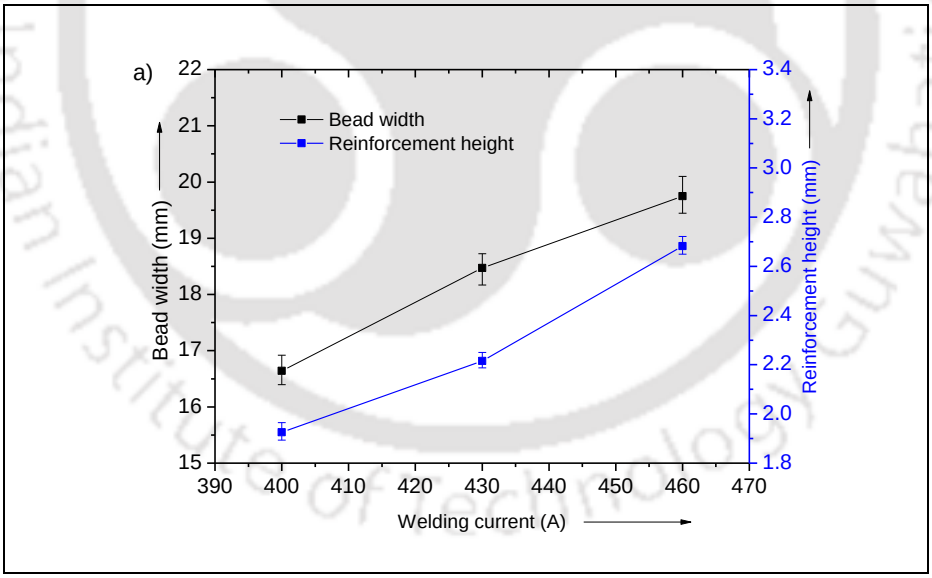

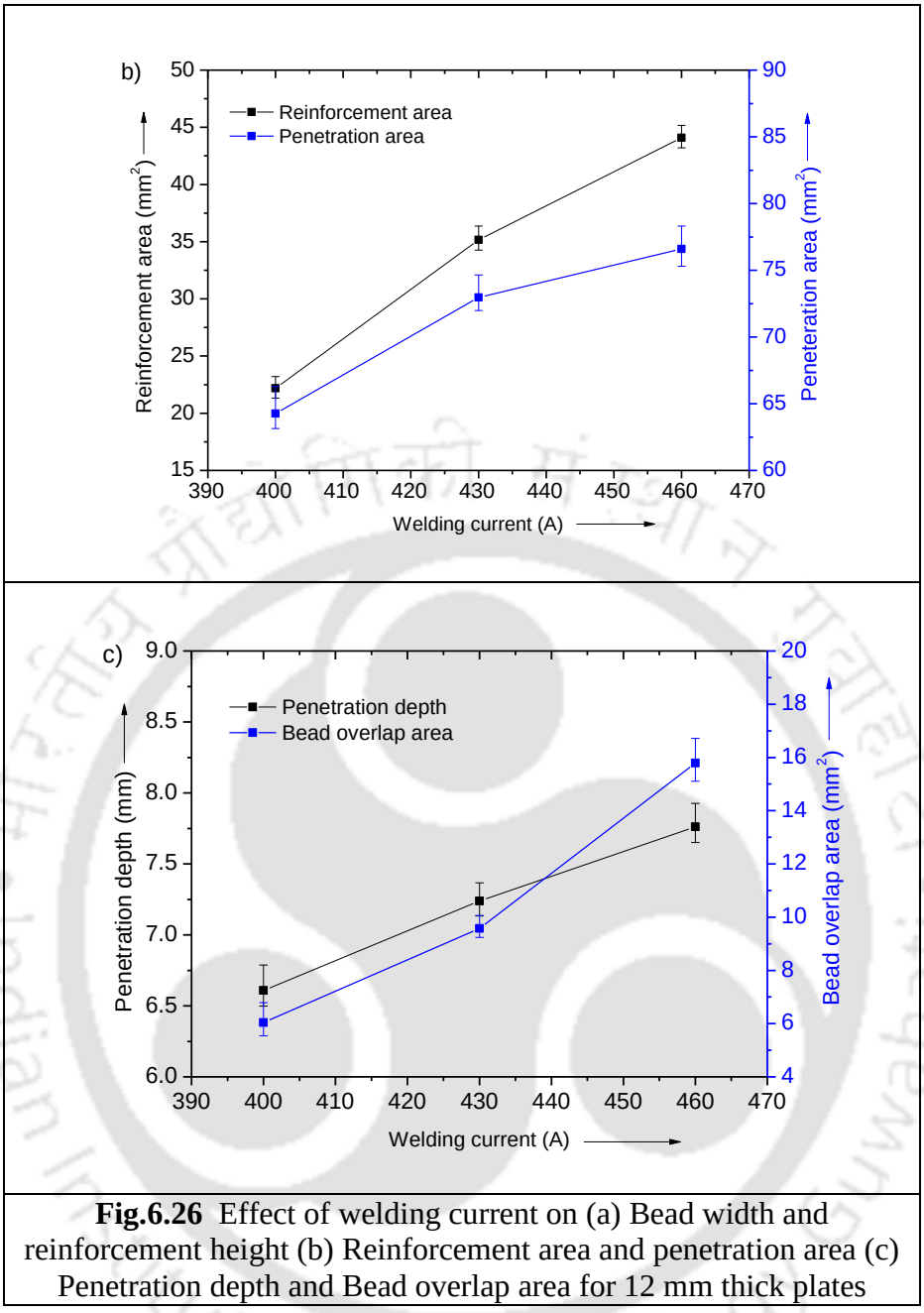

Fig.6.26 Effect of welding current on (a) Bead width and reinforcement height (b) Reinforcement area and penetration area (c) Penetration depth and Bead overlap area for 12 mm thick plates

Table.6.17 Average results of influence of welding current on bead profile for 12 mm thick plate

Parameter set	B_w (mm)	R_h (mm)	P_d (mm)	R_a (mm^2)	P_a (mm^2)	O_a (mm^2)
Exp.1	16.64	1.92	6.60	22.19	64.25	6.04
Exp.2	18.47	2.21	7.23	35.16	72.69	9.57
Exp.3	19.79	2.68	7.76	44.09	76.60	15.78

It can be observed from Figs.6.26 (a) to (c) that the trend of the weld bead parameters for 12 mm thick plates is almost similar to that of 8 mm thick plates except having higher

magnitude. This is due to the fact that weld process variables utilized in this study were different, since higher thick plates were used in this study.

6.3.9 Summary

Double side submerged arc welding (DSSAW) is used to weld plates of different thickness by varying process variables. A square butt joint configuration was used in this investigation. The effect of process parameters on bead geometry of the DSSAW was investigated. The mechanical properties of the joints were evaluated through tensile and Vickers hardness test. The features of microstructure of the weld were discussed. The welding current and voltage has positive influence on the tensile properties, while welding speed shows negative effect. A significant enhancement in ductility was observed for double sided welds as compared with that of base material. The DSSAW specimens indicated ductile fracture which includes dimple cup shaped in one part of the fracture surface and cone shape on the other part of the surface.

6.4 Effect of surface active flux on bead geometry

The addition of surface active flux changes the weld pool geometry and also it can reduce the welding time, and enhance productivity. For this purpose four different types of oxide fluxes namely SiO_2, TiO_2, Cr_2O_3 and the mixture of all were chosen in the present investigation. The weld pool geometry with surface active and without surface active fluxes are compared in the present work. The sample preparation is explained as follows: The surface active flux is mixed with acetone a volatile solvent. This paste was then applied on the surface prior to welding. The volatile solvent gets evaporated and oxide is adhered on to the surface. A very small portion of the flux coating was removed beneath the electrode to facilitate ease of arc starting process. The thickness of applied flux is not of importance. The output parameters considered are weld width, penetration and reinforcement. The bead on plate experiments were performed with and without surface active flux. Fig.6.27 shows the weld bead with and without surface active flux.

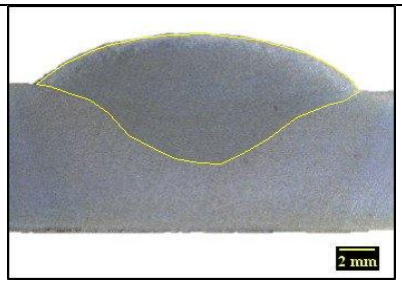

(a)

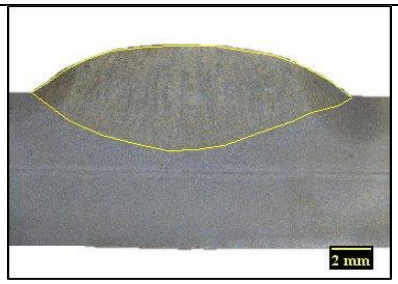

(b)

Fig.6.27 Cross-sectional view of the weld bead (a) with mixture of all fluxes (b) without flux

6.4.1 Influence of surface active flux on bead width

The application of surface active flux causes notable variation in weld bead width. A reduction in the bead width is observed for welds laid on surface active flux as compared without surface active flux. When surface active fluxes such as SiO_2, TiO_2 and Cr_2O_3 were used then the surface tension force dominates at the weld pool center edges and causes shrinkage to bead width. Total of three repetitions were performed for each heat input (HI) and the average values of bead width for welds laid on surface active flux and without surface active flux are tabulated in Table 6.18.

Table 6.18 Average bead width with and without surface active flux

Type of Flux	HI-1 260 A, 28 V, 7.36 (mm/s)	HI-2 280 A, 29 V, 7.36 (mm/s)	HI- 3 300 A, 30 V, 7.36 (mm/s)
	Average bead width (mm)		
SiO_2	14.98	16.23	16.30
Cr_2O_3	13.15	14.23	15.11
TiO_2	16.23	16.68	16.93
(SiO_2+Cr_2O_3+TiO_2)	13.57	15.23	16.48
Without SA elements	15.86	16.52	17.81

Fig.6.28 depicts the bead width for various heat inputs with and without surface active elements. It can be observed that average highest bead width was observed in case of TiO_2, and when Cr_2O_3 was used lowest bead width was noticed.

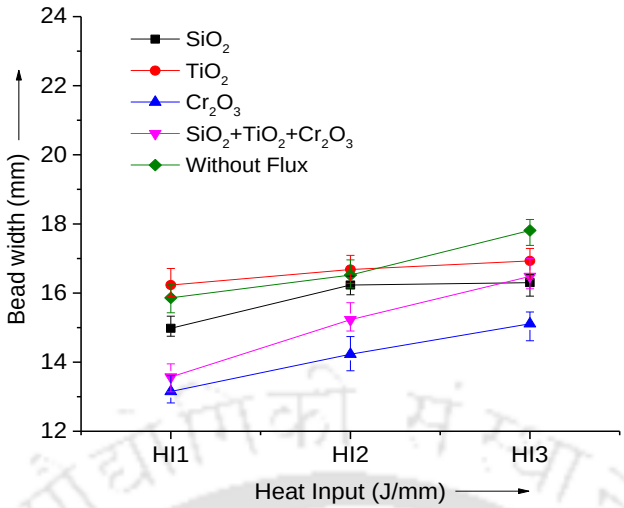

Fig.6.28 Effect of surface active flux on bead width

In arc welding, the molten metal spreads from weld pool center to the edges causing a wider weld pool with low penetration. Application of surface active fluxes alters the molten flow pattern resulting in a narrow and deep weld pool.

6.4.2 Influence of surface active flux on reinforcement

The reinforcement can be defined as the amount of excess molten material deposited on the surface of weld plate after the welding has finished. Table.6.19 represents the average reinforcement height obtained with and without surface active flux for different heat inputs (HI) are shown.

Table 6.19 Average reinforcement height with and without surface active flux

Type of Flux	HI-1 260 A, 28 V, 7.36 (mm/s)	HI-2 280 A, 29 V, 7.36 (mm/s)	HI- 3 300 A, 30 V, 7.36 (mm/s)
	Average reinforcement height (mm)		
SiO_2	2.39	2.41	2.45
Cr_2O_3	2.93	2.81	2.74
TiO_2	2.45	2.24	2.26
(SiO_2+Cr_2O_3+TiO_2)	2.67	2.52	2.50
Without SA elements	2.11	2.13	2.18

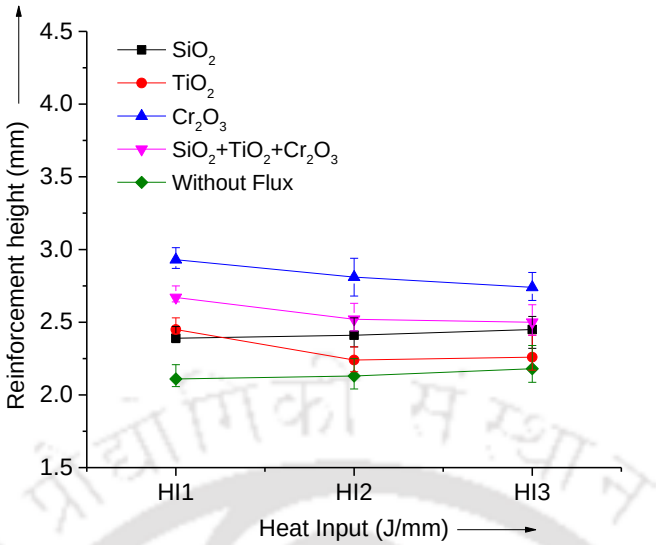

Fig.6.29 Effect of surface active flux on reinforcement height (mm)

Fig.6.29 shows the effect of heat input on reinforcement height for weld with and without application of surface active flux. While keeping welding speed constant and varying current and voltage, it is observed that there is a marginal effect on the reinforcement. The maximum reinforcement height was obtained when Cr_2O_3 is used. The lowest reinforcement height was recorded for welds with TiO_2 as surface active flux. It can be observed that there is a steep decrease in reinforcement height when the mixtures of all fluxes were used.

6.4.3 Influence of surface active flux on penetration

The weld penetration is the depth which stretches out from top surface of the plate to the base of a joint and is estimated on the centreline of root cross sectional area. It is observed that enhanced depth of penetration is obtained with surface active fluxes as compared without flux. The mixture of all three types of fluxes resulted in approximately two times penetration as compared to without flux. A total of three repetitions were performed for each heat input (HI) and average results are shown in Table. 6.20.

Table 6.20 Average depth of penetration with and without surface active flux

Type of Flux	HI-1 260 A, 28 V, 7.36 (mm/s)	HI-2 280 A, 29 V, 7.36 (mm/s)	HI- 3 300 A, 30 V, 7.36 (mm/s)
	Average depth of penetration (mm)		
SiO_2	3.129	3.541	4.023
Cr_2O_3	3.426	3.812	4.253
TiO_2	3.224	3.624	3.932
(SiO_2+Cr_2O_3+TiO_2)	4.332	4.62	5.17
Without SA elements	2.052	2.48	2.65

Fig.6.30 shows the effect of heat input on penetration depth with and without surface active flux.

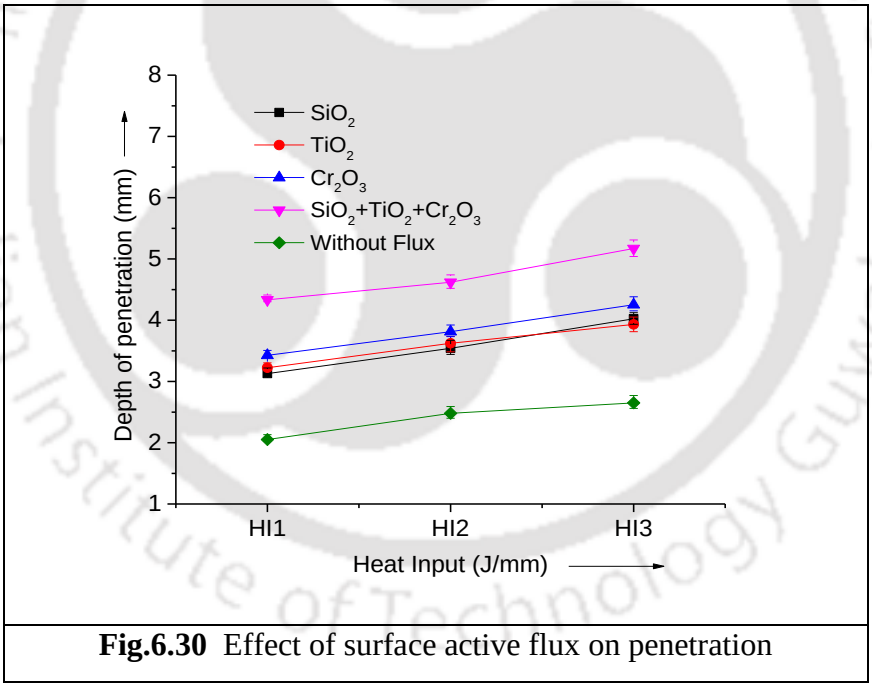

Fig.6.30 Effect of surface active flux on penetration

It is observed from Fig.6.30 that among all the fluxes SiO_2 flux has the lowest influence on penetration depth. Nakhaei et al., (2016) discusses those forces such as Lorenz, Marangoni, buoyancy as well as arc force influence the flow of molten fluid in the weld pool. Marangoni convection which is induced by surface tension gradient plays a significant role in achieving deep penetration, Lu et al., (2002).

6.4.4 Summary

In this section effect of surface active elements on bead geometry is discussed. It can be observed that mixture of all surface active fluxes resulted in better penetration than welds without surface active flux. Almost two times penetration was obtained when mixture of all fluxes were used. Application of TiO_2 resulted in increased bead width while Cr_2O_3 resulted in enhanced penetration.

6.5 Recommendations on selection of welding parameters

In the present investigation stainless steels were welded using automatic submerged arc welding machine. The joint geometry adopted was square butt with a fixed root gap of 2.5 mm for 8 and 12 mm thick plates. SAW process involves number of process variables such as welding current, voltage, speed and length of stickout. The following are guidelines based on the present research work with regard to selection of welding process parameters for welding of stainless steels using submerged arc welding (SAW):

- Welding current is the most important parameter in SAW. It controls the melting rate of the electrode; hence it influences the penetration and deposition rate. For welding of 8 mm thick austenitic stainless steel plates the range of welding current was 410 to 430 A. For double sided welding of 8 mm thick plates the range was 340 to 390 A, while for 12 mm thick plates it is 400 to 460 A. These ranges of welding current were found to be satisfactory for square butt joints.
- Welding voltage directly influences the shape of fusion zone and outer appearance of the weld bead. When welding of 8 mm thick single side square butt joint the range of welding voltage could be 23 to 25 V. For double sided welding of 8 mm thick plates the range was 22 to 26 V, whereas for 12 mm thick plate the voltage was fixed at 27 V. The adopted voltage settings have yielded bead with smooth surface appearance.
- Welding speed is another important variable which dictates the weld zone size and penetration. The welding of 8 mm thick austenitic stainless steels the welding speed can be from 5.55 to 6.66 mm/s. In case of 8 mm thick double sided welds the welding speed of 6.80 to 7.36 mm/s range may be considered, while for 12 mm thick plates, it was fixed at 5.83 mm/s.
- Length of stickout in the present experimentation was fixed at 25 mm. Increase in length of stickout yields higher depositions and increased electrode melting. Hence

for fabrication of butt joints length of stickout as a thumb rule can be up to 7 to 10 times the diameter of the electrode.

- Also welding parameters depends on electrode polarity, electrode size and joint geometry. Hence welding parameters should be carefully set by considering the overall process variables in order achieve good weld qualities.

Chapter 7

Conclusions and Future Scope of the Work

7.0 Conclusions of the present work

Welding is an important joining process used invariably in almost all fields of engineering. Submerged arc welding is a fusion welding process used extensively in fabrication of medium to thick materials due to high thermal efficiency, high joint quality and process can be automated easily. Fabrication of austenitic stainless steel poses challenge due to the low thermal conductivity and high coefficient of thermal expansion. Due to this the structure after welding will be subjected to more distortion, which is a major issue in fabrication. There are several process variables that dictate the weld quality in a SAW process and these can show their influence on the weld quality. Weld distortion is one such quality parameter. By minimization of distortion final quality of the weld can be enhanced. The effect of individual process parameters can be studied by systematically varying the process variables and studying the resultant process output. It is also possible to identify the optimal process variables in a SAW process by use of statistical techniques.

In this research work both numerical and experimental studies were carried out to simulate the temperature distribution using a 3-D volumetric moving heat source. Transient thermal analysis was conducted to study the effect of welding power, speed and plate thickness on peak temperature distribution in a single side single pass SAW process. This was followed by non-linear elasto-plastic thermo-mechanical analysis to study the effect of line energy on residual stresses and distortion. Finally, a numerical simulation was conducted to predict the weld induced distortions in large structures using equivalent loading technique based on average plastic strains.

In the present experimental work, single response and multi-response optimization of SAW process parameters were performed for square butt joints. The output parameter considered in single response optimization was ultimate tensile strength. In addition to this multi response optimization was also carried out on four output parameters such as top weld width, reinforcement, ultimate tensile strength, and angular distortion. This was followed by the detailed investigation of comparative studies on effects of process variables on joint properties which include angular distortion and mechanical properties for conventional single

side butt and heat sink welding. The heat sink welding was performed with the objective of reducing the distortion and improving the joint quality. A new fixture setup was specially designed and fabricated to achieve this purpose. Also a detailed investigation of double side SAW process was carried out for two different plate thicknesses. Furthermore the effect of surface active elements on bead geometry was explored.

The conclusions that can be drawn from the numerical analysis and experimental investigation of the present study are presented as follows:

❖ **Numerical analysis**

- The 3-D transient thermal analysis model was developed for a SAW process of AISI 304 austenitic stainless steel using a volumetric moving heat source. The deviations of peak temperature between numerical analysis and experiments were observed to be about 4.57%. This was ascribed due to the incorporation of actual weld bead geometry in transient thermal analysis.
- The peak temperatures perpendicular to weld line increase with increase in power for both top and bottom side of the plate. An increment of 6.4% in peak temperature on top side of the plate was obtained when welding power was enhanced by 8% (9890 W to 10750 W).
- The welding power as well as traverse speed is important parameters in a SAW process and need to be properly controlled in order to achieve desired weld quality and without compromising on productivity.
- With increase in traverse speed the peak temperatures reduces on top and bottom side of the plate. When traverse speed was reduced by 8.25 % (6.66 mm/s to 6.11 mm/s) there was an enhancement in peak temperature by 3.98 %. This enhancement in peak temperatures can be attributed to increase in heat input to fuse the weld joints.
- The effect of plate thickness on thermal history was studied. With increase in plate thickness the peak temperature was found to reduce transverse to weld line. The reduction of peak temperature of 14 and 19.9 % were attained when plate thicknesses were increased from 8 to 10 mm and 10 to 12 mm respectively. The reduction in peak temperatures with increase in plate thickness can be attributed to higher rate of heat dissipation in case of thicker plates.

- As line energy was increased the longitudinal, transverse and von-Mises residual stresses were found to increase, since there was an increment in heat input per unit length of weld.
- The observed maximum deviation between measured and predicted distortion was 9.82%. It can be inferred that adopted 3D transient elasto-plastic thermo-mechanical model have yielded fairly accurate results in prediction of distortion in stainless steel plates.
- An improved equivalent load method based on average plastic strains was developed to predict the weld induced distortion in large structures. The proposed method was found to be computationally more efficient as compared with that of conventional thermo-mechanical elastic-plastic (TMEP) method.

❖ **Experimental Investigation**

- Taguchi optimization technique was utilized to get optimal parameters for single response optimization and it was found that welding current have contributed 30.27 % to the weld quality.
- Multi-response optimization was conducted using Grey-Taguchi's method and it was found that welding voltage (V) have contributed 31.12 %, and interaction V×I contributed to 26.75%.
- From the optimization study it was found that length of stickout contributes marginally to the weld quality. This may be due to the fact that length of stickout doesn't influence the heat input.
- The comparative study on conventional welding and heat sink welding was performed on AISI 304 austenitic stainless steel. A reduction in fusion zone cross sectional area of about 11.58 % was obtained with same operating parameters for heat sink welding. Hence, this reduction in cross sectional area was attributed due to cooling caused by heat sink.
- As compared with conventional welds, the heat sink assisted welds resulted in enhancement in ultimate tensile strength (UTS) of about 25.82 % and yield strength of about 15 %. A maximum of 10.66 % reduction in angular distortion was observed for heat sink welds to that of conventional welds. The enhancement in mechanical

properties and reduction in angular distortion was attributed to effective removal of heat from the weld zone by the heat sink.

- Double side submerged arc welding (DSSAW) was successfully performed on AISI 304 austenitic stainless steel with square butt geometry. The tensile strength of DSSAW process sample achieved about 93.70 % of the base material. A maximum of 50.2 % elongation with that of the base material was obtained for double sided welds. It can be inferred from the study that double sided welds have retained the ductility of the welds.
- The failure of tensile specimens of DSSAW was ductile in nature, with equiaxed dimples distributed non-homogenously over the entire fracture surface. The fracture surface of the dimple rupture comprises peaks and valleys. It can be established that material have undergone sufficient plastic deformation before its failure and double sided welding have not diminished the weld seam quality.
- A significant reduction of 48.8 % of angular distortion was obtained for double sided weld as with that of single side weld. The reduction in the distortion may be due to more uniform shrinkage forces acts on top and bottom side as a result of double sided welding.
- Use of surface active element i.e. TiO_2 contributes to the enhancement of bead width while Cr_2O_3 resulted in increased penetration. Mixture of all three surface active fluxes yielded better penetration as compared to that of individual surface active fluxes.
- A proper choice of surface active flux can enhance the weld penetration by almost twice for the same set of welding parameters with that of without surface active flux.

7.1 Future Scope of the work

The scope of the future research is proposed based on the current work:

- Fatigue and creep studies on submerged arc welded joints.
- Development of a numerical model for multi passes welding of SAW process.
- Effect of welding sequences on residual stresses and distortion in a SAW process.
- Hot corrosion studies on submerged arc welded joints.

References

Adak, M., Mandal, N.R., 2010. Numerical and experimental study of mitigation of welding distortion. Appl. Math. Model. 34, 146–158.

Alali, M., Todd, I., Wynne, B.P., 2017. Through-thickness microstructure and mechanical properties of electron beam welded 20 mm thick AISI 316L austenitic stainless steel. Mater. Des. 130, 488–500.

Amanie, J., Oguocha, I.N.A., Yannacopoulos, S., 2012. Effect of submerged arc welding parameters on microstructure of SA516 steel weld metal. Can. Metall. Q. 51, 48–57.

Andersson, B.A.B., 1978. Thermal Stresses in a Submerged-Arc Welded Joint Considering Phase Transformations. J. Eng. Mater. Technol. Trans. ASME 100, 356–362.

Ansaripour, N., Heidari, A., Eftekhari, S.A., 2019. Multi-objective optimization of residual stresses and distortion in submerged arc welding process using Genetic Algorithm and Harmony Search. Proc. Inst. Mech. Eng. Part C J. Mech. Eng. Sci. 0, 095440621988597.

Awang, M., 2002. The effects of process parameters on steel welding response in curved plates. West Virginia Uniersity, West Virgina, USA.

Bang, K.S., Park, C., Jung, H.C., Lee, J.B., 2009. Effects of flux composition on the element transfer and mechanical properties of weld metal in submerged arc welding. Met. Mater. Int. 15, 471–477.

Bhide, S.R., Michaleris, P., Posada, M., Deloach, J., 2006. Comparison of buckling distortion propensity for SAW, GMAW, and FSW. Weld. J. 85, 189–195.

Biswas, P., Mahapatra, M.M., Mandal, N.R., 2010. Numerical and experimental study on prediction of thermal history and residual deformation of double-sided fillet welding. Proc. Inst. Mech. Eng. Part B J. Eng. Manuf. 224, 125–134.

Biswas, P., Mandal, N.R., 2010. Thermomechanical finite element analysis and experimental investigation of single-pass single-sided submerged arc welding of C-Mn steel plates. Proc. Inst. Mech. Eng. Part B J. Eng. Manuf. 224, 627–639.

Biswas, P., Mandal, N.R., Das, S., 2011. Prediction of welding deformations of large stiffened panels using average plastic strain method. Sci. Technol. Weld. Join. 16, 227–231.

Canonsburg, T.D., 2013. ANSYS Mechanical APDL Coupled-Field Analysis Guide.

Chandel, R.S., 1998. The Effect of Process Variables on the Flux Consumption in Submerged Arc Welding. Mater. Manuf. Process. 13, 181–188.

Chandel, R.S., 1987. Mathematical Modeling of Melting Rates for Submerged Arc Welding. Weld. Res. Suppplement 135s-140s.

Chandel, R.S., Seow, H.P., Cheong, F.L., 1998. Effect of metal powder addition on mechanical properties of submerged arc welds. J. Mater. Sci. Lett. 17, 1785–1786.

Chandel, R.S., Seow, H.P., Cheong, F.L., 1997. Effect of increasing deposition rate on the bead geometry of submerged arc welds. J. Mater. Process. Technol. 72, 124–128.

Chi, K., Maclean, M.S., McPherson, N.A., Baker, T.N., 2007. Single sided single pass submerged arc welding of austenitic stainless steel. Mater. Sci. Technol. 23, 1039–1048.

Cho, D.W., Kiran, D.V., Song, W.H., Na, S.J., 2014. Molten pool behavior in the tandem submerged arc welding process. J. Mater. Process. Technol. 214, 2233–2247.

Colegrove, P., Ikeagu, C., Thistlethwaite, A., Williams, S., Nagy, T., Suder, W., Steuwer, A., Pirling, T., 2009. Welding process impact on residual stress and distortion. Sci. Technol. Weld. Join. 14, 717–725.

Coules, H.E., 2013. Contemporary approaches to reducing weld induced residual stress. Mater. Sci. Technol. (United Kingdom) 29, 4–18.

Culha, O., 2014. Finite element modelling of submerged arc welding process for a symmetric T-beam. Mater. Tehnol. 48, 243–248.

Datta, S., Bandyopadhyay, A., Kumar Pal, P., 2008a. Modeling and optimization of features of bead geometry including percentage dilution in submerged arc welding using mixture of fresh flux and fused slag. Int. J. Adv. Manuf. Technol. 36, 1080–1090.

Datta, S., Bandyopadhyay, A., Pal, P.K., 2008b. Solving multi-criteria optimization problem in submerged arc welding consuming a mixture of fresh flux and fused slag. Int. J. Adv. Manuf. Technol. 35, 935–942.

Datta, S., Bandyopadhyay, A., Pal, P.K., 2008c. Application of Taguchi philosophy for parametric optimization of bead geometry and HAZ width in submerged arc welding using a mixture of fresh flux and fused flux. Int. J. Adv. Manuf. Technol. 36, 689–698.

Datta, S., Bandyopadhyay, A., Pal, P.K., 2008d. Grey-based taguchi method for optimization of bead geometry in submerged arc bead-on-plate welding. Int. J. Adv. Manuf. Technol. 39, 1136–1143.

Davis, J.R., 1994. ASM Speciality Hand book : Stainless Steels. ASM International, Metals Park, Ohio, USA.

Davis, O.L., 1978. Design and analysis of industrial experiments. Orient Longman, New York.

De Brito, V.L.O., Voorwald, H.J.C., Das Neves, N., De, I., 2001. Effects of a postweld heat treatment on a submerged arc welded ASTM A537 pressure vessel steel. J. Mater. Eng. Perform. 10, 249–257.

Debroy, T., David, S.A., 1995. Physical processes in fusion welding. Rev. Mod. Phys. 67, 85–112.

Deng, D., Murakawa, H., 2006. Numerical simulation of temperature field and residual stress in multi-pass welds in stainless steel pipe and comparison with experimental measurements. Comput. Mater. Sci. 37, 269–277.

Dhas, J.E.R., Kumanan, S., 2011. Optimization of parameters of submerged arc weld using non conventional techniques. Appl. Soft Comput. J. 11, 5198–5204.

Easterling, K., 1992. Introduction to Physical Metallurgy of Welding, 2nd ed. Butterworth Heinemann Ltd, Oxford.

Fanous, I.F.Z., Younan, M.Y.A., Wifi, A.S., 2003. 3-D finite element modeling of the welding process using element birth and element movement techniques. J. Press. Vessel Technol. Trans. ASME 125, 144–150.

Feng, Z., 2005. Processes and mechanisms of welding residual stress and distortion. WoodHead Publishing Ltd., Cambridge, England.

Fletcher, L., Zhu, Z., Marimuthu, M., Zheng, L., Bai, M., Li, H., Barbaro, F., 2011. Effect of Ti and N concentrations on microstructure and mechanical properties of microalloyed high strength line pipe steel welds. Univ. Wollongong Res. Online 1–13.

Forouzan, M.R., Mirfalah Nasiri, S.M., Mokhtari, A., Heidari, A., Golestaneh, S.J., 2012. Residual stress prediction in submerged arc welded spiral pipes. Mater. Des. 33, 384–394.

Ghosh, A., Chattopadhyaya, S., Das, R.K., Sarkar, P.K., 2011a. Prediction of submerged arc welding yield parameters through graphical technique. Procedia Eng. 10, 2797–2802.

Ghosh, A., Chattopadhyaya, S., Das, R.K., Sarkar, P.K., 2011b. Assessment of heat affected zone of submerged Arc welding process through digital image processing. Procedia Eng. 10, 2782–2785.

Ghosh, A., Chattopadhyaya, S., Sarkar, P.K., 2011c. Critical analysis of confounded parameters of SAW process. Procedia Eng. 10, 2786–2790.

Gowrisankar, I., Bhaduri, A.K., Seetharaman, V., Verma, D.D.N., Achar, D.R.G., 1987. Effect of the Number of Passes on the Structure and Properties of Submerged Arc Welds of AISI Type 316L Stainless Steel. Weld. J. 147–154.

Gunaraj, V., Murugan, N., 2000. Prediction and Optimization of Weld Bead Volume for the Submerged Arc Process — Part 1. Weld. Res. Suppl. 331–338.

Gunaraj, V., Murugan, N., 1999a. Application of response surface methodology for predicting weld bead quality in submerged arc welding of pipes. J. Mater. Process. Technol. 88, 266–275.

Gunaraj, V., Murugan, N., 1999b. Prediction and comparison of the area of the heat-affected zone for the bead-on-plate and bead-on-joint in submerged arc welding of pipes. J. Mater. Process. Technol. 95, 246–261.

Hayajneh, M.T., Al-Dwairi, A.F., Obeidat, S.F., 2018. Optimization and control of bending distortion of submerged arc welding I-beams. J. Constr. Steel Res. 142, 78–85.

Houldcroft, P.T., 1989. Submerged Arc Welding, 2nd ed. WoodHead Publishing Ltd., Cambridge, UK.

Jang, A.Y., Lee, D.J., Lee, S.H., Shim, J.H., Kang, S.W., Lee, H.W., 2011. Effect of Cr/Ni equivalent ratio on ductility-dip cracking in AISI 316L weld metals. Mater. Des. 32, 371–376.

Jiang, W., Zhang, Y., Woo, W., 2012. Using heat sink technology to decrease residual stress in 316L stainless steel welding joint: Finite element simulation. Int. J. Press. Vessel. Pip. 92, 56–62.

Kanjilal, P., Pal, T.K., Majumdar, S.K., 2007. Prediction of mechanical properties in submerged arc weld metal of C-Mn steel. Mater. Manuf. Process. 22, 114–127.

Kanjilal, P., Pal, T.K., Majumdar, S.K., 2006. Combined effect of flux and welding parameters on chemical composition and mechanical properties of submerged arc weld metal. J. Mater. Process. Technol. 171, 223–231.

Karaoğlu, S., Seçgin, A., 2008. Sensitivity analysis of submerged arc welding process parameters. J. Mater. Process. Technol. 202, 500–507.

Kasman, Ş., 2013. Multi-response optimization using the Taguchi-based grey relational analysis: A case study for dissimilar friction stir butt welding of AA6082-T6/AA5754-H111. Int. J. Adv. Manuf. Technol. 68, 795–804.

Khallaf, M.E., Ibrahim, M.A., El-Mahallawy, N.A., Taha, M.A., 1997. On crack susceptibility in the submerged arc welding of medium-carbon steel plates. J. Mater. Process. Technol. 68, 43–49.

Kiran, D. V., Basu, B., De, A., 2012. Influence of process variables on weld bead quality in two wire tandem submerged arc welding of HSLA steel. J. Mater. Process. Technol. 212, 2041–2050.

Kohnke, P., 2009. Theory Reference for the Mechanical APDL and Mechanical Applications. Canonsburg.PA.

Koilraj, M., Sundareswaran, V., Vijayan, S., Koteswara Rao, S.R., 2012. Friction stir welding of dissimilar aluminum alloys AA2219 to AA5083 - Optimization of process parameters using Taguchi technique. Mater. Des. 42, 1–7.

Kolhe, K.P., Datta, C.K., 2008. Prediction of microstructure and mechanical properties of multipass SAW. J. Mater. Process. Technol. 197, 241–249.

Kou, S., 2003. Welding Metallurgy, 2nd ed. Wiley-Interscience, New Jersey, USA.

Kumar, P., Batish, A., Bhattacharya, A., Duvedi, R.K., 2011. Effect of process parameters on microhardness and microstructure of heat affected zone in submerged arc welding. Proc.

Inst. Mech. Eng. Part B J. Eng. Manuf. 225, 711–721.

Kumar, S., Shahi, A.S., 2014. On the influence of welding stainless steel on microstructural development and mechanical performance. Mater. Manuf. Process. 29, 894–902.

Lampman, S., 1997. Weld Integrity and Performance, Ist. ed. ASM International, Materials Park, Ohio, USA.

Lan, L., Qiu, C., Zhao, D., Gao, X., Du, L., 2012. Analysis of microstructural variation and mechanical behaviors in submerged arc welded joint of high strength low carbon bainitic steel. Mater. Sci. Eng. A 558, 592–601.

Lee, C.S., Chandel, R.S., Seow, H.P., 2000. Effect of welding parameters on the size of heat affected zone of submerged arc welding. Mater. Manuf. Process. 15, 649–666.

Lim, Y.-S., Kim, S.-H., Lee, K.-J., 2018. Effect of residual stress on the mechanical properties of fsw joints with sus409l. Adv. Mater. Sci. Eng. 2018.

Lin, C.L., 2004. Use of the Taguchi method and grey relational analysis to optimize turning operations with multiple performance characteristics. Mater. Manuf. Process. 19, 209–220.

Lindgren, L.E., 2007. Computational welding mechanics, 2nd ed. Woodhead Publishing in Materials.

Lippold, J.C., 2015. Welding Metallurgy and Weldability, Ist. ed. John Wiley & Sons, Inc.

Lippold, J.C., Kotecki, D.J., 2005. Welding Metallurgy and Weldability of Stainless Steels. Wiley-Interscience.

Lu, S., Fujii, H., Sugiyama, H., Tanaka, M., Nogi, K., 2002. Weld penetration and Marangoni convection with oxide fluxes in GTA welding. Mater. Trans. 43, 2926–2931.

Luo, J., Yuan, Y., Wang, X., Yao, Z., 2013. Double-sided single-pass submerged arc welding for 2205 duplex stainless steel. J. Mater. Eng. Perform. 22, 2477–2486.

Mahapatra, M.M., Datta, G.L., Pradhan, B., Mandal, N.R., 2008. Modelling of angular distortion of double-pass butt-welded plate. Proc. Inst. Mech. Eng. Part B J. Eng. Manuf. 222, 391–401.

Mahapatra, M.M., Datta, G.L., Pradhan, B., Mandal, N.R., 2007. Modelling the effects of constraints and single axis welding process parameters on angular distortions in one-sided fillet welds. Proc. Inst. Mech. Eng. Part B J. Eng. Manuf. 221, 397–407.

Mahapatra, M.M., Datta, G.L., Pradhan, B., Mandal, N.R., 2006. Three-dimensional finite element analysis to predict the effects of SAW process parameters on temperature distribution and angular distortions in single-pass butt joints with top and bottom reinforcements. Int. J. Press. Vessel. Pip. 83, 721–729.

McPherson, N.A., Chi, K., Baker, T.N., 2003. Submerged arc welding of stainless steel and

the challenge from the laser welding process. J. Mater. Process. Technol. 134, 174–179.

Mandal, N.R., 2017. Ship Construction and Welding.1st ed. Springer Nature Pte Ltd, Singapore.

Mandal, N.R., 2004. Welding and Distortion Control, 1st ed. Narosa Publishing House Pvt. Ltd., New Delhi.

Mandal, N.R., 2009. Welding Techniques, Distortion Control and Line Heating, Ist. ed. Alpha Science International Ltd, New Delhi.

Masubuchi, K., 1980. Analysis of welded structures, 1st ed. Pergamon Press, London.

Meena, V.K., Azad, M.S., 2012. Grey relational analysis of micro-EDM machining of Ti-6Al-4V alloy. Mater. Manuf. Process. 27, 973–977.

Michaleris, P., 2011. Introduction to welding residual stress and distortion, Woodhead publishing Ltd. Woodhead Publishing Limited.

Michler, T., 2015. Austenitic Stainless Steels, in: Reference Module in Materials Science and Materials Engineering. pp. 1–6.

Mirshekari, G.R., Tavakoli, E., Atapour, M., Sadeghian, B., 2014. Microstructure and corrosion behavior of multipass gas tungsten arc welded 304L stainless steel. Mater. Des. 55, 905–911.

Mochizuki, M., Mikami, Y., Yamasaki, H., Toyoda, M., 2007. Elastic predicting method of weld distortion of large structures using numerical simulation results by thermal-elastic-plastic analysis of small components. Weld. World 51, 60–64.

Moeinifar, S., Kokabi, A.H., Hosseini, H.R.M., 2011. Role of tandem submerged arc welding thermal cycles on properties of the heat affected zone in X80 microalloyed pipe line steel. J. Mater. Process. Technol. 211, 368–375.

Mondal, A.K., Biswas, P., Bag, S., 2017. Experimental and FE analysis of submerged arc weld induced residual stress and angular deformation of single and double sided fillet welded joint. Int. J. Steel Struct. 17, 9–18.

Murugan, N., Gunaraj, V., 2005. Prediction and control of weld bead geometry and shape relationships in submerged arc welding of pipes. J. Mater. Process. Technol. 168, 478–487.

Murugan, N., Parmar, R.S., 1997. Effect of Welding Conditions on Microstructure and Properties of Type 31 6L Stainless Steel Submerged Arc Cladding. Weld. Res. Suppplement 210s-220s.

Muthuramalingam, T., Mohan, B., 2013. Taguchi-grey relational based multi response optimization of electrical process parameters in electrical discharge machining. Indian J. Eng. Mater. Sci. 20, 471–475.

Nagalakshmi, R., Rathinam, A., Manimozhi, S., Suresh, S., Jegan, N., 2010. Fracture toughness of modified P91 weldments. Trans. Indian Inst. Met. 63, 587–594.

Nakhaei, R., Khodabandeh, A., Najafi, H., 2016. Effect of active gas on weld shape and microstructure of advanced A-TIG-welded stainless steel. Acta Metall. Sin. (English Lett. 29, 295–300.

Nart, E., Celik, Y., 2013. A practical approach for simulating submerged arc welding process using FE method. J. Constr. Steel Res. 84, 62–71.

Nezamdost, M.R., Esfahani, M.R.N., Hashemi, S.H., Mirbozorgi, S.A., 2016. Investigation of temperature and residual stresses field of submerged arc welding by finite element method and experiments. Int. J. Adv. Manuf. Technol. 87, 615–624.

Niagaj, J., 2014. Ways to improve the efficiency of welding stainless steel. Weld. Int. 28, 45–53.

Nowacki, J., Rybicki, P., 2005. The influence of welding heat input on submerged arc welded duplex steel joints imperfections. J. Mater. Process. Technol. 164–165, 1082–1088.

Om, H., Pandey, S., 2013. Effect of heat input on dilution and heat affected zone. Sadhana - Indian Acad. Sci. 38, Part 6, 1369–1391.

Om, H., Pandey, S., Rathod, D., 2012. Mathematical Modeling of Haz in Submerged Arc Welding Process Using Factorial Design Technique. Proc. Natl. Conf. Trends Adv. Mech. Eng. 616–626.

Pandey, C., Giri, A., Mahapatra, M.M., 2016. On the prediction of effect of direction of welding on bead geometry and residual deformation of double-sided fillet welds. Int. J. Steel Struct. 16, 333–345.

Paniagua-Mercado, A.M., López-Hirata, V.M., Méndez-Sánchez, A.F., Saucedo-Munoz, M.L., 2007. Effect of active and nonactive fluxes on the mechanical properties and microstructure in submerged-arc welds of A-36 steel plates. Mater. Manuf. Process. 22, 295–297.

Parmar, R.S., 2001. Welding Processess and Technology, IInd. ed. khanna Publishers, Delhi.

Piatti, G., Vedani, M., 1990. Relation between tensile properties and microstructure in type 316 stainless steel SA weld metal. J. Mater. Sci. 25, 4285–4297.

Piatti, G., Vedani, M., 1989. Material variability in composition and structure of a Type 316 stainless steel submerged arc weld metal. J. Mater. Sci. 24, 1429–1438.

Podder, D., Mandal, N.R., Das, S., 2014. Heat source modeling and analysis of submerged arc welding. Weld. J. 93, 183–192.

Prasad, K., Dwivedi, D.K., 2008. Microstructure and Tensile Properties of Submerged Arc Welded 1.25Cr-0.5Mo Steel Joints. Mater. Manuf. Process. 23, 463–468.

Radraj, D., 2003. Welding Residual Stresses and Distortion Calculation and Measurement. DVS,Verlag.

Rajani, H.R.Z., Torkamani, H., Sharbati, M., Raygan, S., 2012. Corrosion resistance improvement in Gas Tungsten Arc Welded 316L stainless steel joints through controlled preheat treatment. J. Mater. Des. 34, 51–57.

Ramakrishnan, M., Muthupandi, V., 2013. Application of submerged arc welding technology with cold wire addition for drum shell long seam butt welds of pressure vessel components. Int. J. Adv. Manuf. Technol. 65, 945–956.

Ramakrishnan, M., Padmanaban, K., Muthupandi, V., 2013. Studies on fracture toughness of cold wire addition in narrow groove submerged arc welding process. Int. J. Adv. Manuf. Technol. 68, 293–316.

Rao, R.V., Kalyankar, V.D., 2013. Experimental investigation on submerged arc welding of Cr-Mo-V steel. Int. J. Adv. Manuf. Technol. 69, 93–106.

Rao, S.S., 2011. The Finite Element Method in Engineering, 5th ed. Butterworth-Heinemann.

Renwick, B.G., Patchett, B.M., 1976. Operating Characteristics of the Submerged Arc Process. Weld. Res. Suppl. 55, 69s-76s.

Robinson, M.H., 1961. Observations on electrode melting rates during submerged arc welding. Weld. J. 40, 503s-515s.

Roy, R.K., 2010. A Primer on the Taguchi Method, Second Edition.

Sarkar, A., Roy, J., Majumder, A., Saha, S.C., 2014. Optimization of Welding Parameters of Submerged Arc Welding Using Analytic Hierarchy Process (AHP) Based on Taguchi Technique. J. Inst. Eng. Ser. C 95, 159–168.

Shen, S., Oguocha, I.N.A., Yannacopoulos, S., 2012. Effect of heat input on weld bead geometry of submerged arc welded ASTM A709 Grade 50 steel joints. J. Mater. Process. Technol. 212, 286–294.

Singh, K., Pandey, S., 2009. Recycling of slag to act as a flux in submerged arc welding. Resour. Conserv. Recycl. 53, 552–558.

Singh, R.P., Garg, R.K., Shukla, D.K., 2016. Mathematical modeling of effect of polarity on weld bead geometry in submerged arc welding. J. Manuf. Process. 21, 14–22.

Smith, J.J., Farrar, R.A., 1993. Influence of microstructure and composition on mechanical properties of some AISI 300 series weld metals. Int. Mater. Rev. 38, 25–51.

Srinivasan, P.B., Sharkawy, S.W., Dietzel, W., 2004. Environmental Cracking Behavior of Submerged Arc-Welded Supermartensitic Stainless Steel Weldments. J. Mater. Eng. Perform. 13, 232–236.

Taban, E., Deleu, E., Dhooge, A., Kaluc, E., 2008. Submerged arc welding of thick ferritic

martensitic 12Cr stainless steel with a variety of consumables. Sci. Technol. Weld. Join. 13, 327–334.

Taguchi, G., Chowdhury, S., Wu, Y., 2007. Taguchi's Quality Engineering Handbook, Taguchi's Quality Engineering Handbook.

Tai-Ran, H., 1986. The Finite Element Method in Thermomechanics. Allen & Unwin.

Tarng, Y.S., Juang, S.C., Chang, C.H., 2002. The use of grey-based Taguchi methods to determine submerged arc welding process parameters in hardfacing. J. Mater. Process. Technol. 128, 1–6.

Tarng, Y.S., Yang, W.H., 1998. Application of the Taguchi method to the optimization of the submerged arc welding process. Mater. Manuf. Process. 13, 455–467.

Toma, R.E., Brandi, S.D., Souza, A.C., Moris, Z., 2011. Comparison between DC (+) and Square Wave AC SAW Current Outputs to Weld AISI 304 for Low-Temperature Applications. Weld. J. 90, 153s-160s.

Tsai, H.L., Tarng, Y.S., Tseng, C.M., 1996. Optimisation of Submerged Arc Welding Process Parameters in Hardfacing. Int. J. Adv. Manuf. Technol. 12, 402–406.

Ueda, Y., Murakawa, H., Ma, N., 2012. Welding Deformation and Residual Stress Prevention. Elsevier B.H, MA. USA.

Unnikrishnan, R., Idury, K.S.N.S., Ismail, T.P., Bhadauria, A., Shekhawat, S.K., Khatirkar, R.K., Sapate, S.G., 2014. Effect of heat input on the microstructure, residual stresses and corrosion resistance of 304L austenitic stainless steel weldments. Mater. Charact. 93, 10–23.

Wen, S.W., Hilton, P., Farrugia, D.C.J., 2001. Finite element modelling of a submerged arc welding process. J. Mater. Process. Technol. 119, 203–209.

Withers, P.J., Bhadeshia, H.K.D.H., 2001. Residual stress part 1 - Measurement techniques. Mater. Sci. Technol. 17, 355–365.

Xu, J., Chen, Jingyao, Duan, Y., Yu, C., Chen, Junmei, Lu, H., 2017. Comparison of residual stress induced by TIG and LBW in girth weld of AISI 304 stainless steel pipes. J. Mater. Process. Technol. 248, 178–184.

Yang, L.J., Chandel, R.S., Bibby, M.J., 1992. The effects of process variables on the bead width of submerged-arc weld deposits. J. Mater. Process. Tech. 29, 133–144.

Yan, J., Gao, M., Zeng, X., 2010. Study on microstructure and mechanical properties of 304 stainless steel joints by TIG, laser and laser-TIG hybrid welding. Opt. Lasers Eng. 48, 512–517.

Yangida, N., Koide, H., 2008. Reduction of Residual Stress in Multi-layer Welded Plates by Applying Water-shower Cooling During Welding. J. Solid Mech. Mater. Eng. 2, 943–954.

Yilmaz A, F., Mustafa, G., 2017. Investigation of Mechanical Strength and Distortion in Submerged Arc Welding of AH36 Ship Steel Plate. J. Sh. Prod. Des. 33, 335–341.

Zargar, S.H., Farahani, M., Givi, M.K.B., 2016. Numerical and experimental investigation on the effects of submerged arc welding sequence on the residual distortion of the fillet welded plates. Proc. Inst. Mech. Eng. Part B J. Eng. Manuf. 230, 654–661.

Zhang, X.P., Dorn, L., 1999. Investigation on the possibility of using the microshear test as a surveillance method to estimate the mechanical properties and fracture toughness of nuclear pressure vessel steel, A508CL3, and its joints welded by narrow-gap submerged-arc welding. Int. J. Press. Vessel. Pip. 76, 35–41.

Zhang, L., Lu, J.Z., Luo, K.Y., Feng, A.X., Dai, F.Z., Zhong, J.S., Luo, M., Zhang, Y.K., 2013. Residual stress, micro-hardness and tensile properties of ANSI 304 stainless steel thick sheet by fiber laser welding. Mater. Sci. Eng. A 561, 136–144.

List of Publications

- **Journal papers**

1. Sridhar, P.V.S.S., Biswas, P. and Mahanta, P.,(2019). Influence of welding current on bead profile and mechanical properties of double sided submerged arc welding of AISI 304 austenitic stainless. Materials Today (Proceedings), Vol 19(2), pp. 831-836.
2. Saurav Suman, P. V. S. S. Sridhar, Pankaj Biswas, Deepjyoti Das.,(2020). Prediction of Welding Induced Distortions in Large Welded Structure through Improved Equivalent Load Method. Welding in the world, Vol 64, pp.179-200.
3. Narang, H.K., Mahapatra, M.M., Jha, P.K., Sridhar, P.V.S.S., and Biswas, P. (2018). Experimental and Numerical Study on Effect of Weld Reinforcement on Angular Distortion of SAW Square butt Welded Plates, Journal of Welding and Joining, Vol. 36(2), pp. 48-59.
4. Sridhar, P.V.S.S., Biswas, P. and Mahanta, P., Effect of Process Parameters on Bead Geometry, Tensile and Microstructural Properties of Double Sided Butt Submerged Arc Welding of SS 304 Austenitic Stainless Steel. (*Revised paper submitted*).
5. Comparative studies on effect of process parameters on mechanical properties and angular distortion between conventional and heat sink welding. (Under preparation).
6. Experimental investigation and Numerical study on single sided single pass submerged arc welding of austenitic stainless steel.(Under preparation).
7. Effect of surface active flux and heat sink on mechanical and microstructural properties on submerged arc welding of AISI 304 stainless steel (Under preparation).

- **Book chapters**

1. Sridhar, P.V.S.S., Vishnu, N, Biswas, P and Mahanta. 2019. Thermomechanical Analyses of Single Sided Single Pass Submerged Arc Welding of AISI 304 Austenitic Stainless Steel. *Advances in Computational Methods in Manufacturing, Lecture Notes on Multidisciplinary Industrial Engineering.*(Springer).
2. Sridhar, P.V.S.S., Kumar, S., K., Pal, K., Chakraborty, B.K., Bhattacharjee. R.,Majumder, S.,Biswas, P., and Mahanta., 2019. Experimental Investigation and Mechanical Characterization of Double-Sided Submerged Arc Welding of AISI 304

Austenitic Stainless Steel. *Advances in Additive Manufacturing and Joining.*(Springer).

- **Conferences papers**

1. Sridhar, P.V.S.S., Biswas, P., and Mahanta, P., 2016. Effect of Process Parameters on Tensile Strength of Submerged Arc Welded Austenitic Stainless Steel. *6th International & 27th All India Manufacturing Technology, Design and Research Conference (AIMTDR-2016), December 16-18, 2016 at College of Engineering., Pune, Maharashtra, INDIA.*
2. Sridhar, P.V.S.S., Biswas, P., and Mahanta, P., 2016. Experimental and Numerical Prediction of Thermal history in Single Sided Single pass Submerged Arc Welding of Austenitic Stainless Steel. *6th International & 27th All India Manufacturing Technology, Design and Research Conference (AIMTDR-2016), December 16-18, 2016 at College of Engineering., Pune, Maharashtra, INDIA.*
3. Sridhar, P.V.S.S., Kumar, S., K., Pal, K., Chakraborty, B.K., Bhattacharjee. R.,Majumder, S., Biswas, P., and Mahanta., 2018. Experimental Investigation and Mechanical Characterization of Double-Sided Submerged Arc Welding of AISI 304 Austenitic Stainless Steel. *7th International & 28th All India Manufacturing Technology, Design and Research Conference (AIMTDR-2018), December 13-15, 2018 at College of Engineering., Anna University., Chennai, Tamilnadu, INDIA.*
4. Sridhar, P.V.S.S., Vishnu, N, Biswas, P and Mahanta. 2019. Thermomechanical Analyses of Single Sided Single Pass Submerged Arc Welding of AISI 304 Austenitic Stainless Steel. *2nd International Conference on Computational Methods in Manufacturing. ICCMM 2019.,March 8-9, 2019., Indian Institute of Technology Guwahati, India.*
5. Sridhar, P.V.S.S., Biswas, P., and Mahanta, P., 2019. Influence of Welding Current on Bead profile and Mechanical properties of Double sided submerged arc welding of AISI 304 Austenitic stainless steel. *1nd International Conference on Manufacturing, Material Science and Engineering, ICMMSE 2019, August 16-17, 2019., CMRIT, Hyderabad.*